Effect of Sinter Additives on the Consolidation and Properties of Titanium Diboride Composites

By

T.S.R.Ch.Murthy
Enrolment Number: ENGG01200704007

BHABHA ATOMIC RESEARCH CENTRE

A thesis submitted to the
Board of Studies in Engineering Sciences Discipline

In partial fulfillment of requirements

For the Degree of

DOCTOR OF PHILOSOPHY

of

HOMI BHABHA NATIONAL INSTITUTE

October, 2012

Homi Bhabha National Institute

Recommendation of the Viva Voce Board

As members of the Viva Voce Board, we certify that we have read the dissertation prepared by Sri. T.S.R.Ch.Murthy entitled "Effect of Sinter Additives on the Consolidation and Properties of Titanium Diboride Composites" and recommended that it may be accepted as fulfilling the dissertation requirement for the Degree of Doctor of Philosophy,

____________________ Date: 2nd May, 2014
Chairman- Prof. P.K.Tewari

____________________ Date: 2nd May, 2014
Guide-Prof. A. K. Suri

____________________ Date: 2nd May, 2014
External Examiner-Prof. Anish Upadhyaya

N. Krishnamurthy ____________________ Date: 2nd May, 2014
Co-Guide-Prof. N. Krishnamurthy

2/5/2014 ____________________ Date: 2nd May, 2014
Member-1: Prof. R. C. Hubli

____________________ Date: 2nd May, 2014
Member-2: Prof. Dinesh Srivastava

2/5/2014 ____________________ Date: 2nd May, 2014
Member-3:Prof. (Smt) Sulekha Mukhopadhyay

Final approval and acceptance of this dissertation is contingent upon the candidate's submission of the final copies of the dissertation to HBNI.
I hereby certify that I have read this dissertation prepared under my direction and recommend that it may be accepted as fulfilling the dissertation requirement.

Date: 2nd May, 2014

Place: Mumbai **Guide:**

N. Krishnamurthy

CERTIFICATE

This is to certify that the thesis titled, "Effect of Sinter Additives on the Consolidation and Properties of Titanium Diboride Composites" submitted by Shri Tammana Sree Rama Chandra Murthy to Homi Bhabha National Institute, Mumbai for the award of the degree of Doctor of Philosophy is a bona fide record of the research work carried out by him under my (our) supervision and guidance. The content of the thesis, in full or parts have not been submitted to any other Institute or University for the award of any other degree or diploma.

Place: HBNI, Mumbai **Signature of guide:**

Date: May 2, 2014 **Name of guide: Prof. A.K.Suri**

Place: HBNI, Mumbai **Signature of co-guide:** N. Krishnam

Date: May 2, 2014 **Name of co-guide: Prof. N. Krishnamurthy**

STATEMENT BY AUTHOR

This dissertation has been submitted in partial fulfillment of requirements for an advanced degree at Homi Bhabha National Institute (HBNI) and is deposited in the library to be made available to borrowers under rules of the HBNI.

Brief quotations from this dissertation are allowable without special permission, provided that accurate acknowledgement of source is made. Requests for permission for extended quotation from or reproduction of this manuscript in whole or in part may be granted by the Competent Authority of HBNI when in his or her judgment the proposed use of the material is in the interests of scholarship. In all other instances, however, permission must be obtained from the author.

(T.S.R.Ch.Murthy)

DECLARATION

I, hereby declare that the investigations presented in the thesis have been carried out by me. The work is original and has not been submitted earlier as a whole or in part for a degree / diploma at this or any other Institution / University.

(T.S.R.Ch.Murthy)

International Journal Publications out of this thesis

[1] T.S.R.Ch.Murthy, J.K.Sonber, C.Subramanian, R.C.Hubli N.Krishnamurthy and A.K.Suri, "Densification, characterization and oxidation studies of (TiCr)B_2+20%$MoSi_2$," Int. J. Refract. Met. Hard Mater. 37, 12-28 (2013).

[2] T.S.R.Ch.Murthy, J.K.Sonber, C.Subramanian, R.C.Hubli N.Krishnamurthy and A.K.Suri, "Densification and Oxidation behavior of a novel TiB_2 - $MoSi_2$ - CrB_2 composite" Int. J. Refract. Met. Hard Mater. 36, 243-253 (2013)

[3] T.S.R.Ch.Murthy, J.K.Sonber, C.Subramanian, R.C.Hubli and A.K.Suri, "Densification, Characterization and Oxidation studies of TiB_2 + WSi_2 composite" Int. J. Refract. Met. Hard Mater. 33, 10-21 (2012)

[4] T.S.R.Ch.Murthy, J.K.Sonber, C.Subramanian, R.K.Fotedar, Sunil Kumar, M.R.Gonal and A. K. Suri, "A New TiB_2 + $CrSi_2$ composite - Densification, Characterization and oxidation studies" Int. J. Refract. Met. Hard Mater.28, 529-540 (2010)

[5] T.S.R.Ch.Murthy, C.Subramanian, R.K.Fotedar, M.R.Gonal, P.Sengupta, Sunil Kumar, A.K.Suri "Preparation and property evaluation of TiB_2+$TiSi_2$ composite" International Journal of Refractory Metals and Hard Materials; 27, 629–636 (2009)

[6] T.S.R.Ch.Murthy, J.K.Sonber, C.Subramanian, R.K.Fotedar, M.R.Gonal and A. K. Suri; "Effect of CrB_2 addition on densification, properties and oxidation resistance of TiB_2", Int. J. Refract. Met. Hard Mater., 27[6], 976-984 (2009)

[7] J. K. Sonber, T. S. R. Ch. Murthy, C. Subramanian, Sunil Kumar, R. K. Fotedar and A. K. Suri, Investigation on synthesis, pressureless sintering and hot pressing of chromium diboride Int. J. Refract. Met. Hard Mater.; 27, 912-918 (2009)

(T.S.R.Ch.Murthy)

Dedicated to my dear Parents,
Spouse and Guruji

ACKNOWLEDGEMENT

It is a great pleasure in presenting my thesis on completion of my project and in expressing my deepest regards and deep sense of gratitude and sincere thanks to my research guide Prof. Ashok Kumar Suri,, former Director, Materials Group and co-guide Prof. N. Krishnamruthy, Head, Fusion Reactor Materials Section for their valuable guidance in hours of need, constant encouragement, keen interest, good wishes and valuable suggestions throughout my entire research tenure. I am also grateful to them for critically reviewing this thesis.

It gives me immense pleasure to acknowledge my doctoral committee chairman Prof. P.K. Tewari, Head, Desalination Division (DD) and Prof. D. Sathiyamoorthy, former Head, Powder Metallurgy Division (PMD), for their constant support and for critically evaluating my research activities time to time.

It is also my great pleasure to thank Prof. R. C. Hubli, Head, Materials Processing Division, Shri. R.K.Fotedar and Shri. C.Subramanian for their support in carrying out the research work.

I wish to express my sincere thanks to my colleague Shri J.K.Sonber, Dr. Sanjay kumar for their diversified help, fruitful scientific discussions and moral support offered to me from time to time throughout the course of the PhD work. My special thanks goes to my colleagues and my dear friends Shri R D Bedse, Shri P.K.Mollick and Shri D. K Sahoo, for their moral support, diversified help, and several funs which will always be remembered. I would like to thank Dr A.K.Sahu, Dr. Vivekanand kain, Dr. Roy choudhary, Shri. Bhaskar Paul and Dr. Abhijit Ghosh for helping out with SEM analysis. Also special thanks to Shri. Nagarj Allangi for general support and fruitful discussions. I would like to thank Sri. Uttam Jain and Sairam K for their help during experiments. I would like to thank my colleagues Smt. D.S. Arati, Shri. K.M.Prasad, Shri. P.S.Yadav, Shri. S.B.Chavan, Shri. V. Ramdas and Shri Sumantha Behra for their co-operation and help during the experiments. It gives *me immense pleasure to thank the members of the doctoral committee Prof. P.K.Tewari (Chairman), Prof. R.C.Hubli (Member), Prof. Dinesh Srivastava (Member) and Prof. (Smt) Sulekha Mukhopadhyay (Member) for their critical review and suggestions. I also gratefully acknowledge the help rendered by all the members of Materials Processing Division, Materials Science Division and Fusion Reactor Materials Section for their co-operation and help during my PhD work. I would like to express my sincere salutes to all my professors at NIT-Warangal and IIT-Kanpur. Special thanks to Prof. Bikramjit Basu for his invaluable guidance during my M.Tech period. I wish to express my sincere gratitude and indebtedness to my parents, parents-in-laws, brothers and sisters for their blessings, for their love and support to me. I am extremely thankful to my spouse Smt. T. Padmavathi and my daughter Kum. T. Aamuktha for their patience and understanding. At the last, I am thankful to all the reviewers of my published papers whose comments on my manuscript always upgraded my scientific thought and open a new way of thinking.*

(T.S.R.Ch.Murthy)

Preface

Completing the Ph.D degree has been one of the most cherished dreams of my life right from the early days of my graduation. The outcome of the dreams comes in the form of the present Ph.D thesis. This thesis is submitted in partial fulfillment of the requirements for the Ph.D degree at the Homi Bhabha National Institute, Mumbai, India. The thesis presents the results obtained during my work at the Materials Processing Division, Materials Group, BARC during the period of September, 2007 to August, 2012. The work has been performed under the supervision of **Professor Ashok Kumar Suri**, former Director, Materials Group (MG), BARC and **Professor Nagaiyar Krishnamurthy**, Outstanding Scientist and Head, Fusion Reactor Materials Section, MG, BARC. The motivation for the work presented in this thesis is the fact that titanium diboride (TiB_2) is a structural ceramic material that is attracting attention as the base material for a range of high technological applications. However, consolidation of TiB_2 is difficult due to low self-diffusion coefficient and existence of surface oxides on the powder particles. Silicides were considered as possible additives because of their ability to reduce the surface oxides thereby enhancing densification. Moreover silicides are also expected to improve high temperature oxidation resistance by the formation of a protective glassy layer on the surface which would impede further oxidation. The ultimate aim of this thesis is to arrive at a high performance TiB_2 material which should have full density, high fracture toughness and superior oxidation resistance as compared to the conventional TiB_2. Carrying out experimental studies on these aspects has resulted in a number of peer-reviewed international publications. Paper 1 & 7 are directly related to materials synthesis and it served as the foundation of this thesis. Papers 1 to 6 are related to densification, microstructural characterization and oxidation studies of six different composites, which were developed in our laboratory.

In addition, results have been presented and published in a number of international and national meetings and symposium proceedings.

Peer-reviewed International Publications from the PhD work are listed below:

[1] T.S.R.Ch.Murthy, J.K.Sonber, C.Subramanian, R.C.Hubli N.Krishnamurthy and A.K.Suri, "Densification, characterization and oxidation studies of $(TiCr)B_2$+20%$MoSi_2$," Int. J. Refract. Met. Hard Mater. 37, 12-28 (2013).

[2] T.S.R.Ch.Murthy, J.K.Sonber, C.Subramanian, R.C.Hubli N.Krishnamurthy and A.K.Suri, “Densification and Oxidation behavior of a novel TiB_2 - $MoSi_2$ - CrB_2 composite” Int. J. Refract. Met. Hard Mater. 36, 243-253 (2013)

[3] T.S.R.Ch.Murthy, J.K.Sonber, C.Subramanian, R.C.Hubli and A.K.Suri, “Densification, Characterization and Oxidation studies of TiB_2 + WSi_2 composite” Int. J. Refract. Met. Hard Mater. 33, 10-21 (2012)

[4] T.S.R.Ch.Murthy, J.K.Sonber, C.Subramanian, R.K.Fotedar, Sunil Kumar, M.R.Gonal and A. K. Suri, **“**A New TiB_2 + $CrSi_2$ composite - Densification, Characterization and oxidation studies” Int. J. Refract. Met. Hard Mater.28, 529-540 (2010)

[5] T.S.R.Ch.Murthy, C.Subramanian, R.K.Fotedar, M.R.Gonal, P.Sengupta, Sunil Kumar, A.K.Suri “Preparation and property evaluation of TiB_2+$TiSi_2$ composite” International Journal of Refractory Metals and Hard Materials; 27, 629–636 (2009)

[6] T.S.R.Ch.Murthy, J.K.Sonber, C.Subramanian, R.K.Fotedar, M.R.Gonal and A. K. Suri; “Effect of CrB_2 addition on densification, properties and oxidation resistance of TiB_2”, Int. J. Refract. Met. Hard Mater., 27[6], 976-984 (2009)

[7] J. K. Sonber, T. S. R. Ch. Murthy, C. Subramanian, Sunil Kumar, R. K. Fotedar and A. K. Suri, Investigation on synthesis, pressureless sintering and hot pressing of chromium diboride Int. J. Refract. Met. Hard Mater.; 27, 912-918 (2009)

(T.S.R.Ch.Murthy)

Acronyms

K : Kelvin
T : temperature
G : Gibbs free energy
t : time
μ : micron
Ω : resistance
Δ : change
m : mass
Q : activation energy
P_a : Pascal
p : pressure
ρ : density
σ : conductivity
V : volume
%: weight percent (unless otherwise specified)
K_p: parabolic rate constant
K_m: general rate constant
m: general rate equations exponent
Δw: change in weight
A: surface area
R: resistance
I: current
TD: theoretical density
RD: relative density
Kg: kilogram
g: gram

Contents

Page Number

Introduction, Objectives and Work Plan of Present Study

Literature Survey

Experimental Procedure

Synthesis of starting Powders

Densification, Microstructure, Mechanical and Physical Properties

Summary and Scope for Future Work

SYNOPSIS OF THE THESIS TO BE SUBMITTED TO THE HOMI BHABHA NATIONAL INSTITUTE FOR THE DEGREE OF DOCTOR OF PHILOSOPHY IN ENGINEERING SCIENCES

Name of the Candidate : T.S.R.Ch.Murthy

Name of the Guide : Prof. Ashok Kumar Suri
Engineering Sciences,
Homi Bhabha National Institute, Mumbai, INDIA

Name of the Co-Guide : Prof. N.Krishnamurthy
Chemical Sciences,
Homi Bhabha National Institute, Mumbai, INDIA

Registration Number : ENGG01200704007

Date of Registration : 04-06-2007

Title of the Thesis : Effect of Sinter Additives on the Consolidation and Properties of Titanium Diboride Composites

Place of Research Work : Materials Processing Division,
Bhabha Atomic Research Centre, Trombay,
Mumbai – 400 085, INDIA

Title: Effect of Sinter Additives on the Consolidation and Properties of Titanium Diboride Composites

Preamble

Titanium diboride is a material of interest for future high temperature applications in aggressive environments and it would be one of the attractive materials in nuclear reactors as a neutron absorber. However, there are difficulties in the fabrication of this material with high density and high fracture toughness. Though these properties can be achieved with some additives which may be either in the form of metal or ceramic, the choice of appropriate additives hitherto remains challenge. Our study is focused on the experimental investigations of ceramic additives to enhance the densification and fracture toughness. Metallic additives by and large were not considered due to limitation of their use at high temperatures.

The additive to start with should have low vapour pressure and high melting point. Its thermal conductivity and co-efficient of thermal expansion should be similar to the matrix material viz. titanium diboride. It is also important that these additives form protective or passive oxide layer for protection in aggressive environment.

The objective of present study is to synthesize and consolidate TiB_2 with various ceramic additives such as silicides, borides and combined borides and silicides ($CrSi_2$, $TiSi_2$, WSi_2, CrB_2, CrB_2 + $MoSi_2$ to TiB_2). This study also includes the compound such as pre alloyed $(TiCr)B_2$ with the aim of investigating the advantages and properties of composite formed with this additive. The ultimate aim of this thesis is to arrive at a high performance TiB_2 material which should have high density, high fracture toughness and superior oxidation resistance as compared to the monolithic TiB_2.

Figure 1 summarises the scheme of present study i.e. effect of silicide additives on densification and oxidation behaviour of TiB_2. Our investigations and results on the addition of ceramic additives are presented in this thesis in seven chapters, a brief account of each chapter is given below.

Chapter-I presents the introduction, objectives and work plan of the present work. Titanium diboride (TiB_2) is a structural ceramic material that is attracting attention as the base material for a range of high technological applications. However, consolidation of TiB_2 is difficult due to low self-diffusion coefficient and existence of surface oxides on the powder particles. Silicides were considered as possible additives because of their ability to reduce the surface oxides thereby enhancing densification. Moreover silicides are also expected to improve high temperature oxidation resistance by the formation of a protective glassy layer on the surface which would impede further oxidation.

Chapter II (Literature Survey)

A detailed literature survey on the synthesis and consolidation of TiB_2 is presented. Effect of various metallic and non-metallic additives on densification and thermo mechanical behaviour of TiB_2 with relative merits and de-merits are enumerated. The potential applications of this material and need for a high performance TiB_2 composite is emphasised.

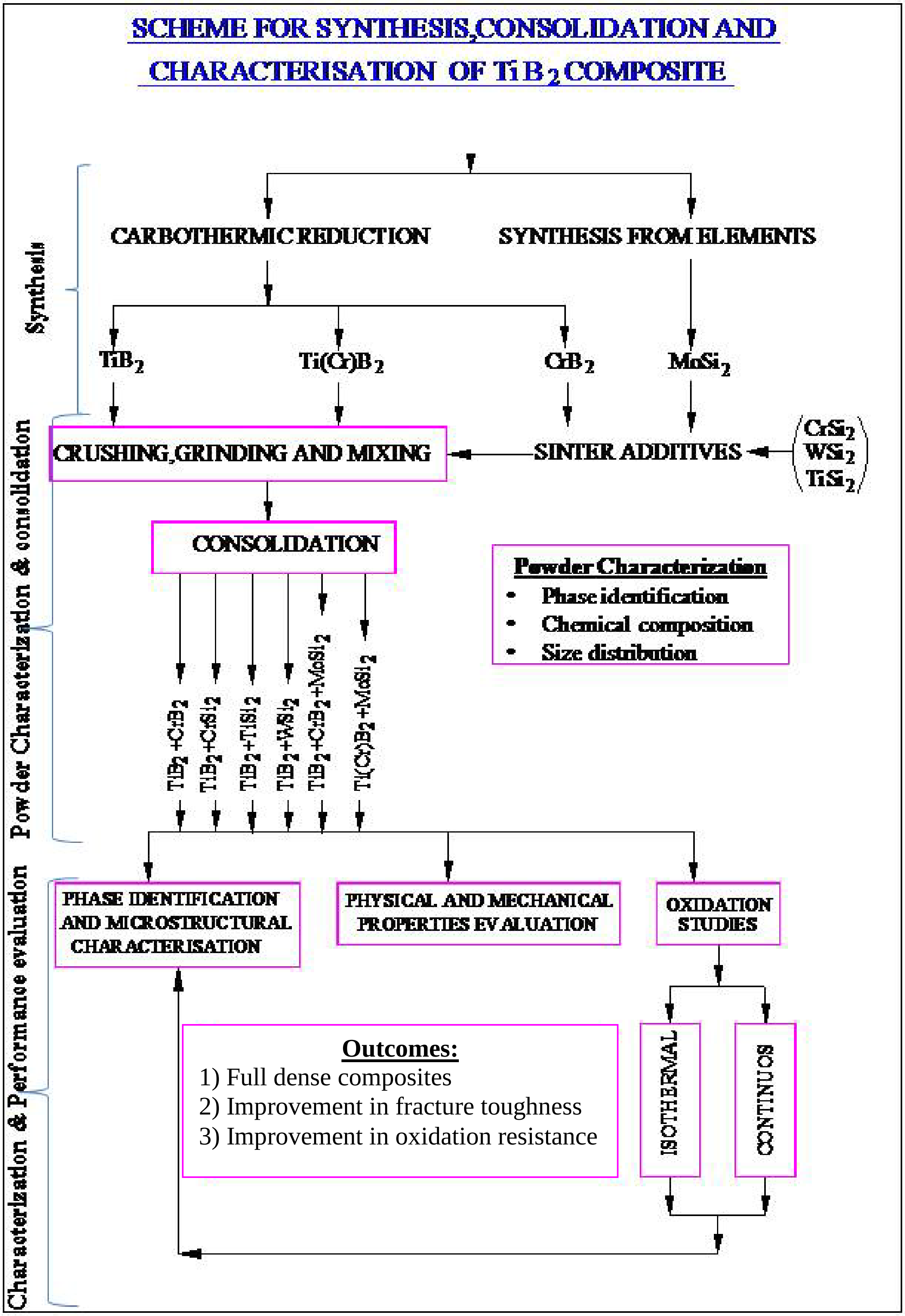

Fig. 1 Scheme for the present thesis work

Chapter III (Materials, Equipments and Experimental Procedure)

In this chapter, experimental details of the preparation of TiB_2 and various other materials used as sinter additives, densification, and characterization of start and sintered materials as well as the equipment used are described.

A number of equipments and instruments have been used in the present study. A description and working principle of each of the instrument/equipment is given in this chapter in a chronological order. These facilities are broadly classified into four categories: 1) milling equipments 2) furnaces 3) sample preparation/fabrication equipment and 4) characterization instruments.

In the present work, TiB_2, CrB_2 and pre-alloyed $(TiCr)B_2$ were synthesized by carbothermic reduction of the respective oxides in the presence of boron carbide. Various sinter additives (silicides and boride) are used in the present study. These materials were either prepared in the laboratory or procured from the commercial sources.

Starting powders viz., TiB_2, $(TiCr)B_2$, CrB_2 and $MoSi_2$ were synthesized and characterized. Experimental procedure adopted to carry out the synthesis and characterization of these materials is fully described. Similarly experimental procedure of consolidation of composites, which were carried out by vacuum hot pressing and pressureless sintering are also described. Phase identification and microstructural characterization method of dense pellets are described. Mechanical and physical property evaluation methods and experimental procedure of densified samples are described.

Oxidation studies of these composites were carried out in the temperature range of 1023 to 1273K (750 to 1000^{o}C). Continuous oxidation studies were carried out in TGA and isothermal oxidation studies in muffle furnace for all the composites. Oxidized samples were characterized by XRD, XPS and SEM-EDS.

Chapter-IV (Results and Discussion on Synthesis of starting powders)

This chapter presents the results of investigations carried out on synthesis of titanium diboride and, chromium diboride by carbothermic reduction of respective oxides with boron carbide and carbon. Pre-alloyed $(TiCr)B_2$ synthesized by co-reduction of mixed oxides with boron carbide and carbon. Details of synthesis of $MoSi_2$ by direct elemental reaction are also presented in this chapter. CrB_2 and $MoSi_2$ were used as sintering additives to TiB_2 and $(TiCr)B_2$ for preparing the composites.

Chapter V (Results and Discussion on Densification, Microstructure, Mechanical and Physical Properties)

This chapter has been divided in to three sections. Section I presents the results of densification of the composites. Section II is concerned with the phase identification and microstructural characterization together with thermodynamic analysis to understand the densification mechanism. Section III presents results on the physical and mechanical properties of the developed composites and structure property relations to understand the toughening mechanisms.

Section-I: (Densification)

Effect of various sinter additives on densification of TiB_2 by hot pressing are presented in Fig. 2. Near theoretical density was obtained with the addition of 5 wt.% WSi_2 to TiB_2 as compared with all the other additives. It was observed that with increase in amount of sinter additive the density value was found to decrease in the case of TiB_2 composites with CrB_2 and $CrSi_2$. However the density remained constant in the case of

WSi_2 and $TiSi_2$ content in TiB_2. Combined addition of CrB_2 and $MoSi_2$ however improved the density to ≥95% TD.

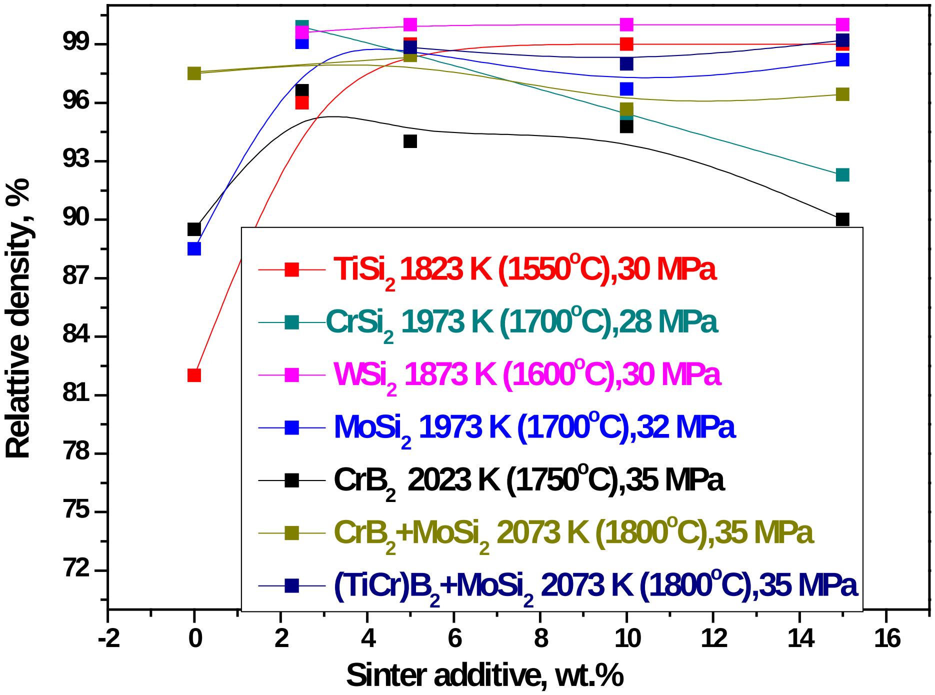

Fig. 2: Effect of various sinter additives on densification of TiB_2 (Line joining points are for visual aid only)

Section-II: (Phase identification and Microstructural characterization)

Densified pellets were characterized by XRD, SEM-EDS, EPMA and attempt has been made to explain the mechanisms of densification and strengthening. XRD analysis confirmed that the hot pressed pellets contained several reaction products between TiB_2 and the additives.

XRD pattern of the hot pressed TiB_2 + $TiSi_2$ samples showed the presence of Ti_5Si_3 in all the samples. XRD patterns of hot pressed TiB_2 + $CrSi_2$ pellets revealed the presence of TiB_2 and $CrSi_2$ phases, thus indicating the absence of any new phase due to reaction. Although TiB_2 and $CrSi_2$ peaks were identified in both the starting mixture and the hot pressed pellet, the decrease in intensity and number of $CrSi_2$ peaks, absence of any reaction products and small shift in TiB_2 peaks, indicate the formation of solid solution of TiB_2 with $CrSi_2$ in the hot pressed pellets. Similar observations were also noticed in the case of TiB_2 + CrB_2 composites. The disappearance of CrB_2

and a slight shift in the position of TiB_2 peaks clearly indicated the formation of solid solution of TiB_2 and CrB_2. In TiB_2 + WSi_2 system, XRD patterns of starting powders showed the presence of TiB_2, WSi_2 and Ti_6O_{11}, whereas hot pressed pellet showed the presence of W_5Si_3, SiO_2 and TiB_2 phases. SiO_2 formation helped in enhancing the densification by liquid phase sintering. The number of peaks and the intensity of W_5Si_3 and SiO_2 peaks are seen to increase with increase in the addition of WSi_2 from 5 to 15%.

The quantity of reaction products with less than 5% additive was not sufficient and therefore analysis by SEM-EDS was rather difficult. Hence, samples with 10% sinter additive were chosen for SEM - EDS analysis. Back Scattered Electron (BSE) image of TiB_2 + 10%WSi_2 sample revealed two distinct types of regions in the microstructure: grey matrix and white regions. The white region shows the presence of silicon and W whereas Ti was present in grey region. Line scan and elemental mapping for Ti, Si and W across the grey and white regions are presented in this chapter. Back Scattered Electron image (BSE) of TiB_2 + 10%$TiSi_2$ sample showed three distinct regions as grey matrix, and black & white spots in the matrix. More details on the origin of phases and their chemical composition will be elaborately discussed in this chapter. BSE image of TiB_2 + 10%$CrSi_2$ sample revealed three distinct types of regions; dark grey matrix, black and white regions. Line scan for Ti, Si and Cr across the white and black regions were carried out. The black region showed the presence of silicon only (Cr is absent) whereas Ti and Cr are present in white region. BSE image of $(TiCr)B_2$ + $MoSi_2$ sample revealed three types of regions; grey matrix, black and white spots. More details on the EPMA/EDS results and analysis of all the composites will be presented in this chapter. In addition fractography and crack propagation patterns were analyzed to explain the mode of fracture and the crack propagation mechanisms in all the composites. Crack deflection, bridging and branching mechanisms were mainly observed in these composites.

Section-III: (Physical and Mechanical Properties)

Hardness and fracture toughness values of all the composites were measured. Variation of the hardness value is dependent on the density, nature of second phase and its quantity in the composite. Similarly the fracture toughness also depends on the above cited parameters. Physical properties like coefficient of thermal expansion (CTE), electrical resistivity were measured in the temperature range of RT – 1273K (1000°C).

Vickers hardness values of composites of TiB_2 with 2.5% and 5% $TiSi_2$ were found to be 18 ± 2 and 25 ± 2 GPa respectively. The hardness value of composite with 2.5% $CrSi_2$ (99.89% TD) was 29 ± 2 GPa. With increased addition of $CrSi_2$ the hardness decreased linearly and the hardness of composites with 5%, 10% and 15% $CrSi_2$ were measured as 28 ± 3, 26 ± 2 and 22 ± 3 GPa respectively. Hardness values of the composite with varying WSi_2 were measured to be in the range of 24 - 26 GPa. Hardness values of all the TiB_2 + CrB_2 composites are close to 24 GPa. With increased addition of CrB_2 in TiB_2 + x%CrB_2 + 20%$MoSi_2$ composite the hardness decreased linearly and the hardness of composites with 5%, 10% and 15% CrB_2 were measured as 24 ± 1, 19 ±1 and 18 ± 1 GPa respectively. Hardness values of all the $(TiCr)B_2$ + 20%$MoSi_2$ composites are in the range of 24 - 27 GPa.

Measured indentation fracture toughness of monolithic TiB_2 was 3.78 ± 1.5 $MPa.m^{1/2}$, and those with the addition of $TiSi_2$ were in the range of 4-6 $MPa.m^{1/2}$. Indentation fracture toughness of TiB_2 + 2.5% $CrSi_2$ was found to be 5.97 ± 0.61 $MPa.m^{1/2}$, which decreased to 3.41 ± 0.94 $MPa.m^{1/2}$ with increased addition of 15% $CrSi_2$. Fracture toughness of TiB_2+WSi_2 composite was moderately higher i.e., in the range of 4-6 $MPa.m^{1/2}$ compared to 3-4 $MPa.m^{1/2}$ for monolithic TiB_2. Average indentation fracture toughness of 2.5, 5 and 10% CrB_2 composites were found as 2.80 ± 0.13, 4.30 ± 0.38 and 4.99 ± 0.99 $MPa{\cdot}m^{1/2}$ respectively.

Average CTE values of 6.4, 6.6, 7.2 and 6.8 x 10^{-6} K^{-1} were measured over a temperature range i.e. 473 – 1173 K (200 - 900^o C) for TiB_2 + $TiSi_2$, TiB_2 + $CrSi_2$, TiB_2 + WSi_2 and TiB_2 + CrB_2 composites respectively.

Chapter VI (Results and Discussion on Oxidation studies)

This chapter discusses about the continuous and isothermal oxidation studies of the developed TiB_2 composites. Specific weight gain vs. time plots were fitted in parabolic and general rate equations to calculate the rate constants and to determine the slope of the oxidation curve. Salient results of the oxidation studies are given briefly in the following two sections.

Section I (Non Isothermal/Continuous Oxidation)

TGA plot on continuous oxidation of TiB_2 composites in O_2 showed three different stages of weight gain: 1) no change in sample weight up to 673-873K (400-600^{o}C), 2) a gradual weight gain between 873 to 1073K (600 to 800^{o}C)/ sudden increase in weight gain and 3) a steep weight gain above 1073K (800^{o}C). For all composites (except TiB_2 + CrB_2), the total specific weight gain is found to be less than 30 x 10^{-3} kg/m^2 and the rate of weight gain are similar. In case of TiB_2+CrB_2, the total specific weight gain is found to be in the range of 55 to 65 x 10^{-3} kg/m^2. Morphology of the oxidized surfaces was taken in SEM.

Section II (Isothermal Oxidation)

This section presents on the results and discussion of isothermal oxidation studies. Mechanism of oxidation was understood from the kinetics data. XRD and SEM analysis were used to identify the oxidized products and their morphology.

An increase in weight with time is noted in all the samples. With increasing quantity of sinter additive, decrease in weight gain rate is seen in all the samples. In order to understand the nature of oxidation, the oxidation data was fitted in the general rate equation: $(\Delta w/A)^m = K_m.t$; The nature of oxidation was observed from linear to parabolic as seen by the slope of the curve (‘m’ value) in different composites. To understand the kinetics of oxidation, the data was analyzed using the parabolic law: $(\Delta w/A)^2 = K_p.t$. Parabolic rate constants of the composites are in the order 10^{-7} to 10^{-11} Kg m^{-4} s^{-1}. More details of the oxidized surfaces were analyzed by XRD, SEM-EDS and XPS. Cross section of the TiB_2 + 15%CrB_2 + $MoSi_2$ oxidized surface after 256h was characterized by SEM-EDS. Outer most layer of oxidized surface is seen to be that of boron oxide. The next inner layer is seen to be that of silicon oxide. Higher silicon content is seen from 5 to 60 μm from the outer layer. This shows that silicon and boron migrates to the outer surface. Various possible overall oxidation reactions are presented and the free energy of formation for these reactions at 0.21 atm partial pressure of oxygen was calculated. Effect of various sinter additives ($TiSi_2$/$CrSi_2$/CrB_2/WSi_2/$MoSi_2$) and its quantity on oxidation behavior of TiB_2 is analyzed and presented in this chapter.

Chapter VII (Summary)

Synthesis of borides by a process (boron carbide reduction) which avoid elemental constituent process is amenable to control the yields product consistently and robust for execution. A persistent challenge in the use of (TiB_2) borides is getting in the form of consolidated dense bodies. The inapplicability of cold compaction and sintering is established and the superiority of hot pressing for consolidation is also demonstrated for obtains the dense composites. Possible mechanisms for densification by hot pressing are brought out. Technological useful properties (hardness, fracture toughness, flexural strength, coefficient of thermal expansion and electrical resistivity) of the consolidated composites have been measured and the oxidation behavior of these composites also has been evaluated. The role of various additives in consolidation and their influence on the properties including oxidation resistance also has been brought out. The major findings of the present thesis have been summarized below:

1) WSi_2 and $TiSi_2$ have been found to be effective sinter additives to TiB_2. Compacts with near theoretical density were obtained with the addition of ≥5% $WSi_2/TiSi_2$ by hot pressing at 1823/1873 K (1550/1600° C), 30 MPa.

2) Improved fracture toughness (4.6-6.3 $MPa.m^{1/2}$) values were measured in TiB_2 composites. Crack branching, deflection and bridging mechanisms were responsible for improved fracture toughness values. However, hardness values decreased from 32 to 20-29 GPa in the developed composites compared with monolithic TiB_2.

3) Isothermal and continuous oxidation studies show the minimum weight gain in the developed composites. Nature of the oxidation changed from linear to parabolic with increasing quantity of sinter additive. TiB_2 + WSi_2 composite exhibits superior oxidation resistance as compared to other TiB_2 composites with $MoSi_2$, $TiSi_2$, CrB_2 and $CrSi_2$.

4) Microscopic observation of the oxidized surface (≥10% sinter additive) presented a crack free continuous, dense and protective glassy layer.

5) From the present studies, $(TiCr)B_2$ +20%$MoSi_2$ composite is found as the best composite with respect to densification, fracture toughness and oxidation resistance.

List of International Journal Publications included in the present thesis

1. T.S.R.Ch.Murthy, J.K.Sonber, C.Subramanian, R.C.Hubli N.Krishnamurthy and A.K.Suri, "Densification, characterization and oxidation studies of $(TiCr)B_2$+20%$MoSi_2$," Int. J. Refract. Met. Hard Mater. . 37, 12-28 (2013)

2. T.S.R.Ch.Murthy, J.K.Sonber, C.Subramanian, R.C.Hubli N.Krishnamurthy and A.K.Suri, "Densification and Oxidation behavior of a novel TiB_2 - $MoSi_2$ - CrB_2 composite" Int. J. Refract. Met. Hard Mater. 36, 243-253 (2013)

3. T.S.R.Ch.Murthy, J.K.Sonber, C.Subramanian, R.C.Hubli and A.K.Suri, "Densification, Characterization and Oxidation studies of TiB_2 + WSi_2 composite" Int. J. Refract. Met. Hard Mater. 33, 10-21 (2012)

4. T.S.R.Ch.Murthy, J.K.Sonber, C.Subramanian, R.K.Fotedar, Sunil Kumar, M.R.Gonal and A. K. Suri, **“**A New TiB_2 + $CrSi_2$ composite - Densification, Characterization and oxidation studies” Int. J. Refract. Met. Hard Mater.28, 529-540 (2010)

5. T.S.R.Ch.Murthy, C.Subramanian, R.K.Fotedar, M.R.Gonal, P.Sengupta, Sunil Kumar, A.K.Suri “Preparation and property evaluation of TiB_2+$TiSi_2$ composite” Int. J. Refract. Met. Hard Mater., 27, 629–636 (2009)

6. T.S.R.Ch.Murthy, J.K.Sonber, C.Subramanian, R.K.Fotedar, M.R.Gonal and A. K. Suri; “Effect of CrB_2 addition on densification, properties and oxidation resistance of TiB_2”, Int. J. Refract. Met. Hard Mater., 27[6], 976-984 (2009)

7. J. K. Sonber, T. S. R. Ch. Murthy, C. Subramanian, Sunil Kumar, R. K. Fotedar and A. K. Suri, Investigation on synthesis, pressureless sintering and hot pressing of chromium diboride Int. J. Refract. Met. Hard Mater.; 27, 912-918 (2009)

<u>Conferences</u>

1. T.S.R.Ch.Murthy, J.K.Sonber, R.D.Bedse, K. Sairam, R.C. Hubli and A.K. Suri, “Oxidation and Thermal Shock behavior of TiB_2 based Composites”, 49th NMD and 65th Annual Technical meeting of the Indian Institute of Metals (IIM), at Leonia Resorts, Hyderabad, (2011).

2. T.S.R.Ch.Murthy, J.K.Sonber, R.D.Bedse, R.K.Fotedar, N.Krishnamurthy and A. K. Suri; “Development and characterization of Titanium diboride (TiB_2)+ silicide composites” 48th NMD and 64th Annual Technical meeting of the Indian Institute of Metals (IIM), at IISc, Bangalore, (2010).

3. T.S.R.Ch.Murthy and J.K.Sonber; “High temperature oxidation studies of titanium diboride (TiB_2) and its composites”, Proceedings of the 17th National Symposium on thermal analysis, Kurukshetra (2010).

4. T.S.R.Ch.Murthy, J.K.Sonber, C.Subramanian, N. Krishnamurthy, Sunil Kumar and A. K. Suri; “Effect of CrB_2 addition on the oxidation behavior of TiB_2+$MoSi_2$“ International conference on Advances in Electron Microscopy and Related Techniques & XXXI Annual meeting of EMSI, (EMSI-2010), Mumbai.(2010).

5. T.S.R.Ch.Murthy, J.K.Sonber; “Evaluation of sintering mechanism and mechanical properties of boride based composites by microstructure using EPMA /SEM with EDAX” Microtexture and Microstructure (Microstructure-2009) organized by Materials Research Society of India (MRSI), Mumbai Chapter. (2009)

6. T.S.R.Ch.Murthy, J.K.Sonber, C.Subramanian, A.K.Suri; “Synthesis of Refractory Metal Diborides” 45th NMD and 61st Annual Technical meeting of the Indian Institute of Metals (IIM), at Nehru centre, Mumbai, 2007. (Awarded as Best Technical poster)

LIST OF FIGURES

LIST OF TABLES

CHAPTER 1

CHAPTER 1

INTRODUCTION, OBJECTIVES AND WORK PLAN OF PRESENT STUDY

1.1 Introduction

Structural ceramics are suitable for high temperature applications due to their high melting point and retention of strength up to high temperatures. Titanium diboride (TiB_2) is a structural ceramic material that is attracting attention as the base material for a range of high technological applications [1-5]. TiB_2 has many attractive properties, including exceptional hardness (approximately 25–35 GPa at room temperature which makes it more than three times harder than fully hardened structural steel), which is retained up to high temperature. It has high melting point (~3500K), good creep resistance, good thermal conductivity (65 W/m/K), high electrical conductivity and considerable chemical stability [5]. This combination of properties makes TiB_2 a candidate material for heavy duty wear applications, at elevated temperatures. TiB_2 can also be used as control rod and shielding material in nuclear reactors because it contains boron and which has ability to absorb fast and slow neutrons without forming long lived radionuclide. Absorption cross section of TiB_2 for fast neutrons can be enhanced by having compounds with enriched B^{10} isotope during the synthesis of TiB_2. Natural boron contains about 19% B^{10} isotope and remaining is B^{11} [1-8].

For high temperature applications, chemical stability is an important factor. TiB_2 is more stable in contact with pure iron as compared to WC or Si_3N_4. TiB_2 based materials should therefore be preferable for engineering applications as compared to WC based materials for high temperature applications [5]. Its chemical inertness at high temperatures and good electrical conductivity (~10^5 S/cm) make TiB_2 an excellent candidate for special electrical applications, e.g. cathodes for aluminum electrosmelting (Hall-Heroult process) [5,8-10].

However, monolithic TiB_2 has relatively low fracture toughness (<5 $MPa.m^{1/2}$), it's sensitive to slow subcritical crack growth and its oxidation resistance is only moderate. These characteristics limit its use in many engineering applications. The self-diffusion coefficient of monolithic TiB_2 is also low and this makes it very difficult to densify [4,5]. One option to improve the sinterability/toughness of boride and carbide materials leads to an important class of composite structural materials, popularly known as cermets, wherein a metallic binder is used to obtain dense bulk materials. TiB_2 based cermets typically contain TiB_2 as the major phase, bonded with a metallic phase (Co–Ni). Cemented borides with a metallic binder have been developed in the TiB_2–Fe system. These materials are novel lower density and higher hardness substitutes for the WC–Co system [1-10].

Metallic additives like Ni, Fe, Cr, Al have been used to densify TiB_2 with retention of room temperature properties, but the presence of metallic additives in TiB_2 is not acceptable for high temperature applications. The presence of metallic binder is problematic due to the low melting point of either metallic additives or sintering reaction product which may lead to incipient fusion and consequent degradation of high temperature properties [4,5]. In view of the above, research has progressed towards the densification of TiB_2 using non-metallic sinter additives like oxides (Al_2O_3, ZrO_2), carbides (B_4C, SiC, TiC, WC), nitrides (AlN, Si_3N_4), silicides ($MoSi_2$, $TiSi_2$), and borides (CrB_2, ZrB_2). Among these additives, silicides have attracted considerable interest due to their compatibility with borides to densify at lower temperatures [5,8]. Silicides were considered as possible additives because of their ability to reduce the surface oxides thereby enhancing densification. Moreover silicides are also expected to improve high temperature oxidation resistance by the formation of a protective glassy layer on the surface which would impede further oxidation.

As reinforcement, TiB_2 is also incorporated in several ceramic microstructures to obtain improved mechanical properties. The addition of TiB_2 to an Al_2O_3 or Si_3N_4 matrix considerably increases hardness, strength, fracture toughness and electrical conductivity. Such composites have been used in wear parts, cutting tools and heat exchangers. These electro-conductive toughened ceramics can be shaped by electro discharge machining (EDM) to manufacture complex components, greatly increasing the number of potential industrial applications [5,8].

1.2 Objectives

Though some work has been reported earlier with the addition of $TiSi_2$, WSi_2, $MoSi_2$ and CrB_2 in pressureless/ microwave sintering and hot pressing of TiB_2 composites, detailed studies on the preparation and characterization of TiB_2+WSi_2, TiB_2+CrB_2,TiB_2+$CrSi_2$ and combined addition of $MoSi_2$ and CrB_2 composite have not been reported so far. Available Literature data on these composites are summarized in Table 1.1. The objective of present study is to synthesize and consolidate TiB_2 with various ceramic additives such as silicides, borides and a combination of borides and silicides ($CrSi_2$, $TiSi_2$, WSi_2, CrB_2, CrB_2 + $MoSi_2$ to TiB_2). This study also includes the compound such as pre alloyed $(TiCr)B_2$ with the aim of investigating the advantages and properties of composite formed with this additive. The ultimate aim of this thesis is to arrive at a high performance TiB_2 material which should have high density, high fracture toughness and superior oxidation resistance as compared to the conventional TiB_2.

1.3 Work Plan

Figure 1.1 summarizes the scheme of the present study i.e. synthesis of start materials, the additives that have been studied, the effect of silicide additives on densification and oxidation behaviour of TiB_2 and on the physical and mechanical properties. All these are presented in this thesis in seven chapters.

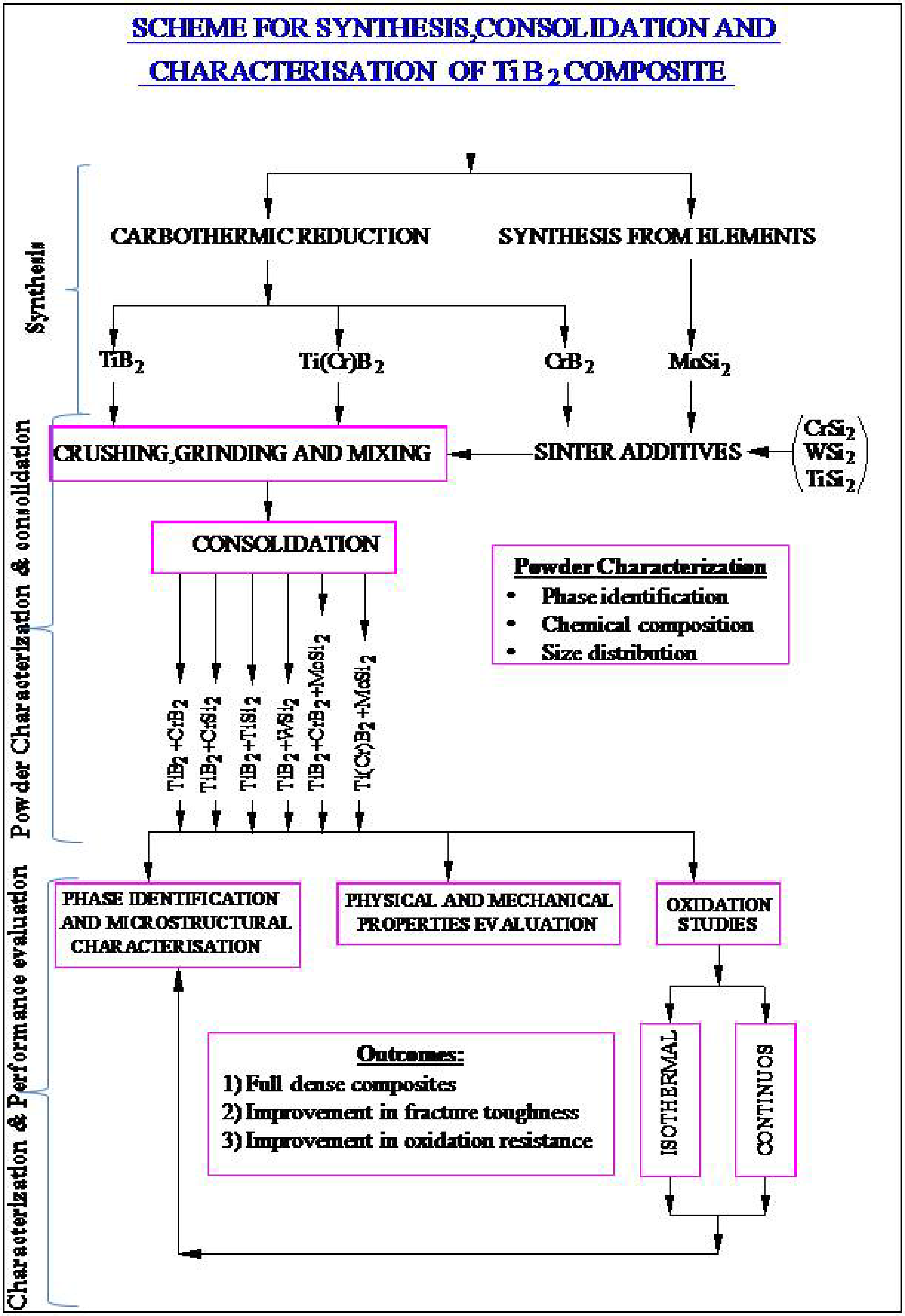

Fig. 1.1 Scheme for the present thesis work

Table 1.1 Summary on the available literature data of the similar TiB_2 composites

Sr. No.	Sinter additive	Processing conditions	Densification results	Mechanical properties	Physical properties	Oxidation results	Ref. no.
1	$TiSi_2$	HP 1650° C, 30MPa, Ar	>99%TD and reaction product: Ti_5Si_3	Hv- 23-25 GPa K_{IC}- 4-6 MPa $m^{1/2}$	Elastic Modululs: 470-520 GPa	Near parabolic covered with SiO_2, borosilicate glass and TiO_2	Raju et.al [11-13]
2	$CrSi_2$	No work reported					
3	WSi_2	1700° C, 60 min	>98%TD	Not studied		Resistant to aluminum liquid corrosion	Lu et.al. [14]
4	$MoSi_2$	HP 1700° C,60 min, vacuum	>98%TD and reaction product: $TiSi_2$	Hv- 25-27 GPa K_{IC}- 4-5 MPa $m^{1/2}$	TC: 50 W/m/K	Very poor due to Pesting of $MoSi_2$	Murthy et.al. [4,15]
5	CrB_2	MW at 2100°C,30 min, Ar	98%TD	27.0 DPH K_{IC}- 6.1 MPa.$m^{1/2}$	Not studied		Holcombe et.al [16]
6	CrB_2+MoSi_2	No work reported					
7	$(TiCr)B_2$	No work reported					
8	$(TiCr)B_2+MoSi_2$	No work reported					

Detailed literature survey on the synthesis and consolidation of TiB_2 is presented in chapter 2. Effect of various metallic and non-metallic additives on densification and thermomechanical behaviour of TiB_2 with attendant merits and de-merits are enumerated. The potential applications of this material and need for a high performance TiB_2 composite is emphasised in chapter-2. Chapter 3 presents the experimental procedures. Results and discussions are presented in Chapters 4, 5 and 6 respectively. Synthesis of starting powders such as TiB_2, CrB_2 and $MoSi_2$ is described in chapter 4. Chapter 5 is divided into three sub-sections, which include consolidation by pressureless sintering and hot pressing, physical and mechanical properties and microstructural characterization. Isothermal and continuous oxidation studies and its results are presented in chapter 6. Major findings of the present thesis are summarized in chapter 7. Future scope of the work is also included in chapter 7.

1.4 Summary

Titanium diboride (TiB_2) is a structural ceramic material that is attracting attention as the base material for a range of high technological applications. However, consolidation of TiB_2 is difficult due to low self-diffusion coefficient and existence of surface oxides on the powder particles. Silicides were considered as possible additives because of their ability to reduce the surface oxides thereby enhancing densification. Moreover silicides are also expected to improve high temperature oxidation resistance by the formation of a protective glassy layer on the surface which would impede further oxidation. The outline of the thesis is brought out below:

Synthesis of borides by a process (boron carbide reduction) which avoid elemental constituent process is amenable to control the yields product consistently and robust for execution. A persistent challenge in the use of (TiB_2) borides is getting in the form of consolidated dense bodies. The inapplicability of cold compaction and sintering is established and the superiority of hot pressing for consolidation is also demonstrated for obtaining the dense composites. Possible mechanisms for densification by hot pressing are brought out. Technological useful properties of the consolidated composites have been measured and the oxidation resistance of these composites also has been evaluated. The role of various additives in consolidation and their influence on the properties including oxidation resistance also has been brought out.

1.5 References

[1] Munro, R.G., Material properties of titanium diboride. Journal of Research of the National Institute of Standards and Technology., 2000;105:709-720

[2] Cahn, R.W., Hassen, P., Kramer., Materials Science and Technology, V.11, 175-258

[3] Weimer, A.W., Carbide., Nitride and boride materials synthesis and processing. Chapman & Hall, London, 1997;641-645

[4] Murthy T.S.R.Ch., Basu B., Balasubramaniam R., Suri A.K., Subramanian C., and Fotedar R.K.., Processing and properties of TiB_2 with $MoSi_2$ sinter-additive: A first report. Journal of American Ceramic Society., 2006;89[1]:131-138

[5] Basu B, Raju GB, Suri AK. Processing and properties of monolithic TiB_2 based materials.Int Mater Rev 2006;51[6]:354-374

[6] Subramanian C, Suri AK. Development of boron based neutron absorber materials. Metals Materials and Processes 2004;16[1]:39-52.

[7] Suri A. K., Subramanian C., Sonber J. K. and Murthy T. S. R. Ch.; Synthesis and consolidation of boron carbide: A Review; (Full critical review) International Materials Review, 2010;55[1]:4-40

[8] Raju G.B, Basu B. Development of high temperature TiB_2-based ceramics. Key Eng Mater 2009;395:89-124

[9] Matkovich, V.I., Boron and Refractory Borides, Springler-Verlag, Berlin, Heidelberg, New York, 1977

[10] Duygu A˘gao˘gulları, Hasan Gökc¸e, ˙Ismail Duman, M. Lütfi Övec¸o˘glu Influences of metallic Co and mechanical alloying on the microstructural and mechanical properties of TiB_2 ceramics prepared via pressureless sintering. Journal of the European Ceramic Society 2012;32:1949–1956

[11] Raju G.B., and Basu B., Densification, Sintering Reactions, and Properties of Titanium Diboride with Titanium Disilicide as a sintering Aid, J. Am. Ceram. Soc. 2007; 90[11]:3415-3423

[12] Raju G.B., Biswas K.and Basu B., Microstructural characterization and isothermal oxidation behavior of hot-pressed TiB_2-10wt.% $TiSi_2$ composites, Scripta Materialla 2009;61:104-107

[13] Raju G.B, Basu B, Tak N.H, Cho S.J. Temperature dependent hardness and strength properties of TiB_2 with $TiSi_2$ sinter-aid. J Eur Ceram Soc 2009;29[10]:2119-2128

[14] Lu H, Han H, Ma R, Wang Y, Qiu D. Titanium diboride and wolfram silicide composite used as aluminum electrolysis inert cathode materials. TMS Light Metals 2006:687-690. devices, 1992;39[10]:2341-2345

[15] Murthy T. S. R. Ch., Balasubramaniam R., Basu B., Suri A. K. and Mungole M. N., Oxidation of Monolithic TiB_2 and TiB_2-20 wt% $MoSi_2$ Composite at 850^o C, J. Eur. Ceram. Soc., 2006; 26[1–2]:187–192

[16] Holcombe C. E. and Dykes N. L., Microwave sintering of titanium diboride, J. Mater. Sci., 1991;26:3730–3738

CHAPTER 2

CHAPTER 2

LITERATURE SURVEY

2.1 Introduction

The refractoriness and high strength of non oxide structural ceramics make them ideally suited for applications at high temperature. Titanium diboride (TiB_2) is a ceramic that is being considered as the base material for a range of high technological applications [1]. It has many attractive properties, such as exceptional hardness (25–35 GPa at room temperature, more than three times harder than fully hardened structural steel), which is retained up to high temperature, high melting point (>3000^oC), good creep resistance, good thermal conductivity (~65 W/m/K), high electrical conductivity (10-30 x 10^4 S/cm) and considerable chemical stability [2,3]. TiB_2 is very similar to TiC, an important base material for cermets, and many of the boride's properties (e.g. hardness, thermal conductivity, electrical conductivity and oxidation resistance) are superior to those of TiC. Such combination of properties makes TiB_2 a candidate material for heavy duty wear applications, particularly at elevated temperatures [1-3].

However, the relatively low fracture toughness of monolithic TiB_2 (~5 $MPa.m^{1/2}$) and its sensitivity to slow subcritical crack growth, limit its use in many engineering applications. The low self-diffusion coefficient makes pure TiB_2 very difficult to densify. These shortcomings are shared by many structural ceramics, e.g. ZrB_2, HfB_2 and SiC, and considerable research efforts are on to improve both the toughness and sinterability of these materials [1-3].

The development of TiB_2 and its composites, and their potential for high temperature structural/nuclear applications are reviewed in this chapter. The phase diagram and crystal structure of TiB_2 are also discussed. Densification, with and without sinter additives, and the microstructures obtained are considered, followed by a summary of data on mechanical, physical and oxidation properties. Important applications of TiB_2 are also listed.

2.2 Phase diagram and crystal structure

The Ti–B binary phase diagram is shown in Fig.2.1[3]. Three intermetallic phases, orthorhombic TiB, orthorhombic Ti_3B_4 and hexagonal TiB_2 are present[3]. TiB and Ti_3B_4 decompose peritectically at 2453K (2180^{o}C) and 2473 K (2200^{o}C) respectively and TiB_2 melts congruently at 3498K (3225^{o}C). Whereas Ti_3B_4 is a line compound but TiB and TiB_2 have a narrow homogeneity range. TiB_2 exists over a narrow stoichiometry range of 28.5–30 wt% B [3].

Titanium atoms in TiB_2 form a hexagonal close packed (HCP) structure. The hexagonal unit cell of single crystal TiB_2 [a=b= 3.029 A°, c=3.229 A°; $\alpha=\beta=90^{o}$, $\gamma=120^{o}$] is shown in Fig. 2.2a [7,8]. Ti atoms are located at (0,0,0) and B atoms at (1/3,2/3,1/2) and (2/3,1/3,1/2) lattice sites [3,4]. In analogy with the usual notation of ABABAB for HCP structure, the stacking sequence of Ti will be AAA. Boron (B) atoms are located interstitially between the A-layers, forming a strong covalently bonded hexagonal network structure as shown in Fig. 2.2b. High hardness and elastic modulus of TiB_2 as well as its chemical resistance are attributed to its crystal structure and covalent bonding [3-6].

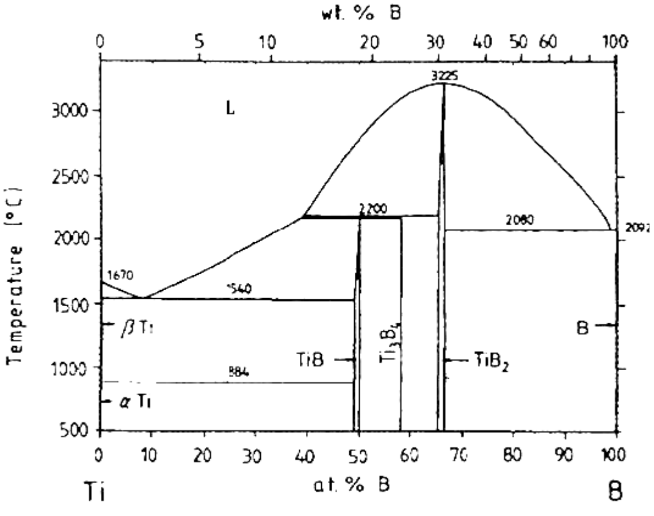

Fig.2.1 Ti–B binary equilibrium phase diagram [3]

The important physical and mechanical properties of TiB_2 are listed in Table 2.1 along with those of other similar engineering ceramics. TiB_2 is superior in terms of hardness, toughness and electrical & thermal conductivity [3]. TiB_2 combines superior hardness and a high melting point with corrosion resistance. In addition, the TiB_2 is electrically conductive, which is important in some electrical applications and also enables the solid bodies formed to be shaped into complex geometry using electrical discharge machining (EDM).

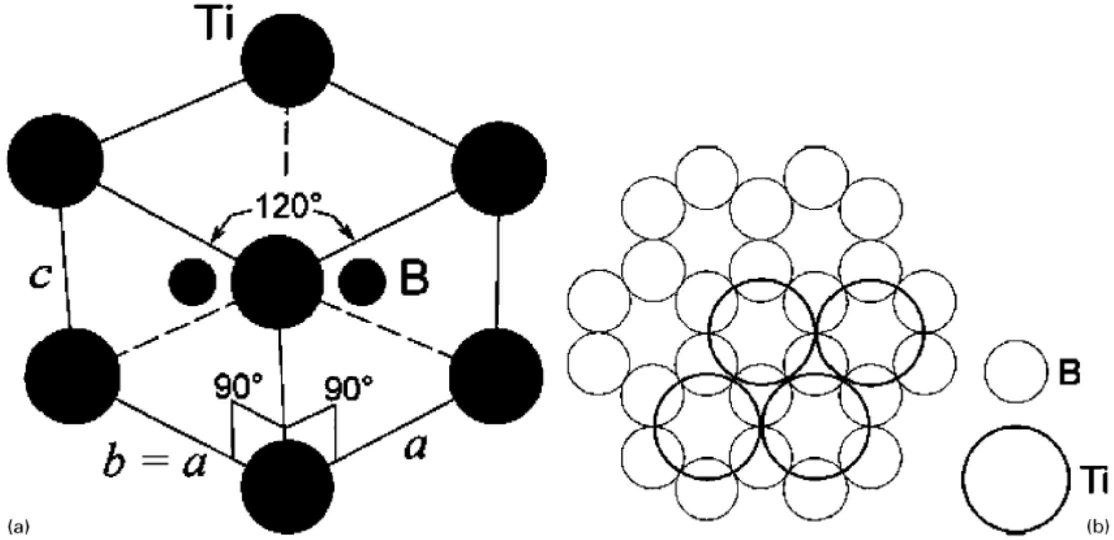

Fig. 2.2 a) hexagonal unit cell of single crystal TiB_2 and b) illustration of hexagonal net of boron atoms. [7,8]

The engineering applications of monolithic TiB_2 are restricted due to its poor sinterability and toughness, exaggerated grain growth and a limited oxidation resistance. Since densification has been a major challenge, sintering of monolithic/bulk borides is reviewed in the following section. [3,9].

Table 2.1 Summary of important physical and mechanical properties of TiB_2 and other important high temperature ceramics [3,9]

Property	TiB_2	ZrB_2	B_4C	SiC	WC	TiC	Si_3N_4	Al_2O_3
Crystal Structure*	Hex	Hex	Rho	Hex	FCC	FCC	Hex	Tet
Melting point, K	3498	3273	2723	2473	2873	3340	2173	2316
Density, kg/m^3	4520	6100	2520	3200	15700	4930	3440	3990
Linear thermal expansion α, 10^{-6} K^{-1}	α_a=6.6 α_c=8.6	6.83	4.5	5.68	5.2-7.3	7.42	2.4	8.0
Electrical resistivity, $\mu\Omega$-cm	10-30	9.2	10^6	$>10^5$	17	52	10^{18}	10^{20}
Fracture toughness $K_{IC,}$ $MPa.m^{1/2}$	5-7	3.5	3-3.5	2.5-6	-	4	4-6	2.5-4
Elastic modulus, GPa	560	350	450	480	720	400	210	400
Hardness, GPa	25-35	22-26	37-47	20-35	20-24	24-32	14-25	18-21
Three point flexural strength, MPa	700-1000	305	300	300-800	480-830	240-270	1000-1200	323

* Hex: hexagonal; Rho: rhombohedral/trigonal; FCC: Face centered cubic; Tet: tetragonal

2.3 Processing, microstructure and properties of bulk TiB_2

Synthesis of fine powders is the first step in the fabrication of ceramic components by powder metallurgy. The process then proceeds through densification of monolithic TiB_2 (without additive) or sintering with metallic and non-metallic additives. The properties of the material obtained are related to the microstructure developed in these steps.

2.3.1 Synthesis of TiB_2

Titanium diboride powder can be prepared by a variety of methods [10-16], such as the direct reaction of titanium or its oxides/hydrides, with elemental boron over 1273K (1000°C)[12], carbothermic /aluminothermic/ silicothermic/ magnesiothermic reduction of titanium oxide and boron oxide mixture [12], or hydrogen reduction of boron halides in the presence of the metal or its halides[12], sol-gel [15,16], self-propagating high-temperature synthesis (SHS) [13], mechanical milling of TiO_2 and B_2O_3 with metallic magnesium [11,12]. Apart from these routes, electrochemical synthesis has been developed to prepare pure titanium diboride.

An example of solid state reaction is the carbothermic reduction of mixture of TiO_2 and B_2O_3 by the reaction

$$TiO_2 + B_2O_3 + 5C \rightarrow TiB_2 + 5CO \qquad (2.1)$$

carried out in electric furnaces. However, this reaction is highly endothermic and needs temperatures above 2073K [16]. Another method for large-scale production of titanium diboride is based on the reduction of TiO_2 with carbon and boron carbide (boron carbide method)[10]:

$$2TiO_2 + B_4C + 3C \rightarrow 2TiB_2 + 4CO \qquad (2.2)$$

Purity of the product in this method is >99%. Production of pure TiB_2 powders in a large quantity (kilogram scale) on both laboratory and commercial scale using this method is the main advantage. However, this reaction is also highly endothermic and needs temperatures above 2073K [16].

TiB_2 powder is also obtained by the hydrogen reduction of $TiCl_4$ and BCl_3 mixture as per the reaction:

$$TiCl_4+2BCl_3+5H_2 \rightarrow TiB_2+10HCl \qquad (2.3)$$

This method is simple and can yield a pure TiB_2 powder. Handling of chlorides is however difficult due to their corrosive nature.

Self-propagating high-temperature synthesis (SHS), reactive synthesis, and combustion synthesis are methods by which ceramic materials can be produced. All these processes involve exothermic reactions between starting powders as a driving force yielding the desired final product. Commonly, these processes comprise an ignition of the reaction, followed by self-propagating combustion fronts that transform the green body to a solid piece. The ignition temperature for the stoichiometric mixture of TiO_2, H_3BO_3 and Mg/Al was found to be as low as 958K (685^oC) [14]. Titanium diboride powder has been synthesized by reaction of Ti and B inorganic precursors followed by heat treatment in argon atmosphere. SHS is simple, low cost, and needs no expensive facilities. TiB_2 can produce at lower temperatures and in very short time. However, the products were reported to be contaminated with metallic titanium, titanium carbide Al_2O_3 or titanium oxide [13,16].

Mechanosynthesis has been shown to be very effective for the preparation of many metals and ceramic materials with high melting point [12]. In the case of TiB_2, another route to form the compound is by reaction of TiO_2 and B_2O_3 with metallic magnesium during extended ball milling performed at room temperature in a tumbling mill for between 10 and 15 h in an inert atmosphere [11,12]. The final products are TiB_2 and MgO. The oxide can be easily removed by leaching in acid, leaving a powder composed of pure TiB_2, as tested by X-ray diffraction (XRD) analysis [12]. This process is a combustive reaction [12] that takes place once the ignition temperature is reached during ball impacts—the conditions reported in literature allow for TiB_2 production only with long milling times (10 to 15 h) due to the chosen conditions for ball milling and the relatively poor energy transfer during ball impacts. However, the products were reported to be contaminated with unreacted reactants.

It is evident that a number of laboratory scale methods have been successfully developed to synthesize micrometer or sub-micrometer sized TiB_2 powder. Success is, however, limited as far as industrial scale production of TiB_2 is concerned. From the sintering/consolidation point of view, emphasis should be placed on obtaining finer TiB_2 powders with a narrow size distribution and with limited impurities. From a classical Herring approach, it can be predicted that a decrease in particle size by one order of magnitude will produce 3–4 orders of magnitude reduction in sintering time, depending on the dominant densification mechanism (lattice diffusion, grain boundary diffusion) [17,18]. The presence of impurities in the starting powders causes a decrease in sinterability. For example, TiB_2 powders containing >1 wt% oxygen can be densified only to 90% theoretical density, even at higher sintering temperatures (2273K) [19].

2.3.2 Densification and microstructure of monolithic TiB_2

Consolidation methods by powder metallurgy route are i) pressureless sintering, ii) hot pressing and iii) special methods (hot isostatic pressing, microwave sintering, spark plasma sintering, etc.). Pressureless sintering is simple and gets the intricate shapes. However, some of the materials cannot densify by pressureless sintering. In hot pressing, external pressure is applied in order to achieve the full density. In case of hot isostatic pressing, uniform pressure is applied from all the directions. More details of the spark plasma sintering (SPS) are given in the next section.

The densification of transition metal borides such as TiB_2 is inherently difficult because of three characteristics of these compounds: i) high melting point, ii) low self-diffusion coefficient and iii) the comparatively high vapor pressure of the constituents. To obtain good densification, sintering temperatures exceeding 70% of the absolute melting temperature are usually necessary during consolidation to ensure appreciable grain boundary and volume diffusion induced material transport to occur to result in >95% theoretical density [3]. This implies that TiB_2 ($T_m \approx 3523K$) requires sintering temperatures of 2073-2573K (1800–2300^{o}C). However, borides undergo an abnormal grain growth at high temperatures. The occurrence of microcracking at the grain boundaries is also promoted with the increase in grain size. Thus, it is very difficult to achieve crack free dense borides by the conventional cold compaction and sintering, as no shape accommodation occurs without an external pressure and large pores tend to coarsen during high temperature sintering [20].

A thin oxygen rich layer (mainly TiO_2 and B_2O_3) is usually present on the surface of TiB_2 powder, irrespective of synthesis route [19]. The presence of oxygen finally results in increase in grain size and coarsening of pores because the presence of oxides increases the surface diffusivity. In order to achieve higher density and to inhibit abnormal grain growth, the total oxygen content of the powder must be limited to <0.5 wt% or strong reducing additives need to be used to remove TiO_x below 1873K (1600^oC) [19].

Table 2.2 [21-32] presents reported data on densification and material property of monolithic TiB_2 (without sinter additive). A point to note in Table 2.2 is that while hot pressing at or above 2073K (1800^oC) can produce >95% theoretical density, hipping at 1773-1873K (1500–1600^oC) enables the attainment of similar density with good mechanical properties (hardness is ~ 26 GPa and three point flexural strength ~ 450 MPa) [21-23]. Additionally a sintering route, high pressure sintering (HPS) at temperature greater than 2173K (1900^oC) and at a pressure of 3 GPa, has been shown to be capable of producing >95% density TiB_2 with good hardness [24] (Table 2.2). In addition to the commercial powders, as utilized in obtaining the results mentioned above, a group of researchers used elemental powders Ti and B in 1 : 2 weight ratio and obtained 95% or higher theoretical density via high pressure self-combustion synthesis (HPCS) route[24]. A better densification result (~98%) was obtained with carbon addition to (Ti+B) elemental powder mix. For comparison, representative data of other high temperature ceramics are also included in Table 2.2 [21-32]. Near theoretical density was obtained for Si_3N_4

and Al_2O_3 ceramics when hipping at 1923K and hot pressing at 1823K respectively [30]. Whereas for ZrB_2 only 98% TD was obtained even after hot pressing at 2173K [32].

Ferber and co-workers [33] reported that materials with anisotropic thermal expansion, such as TiB_2, often develop microcracks, relieving localized residual stresses generated during cooling from hot pressing temperature. Such stresses arise primarily from the mismatch of thermal expansion between individual grains and anisotropic thermal expansion. For example, the thermal expansion coefficients of TiB_2 along the crystallographic'a' and 'c' axes are 7.19×10^{-6} and 9.77×10^{-6} /K respectively. The experimental observations suggested that the critical grain size for microcracking to occur in case of TiB_2 based ceramics is ~15 μm [33].

Baumgartner and Steiger [34] reported almost full densification (99% TD) of titanium diboride powder by pressureless sintering. The high purity micrometer sized titanium diboride powder was produced by the reaction of titanium tetrachloride and boron trichloride gases in the presence of excess hydrogen in arc plasma heating, according to the following reaction:

$$TiCl_4\,(g) + 2BCl_3\,(g) + 5H_2\,(g) \rightarrow TiB_2\,(s) + 10HCl\,(g) \qquad (2.4)$$

The densification proceeds by self-diffusion and requires a high grain boundary surface area (small grain size) to reach completion. The reported difficulties in achieving full dense titanium diboride by the pressureless sintering of carbothermic powder are attributed to rapid grain growth (activation energy is ~1.02 MJ/mol) before completion of the densification [34]. This is due to the presence of small amount of oxygen as impurity, which enhances the surface diffusion instead of lattice diffusion.

Spark Plasma Sintering (SPS) is a sintering technique with some similarities to conventional hot pressing. However, in SPS, a strong-pulsed current is directly passed through the electrically conducting pressure die instead of using an external heating source. In appropriate cases, electric current also passes through the sample, implying self-heating of the sample. The unique features of SPS process are the possibilities to apply very high heating rates up to several hundred degrees per minute and subsequently to achieve full densification within minutes. High heating rate (100 K/min) yielded more homogeneous microstructures than those achieved with the slow heating rate (20 K/min), and therefore a rapid reaction yields a more homogeneous microstructure. Hardness and fracture toughness of SPS samples were 29.6±2.5 GPa and 5.2±0.4 MPa.m$^{1/2}$ respectively [35].

Summarizing, size and purity of the starting powders plays a strong role for densification of TiB_2 ceramics. >99% TD obtained by using the high purity micrometer sized TiB_2 powders, where as only 90% TD achieved when TiB_2 powder contains >1% oxygen as impurity. The literature indicates that high sintering temperatures (>2073^o C) are required to obtain high density monolithic TiB_2. Also, the grain size of TiB_2, sintered from commercial powders, is >4 μm, which limits hardness/strength. Additionally, the influence on modulus, strength, electrical and thermal conductivity is most pronounced, if the grain size is large enough to induce microcracking. It should be noted that the strength could be significantly affected by internal stresses, even in the absence of microcracking.

Table 2.2 Density, microstructural characteristics and mechanical properties of TiB_2 and other high temperature ceramics, sintered without additive under various processing conditions

Material composition, wt%	Processing conditions*	Sintered density, %TD	Microstructural phases, μm	Hardness, GPa	Fracture toughness $K_{IC,}$ $MPa.m^{1/2}$	Flexural strength*, MPa	Ref.
commercial TiB_2 powder	PS at 2423 K’ Ar	93.1	TiB_2	---	5.4	---	25
	Hipping at 1773 K, 196MPa, 2h,Ar	97.6	1.8 equiaxed	---	3.7	650(3P)	23
	Hipping at 1873 K, 200MPa, 2h,Ar	---	GG:2->4-6	26	3.5	450 (3P)	22
	HP at 1873 K, 1h, Ar	91.0	4.8 equiaxed	---	4.1	305 (3P)	21
	HP at 1973 K, 1h, Ar	95.0	5.0 equiaxed	---	4.3	498 (3P)	21
	HP at 2073 K, 0.5h, Ar	96.0	5.3 equiaxed	---	5.3	545 (3P)	21
	HP at 2073 K, 1h, Ar	97.0	8.1 equiaxed	---	5.7	558 (3P)	21
	HP at 2073 K, 1.5h, Ar	--	10.5	---	6.3	538 (3P)	21
	HP at 2073 K, 2h, Ar	--	12.7	---	6.8	475 (3P)	21
	HP at 2173 K, 1h, Ar	--	12.2	---	6.2	521 (3P)	21
	HP at 2273 K, 1h	--	--	26.7	4.8	498 (3P)	26
	HPS at 2250 K, 5min, 3GPa	94.6	1.4 equiaxed	19.2	--	--	24
	HPS at 2500 K, 5min, 3GPa	97.1	--	21.7	2.8	--	24
	HPS at 2750 K, 5min, 3GPa	98.0	--	24.5	3.2	--	24
elemental Ti+B (1:2) powders	HPCS at 2250 K	97.8	--	23.6	3.5	--	24
	HPCS at 2500 K	98.0	--	24	3.8	--	24
	HPCS at 2750 K	98.0	--	23.9	3.6	--	24
Other high temperature ceramics							
Al_2O_3	HP at 1823 K, 45 min	100	2	19.4	4.6	420 (4P)	27
B_4C	HP at 2423 K, 65 min	95.0	6-10	29	2.5	220 (3P)	28
β-SiC	HP at 2223 K, 2h	--	0.8-3	--	2.5	394 (4P)	29
Si_3N_4	Hipping at 1923 K,2h,18MPa,Ar	100	--	15.5	4.6	--	30
WC	PPC at 1873 K, 4 min, 35 MPa	--	5.5	19.2	8.2	--	31
ZrB_2	HP at 2173 K, 45 min	98	4.0	23	--	565 (4P)	32

* PS: pressureless sintering; hipping; HP: hot isostatic pressing; 3P: three point bending; 4P: four point bending; HPS: high pressure sintering; HPCS: high pressure self-combustion synthesis; PPC: plasma pressure compaction

2.3.3 Effect of metallic sinter additives

Various sinter additives have been used to reduce sintering temperature and hence restrict grain growth in the densification of TiB_2. The influence of metallic binders (as sinter additives) on the densification and properties of TiB_2 has been investigated extensively [33,36-43]. Table 2.3 is a summary of these reports, and includes information on some important cermets. High density TiB_2 (>99%) has been obtained through small additions 1–2 wt% of Fe, Cr or Ni [33,44-45]. Very high hardness (23–31 GPa) is achieved with a moderate toughness of 4–6 $MPa.m^{1/2}$ and four point flexural strength value > 500 MPa [46]. Except fracture toughness, the properties of TiB_2 materials are superior to many other engineering materials. In particular, the hardness of TiB_2 at >18 GPa is higher than those of ZrC/TiC/WC (≤14 GPa) based materials. Thus, TiB_2 based materials could be expected to show greater resistance to abrasive/sliding wear. Cemented TiB_2 has a toughness of 9.2 MPa $m^{1/2}$, which is comparable with WC and TiC based cermets [41].

Table 2.3 Summary of the influence of metallic additives on microstructure and mechanical properties

Material composition, wt.%	Processing conditions*	Sintered density, %TD	Microstructural phases, μm	Vickers hardness, Hv, GPa	Indentation toughness, MPa $m^{1/2}$	Flexural strength*, MPa	Reference
TiB_2+0.014Ni	HP at 2523 K, 30MPa, 20min	97.9	1.5 (equiaxed TiB_2 grains of traces of Ni_4B_3,Ni_3B)	23.3	5.8	716 (4P)	37
TiB_2+0.7Ni	HP at 1823 K, 1h, vacuum	97.9	---	23.3	5.1	716 (4P)	38
TiB_2+1.4Ni	HP at 1698 K	>99	---	---	6.4	670 (4P)	33
TiB_2+7.9Ni	HP at 1698 K	>99	---	---	4	420 (4P)	33
TiB_2+0.017Fe	HP at 1973 K,1h,Ar	99	6.4(equiaxed TiB_2 grains)	---	6.6	520 (3P)	39
TiB_2+0.5Fe+0.5 Cr	PS at 2073 K,2h,Ar	97.6	--	27.0	6.2	506 (4P)	36
TiB_2+0.5Fe+0.5 Cr	PS at 2173 K,2h,Ar	98.6	--	31.3	5.9	262 (4P)	36
TiB_2+Ti	HP at 2173 K,2h,Ar	99.6	Needle like of TiB_2	19.0	4.5	360 (3P)	40
TiB_2+14.4Fe+6.1Ni-8$TiAl_3$	PS+hipping at 1773 K,Ar	--	5.0(TiB_2 grains)	17.8	9.2	1019 (4P)	41
ZrB_2+4.0Ni	HP at 2123 K,30min	98	--	14.4	2.8	371 (4P)	42
WC+6.5Co	PS at 1823 K,4h	--	2.5	15.8	10	--	43
TiC+10Mo_2C+25Ni	PS at 1823 K,4h	--	4.2	15.1	6.1	--	43
TiC+10TiN+10Mo_2C+25Ni	PS at 1823 K,4h	--	2.4	12.7	10	--	43

*HP: hot pressing; 3P: three point bending; 4P: four point bending; PS pressureless sintering; hipping: hot isostatic pressing

Earlier experiments, using metallic additives such as nickel, iron, cobalt, titanium, stainless steel and manganese have demonstrated that 99% of theoretical density can be achieved by liquid phase sintering (LPS) [33,39,40]. Ferber et al. [33] have used up to 10 wt% Ni to achieve >99% theoretical density by hot pressing (1698K). As regards the densification mechanism, the transition metals (Ni, Co, Cr) react with TiB_2 forming metal borides with a low melting point (approximately 1173–1373K) and these borides also exhibit good wetting behavior. In case of Ni bonded TiB_2, a ternary 'τ' phase with the composition, $Ni_{21}Ti_2B_6$ forms by the dissolution of TiB_2[33]. At 1073K (800°C), the 'τ' phase is in equilibrium with Ni, Ni_3B, Ni_3Ti and TiB_2. Typical metal contents required for the optimum liquid phase sintering of TiB_2 are 5–25 wt% (2–12 at%) of either Ni or Co[33]. In order to avoid reactions consuming TiB_2, the borides of Ni or Co have also been used [20]. In LPS, the sintering temperatures have been decreased from 2373 to 1673K (2100 to 1400°C).

Phenomenologically, the liquid phase sintering, as commonly observed with the use of metallic additives in sintering of TiB_2, enhances the mass transport but simultaneously causes exaggerated grain growth. Extensive nickel intermetallic phase ($Ni_{21}Ti_2B_6$, Ni_3B, Ni_3Ti) formation was also found to have deleterious effect on both fracture strength and fracture toughness. Hence, the strength and toughness are significantly retained for TiB_2 ceramics with a fine grain size (4 μm) and low Ni content (<2 wt%). The microstructures of bulk TiB_2, prepared by liquid phase sintering, are similar to those of other hard metals, such as WC+Co (Hardness ~22 GPa). For example, hardness and fracture toughness of spark plasma sintering (SPS) samples (TiB_2 +2.5%Ti) were 26.8±1.6 GPa and 5.9±0.3 $MPa.m^{1/2}$ respectively[47]. In liquid phase sintered TiB_2, the boride particles form a rigid skeleton of faceted crystals, when it reacts with transition metals such as iron, nickel or cobalt to form the metallic borides Fe_3B, Ni_3B,

Ni_2B and Co_3B, which can dissolve titanium [48]. Depending upon the wetting behavior, typically influenced by the surface oxidation of the hard phase. Round pores accumulate at particle/matrix interfaces or close to triple pocket. Such pores cannot be completely infiltrated by the liquid phase during sintering. Moreover, the evaporation of Fe, Co or Ni borides potentially cause entrapped gas pores [48].

Relatively small additions (1–5 wt%) of nickel, nickel boride (NiB) and iron have been found to promote liquid phase sintering of TiB_2. High density (>94%) was obtained at temperatures >1773K. Significant grain growth was observed in TiB_2 samples with Ni, NiB and Fe binders during sintering at 1973K (1700°C)[45]. The grain growth was observed to be closely related to the oxygen content of the samples and sintering temperature. It has been observed by Einarsrud et.al [45] that addition of carbon to act as a strong reducing agent to remove the surface oxides of the particles does inhibit the grain growth. Therefore, to obtain fine grained microstructures it is essential to optimize the sinter additive content and the processing conditions (temperature, time, etc.). A liquid phase sintered microstructure, obtained with TiB_2+1.5wt% Ni material is shown in Fig. 2.3a[45]. All the triple pockets appear to contain sintering liquid residue.

Combined addition of various metallic additives has also been investigated [36]. Simultaneous addition of 0.5 wt% Cr and 0.5 wt% Fe was found to enhance the densification of TiB_2 up to 98.8%[36]. A typical microstructure of TiB_2+0.5Cr+0.5Fe shows equiaxed grain with sizes between 2 and 10 μm (Fig. 2.3b). In Fig. 2.3c, high resolution TEM image reveals the existence of sintering liquid, rich in Fe and Cr[36]. Mechanical properties of the TiB_2+0.5Cr+0.5Fe, sintered at 2073K (strength of 506 MPa and a fracture toughness of 6.2 $MPa.m^{1/2}$), were much better than those measured in the TiB_2+0.5Cr+0.5Fe sintered at 2173K

(1900^{o}C)[36]. In the case of 0.5 wt% Fe addition to TiB_2 along with 0.5 wt% Cr, abnormal grain growth was suppressed remarkably and an increase in sintered density was recorded. Microstructural observations confirmed the existence of Fe rich phase at the triple pockets and at grain boundaries [44].

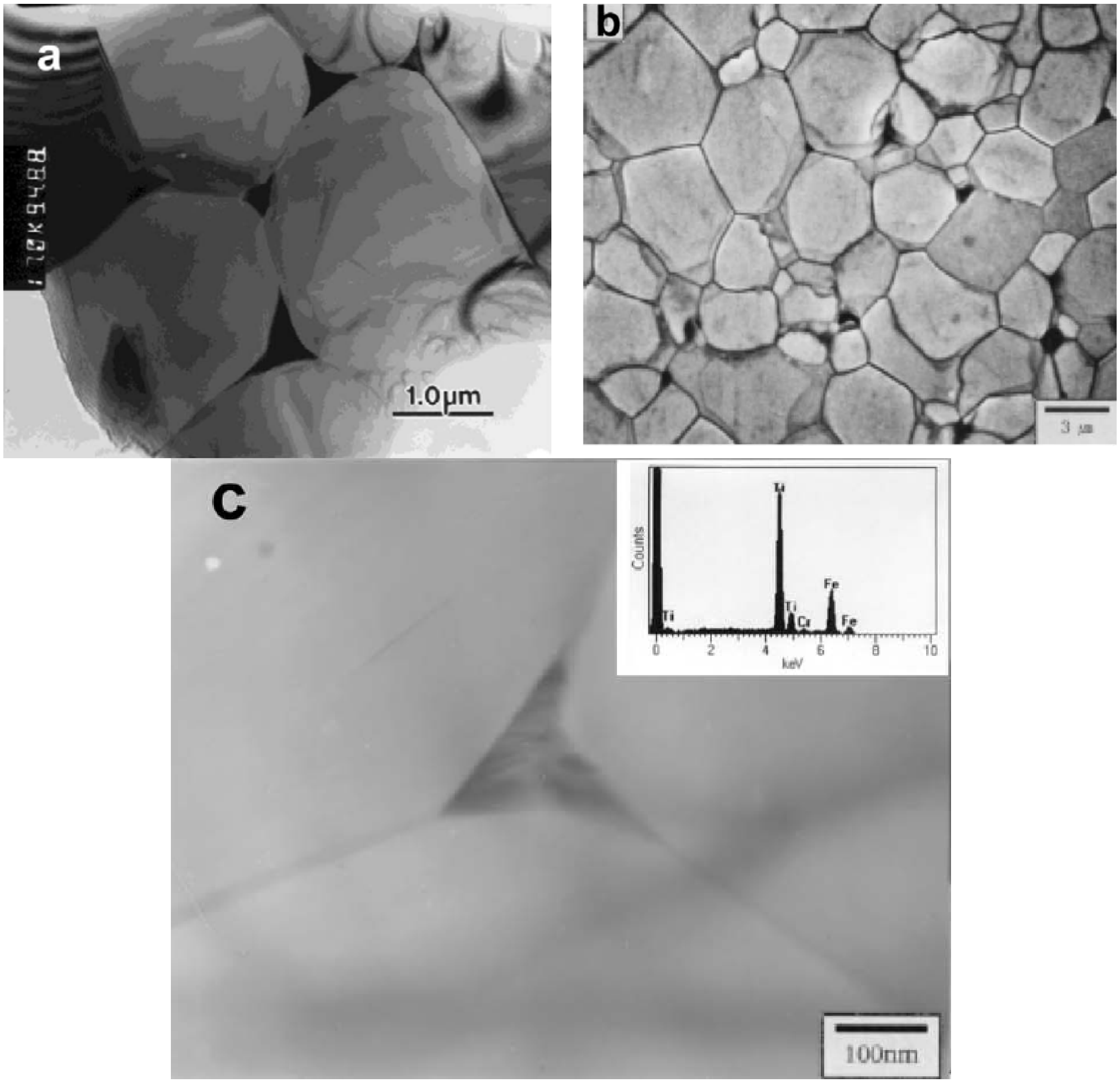

Fig. 2.3 a) bright field (BF) TEM image showing wetting behavior of liquid phase in TiB_2–1.5Ni (wt. %)[45], b) SEM image of TiB_2–0.5Fe–0.5Cr (wt. %)[45] and c) BF TEM image along with EDS analysis revealing presence of Fe and Cr in sintering liquid residue at triple pocket of TiB_2–0.5Fe–0.5Cr[36]

Wettability and dissolution of TiB_2 in the transient liquid phase have been widely identified as critical factors when sintering with metallic additives. In most cases the hardness is inferior to that of the monolithic TiB_2 (Table 2.3). From the perspective of high temperature applications, the presence of metallic binder is not desirable, the low melting point of either sintering liquid or metallic additives leads to incipient fusion and consequent degradation of high temperature properties.

2.3.4 Effect of non-metallic sinter additives

The principal objective of non-metallic additives is therefore to improve sinterability of TiB_2 without promoting grain growth thus circumventing limitations of metallic additives. Various non-metallic additives (AlN, SiC, Si_3N_4, CrB_2, B_4C, TaC) have been used for attaining densification of TiB_2 with good mechanical properties [22-26,49,50]. Table 2.4 [22,26,46,49-53] presents the summary of the published results. A comparison of Tables 2.3 and 2.4 indicates that higher amount of non-metallic additives, more than 5–10 wt%, is typically added to densify TiB_2, while a smaller amount of metallic additive, even less than 2 wt% was sufficient to obtain dense TiB_2. As with the use of metallic binders, a combination of high Vickers hardness (~20–27 GPa) and moderate indentation toughness (~4–7 MPa $m^{1/2}$) and also a modest flexural strength of 500 MPa is obtainable with the use of a variety of non-metallic sinter additives [46].

The addition of non-metallic binders has an important influence on the sinterability and microstructure of the TiB_2. Representative SEM images of polished bulk TiB_2 ceramics are shown in Fig. 2.4(a–c). All these materials were hot pressed at 2073K (1800^oC) for 1h in vacuum. It can be noticed in Fig. 2.4a that monolithic bulk TiB_2, without any sinter additive, exhibits coarse grains of sizes around 10 μm [46]. The presence of large pores at multiple grain junctions is also commonly observed.

The pore sizes appear to have reduced with the addition of 2.5 wt %Si_3N_4 to TiB_2 (Fig. 2.4b) [50]. Near full dense microstructure with finer TiB_2 grain sizes of 5 μm or less is observed, when AlN is used as sinter additive with an optimal amount of 5 wt% (Fig. 2.4c) [52]. Evidence of sintering liquid residue at triple pocket is presented in TiB_2+$MoSi_2$ composite (Fig. 2.4d). As in the case of addition of metallic additive, the liquid phase sintering is reported to occur for TiB_2 with non-metallic additives also. For example with $MoSi_2$ addition, $TiSi_2$ forms and liquid $TiSi_2$ (T_m<1733K) is reported to enhance densification of TiB_2 [50]. Similarly, Torizuka et al. [54,55] observed the formation of grain boundary liquid phase (amorphous SiO_2), when SiC was used as an additive. According to Murata et al. [51], TaC and TaN were effective for densification of TiB_2 by formation of (Ti,Ta)B_2 and (Ti,Ta)(C,N) solid solutions when hot pressed at 2273K (2000^oC) [52]. The presence of reaction products such as TiN and BN has been observed in TiB_2+Si_3N_4 composite system [52].

Fracture mechanisms are considerably influenced by binder additions, as can be observed in Fig. 2.5. The fracture of monolithic TiB_2 occurred mainly by an intergranular mode along with noticeable evidence of transgranular fracture, apparently owing to high porosity and large grain size. However, TiB_2 with non-metallic sinter additives such as AlN, Si_3N_4 exhibited predominant intergranular fracture (Fig. 2.5 b & c) [36,46,52]. In Fig. 2.5d, it can be noticed that the fracture mode is mixed in case of using metallic binder (0.5Cr+0.5Fe) with large TiB_2 grains, exhibiting transgranular fracture. Sintering additives enhance the density significantly and reduce the grain size by the secondary phase formation. However, the addition of sinter additives, such as AlN, SiC, Si_3N_4, beyond an optimal amount resulted in lowering of the density and reducing the grain size owing to grain boundary phase formation [46,53].

Table 2.4 Overall summary illustrating influences of non-metallic additives on microstructure and mechanical properties

TiB_2 composite	Processing conditions*	Sintered density, %TD	Microstructural phases, μm	Vickers hardness, Hv, GPa	Fracture toughness, MPa m$^{1/2}$	Flexural strength*, MPa	Reference
Influence of Nitride based additives:							
0%additive	HP at 2073 K,60 min,30MPa,Ar	89.0	TiB_2	12.5	4.5	360 (4P)	46
2.5%AlN		94.0	TiB_2,BN,TiN,Al_2O_3	16.1	5.0	500 (4P)	46
5.0%AlN		98.0	TiB_2, BN, TiN, Al_2O_3, unreacted AlN	22.0	6.8	650 (4P)	46
10%AlN		88.5		14.0	5.2	500 (4P)	46
20.0%AlN		87.5		12.1	4.6	400 (4P)	46
0%additive	HP at 2073 K,60 min, Ar	90.0	3-7 μm TiB_2	23.0	5.8	380 (4P)	52
2.5%Si_3N_4		99.0	TiB_2,TiN,BN	27.0	5.1	810 (4P)	52
5.0%Si_3N_4		97.5		21.0	4.8	510 (4P)	52
10%Si_3N_4		96.0		20.0	4.4	400 (4P)	52
5.0%Si_3N_4	HP at 2273 K, 30 min	86.0	…	15	…	…	51
0%additive		90.0	…	15	…	….	51
5.0%TaN		96.8	…	15	…	…	51
5.0%TiN		95.0	…	15	…	…	51
5.0%ZrN		83.9	…	15	…	…	51
Influence of Carbide based additives:							
0%additive	PS at 1973 K, vacuum+hipping at 1873 K, 200MPa, Ar	62	TiB_2	…	3.3	450(3P)	53
2.5%SiC		99.0	Amorphous SiO_2, liquid phase along GB	…	4.3	660 (3P)	53
5.0%SiC		93.0	TiB_2,SiC,TiC	…	4.9	850 (3P)	53
0%additive	HP at 2273 K,30 min	90.0	---	15	…	---	51
1.0%TaC	HP at 2273 K,60 min	98.0	(Ti,Ta)B_2,(Ta,Ti)(C,N) solid soln.	15	…	…	51
5.0%TaC		99.4		15	…	…	51
5.0%TiC	HP at 2273 K,30 min	96.5	….	15	…	…	51
5.0%WC		95.9		15	…	…	51

Contd…

Material composition, wt%	Processing conditions*	Sintered density, %TD	Microstructural phases, μm	Vickers hardness, Hv, GPa	Fracture toughness, MPa m$^{1/2}$	Flexural strength*, MPa	Reference
Influence of Silicide based additives:							
0%additive	HP at 2073 K,60 min, vacuum	97.5	TiB_2	26	5.1	…	49,50
10%$MoSi_2$	HP at 1973 K,60 min, vacuum	99.3	TiB_2,$MoSi_2$, trace $TiSi_2$	27	4.0	…	49,50
20%$MoSi_2$		98.7		25	5.0	…	49,50
10%$MoSi_2$	PS at 2173 K,120 min,Ar+H_2	82.4	…	…	…	…	49,50
15%$MoSi_2$		84.9	…	…	…	…	49,50
20%$MoSi_2$		88.5	…	…	…	…	49,50
25%$MoSi_2$		91.3	…	…	…	…	49,50
2.5%$TiSi_2$	HP at 1923 K, 30MPa, Ar	98.8	TiB_2 ,Ti_5Si_3	25	4.3	381	89-91
5%$TiSi_2$		99.6	TiB_2 ,Ti_5Si_3	25	5.8	426	
10%$TiSi_2$		99.6	TiB_2 , $TiSi_2$, Ti_5Si_3	24	4.2	338	
10%WSi_2	1973 K, 60 min	>98	…	…	…	…	92
Influence of Boride based additives:							
5.0%ZrB_2	HP at 2273 K,60 min	79.6	…	15	…	…	51
3.0%CrB_2	MW at 2173 K,30 min,Ar	95.0	…	28.9DPH	6.2	…	26
3.0%CrB_2	MW at 2373 K,30 min,Ar	98.0	…	27.0DPH	6.1	…	26

*HP: hot pressing; 4P: four point bending; 3P: three point bending; PS: pressureless sintering; hipping: hot isostatic pressing; MW: microwave sintering

It was commonly noted that the optimum non-metallic additive content to achieve near theoretical density in TiB_2 is around 5–10 wt%. The influence of sinter additives on density, grain size and mechanical properties is discussed in this section. As will be shown below, optimizing the amount of binder and sintering temperature is critical for obtaining higher densification and improved mechanical properties through a finer grain size.

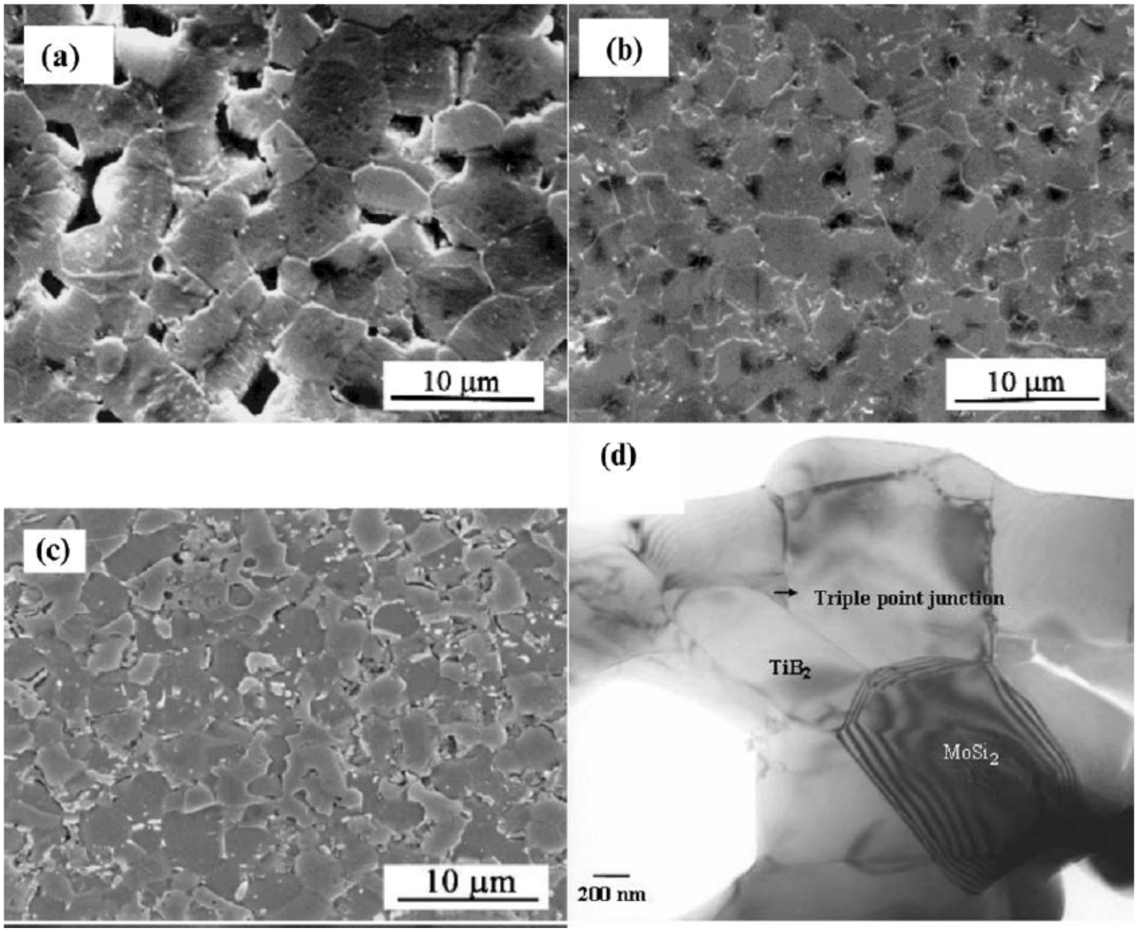

Fig. 2.4 SEM Images of TiB_2 specimens hot pressed at 2073K (1800^oC) for 1h containing a) 0 wt% sinter additive, b) 2.5 wt%Si_3N_4 and c) 5 wt%AlN, d) TEM image of TiB_2+20wt% $MoSi_2$, hot pressed at 1973K (1700^oC) [46,50,52].

The relative density of pure TiB_2 (90%TD, average grain size ~7 μm) increased markedly to >99%, and a fine microstructure (~3 μm) obtained by hot pressing on addition of 2.5 wt% Si_3N_4 [52]. Density decreased slightly and the grain size remained approximately constant with higher Si_3N_4 additions. The hardness of TiB_2 also enhanced, as reported, owing to the higher density. Further increase in Si_3N_4 content resulted in lower hardness, apparently because of the formation of secondary phases TiN and BN. This trend was also observed for the flexural strength [52]. In contrast, the fracture toughness decreased steadily as the Si_3N_4 addition was increased. The high fracture toughness is believed to be related to the fine grain size and high porosity of the specimen. In particular, crack deflection along the grain boundaries and pinning of the propagating cracks by pores were believed to contribute to enhance the fracture toughness. However, it is also possible that the presence of interconnected pores can favor for the initiation of cracks.

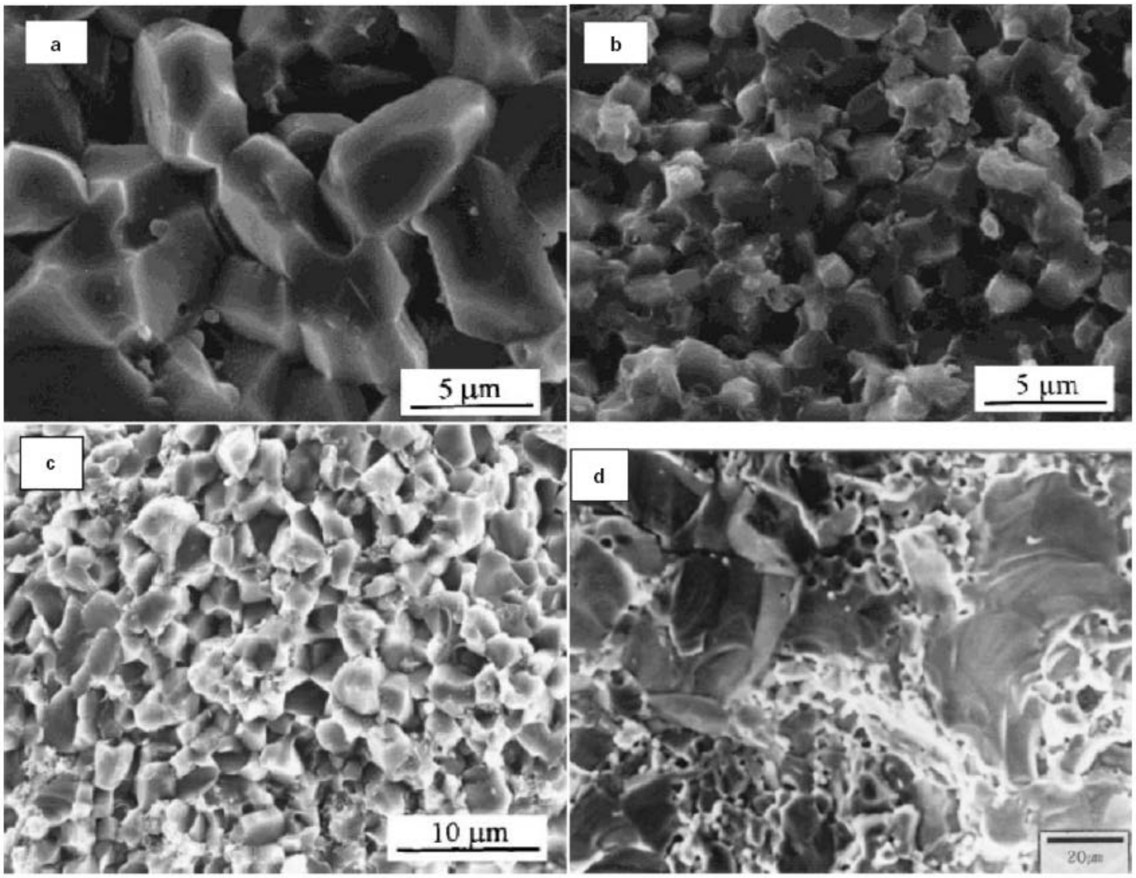

Fig. 2.5 SEM Images revealing fracture surface morphology/fracture characteristics of bulk TiB_2 containing a) 0 wt.% sinter additive, b) 2.5 wt.% Si_3N_4, c) 5 wt.% AlN and d) TiB_2 with metallic additives[36,46,52]

A thin oxide rich layer is usually present on the surface of non oxide ceramic powders, in case of TiB_2, mainly TiO_2 and B_2O_3 were reported [19]. Presence of surface oxide layer is detrimental for densification due to enhanced surface diffusivity [3]. In order to achieve higher density strong reducing additives need to be used to remove surface oxides. Following few case studies address the role of sinter additives on reducing the surface oxides of TiB_2 powders. Table 2.5 presents the reactions that play an important role on reduction of surface oxides of TiB_2 powders.

Park et al. [56] investigated the effect of hot pressing temperature (1773–2073K) on the densification behavior of TiB_2+2.5wt% Si_3N_4. A considerable increase in density at 1773–1873K (1500–1600^{o}C) is attributed to the formation of silica (SiO_2) during hot pressing. Such microstructural evolution suggests that to densify TiB_2 at low temperatures, the elimination of the oxide layer is necessary and the formation of a liquid phase during sintering is of critical importance.

The hardness and fracture toughness of the specimens, as a function of the hot pressing temperature, are also reported in literature [46,56]. These results illustrate that TiB_2 with good combination of mechanical properties can be densified at temperatures as low as 1873K (1600^{o}C) with the addition of a small amount of Si_3N_4 sinter additive [56]. AlN has been reported to have a similar influence on the sinterability and mechanical properties of TiB_2 [46]. When a small amount of AlN ($\leq$5 wt%) was added to TiB_2, the rutile phase (TiO_2), present on the TiB_2 powder surface was eliminated by a reaction with AlN to form TiN and Al_2O_3, according to the following reaction:

$$3TiO_2\ (s) + 4AlN\ (s) \rightarrow 3TiN\ (s) + 2Al_2O_3\ (s) + 0.5N_2\ (g) \qquad (2.5)$$

$$TiB_2\ (s) + 1.5N_2\ (g) \rightarrow TiN\ (s) + 2BN\ (s) \qquad (2.6)$$

The elimination of TiO_2 markedly improved the sinterability and consequently the mechanical properties of TiB_2. BN formation at grain triple pockets is confirmed in TEM analysis. It should be pointed out that large AlN additions (>10 wt%) decreased the sinterability and mechanical properties, apparently owing to residual/unreacted Al_2O_3 or AlN [46].

The effect of ZrO_2 and SiC on sinterability and mechanical properties of titanium nitride, titanium carbonitride and titanium diboride was investigated by Torizuka et al. [54] The combined addition of ZrO_2 and SiC was found to be effective in improving the sinterability and mechanical properties of TiB_2. The density of TiB_2 and TiB_2+20%ZrO_2 after sintering at 1973K (1700^{o}C) was 70%TD. Therefore, the addition of ZrO_2 alone had little effect in improving the sinterability of TiB_2. Although TiB_2 and TiB_2+20%ZrO_2 lacked sinterability, the addition of SiC was found to be effective in improving the density. For example, the density of TiB_2+19.5ZrO_2+2.5SiC was 97%TD. It was reported that TiO_2, existing on the surface of TiB_2 powder, reacts with SiC and formed TiC and SiO_2, according to the reaction [53]

$$TiO_2 + SiC \rightarrow TiC + SiO_2 \tag{2.7}$$

In the case of sintered TiB_2+2.5wt% SiC compacts, the added SiC was transformed to SiO_2; ~3.5 vol%SiO_2 was reported to form as a result of this reaction. The residual amount of TiO_2 and B_2O_3 contributed to lowering the melting point of SiO_2 and increasing the liquid volume. The existence of amorphous SiO_2 in the microstructure suggests that the densification is enhanced by liquid phase sintering [53].

$MoSi_2$ additions can reduce the hot pressing temperature to 1973K (1700^{o}C), for obtaining the near theoretical density [49,50]. However, no noticeable improvement in mechanical properties was found on addition of 10–20 wt% $MoSi_2$ (Table 2.4). This could be due to the presence of residual/unreacted $TiSi_2$ or $MoSi_2$. As mentioned above, the densification is enhanced by liquid phase sintering, promoted by the formation of a reaction product $TiSi_2$. In a follow-up study detailed transmission electron microscopy, in combination with thermodynamic analysis, revealed that the most likely reaction pathways for the formation of $TiSi_2$ is [49,50]:

TiB_2+3O_2 (g)+$MoSi_2 \rightarrow TiSi_2+B_2O_3$ (g)+MoO_3 (g) (2.8)

$5TiO_2+5.714MoSi_2 \rightarrow 1.143Mo_5Si_3+ Ti_5Si_3+5SiO_2$ (2.9)

Additionally, the maximum density achievable with pressureless sintering was found to be 90–91% with 25 wt% $MoSi_2$ at 2173K (1900°C) [49,50].

Table 2.5 presents the reaction of sinter additives on the role of reduction of surface oxides of TiB_2 powders

Sinter additive	Mechanism	Ref.
Si_3N_4	$3TiO_2+ Si_3N_4 \rightarrow 3TiN+ 3SiO_2 + 1/2N_2$	56
$TiSi_2$	$7TiO_2+8TiSi_2 \rightarrow 3Ti_5Si_3 + 7SiO_2$	89
AlN	$3TiO_2+4AlN \rightarrow 3TiN + 2Al_2O_3 + 0.5N_2$	46
SiC	$TiO_2 + SiC \rightarrow TiC + SiO_2$	53
$MoSi_2$	$5TiO_2+5.714MoSi_2 \rightarrow 1.143Mo_5Si_3+ Ti_5Si_3+5SiO_2$	49,50

Besides hot pressing and pressureless sintering, limited investigations of advanced sintering techniques, such as microwave sintering, have been reported for densification of TiB_2 and composite with CrB_2 addition. Using a 2.45 GHz, 6 kW microwave furnace adapted for inert gas sintering, titanium diboride (TiB_2) was rapidly sintered to >90% theoretical density at sintering temperatures of 2173 – 2373K (1900–2100°C) with soaking time of 30 min or less [26]. A comparison with conventional sintering indicated that microwave sintering of TiB_2+ 3wt% CrB_2 occurred at 200K lower temperature and yielded material with significantly improved hardness, grain size and fracture toughness[26].

Thermal stability of monolithic TiB_2 is of critical importance and has been widely reported in literature. Oxidation resistance is one of the important properties for the high temperature structural materials to be critically considered. The phenomenological aspects of

TiB_2 oxidation, surface and subsurface oxide scale formation, and oxidation induced degradation are discussed in the following section.

2.4 High temperature oxidation behavior

High temperature oxidation is sometimes termed ‘dry corrosion’ or ‘scaling’. The oxidation mechanism depends on the temperature, partial pressure of oxygen, duration of exposure, porosity and composition, i.e. addition of sinter additives in the case of TiB_2. Kulpa et al. [57] reported that oxidation of TiB_2 powder in 0.05 ppm oxygen in argon, started below 673 K (400°C) and proceeded with the formation of $TiBO_3$. The reactions are:

At 673K and 0.05 ppm oxygen

$$4TiB_2 + 9O_2 \rightarrow 4TiBO_3 + 2B_2O_3 \qquad (2.10)$$

At 673 – 1173 K (400 – 900° C) and 10 ppm O_2:

$$4TiBO_3 + O_2 \rightarrow 4TiO_2 + 2B_2O_3 \qquad (2.11)$$

It has been experimentally observed [54] that both reactions occur concurrently in the range 673 – 1173 K (400–900° C). A comparison of oxidation resistance of various TiB_2 based materials reveals that monolithic TiB_2 without sinter additive has poor oxidation resistance, compared with TiB_2 containing Cr, Si or Al based sinter additives. These additives can potentially form protective glassy/amorphous Cr_2O_3, SiO_2 [54,58] or Al_2O_3 [46] or borosilicate glass layers [109] on the surface of composites that act as a barrier to diffusion of oxygen to the bulk.

Oxidation rate constant values at various temperatures for monolithic TiB_2 and TiB_2 based materials are compared with those of other structural ceramics in Table 2.6. Up to 1173K

(900^{o}C), all materials, except TiB_2 cermet and WC followed diffusion controlled kinetics, i.e. parabolic rate law

$(\Delta w/s)^2 \approx K_P\, t$ (2.12)

where K_P is the parabolic oxidation rate constant, Δw is the weight gain (kg) in time t (sec) and s the surface area (m^2) of the material exposed to oxidizing environment. In the range 1073 – 1273K (800–1000^{o}C), the oxidation of TiB_2 cermet was governed by linear behavior

$\Delta w/s = K_L t$ (2.13)

where K_L is the linear oxidation rate constant. Similar linear oxidation behavior was also observed for TiB_2, without any sinter additive [59]. Comparing the data presented in Table 2.6, it can be seen that while the oxidation rate constants of TiB_2 based materials are comparable with those of other ceramics, they are not good enough for extended exposure in air at >1273K (1000^{o}C).

Surface oxide morphologies on monolithic TiB_2 after oxidation under various test conditions are presented in Fig. 2.6[58,59,66]. After oxidation at 1123K (850^{o}C) for 1h, the cracks are noticeable on oxide scale; however, on continued oxidation for 4h at 1123K (850^{o}C), the oxide scale becomes severely fractured and non-protective (Fig. 2.6a and b). It was reported [59] that monolithic TiB_2 in bulk form starts to oxidize in air at around 673 – 773K (400–500^{o}C) and the process was governed by a diffusion controlled mechanism up to 1173K (900^{o}C). The overall oxidation reaction was as follows:

$TiB_2 + 2.5O_2 \rightarrow TiO_2 + B_2O_3$

(2.14)

Crystalline B_2O_3 and TiO_2 were identified on the surfaces of monolithic TiB_2 after oxidation at 973 and 1073K[59]. The grain morphology at 1073K is clearly revealed in Fig. 2.6c and intergranular cracking is commonly observed after oxidation in air for 10 h.

Table 2.6 Comparison of weight gain and oxidation rate constant of TiB_2 based materials with other high temperature ceramic materials

Material	Oxidation conditions	Weight gain, kg/m^2	Parabolic oxidation rate constant K_P, $kg^4m^{-4}s^{-2}$	Linear oxidation rate constant K_L, $kg^2m^{-2}s^{-1}$	Ref.
TiB_2+Fe+Ni+Al cermet	1273 K,70h, air, Pellet	250	-	$9.92x10^{-7}$	60
TiB_2	1373 K,8h, air, pellet	60	$1.2x10^{-7}$	-	59
Al_2O_3+30vol% TiB_2	1073 K,20h, air, pellet	05	$6.94x10^{-10}$	-	59
HfB_2+19SiC+ 5.8Si_3N_4 (Vol%)	1773 K,1h, air, pellet	16	$6.91x10^{-8}$	-	61
SiC+3 wt%AlN	1673 K,192h, air, pellet	19.9	$3.67x10^{-9}$	-	62
WC+18wt%Co	973 K,8h, air, pellet	280	-	$1.36x10^{-5}$	63
AlN+10TiB_2+ 10$TiSi_2$(wt%)	1723 K,3h, air, pellet	41	$1.65x10^{-7}$	-	64
$MoSi_2$	1473 K,75h, air, pellet	01	$2.29x10^{-12}$	-	65

The large volume expansion (~7 vol%) that occurred during the oxidation of TiB_2 to TiO_2 subsequently caused cracking in the oxide layer, resulting in an increase in the active area for oxidation by allowing oxygen ingress through surface cracks in the oxide layer. Linear oxidation behavior was also noted for longer periods (8–13h) of oxidation at 1273 and 1373K[59]. It was also observed that the oxide scale was composed of highly textured TiO_2

crystals, as revealed in Fig. 2.6d. At high temperatures (>1273K) for longer periods, monolithic TiB_2 exhibits linear oxidation behavior owing to the increase in the active area for oxidation.

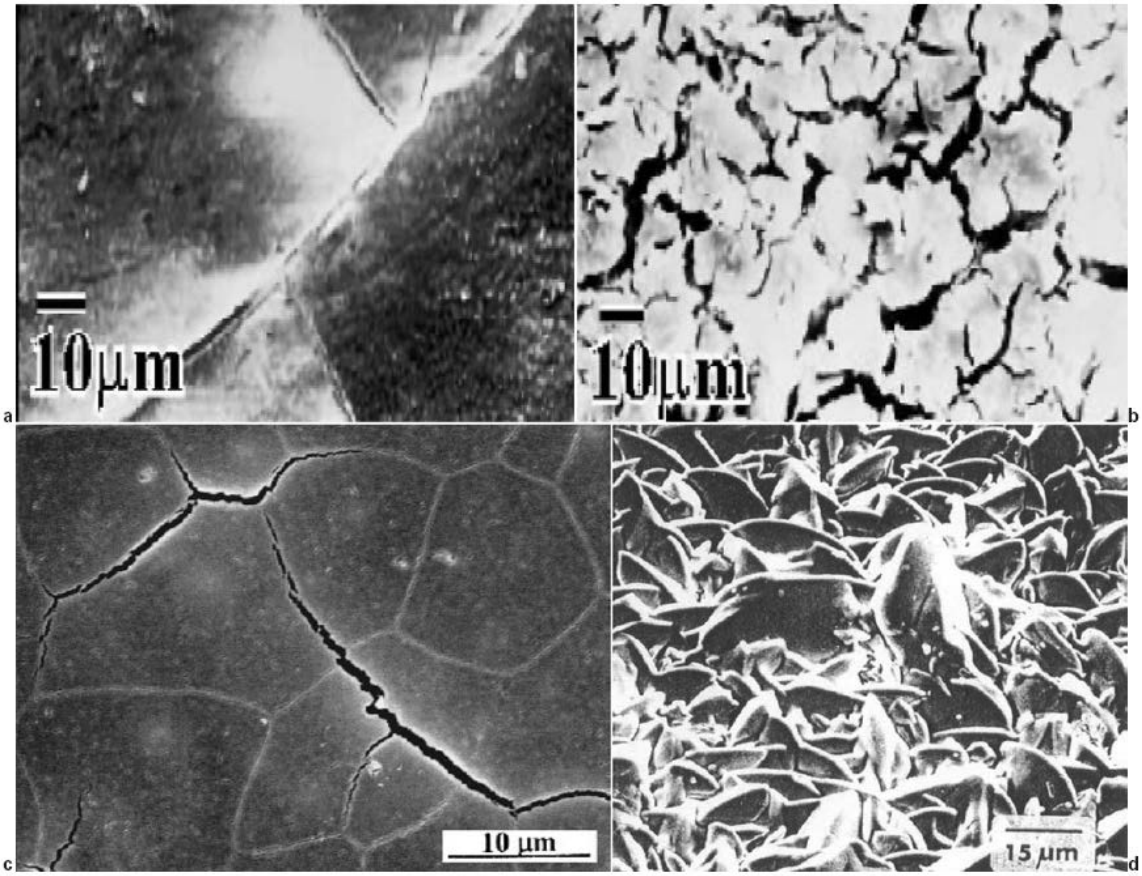

Fig. 2.6 SEM images revealing nature of oxide scale as well as severity of cracking and oxide scale morphology on oxidized surface of monolithic TiB_2, after oxidation at 1123K for a) 1h and for b) 4h, at 1073K for c) 10h and at 1273K for d) 30h [58,59,66]

Koh et al. [67] investigated the oxidation behavior of hot pressed TiB_2+2.5wt% Si_3N_4 at temperatures between 1073 and 1473K for up to 10h in air. TiB_2+2.5wt% Si_3N_4 exhibited better oxidation resistance at high temperatures (<1273K) owing to protective oxide layer formation on the surface. At temperature <1273K, parabolic weight gains were recorded as a result of the formation of TiO_2 and B_2O_3 on the surface. The oxide layer was severely cracked during post oxidation cooling owing to the thermal expansion mismatch between the oxide layer and the underlying bulk material (Fig. 2.7a). At temperatures >1273K, crystalline TiO_2 was identified along with volatile B_2O_3. In this case, the surface was covered with only thick crystalline TiO_2 layer. Fig. 2.7b shows the spheroidal crystalline phase of TiO_2 on the oxidized surface (1273K, air) of TiB_2+2.5wt%Si_3N_4.

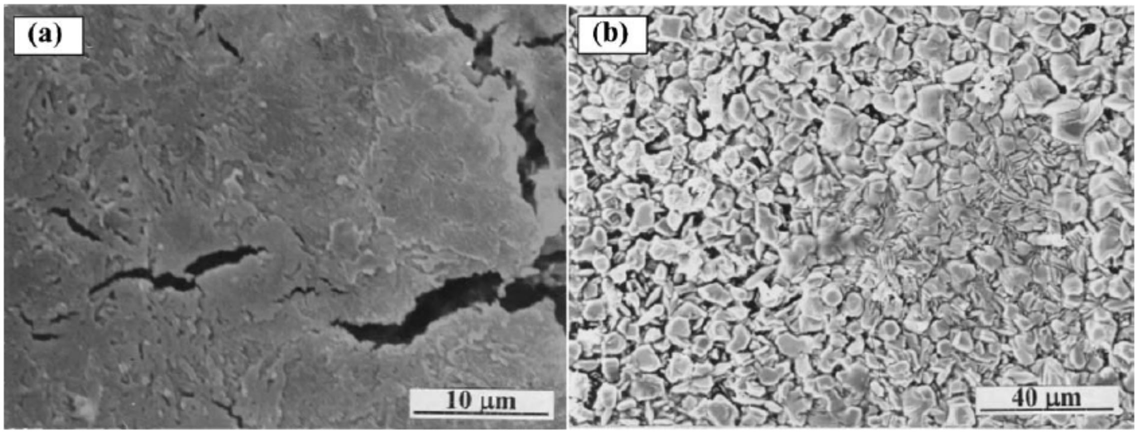

Fig. 2.7 SEM images of severely cracked oxide film on oxidized surfaces of TiB_2+2.5 wt.% Si_3N_4, exposed to air for 10h at a) 1073K and b) 1273K[67]

In understanding the oxidation resistance property, it is also important to study the morphology of subsurface oxide scale. Fig. 2.8 illustrates the subsurface oxide scale formation of TiB_2 after oxidation at 1073 and 1273K [67]. At the lower temperature (1073K) a thick B_2O_3 top layer (~ 50 μm thickness), above a rather thin TiO_2 layer (~ 10 μm thickness) was formed (Fig. 2.8a). Owing to evaporation of B_2O_3 layer during oxidation treatment at T~1273K, only TiO_2 layer was found to be present at the subsurface region after oxidation at 1273K (1000^{o}C). Also, to be noted is the formation of a rather thick TiO_2 layer of ~100 μm thickness at 1273K (1000^{o}C) (Fig. 2.8b). Such a thick layer was observed to be heavily cracked, which implies the non-protectiveness of this oxide scale. However, on oxidation of TiB_2 with $MoSi_2$ additive at

1123K (850^{o}C), the presence of glassy B_2O_3 could not have been detected by XRD, because of its non-crystallinity [66].

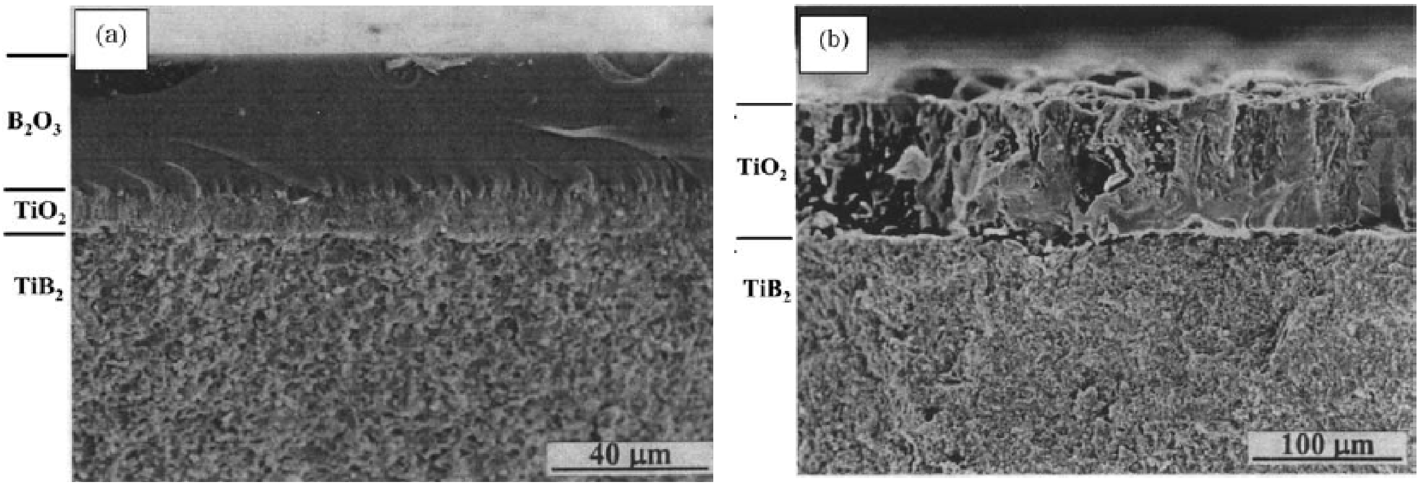

Fig 2.8 Illustration of formation of subsurface oxide scale on fracture surface of TiB_2, oxidized in air at a) 1073K (800^{o}C) for 10h and b) 1273K (1000^{o}C) for 2h[67]

The oxidation behavior of hot pressed TiB_2+12.1 wt%B_4C+2.1 wt%Ni is similar to that of monolithic TiB_2 up to 1173K (900^{o}C), the parabolic kinetics indicating a diffusion limited reaction[68]. At 1273K (1000^{o}C), the best fit of the oxidation data was obtained with the Ginstiling–Brounshtein equation[68]:

$$(1-2/3\alpha) - (1-\alpha)^{2/3} \approx kt \tag{2.15}$$

where $\alpha \approx \Delta w/s$, which considers a three-dimensional diffusion process associated with a decrease in the reaction surfaces, owing to the growth of a product layer around the reactants (spherical particles). As regards the kinetics, the formation of B_2O_3 was detected initially, because of the small radius of the boron atom [69,70]. Its diffusion to the surface is more rapid than the diffusion of the metal atom of the boride and this leads to the formation of large amounts of B_2O_3. The glassy nature of the B_2O_3 film provides additional diffusion barrier for atmospheric oxygen during oxidation.

While oxidation studies have been conducted on a few TiB_2 based materials, the attempts to improve oxidation resistance on an engineering scale are very limited. In an innovative approach, TiB_2 materials were coated with SiO_2 by exposing the specimens in a bed of SiC powder in a flowing H_2 containing 0.1%H_2O at 1723K (1450°C) for 2h [58]. The coating was found to be effective in suppressing the oxidation of TiB_2 at 1473K for 10h. The oxidation rate of coated TiB_2 (at 1473K for 10h) was decreased by about a factor of 10, because of the reduced oxygen transport through the coating and also because of the consumption of oxygen via reaction with Ti_2O_3 to form TiO_2 (Ti_2O_3 was formed during coating with SiO_2 by exposing the specimens in a bed of SiC powder in a flowing H_2 containing 0.1%H_2O at 1723K for 2h). When TiB_2 specimen without a coating was exposed at 1073K (800°C) for 10 h, the surface was covered with crystalline B_2O_3 layer, as shown in Fig. 2.8a. Beneath this B_2O_3 layer, crystalline TiO_2 (rutile) was formed. The TiO_2 layer was severely cracked owing to the thermal expansion mismatch between the oxide layer and underlying TiB_2, as mentioned earlier.

The oxidation of TiB_2 can exert a negative influence on the mechanical and physical properties and on the performance of components, made of TiB_2 ceramics. Therefore, one of the important criteria to define the oxidation resistance of a material is the strength retention property of the material after oxidation. Flexural strength of TiB_2 specimens without and with the SiO_2 coating (after treatment in a bed of SiC powder) was measured and the data were plotted in Fig. 2.9 [58]. Without the coating, the strength reduced remarkably after oxidation for 10h above 1273K (1000°C). It was reported [58] that the formation of a thick oxide layer and the presence of cracks were direct causes for this reduction in strength. When TiB_2 specimen was coated with SiO_2 layer, the strength decreased to a much lower extent. Besides, when the coated specimen was oxidized at 1073K (800°C) for 10 h, the reduction in strength was minimal.

Some of the important engineering applications of TiB_2 are presented in the next section.

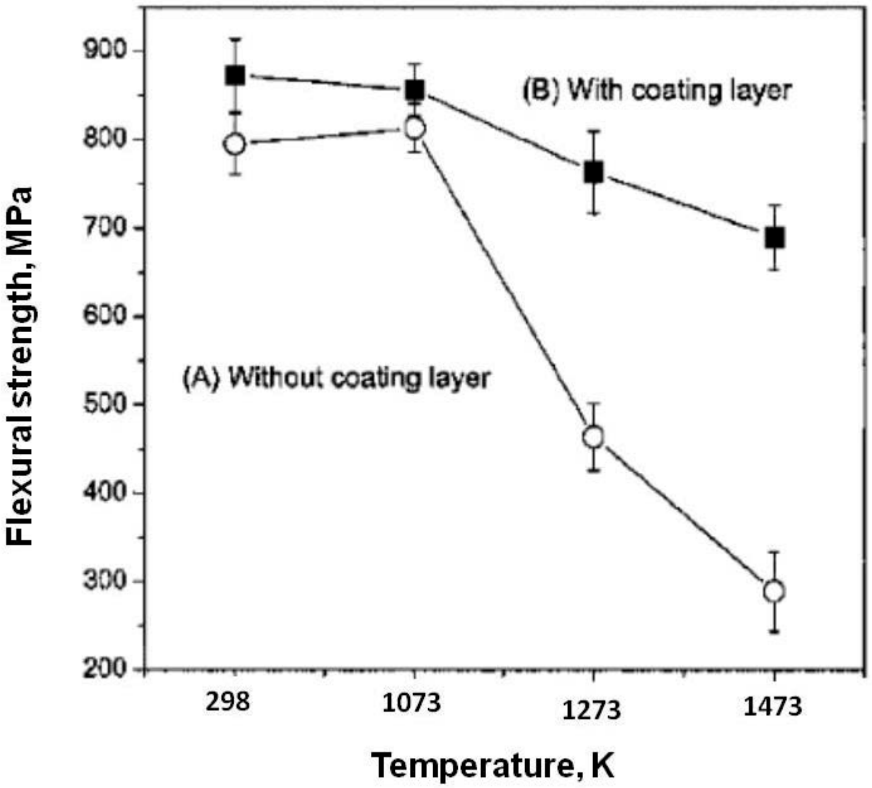

Fig. 2.9 Flexural strength of TiB_2 specimens after oxidation in air for 10h at various temperatures A) without and B) with SiO_2 coating layer [58]

2.5 Applications of bulk TiB_2 materials

TiB_2 can be used as control rod and shielding material in nuclear reactors because it contains boron, which has the ability to absorb fast and slow neutrons without forming any long lived radionuclide. Absorption cross section of TiB_2 for fast neutrons can be enhanced by using compounds which are enriched in ^{10}B isotope during the synthesis of TiB_2. Natural boron contains about 19% ^{10}B and remaining is ^{11}B [1-3]. TiB_2 is also a candidate material for high temperature structural applications like sharp leading edge of hypersonic re-entry vehicles, cutting tools and molten metal crucibles. Apart from re-entry vehicles these materials are candidates for other extreme environment encountered in metal processing industries.

Some of the structural ceramics are considered as potential materials for armor applications owing to their low density, superior hardness and high compressive strength, which enable erosion and ‘defeat of the projectiles’. The desirable characteristics of ceramics, in particular, which are beneficial for the defeat of projectiles, include the combination of high compressive yield strength or hardness, high tensile spall strength, high fracture toughness and high poison’s ratio. In this context, the spall strength of a material can be defined. The stress or strain, at which a further increase in stress or strain causes the material to deform inelastically is Hugoniot Elastic Limit (HEL). Alternatively, the spall strength can be described as the stress, where a material loses its cohesiveness under shock induced tension [72].

Over more than three decades, ballistic performance and dynamic behavior studies have been performed on various ceramics (AlN, Al_2O_3, B_4C, SiC, TiB_2, WC and ZrO_2). As far as armor applications are concerned, TiB_2 exhibits favorable properties, such as high impact velocity for dwell/penetration transition and deformation induced hardening. Dandekar et al. [73] assessed the strength properties of TiB_2 under plane shock wave loading in terms of its spall threshold and the shear stress, when a shock compressive stress of 60 GPa was applied. The break, i.e. cusp in the shock wave loading profile of TiB_2 at 4.5–7.0 GPa is of mechanical nature and its effect is to decrease the spall threshold values at stresses above the cusp, but below the accepted HEL value of 13–17 GPa. The spall strength of TiB_2 decreases with increasing impact stress and becomes negligible at the HEL. Two phase ceramics of titanium diboride/alumina with a range of phase assemblage and phase morphologies have been developed. For armor applications, these materials exhibit a wide range of fracture toughness values, which are often higher than the constituent ceramic phase, in bulk monolithic form [74].

As far as other applications are concerned, TiB_2 is an attractive material for the aluminum industry, because of its wettability and low solubility in molten aluminum and its good electrical conductivity. The wettability of the TiB_2/carbon composite material increased as the TiB_2 content increased [75]. Pure hot pressed TiB_2 is completely wetted by aluminum with contact angle of zero in a cryolite melt at 1253K (980^{o}C) [75].

TiB_2 is extensively used as evaporation boats for vapor coating of aluminum. Fang et al. [76] developed porous TiB_2 electrodes for the alkali metal thermoelectric converter (AMTEC). The electrical performance of these new electrodes was found to be superior to that of the other electrodes, such as TiN or Mo. Because of its chemical inertness, TiB_2 can be expected to show a long time stable operation. Although TiB_2 shows its potential in electrode applications for aluminum extraction, extensive study with various TiB_2 materials (sintered with different sinter aid) is however limited. It is expected that the good wetting property of TiB_2 by aluminum can be affected by the presence of sinter aid.

Other important applications of TiB_2, such as an electrical contact barrier for Si in the semiconductor industry, have also been proposed. However, boron diffusion from TiB_2 into underlying silicon was observed above 1273K (1000^{o}C), which limits its wider application[76].

2.6 Literature on sintering aids used in the present study

In the present study, various silicides $TiSi_2$, $CrSi_2$, WSi_2, $MoSi_2$ and CrB_2 were used. Important physical and mechanical properties of these materials are listed in Table 2.7 [77-88].

Summary of these materials, which were used as sinter aids in TiB_2 or other materials are listed in Table 1.1 (Page no: 1.5).

Table 2.7: Important physical and mechanical properties of various silicides and CrB_2 [77-88]

Property	$TiSi_2$	$CrSi_2$	CrB_2	Ti_5Si_3	WSi_2	W_5Si_3	$MoSi_2$
Crystal structure	Orthorhombic	Hexagonal	Hexagonal	Hexagonal	Hexagonal/Tetragonal	Tetragonal	Tetragonal
Density, kg/m^3	4150	4600	5200	4320	9250	14520	6300
Melting point, K	1813	1750	2473	2403	2437	2597	2323
Hardness, GPa	8-10	11	11-20	9 - 10	13	7-10	13
Fracture toughness, $MPa.m^{1/2}$	2 - 3	-	-	2 - 4	3.7	-	2-2.5
Elastic modulus, GPa	250	354.6	210	150	468	312	384
Flexural strength	-		600	-	-	-	-
Coefficient of thermal expansion, $x10^6\ K^{-1}$	10.4	α_a=9.2, α_c=7.4	6-8	α_a = 5.1 α_c = 22.2	8.5	α_a=5.0, α_c=16.3	8.4
Thermal conductivity, W/m/K	-	10	30	-	-	-	-
Electrical resistivity, $\mu\Omega$□cm	<15/123	70 x 10^3	30	55	20-80	50-60	21
Oxidation resistance, ^oC	-	1200	1000	-	1000	2000	1400

In view of the above concerns, present study focused on the densification of TiB_2 using different additives. Objective of the sinter additive is twofold, one is to lower the sintering temperature to obtain dense body without losing much of its inherent mechanical/ physical properties and other is to improve the oxidation resistance by formation of a protective oxide layer.

One of the major focus areas of recent research is to solve the processing related problems pertaining to the requirement of extremely high sintering temperatures. In this regard, uses of metallic (Telle, 1994; Basu, 2006; Ferber, 1983; Kang, 2001; Kang, 1989; Einarsrud, 1997) as well as ceramic (Basu, 2006; Opila, 2004; Biswas, 2006; Torizuka, 1996; Torizuka, 1992; Murata, 1967; Bellosi, 2006; Monteverde, 2005) sinter-additives have been considered with good results [110-115]. However, incorporation of secondary phases is not devoid of serious drawbacks (Telle, 1994; Basu, 2006) [110-113]. Another important aspect is improving the fracture toughness of borides by microstructural tailoring and incorporation of various reinforcements. However, the important aspect that needs to be considered is that the composition and microstructural design should not have negative impacts over the high temperature performance [110-115].

To date, material researchers have focused on UHTCs (Borides and MAX phase composites) in terms of powders and bulk synthesis, microstructure characterization, physical and mechanical properties evaluation, oxidation and ablation testing, as well as the impact resistance. The powder synthesis is aimed at solving the problem of poor sinterability through modifying the particle morphology and reducing the grains to nano-size. The use of precursor method has also enabled the ability to prepare rod-like and plate-like grains with relative ease. Additionally, in order to enhance the sintering ability, selective sintering additives are necessary to produce low temperature liquid phases in the samples or lowering the grain boundary Gibbs free energy. Generally, the intrinsic strength and modulus of borides are high enough for use in the aircrafts. However, the shortcomings of these ceramics are their brittleness and low damage tolerance, which will have an adverse effect on their wider applications [115].

Nevertheless, the introduction of graphite, carbon fiber, or silicon carbide fiber has contributed to the effectiveness and reliability of borides and carbides. Recently, it has been considered that the microstructure design through texturing is very important to increase their physical and mechanical properties. For instance, Sakka and coworkers [115-117] at NIMS have recently succeeded in using the Strong Magnetic Field Alignment (SMFA) method to design textured microstructures of UHTCs (e.g., ZrB_2, HfB_2 and B_4C) with improved mechanical properties. The oxidation resistance and ablation resistance have also been significantly enhanced through combining silicon carbide and transition metal silicides. [115-117].

2.7 Summary

A significant research activity has been invested to use several sinter-additives and to optimize sintering conditions in order to improve sinterability and mechanical properties of monolithic TiB_2. In particular, an extensive and critical literature analysis has been reported on the role of metallic binders (e.g. Ni, Fe, Cu, Co, Ti) in the densification of TiB_2. More than 99% TD was achieved by liquid phase sintering. However, the presence of metallic binder is not desirable for high temperature structural applications. Therefore, studies related to the use of non-metallic sinter-additives have also been pursued. Several ceramic additives such as AlN, SiC, Si_3N_4, CrB_2, B_4C, TaC were used for attaining the densification of TiB_2 with better mechanical properties. As regards the fabrication routes, it has been noted that hot pressing and pressureless sintering with limited effort of using microwave sintering are employed to densify borides. Despite significant efforts in material development, bulk TiB_2 materials have not yet penetrated into commercial market in a big way. The bottleneck for such limitation is the processing difficulties and poor mechanical properties in terms of fracture toughness.

One of the promising applications of TiB_2 includes high temperature structural materials. As mentioned earlier, room temperature mechanical properties (hardness, toughness, strength, E-modulus) are measured for a large number of bulk TiB_2, sintered using various metallic/ non-metallic additives. Such property measurement at high temperature is lacking. Also, lacking is the measurements of thermal properties (thermal conductivity, thermal expansion coefficient) at high temperature as well as thermal shock resistance property. It can be noted that TiB_2 could be an excellent choice for applications requiring heat dissipation at high temperatures due to its high thermal conductivity. The oxidation resistance of TiB_2 is affected by temperature, partial pressure of oxygen, time of exposure, porosity and sintering additives. It is reported that oxidation resistance of TiB_2 could be improved by coating a protective amorphous SiO_2 layer on the surface of borides. Finally the recent trends in this field are also presented.

2.8 References

[1] Matkovich, V.I., Boron and Refractory Borides, Springler-Verlag, Berlin, Heidelberg, New York, 1977

[2] Subramanian C, Suri AK. Development of boron based neutron absorber materials. Metals Materials and Processes 2004;16[1]:39-52

[3] Basu B, Raju GB, Suri AK. Processing and properties of monolithic TiB_2 based materials.Int Mater Rev 2006;51[6]:354-374

[4] Weimer, A.W., Carbide., Nitride and boride materials synthesis and processing. Chapman & Hall, London, 1997;641-645

[5] Cahn, R.W., Hassen, P., Kramer., Materials Science and Technology, V.11, 175-258.

[6] J. L. Murray, P. K. Liao and K. E. Spear: ‘The B-Ti (boron-titanium) system’, Bull. Alloy Phase Diag.,1986;7[6]:550–554

[7] R. G. Munro: J. Res. Natl. Inst. Stand. Technol., 2000;105[5]:709–720

[8] M. Berger, M. Larsson and S. Hogmark: Surf. Coat. Technol. ,2000;124:253–261

[9] R. Riedel: ‘Handbook of ceramic hard materials’, Vol. 2, 968–990; 2000, Weinheim, WILEY-VCH Verlag GmbH

[10] L. Rao, E. G. Gillan and R. B. Kaner: J. Mater. Res. , 1995;10:333

[11] N.J. Welham, J. Am. Ceram. Soc. 83 (2000) 1290.

[12] R Ricceri, P Matteazzi: Mater. Sci. and Engg. A 379 (2004) 341-346

[13] B. Shahbahrami, R.Sarraf Maamoori, N.Ehsani: Maer. Sci. 25[3] (2007) 719-731

[14] A. K. Khanra, L. C. Pathak, S. K. Mishra and M. M. Godkhindi: Mater. Lett., 2004;58:733–738

[15] H.S.P Fard, H. Baharvandi: Bulletin of Mater. Sci. 34[4] (2011) 883-886.

[16] L.Baca, N.Stelzer: J. Eur. Ceram. Soc. 28 (2008) 907-911

[17] R. A. Cutler: ‘Engineering properties of borides’, in ‘Engineered materials handbook’, Vol. 4, ‘Ceramics and glasses’, 787–801; 1991, Materials Park, OH, ASM International

[18] Y. M. Chiang, D. Birnie and W. D. Kingery: ‘Physical ceramics: principles for ceramic science and engineering’, 398–404; 1997, New York, John Wiley & Sons

[19] S. Baik and P. F. Becher: J. Am. Ceram. S oc. , 1987;70[8]:527–530

[20] R. Telle: ‘Boride and carbide ceramics’, in ‘Materials science and technology’, (ed. R.W. Cahn et al.), Vol. 11, 175; 1994, Weinheim, VCH

[21] W. Wang, Z. Fu, H. Wang and R. Yuan: J. Eur. C eram. S oc. , 2002;22:1045–1049

[22] S. Torizuka, J. Harada and H. Nishio: Ceram. E ng. Sci. Proceed. , 1990;11[9–10]:1454–1460

[23] Y. Muraoka, M. Yoshinaka, K. Hirota and O. Yamaguchi: Mater. Res. Bull. , 1996;31[7]:787–792

[24] S. K. Bhaumik, C. Diwakar, A. K. Singh and G. S. Upadhyaya: Mater. Sci. Eng. A, 2000;279A: 275–281

[25] R. Telle, S. Meyer, G. Petzow and E. D. Franz: Mater. Sci . Eng. A, 1988;105/106A:125–129

[26] C. E. Holcombe and N. L. Dykes: J. Mater. Sci. , 1991;26:3730–3738

[27] Z. S. Rak and J. Czechowski: J. Eur. Ceram. S oc. , 1998;18:373–380

[28] J. Deng, J. Zhou, Y. Feng and Z. Ding: Ceram. Int., 2002;28:425–430

[29] D. H. Kuo and W. M. Kriven: J. Eur. Ceram. S o., 1998;18:51–57

[30] A. H. Jones, R. S. Dobedoe and M. H. Lewis: J. Eur. Ceram. S oc. , 2001;21:969–980

[31] M. H. Satia, I. J. Torres, C. Castillo, T. S. Sudarshan, J. Lesage and D. Chicot: Int. J. Refract. Met. Hard Mater. , 2005;24[1–2]:183–188

[32] A. L. Chamberlain, W. G. Fahrenholtz and G. E. Hilmas: J. Am. Ceram. S oc. , 2006;89[2]:452–456

[33] M. K. Ferber, P. F. Becher and C. B. Finch: Commun. Am. Ceram. S oc. , Jan. 1983; C-2, C-3

[34] H. R. Baumgartner and R. A. Steiger: J. Am. Ceram. S oc. , 1984;67[3]:207–212

[35] Z.H. Zhang, X.B. Shen, F.C. Wang, S.K. Lee, L. Wang, Mater. Sci. Eng. A. 527;2010;5947

[36] S. H. Kang and D. J. Kim, E. S. Kang and S. S. Baek: J. Am. Ceram. S oc. , 2001;84[4]:893–895

[37] T. Graziani and A. Bellosi: Mater. Manufa ct. Process. , 1994;9[4]:767–780

[38] A. Bellosi and F. Monteverde: Proc. Euro PM99, Turin, Italy, November 1999, European Powder Metallurgy Association, 261–268

[39] H. Itoh, S. Naka, T. Matsudaira and H. Hamamoto: J. Mater.Sci., 1990;25:533–536

[40] A. S. Nakane, Y. Takano, M. Yoshinaka, K. Hirota and O. Yamaguchi: J. Am. Ceram. S oc. , 1999;82[6]:1627–1628

[41] J. M. Sanchez, M. G. Barandika, J. G. Sevillano and F. Castro: Scr. Meta ll. Mater. , 1992;26:957–962

[42] F. Monteverde, A. Bellosi and S. Guicciardi: J. Eur. Ceram. S oc. , 2002;22:279–288

[43] J. Russias, S. Cardinast, Y. Aguni, G. Fantozzi, K. Bienvenu and J. Fontaine: Int. J. Refract. Met. Hard Mater., 2005;23:358–362

[44] E. S. Kang, C. W. Jang, C. H. Lee, C. H. Kim and D. K. Kim: J. Am. Ceram. S oc. , 1989;72[10]:1868–1872

[45] M. Einarsrud, E. Hagen, G. Pettersen and T. Grande: J. Am. Ceram. S oc. , 1997;80[12]:3013–3020

[46] L. H. Li, H. E. Kim and E. S. Kang: J. Eur. Ceram. S oc. , 2002;22:973–977

[47] Zhang ZH, Shen XB, Wang FC, Lee SK, Fan QB, Cao MS. Low-temperature densification of TiB_2 ceramic by the spark plasma sintering process with Ti as a sintering aid. Scripta Materialia 2012;66[3-4]:167-170

[48] A. H. Jones, C. Trueman, R. S. Dobedoe, J. Huddleston and M.H. Lewis: Br. C eram. T rans. , 2001;100[2]:49–54

[49] T. S. R. Ch. Murthy, B. Basu, R. Balasubramaniam, A. K. Suri, C. Subramonian and R. K. Fotedar: J. Am. Ceram. S oc. , 2006;89[1]:131–138

[50] K. Biswas, B. Basu, A. K. Suri and K. Chattopadhyay: Scr. Mater., 2006;54:1363–1368

[51] Y. Murata, H. P. Julien and E. D. Whitney: Ceram. B ull. , 1967;46[7]:643–648

[52] J. H. Park, Y. H. Koh, H. E. Kim, C. S. Hwang and E. Kong: J. Am. Ceram. S oc. , 1999;82[11]:3037–3042

[53] S. Torizuka, K. Sato, H. Nishio and T. Kishi: J. Am. Ceram. Soc. ,1995;78[6]:1606–1610

[54] S. Torizuka and T. Kishi: Mater. Trans. JIM , 1996;37[4]:782–787

[55] S. Torizuka, K. Sato, J. Harada, H. Yamamot and H. Nishio: J. Ceram. S oc. Jpn , 1992;100[4]:392–397

[56] J. H. Park, Y. H. Lee, Y. H. Koh, H. E. Kim and S. S. Baek: J. Am. Ceram. S oc. , 2000;83[6]:1542–1544

[57] A. Kulpa and T. Troczynski: J. Am. Ceram. Soc, 1996;79[2]:518–520

[58] Y. H. Koh, H. W. Kim and H. E. Kim: J. Mater. Res., 2001;16[1]:132–137

[59] A. Tampieri and A. Bellosi: J. Mater. Sci., 1993;28:649–653

[60] M. G. Barandika, J. J. Echeberria and F. Castro: Mater. Res. Bull. 1999;34[7]:1001–1011

[61] F. Monteverde and A. Bellosi: J. Eur. Ceram. Soc., 2005;25:1025–1031

[62] H. J. Choi, J. G. Lee and Y. W. Kim: J. Am. Ceram. Soc., 2002;85[9]:2281–2286

[63] B. Casas, X. Ramis, M. Anglada, J. M. Salla and L. Llanes: Int. J. Refract. Met. Hard Mater., 2001;19:303–309

[64] V. A. Lavrenko, J. Desmaison, A. D. Panasyuk and M. Desmaison-Brut: J. Eur. Ceram. Soc., 2003;23:357–369

[65] R. Mitra: Int. Mater. Rev., 2006;51:13–64

[66] T. S. R. Ch. Murthy, R. Balasubramaniam, B. Basu, A. K. Suri and M. N. Mungole, J. Eur. Ceram. Soc., 2006;26[1–2]:187–192

[67] Y. H. Koh, S. Y. Lee and H. E. Kim: J. Am. Ceram. Soc., 2001;84[1]:139–141

[68] T. Graziani, E. Landi and A. Bellosi: J. Mater. Sci. Lett., 1993;12:691–694

[69] Singh M, Wiedemeier H. Chemical interactions in diboride reinforced oxide-matrix composites. J Am Ceram Soc 1991;74[4]:724–727

[70] V. A. Lavrenko, S. S. Chuprov, A. P. Umanskii, T. G. Protsenko, and E. S. Lugovskaya: Sov. Powder Metall. Met. Ceram., 1987;26:761–762

[71] 71.T.A.Parthasarathy, R.A.Rapp, M.Opeka, R.J.Kerans; “A model for the oxidation of ZrB_2, HfB_2 and TiB_2”, Acta Materialia; 2007;55:5999-6010

[72] G. Kennedy, L. Ferranti, M. Zhou and N. Thadhani: J. Appl. Phys., 2002;91[4]:1921–1927

[73] D. P. Dandekar and D. C. Benfanti: J. Appl. Phys., 1993;73[2]:673–679

[74] A. R. Keller and M. Zhou: J. Am. Ceram. Soc., 2003;86[3]:449–457

[75] K. D. Watson and J. M. Toguri: Metall. Mater. Trans. B, 1991;22B:617–621

[76] Q. Fang and R. Knodler: J. Mater. Sci., 1992;27:6725–6729

[77] Yamada S, Hirao K, Yamauchi Y, Kanzaki S. Mechanical and electrical properties of B_4C–CrB_2 ceramics fabricated by liquid phase sintering. Ceram Int ,2003;29:299-304

[78] Emiliani ML. Characterization and oxidation resistance of hot pressed chromium diboride. Mater Sci Eng A 1993;172:111-124

[79] I.Mitra and T.Telle, “Phase formation during anneal of supersaturated TiB_2-CrB_2-WB_2 solid solutions”, Journal of solid state chemistry 1997;133:25-30

[80] Peshev P, Khristov M, Gyurov G. The growth of titanium, chromium and molybdenum disilicide crystals from high-temperature solutions. J Less-Common Met 1989;153:15-22

[81] Ma J, Gu Y, Shi L, Chen L, Yang Z, Qian Y. Synthesis and thermal stability of nanocrystalline chromium disilicide. J Alloys Compd 2004;376:176-179

[82] Shishido T, Okada S, Ishizawa Y, Kudou K, Iizumi K, Sawada Y, et al. Molten metal flux growth and properties of $CrSi_2$. J Alloys Compd 2004;383:319-321

[83] Gang FQ, Jun LH, Hong SX, Ling LX, Zhi LK, Min H. Microstructure and anti-oxidation property of $CrSi_2$-SiC coating for carbon/carbon composites. Appl Surf Sci 2006;252:3475-3480

[84] Xiama T, Philippe J, Catherine C, Jean CT. First-principles study of the structural, electronic and elastic properties of W_5Si_3. Intermetallics 2010;18:688-693

[85] Zmii VI, Kovtun NV, Glushko PI, Ruden’kii SG. Stability and heat resistance of silicide coatings on tungstem and molybdenum at 1500-2000^oC. Powder Metallurgy and Metal Ceramics 2003;42(1-2):50-53

[86] C.L.Yeh, W.H.Chen, C.C. Hsu, “Formation of titanium silicides Ti_5Si_3 and $TiSi_2$ by self-propagating combustion synthesis”, J. Alloys and compounds, 2007;432:90-95

[87] T.C. Chou and T.G. Nieh, “New observations of MoSi2 pest at 500^0C,” Scripta Metallurgica et Materialia; 1992;26:1637-42

[88] C.D. Wirksus and D.R. Wilder, “High-Temperature Oxidation of Molybdenum Disilicide,” *J.Am.Ceram.Soc.*, 1966;49[4]:173-177

[89] G.B.Raju, and B.Basu, “Densification, Sintering Reactions, and Properties of Titanium Diboride with Titanium Disilicide as a sintering Aid,” J. Am. Ceram. Soc. 2007;90[11]:3415-3423

[90] G.B.Raju, K.Biswas and B.Basu, “Microstructural characterization and isothermal oxidation behavior of hot-pressed TiB_2-10wt.% $TiSi_2$ composites,” Scripta Materialla 2009;61:104-107

[91] Raju GB, Basu B, Tak NH, Cho SJ. Temperature dependent hardness and strength properties of TiB_2 with $TiSi_2$ sinter-aid. J Eur Ceram Soc 2009;29(10):2119-2128

[92] Lu H, Han H, Ma R, Wang Y, Qiu D. Titanium diboride and wolfram silicide composite used as aluminum electrolysis inert cathode materials. TMS Light Metals 2006:687-690. devices, 1992;39[10]:2341-2345

[93] W. G. Fahrenholtz, G. E. Hilmas, I. G. Talmy and J. A. Zaykoski, “Refractory Diborides of Zirconium and Hafnium,” J. Am. Ceram. Soc., 2007;90[5]:1347-1364

[94] F. Monteverde, “Progress in the fabrication of ultra high temperature ceramics: in situ synthesis, microstructure and properties of a reactive hot-pressed HfB_2-SiC composite,” Composites Science and Technology, 2005;65:1869-1879

[95] D. Sciti, F. Montevrde, S. Guicciardi, G. Pezzotti and A. Bellosi, “Microstructure and mechanical properties of ZrB_2-$MoSi_2$ cermic composites produced by different sintering techniques,” Mater. Sci. Eng. A,, 2006;434:303-309

[96] D. Sciti, S. Guicciardi, A. Bellosi and G. Pezzotti, “Properties of a pressureless-Sintered ZrB_2-$MoSi_2$ Cermic Composite,” J. Am. Ceram. Soc., 2006;89[7]:2320-2322

[97] D. Sciti, L. Silvestroni and M. Nygren, “Spark plasma sintering of Zr- and Hf borides with decreasing amounts of MoSi2 as sintering aid,” J. Eur. Cearm. Soc., 2008;28:1287-1296

[98] L. Silvestroni and D. Sciti, “Effects of MoSi2 additions on the properties of Hf and Zr-B_2 composites produced by pressureless sintering,” Scripta Materialia, 2007;57:165-168

[99] J. B. Berkowitz-Mattuck, “High-temperature oxidation III. Zirconium and hafnium diborides,” Journal of the Electrochemical Society, 1966;113[9]:908-914

[100] F. Monteverde and L. Scatteia, “Resistance to thermal shock and to oxidation of metal diborides-SiC ceramics for aerospace application,” J. Am. Ceram. Soc., 2007;90[4]:1130-1138

[101] W. G. Fahrenholtz, “Thermodynamic analysis of ZrB2-SiC oxidation: Formation of a SiC-depleted region,” J. Am. Ceram. Soc., 2007;90[1]:143-148

[102] M. M. Opeka, I. G. Talmy and J. A. Zaykoski, “Oxidation-based materials selection for 2000^{o}C hypersonic aerosurfaces: Theoretical considerations and historical experience,” J. Mater. Sci., 2004;39:5887-5904

[103] F. Peng and R. F. Speyer, “Oxidation resistance of fully dense ZrB_2 with SiC, TaB_2, and $TaSi_2$ additives,” J. Am. Ceram. Soc., 2008;91[5]:1489-1494

[104] F. Monteverde and A. Bellosi and S. Guicciardi, “Processing and properties of zirconium diboride-based composites,” J. Eur. Ceram. Soc., 2002;22:279-288

[105] J.K. Sonber, T.S.R.Ch. Murthy, C. Subramanian, R.C. Hubli, and A.K. Suri, “Effect of EuB_6 addition on densification and properties of ZrB_2” Int. J. Refract. Met. Hard Mater. 35, 96-101 (2012)

[106] J.K.Sonber, T.S.R.Ch.Murthy, C.Subramanian, N.Krishnamurthy, R.C.Hubli and A. K. Suri, “Effect of $CrSi_2$ and HfB_2 addition on densification and properties of ZrB_2“, Int. J. Refract. Met. Hard Mater. 2012;31:125-131

[107] J. K. Sonber, T. S. R. Ch. Murthy, C. Subramanian, Sunil Kumar, R. K. Fotedar and A.K. Suri “Investigations on synthesis of ZrB_2 and development of new composites with HfB_2 and $TiSi_2$”, International Journal of refractory metals and hard materials, 2011;29:21-30

[108] J. K. Sonber, T. S. R. Ch. Murthy, C. Subramanian, Sunil Kumar, R. K. Fotedar and A. K. Sur**i** “Investigations on synthesis of HfB_2 and development of a new composite with $TiSi_2$” Int. J. Refract. Met. Hard Mater. 2010;28:201–210

[109] Fahrenhltz WG, Hilmas GE; Oxidation of ultra-high temperatura transition metal diboride ceramics; 2012;57[1]:61-72

[110] Bellosi, A., & Monteverde, F. (2006). Ultra-high temperature ceramics: Microstructure control and Properties improvement related to materials design and Processing procedures. *Proceedings 5th European Workshop on Thermal Protection Systems and Hot Structures*, Noordwijk, The Netherlands (pp. 17 – 19) (ESA SP-631, August 2006).

[111] Bellosi, A., Monteverde, F., & Sciti, D. (2006). Fast Densification of Ultra-High-Temperature Ceramics by Spark Plasma Sintering. *Int J Appl Ceram Technol*, *3*, 32–40. doi:10.1111/j.1744-7402.2006.02060.x.

[112] Ferber, M. K., Becher, P. F., & Finch, C. B. (1983). Effect of microstructure on the properties of TiB_2 ceramics. *Journal of the American Ceramic Society*, *66*, C-2–C-3. doi:10.1111/j.1151-2916.1983.tb09974.x.

[113] Kang, E. S., Jang, C. W., Lee, C. H., Kim, C. H., & Kim, D. K. (1989). Effect of iron and boron carbide on the densification and mechanical properties of titanium diboride ceramics. *Journal of the American Ceramic Society*, *72*, 1868–1872. doi:10.1111/j.1151-2916.1989.tb05993.x.

[114] Kang, S. H., Kim, D. J., Kang, E. S., & Baek, S. S. (2001). Pressureless sintering and properties of titanium diboride ceramics containing chromium and iron. *Journal of the American Ceramic Society*, *84*, 893–895. doi:10.1111/j.1151-2916.2001.tb00763.x.

[115] Book title: "MAX Phase and Ultra-High Temperature Ceramics for Extreme Environments"; ISBN:9781466640665; Publisher: IGI Global; (2013) http://www.igi-global.com/chapter/processing-methods-for-ultra-high-temperature-ceramics/80032

[116] HU.C.F.Sakka, Y., Grasso, S., Nishimura, T., Guo, S. Q., & Tanaka, H. (2011). Shell-like nanolayered Nb_4AlC_3 ceramic with high strength and toughness. *Scripta Materialia*, *64*, 765–768. doi:10.1016/j.scriptamat.2010.12.045.

[117] Hu, C. F., Sakka, Y., Tanaka, H., Nishimura, T., & Grasso, S. (2011). Fabrication of textured Nb_4AlC_3 ceramic by slip casting in a strong magnetic field and spark plasma sintering. *Journal of the American Ceramic Society*, *94*, 410–415. doi:10.1111/j.1551-2916.2010.04096.x.

CHAPTER 3

CHAPTER 3

EXPERIMENTAL PROCEDURE

3.1 Introduction

In this chapter, experimental details of the preparation, densification and characterization of TiB_2 and other materials are presented apart from a description of the equipments used and processes implemented.

Titanium diboride (TiB_2) and pre-alloyed $(TiCr)B_2$ based composites were synthesized by reduction of the respective oxides with a mixture of boron carbide and additional carbon/boron as required. Different sinter additives used in the present study were also synthesized from the constituents or from the precursors. A list of sinter additives and the reasons for investigating them are listed in Table 3.1.

The experimental facilities used broadly come under four categories: (a) milling equipments (b) furnaces (c) sample preparation/fabrication equipments and (d) characterization instruments.

Oxidation studies of composites were carried out in the temperature range of 1023 to 1273K (750 to 1000^{o}C). Non isothermal oxidation studies were carried out in a TGA apparatus and isothermal oxidation studies were carried out in a muffle furnace. After oxidation, the samples were characterized by XRD, XPS and SEM-EDS.

Table 3.1 List of TiB_2 composites covered in the present study

Sr.No.	Sinter additive used	Wt.%	Function of the additive
01	$TiSi_2$	2.5, 5, 10 and 15	To improve fracture toughness, sinterability and oxidation resistance
02	$CrSi_2$	2.5, 5, 10 and 15	
03	WSi_2	2.5, 5, 10 and 15	To improve fracture toughness, strength, sinterability and oxidation resistance
04	CrB_2	2.5, 5, 10 and 15	To improve fracture toughness, strength, sinterability, thermal shock and oxidation resistance
05	CrB_2+20%$MoSi_2$	5, 10 and 15	
06*	$(Ti_{1-x}Cr_x)B_2$+ 20%$MoSi_2$	0.5, 0.10 and 0.15	

***** Composite

3.2 Equipments/Instruments

A description and working principle of each of the major instruments/equipments used in the present study is given below. These equipments/instruments are broadly covered under four categories as given below:

a) Milling equipments

i) Jaw crusher, ii) Planetary ball mill, iii) Vibratory cup grinding mill

b) Furnaces

i) Vacuum induction furnace, ii) Vacuum hot press, iii) Muffle furnace/twin zone furnace

c) Sample preparation/fabrication equipments

i) Diamond wheel cutter, ii) Wire cut EDM, iii) polishing, iv) Sputter coating equipment

d) Characterization Instruments

i) Particle size analyzer, ii) XRD, iii) SEM, iv) EDS, v) TGA, vi) Hardness tester, vii) Flexural strength, viii) Dilatometer, ix) Four probe electrical resistivity measurement unit

a) Milling equipments

i) Jaw crusher

Figure 3.1 (a) is a schematic diagram of a jaw crusher [3] and (b) the actual photograph. The crushing of materials is accomplished within crushing chamber which consists of two lateral side walls, one settable fixed crushing jaw and the other a moveable crushing jaw. The moveable crushing jaw is put into an eccentric movement by means of a fly wheel and a sturdy cam. The special design of the movement of the movable crushing jaw ensures that the material to be crushed is drawn into the crushing chamber and that the blockage of the chamber with crushed pieces is prevented [3,4]. The pre-crushed materials can easily fall out of the crushing chamber. Both lateral side walls are lined with tungsten carbide. In the present study, jaw crusher was used to reduce the size of pellets from 5-20 mm to ≤2 mm size in multiple steps. Further size reduction was carried out in high energy vibratory cup grinding mill.

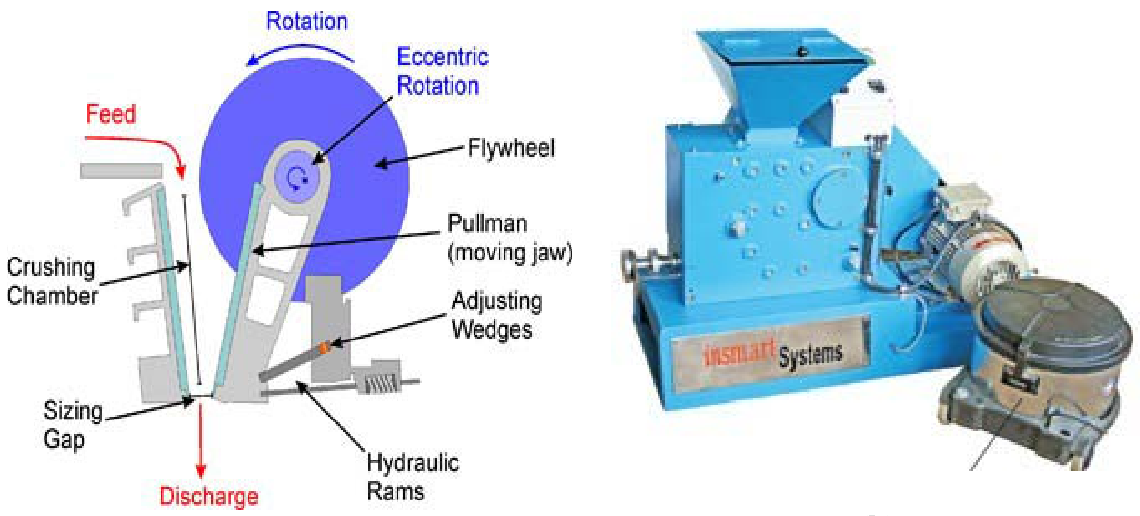

(a) **(b)**

Fig. 3.1 a) Schematic diagram [3] and b) Photograph of a jaw crusher [4]

ii) Planetary ball mill

Figure 3.2 (a) is a schematic diagram of a planetary ball mill [3] and (b) the actual photograph. Planetary ball mill is a type of mixer and/or grinder. Ball mills rotate around a horizontal axis, partially filled with the materials to be mixed /ground plus the grinding medium of WC balls [7]. Mixing is achieved by high energy frequent repeated impact of balls; the energy levels of balls are high as they are accelerated 12 times the acceleration due to gravity. Rotation of sun plate provides the centrifugal force to the grinding balls and independent rotation of bowls make the balls to hit the inner wall of the bowls. Since the bowls are rotating in alternate (one forward cycle and one reverse cycle) directions a considerable part of grinding will take place in addition to homogenous mixing [4,5]. In the present study, planetary ball mill was used to wet mixing of the raw materials. Total four bowls of 500 cc capacity were fitted on the sun plate. Each bowl was filled with 100 g of charge (raw materials), 400 g of WC balls and 150 ml of alcohol. Mixing was carried out for 4 hours with intermittent cooling to avoid overheat of the material. Wet mixing was carried out in isopropyl alcohol; after completion of mixing, powders were dried in vacuum oven.

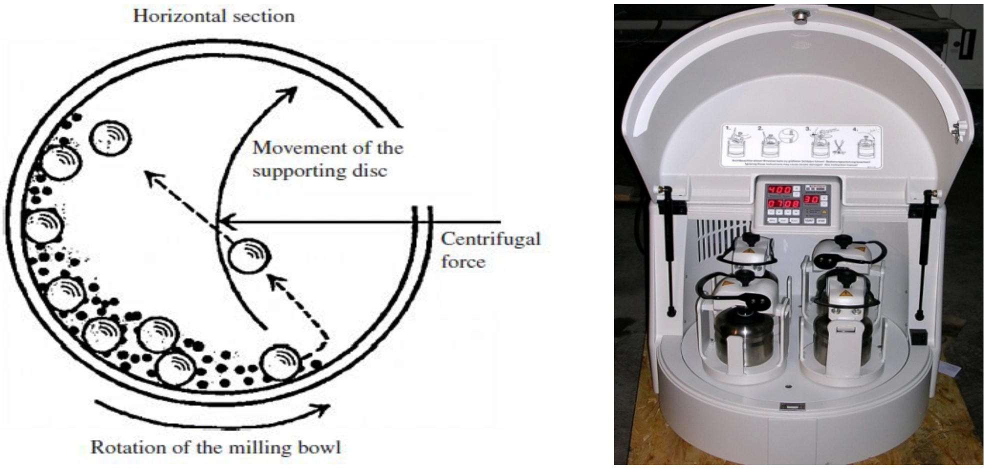

(a) (b)

Fig. 3.2 a) Schematic diagram [3] and b) Photograph of a planetary ball mill [5]

iii) Vibratory cup grinding mill

Figure 3.3(a) is an actual photograph a vibratory cup grinding mill and (b) bowl set. A vibrating cup grinding mill, as the name itself suggests, is a machine which uses heavy mechanical impact and friction to grind the substances and break these down into fine micron size powders. The whole process of breakdown is mechanical and it is the vibrations which impart the kinetic energy to the ring and the hammer for grinding the materials kept in the annular space. Grinding is accomplished by heavy impact and friction. Sample is kept in the annular space between the bowl, the ring and hammer (shown in the Figure 3.3b). A cover is kept on the top of the bowl and then it is clamped on. The vibratory platform imparts the kinetic energy to the ring and the hammer [4]. Grinding is generally carried out for 5 to 20 minutes with intermittent cooling. In the present study, this mill was used to grind the crushed pellets from 1-2 mm size to 1-5 micron size. At a time 100 gm of the powder can be charged in each pot.

(a) (b)

Fig. 3.3 a) Photograph of a vibratory cup grinding and b) mill with bowl set [4]

b) Furnaces

i) Vacuum induction furnace

Figure 3.4(a) presents the schematic and (b) the actual photograph of induction furnace with vacuum system. An induction furnace is powered by an electrical source that is designed to deliver high frequency alternating current (AC), at the proper frequency required to create an alternating electromagnetic field. The AC power is conducted through a coil of copper tubing so that it can generate the magnetic field. Water is pumped through the coil to keep it cool. The material to be heated is put inside a crucible of electrically conducting (fairly high resistance), high melting point material such as graphite (called susceptor), sized to fit inside the coil [7]. The graphite crucible with material charge is exposed to the alternating magnetic field produced by the coil when current is passed. Heat is generated by resistance offered by the susceptor material to the eddy currents induced by the magnetic field in the susceptor (graphite crucible) and passed on to the charge by conduction [6,7]. Power supply and control system for induction furnace is from an insulated gate bipolar transistor (IGBT) unit. Operating frequencies range from utility frequency (50 Hz) to 10 kHz, usually depending on the configuration of the furnace, size and material of the susceptor, and the heating speed required. The advantage of the induction furnace is a clean, energy-efficient and well-controllable heating process compared to most other means of heating.

In the present study, 40 kW capacity vacuum induction furnace was used for synthesis of borides and silicides. Graphite crucible used for synthesize these materials, as it is a good susceptor. This furnace can be used upto 2675K (2400^{o}C) temperature under 0.001Pa vacuum. Rate of heating can be maintained from 300 to 800 K/h. Actual synthesis temperature was measured using a two color optical pyrometer.

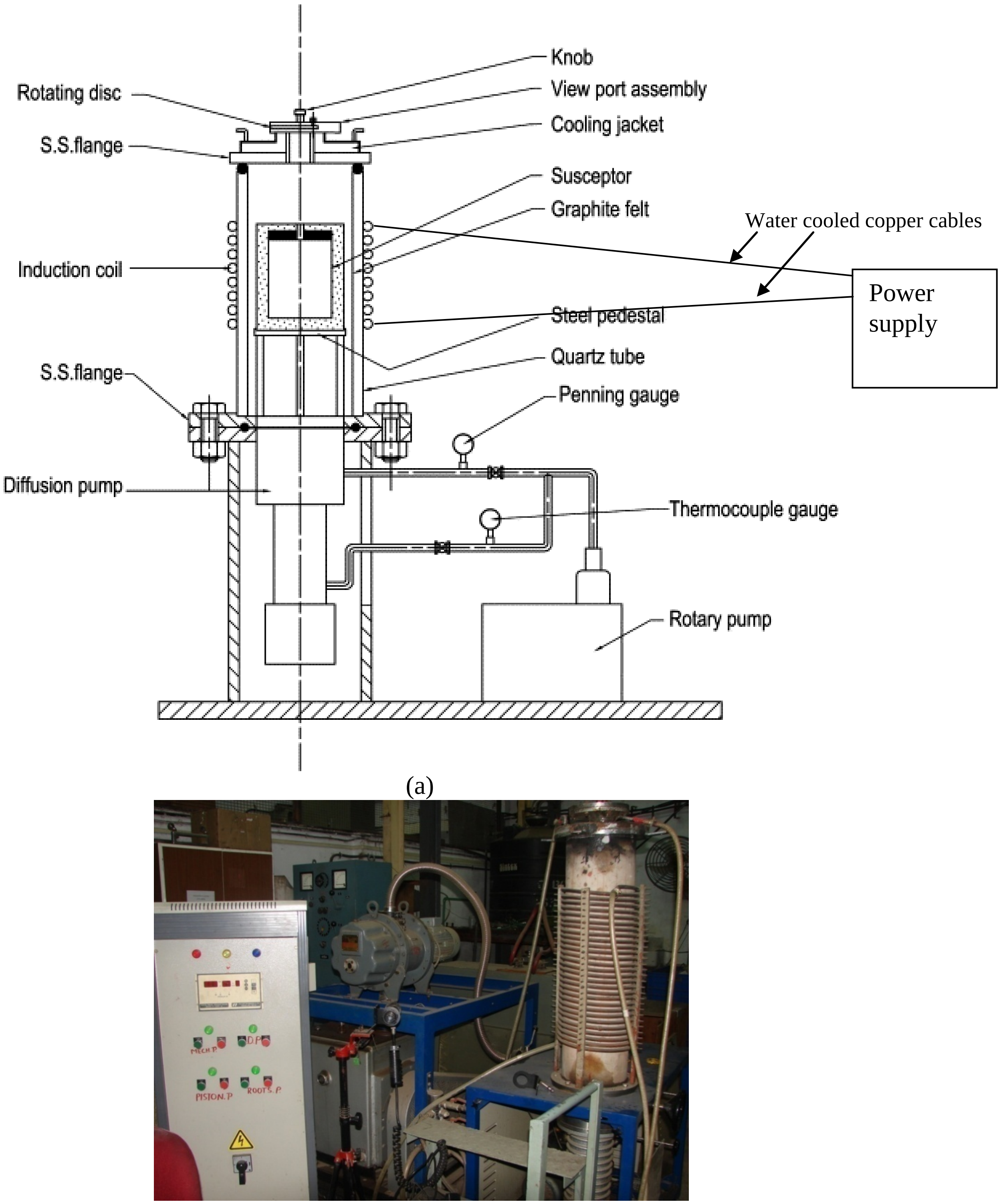

(a)

(b)

Fig.3.4a) Schematic [18] and b) actual photograph of a vacuum induction furnace [8]

ii) Vacuum hot press

Figure 3.5(a) is a schematic diagram of a hot press and (b) the actual photograph. Hot pressing is a high-pressure, low-strain-rate powder metallurgy process for forming a powder or powder compact at a temperature high enough to induce sintering and creep processes. This is achieved by the simultaneous application of heat and pressure. Hot pressing is mainly used for densification of high melting point materials by powder metallurgy route. The densification works through particle rearrangement and plastic flow at the particle contacts [6,7]. The loose powder was filled in a graphite die that withstands up to temperatures of about 2573K (2500^{o}C) under pressures of up to 35MPa.

In the present study, hot press was used to densify the TiB_2 based composites at different temperatures and pressures. Actual temperature of the hot press was measured by a two color optical pyrometer. Graphite plungers and dies were used to consolidate these composites. After loading the die in the hot press, initially a dead load of <50 kg was applied. Full load (350 to 550 kg) was applied after reaching the set temperature. Linear variable differential transducer (LVDT) was used to measure the linear shrinkage during heating as well as holding period. After completion of holding period, load was released slowly and cooled down to room temperature in vacuum. Ejected pellets were cleaned and measured the density and open porosity by Archimedes principle.

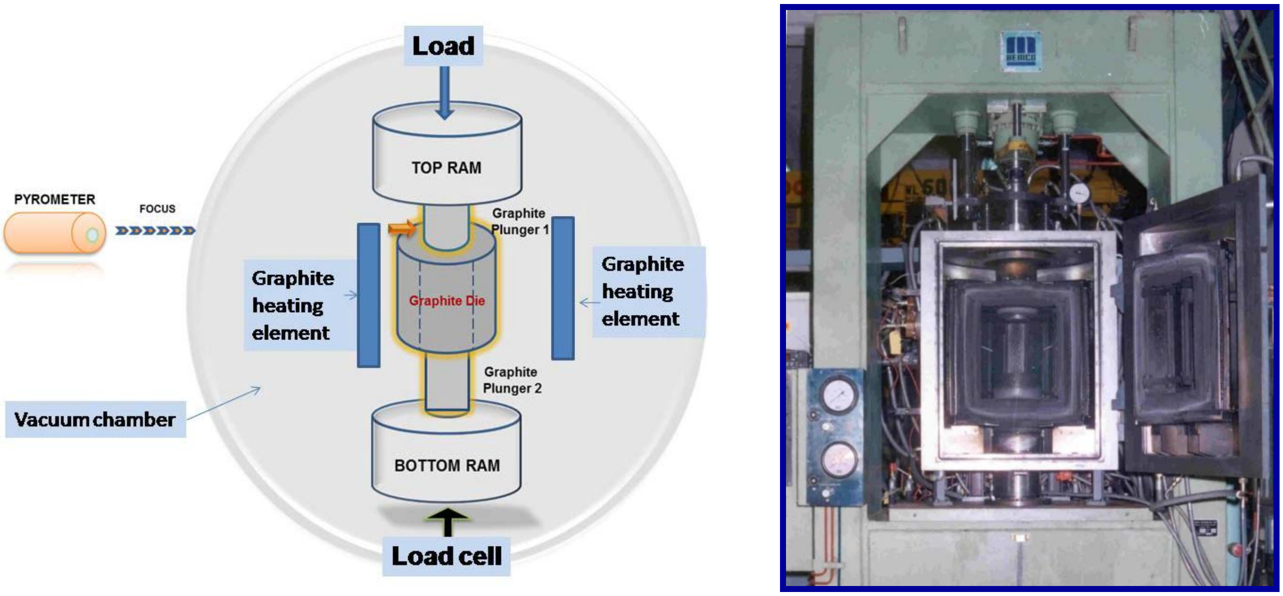

(a) (b)

Fig. 3.5 a) Schematic diagram [3] and b) Photograph of a vacuum hot press [9]

iii) Muffle furnace/Twin zone furnace

Figure 3.6 (a) is an actual photograph of muffle furnace and (b) twin zone heating furnace, which were used for isothermal oxidation and thermal cycling studies respectively. A muffle furnace in historical usage is a furnace in which the subject material is isolated from the fuel and all of the products of combustion including gases and flying ash. Materials for heating elements, such as molybdenum disilicides offered in many models with working temperatures up to 1773K (1500^{o}C), which facilitates more sophisticated metallurgical applications [7].

In the present study, muffle furnace was used for isothermal oxidation studies of the composites. Temperature was measured by using K-type thermocouples. Samples were loaded in a furnace directly, after reaching the set temperature. PID controller and thyristor were used to control the temperature and holding time. Twin zone furnace was used for thermal cycling studies. Thermal cycle study was carried out for composites, using a twin zone vertical furnace with pneumatic movement of the sample holder from hot zone to the cold zone and vice versa. Movement of the sample between zones was rapid (<5 sec). Hot zone and cold zone were maintained at 850^{o}C (1123K) and 150^{o}C (423K) respectively. The samples were tested up to 1000 cycles.

(a) (b)

Fig. 3.6 Actual photograph of a) muffle furnace [10] and b) twin zone furnace [10]

c) Sample preparation/fabrication equipments

i) Diamond wheel cutter

Figure 3.7 (a) & (b) are photographs of a diamond wheel cutting machines. Diamond wheel cutting machine is used for cutting hard samples of different sizes as per requirement. This works on the principle of abrasion cutting. While diamond wafer blade rotates at a very high speed of ~ 3000 rpm, then cutting action takes place at the interface of sample with rotating blade due to abrasion [6,7,11,12]. This machine can be used to cut slices of the ceramic samples. But disadvantage of this cutting method is a time required for very hard materials. In the present study, these cutting machines were used for slicing of various composites for characterization.

ii) Wire cut EDM

Figure 3.7(c) is a photograph of CNC wire cut Electric discharge machining (EDM) machine. EDM is a process of repetitive sparking. A series of electrical pulse generated by the pulse generator unit is applied between the work piece and the traveling wire electrode. In the event of spark discharge, there is a flow of current across the wire electrode – work piece gap. Energy contained in a tiny spark discharge removes a fraction of work piece material. Large number of such time spaced tiny discharges between the work piece and wire electrode cause the electro erosion of the work piece [13]. Electric discharge machine comprises of a machine tool, a power supply unit and a dielectric supply unit.

The machine tool comprises of a main work table (called as X-Y table), an auxiliary table (called as U-V table) and a wire drive mechanism. The work piece is mounted and clamped on the main work table. The main table moves along X and Y axes, in steps of 1 micron, by means of servo motor, and also the U-V table moves by 1 micron, also by means of a servo motor. U & V axes are parallel to X & Y axes. To accommodate jobs of different thickness, movement along another axis is provided (Z). Maximum 250 mm thick material can be cut in this machine. The power supply unit comprises of electric pulse generator, motor drive units for X, Y, U, V axes and controller.

In the present study, this machine was used for cutting of hard composites with different 2-dimensional complex shapes for various characterization studies. In this machine the cutting speed does not depend on the hardness of the material; but cutting speed depends on electrical conductivity. In the present study, all the composites are having the sufficient electrical conductivity to be cut by EDM.

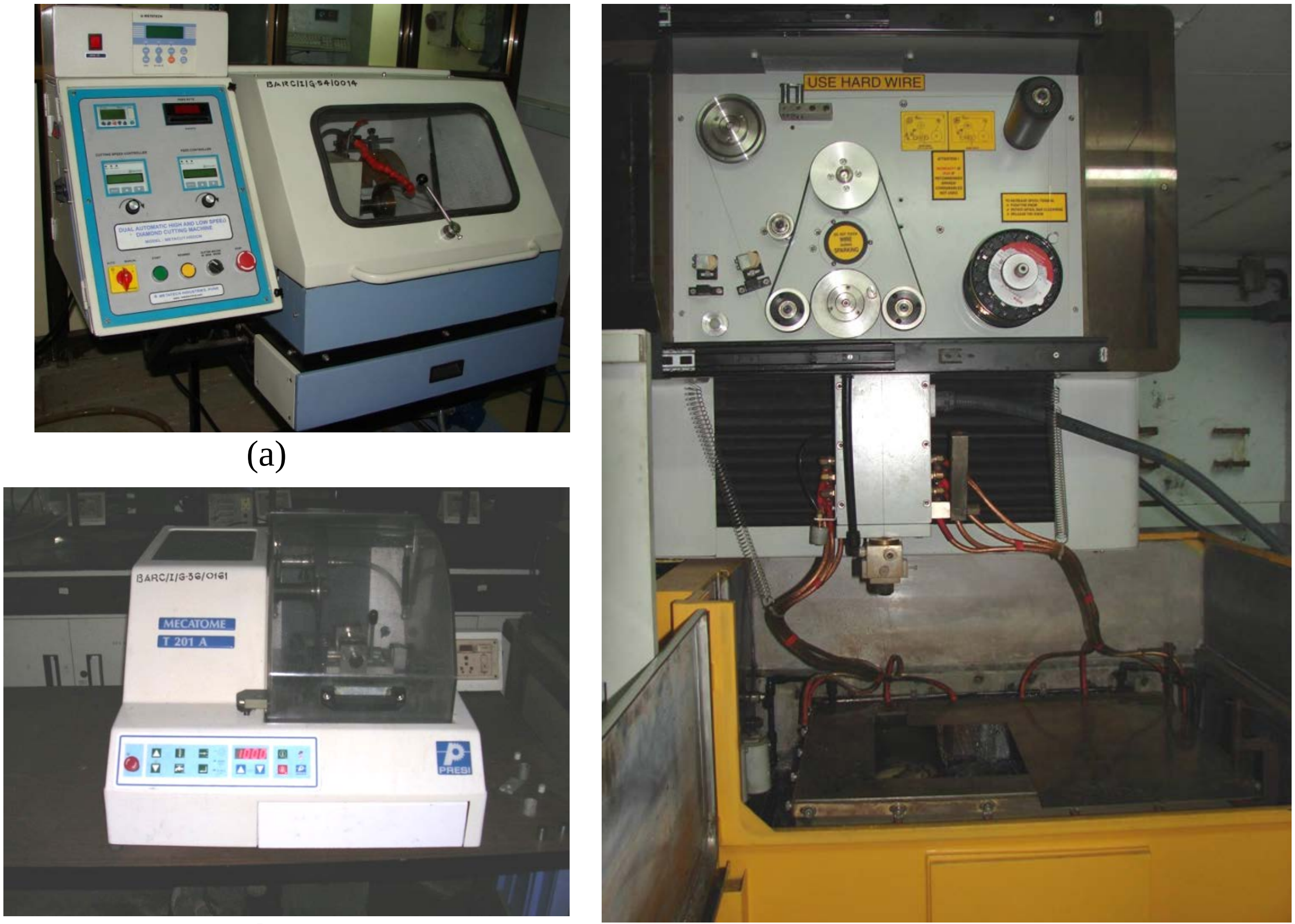

(a)

(b)

(c)

Fig.3.7 Typical diamond wheel cutters (a[11] & b[12]), CNC wire cut EDM machine (c) [13]

iii) Polishing

Mirror finished polished surfaces are required for microstructural characterization. This is achieved sequentially by using the different grades of emery papers and finally by cloth polishing with abrasive particles. Cloth polishing can be carried out by two different processes:1. diamond polishing (DP),and 2. Oxide polishing (OP). Diamond is used as an abrasive to accomplish the fastest material removal and the best possible plainness. Because of its hardness, diamond cuts extremely well through all materials and phases [6,7]. In the present study, the sequence of polishing is as follows: EDM cut sample was hot mounted using conductive resin of 1” diameter mould, hot mounted sample was subjected to grinding using diamond grinding wheel to obtain <50 µm finish. Beveling of the hot mounted sample has been carried out, to remove the sharp edges of sample in order to avoid the damage of polishing cloth. Further polishing was carried out using cloth polishing machine with different diamond slurries of 15, 9, 6, 3, 1 and 0.25 µm. At the end of the polishing with 0.25 µm, the surface appears to be mirror finished.

iv) Sputter coating equipment

Figure 3.8 (a) is a schematic diagram of a sputter coating equipment and (b) the actual photograph. Sputter coating is a process of covering the specimen with a very thin layer of a conducting material, typically a metal, such as silver, gold - palladium (Au - Pd) alloy. Conductive coating is needed to prevent charging of a specimen with an electron beam in conventional SEM (high vacuum, high voltage). Sputter deposition is a physical vapor deposition (PVD) method of depositing conductive material by sputtering, that is ejecting, material from a target, that is source, which then deposits onto a substrate, such as a samples to be analyzed in electron microscopes [6,7]. In the present study, oxidized samples were coated with Ag in order to get the sufficient conductivity for use in SEM.

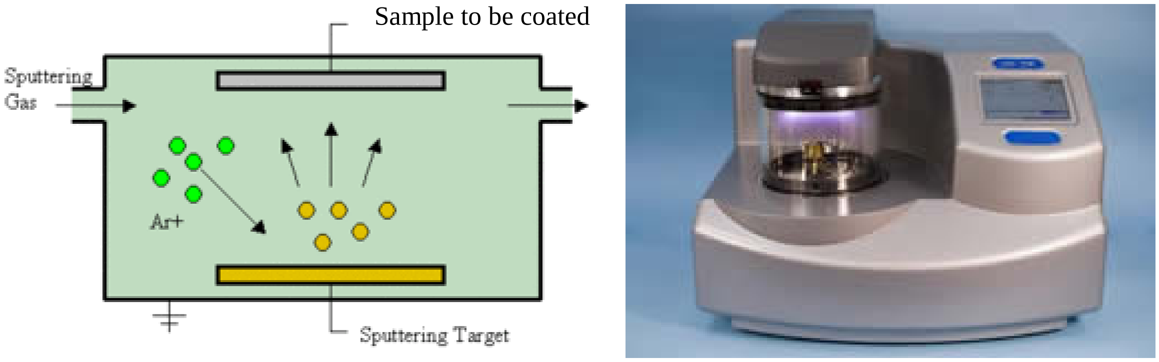

(a) (b)

Fig. 3.8 a) Schematic diagram [3] and b) Photograph of a sputter coating equipment [3]

d) Characterization Instruments

i) Particle size analyzer

Figure 3.9 (a) is a schematic diagram of a laser particle size analyzer and (b) the actual photograph. The operation of laser particle size analyzer is based on the principle of light scattering, the angle of scattered light is inversely proportional to the particle size (i.e. the smaller the particle size, the larger the scattering angle). Mean diameter (also called mean size) is the statistical mean value diameter of particles contained in the sample, which is calculated as per the following formula [15]:

$$\text{MEAN SIZE} = \Sigma(p_i \times MD_i) \tag{3.1}$$

Where: $p_i = C_i - C_{i-1}$: probability for $MD_{i;}$ C_i : cumulative value for diameter of class "i",

MD_i = mean diameter value for class "i" (in μm)

Designated amount of powder is dispersed in distilled water and passed through the optical prism, where laser interacts with particles as schematically shown in the Fig 3.9a. Multiple detectors located at different angles in order to measure the number of counts. In the present study, this instrument is used for measuring the mean particle size and its distribution of starting powders after grinding/mixing.

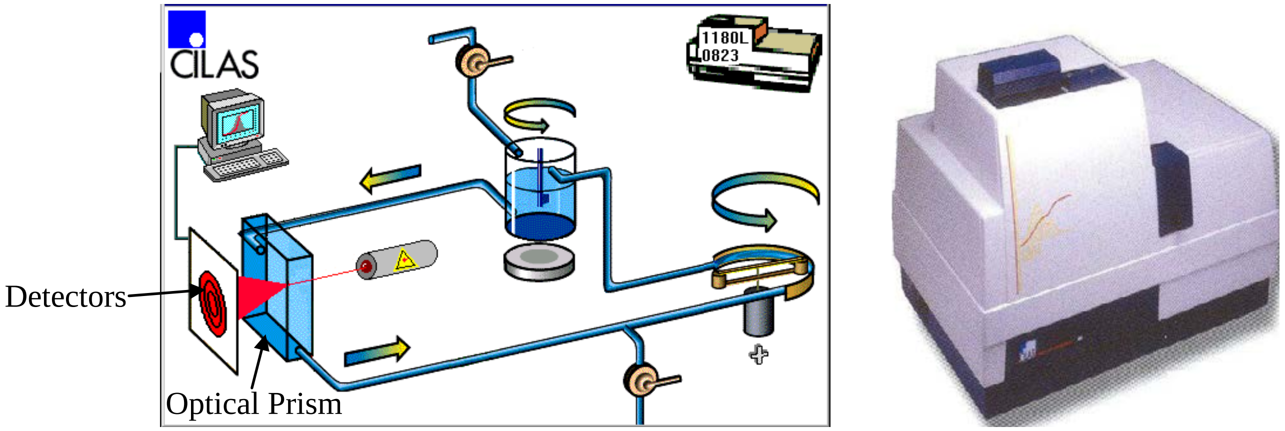

(a) (b)

Fig. 3.9 a) Schematic diagram [15] and b) Photograph of a laser particle size analyzer [15]

ii) X-Ray Diffraction

X-ray diffractometer consist of three basic elements Fig. 3.10(a) shows an X-ray tube, a sample holder, and an X-ray detector and (b) actual photograph. X-rays are generated in a cathode ray tube by heating a filament to produce electrons, accelerating the electrons toward a target by applying a voltage, and bombarding the target material with electrons. When electrons have sufficient energy to dislodge electrons from the inner shell of the target material, characteristic X-ray spectra are produced. These spectra consist of several components, the most common being K_α and K_β. K_α consists, in part, of $K_{\alpha1}$ and $K_{\alpha2}$. $K_{\alpha1}$ has a shorter wavelength and twice the intensity as $K_{\alpha2}$. The specific wavelengths are characteristic of the target material (Cu, Fe, Mo and Cr). Filtering, by foils or crystal monochrometers, is required to produce monochromatic X-rays needed for diffraction. Copper is the most common target material for single-crystal diffraction, with Cu K_α radiation = 1.5418Å. The sample and detector are rotated; the intensity of the reflected X-rays is recorded. When the geometry of the incident X-rays impinging the sample satisfies the Bragg's equation, $2d\sin\theta = n\lambda$, constructive interference occurs and the peak intensity of the diffracted beam is observed. For typical powder patterns, data is collected at 2θ from ~20° to 70° angles that are preset in the X-ray scan. The d-spacing of each peak is then obtained by solution of the Bragg equation for the appropriate value of λ. Because each material has a unique set of d-spacings, matching these d-spacings provides an identification of the unknown sample. Files of d-spacings for hundreds of thousands of inorganic compounds are available from the International Centre for Diffraction Data as the Powder Diffraction File (PDF) [6,7]. In the present study 'Match' software was used to indexing the peaks.

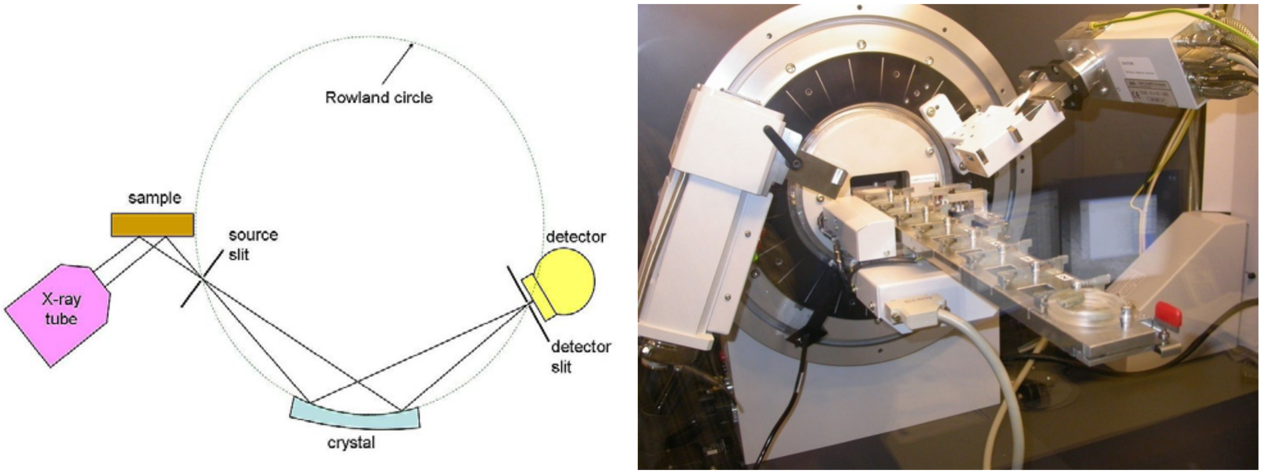

(a) (b)

Fig. 3.10 a) Schematic diagram [16] and b) Photograph of a XRD instrument [3]

iii) Scanning electron Microscope (SEM)

Figure 3.11(a) is a schematic diagram of a scanning electron microscope (SEM) and (b) is actual photograph. SEM is an instrument to study the microstructure of the materials. In a typical SEM, electron is thermionically emitted from an electron gun fitted with a tungsten filament cathode. The electron beam, which typically has an energy ranging from 0.5 to 40 keV, is focused by one or two condenser lenses to a very small spot. The beam passes through pairs of scanning coils or pairs of deflector plates in the electron column, typically in the final lens, which deflect the beam in the *X* and *Y* axes so that it scans over a rectangular area of the sample surface. When the primary electron beam interacts with the sample, the electrons lose energy by repeated random scattering and absorption within a teardrop-shaped volume of the specimen known as the interaction volume, which extends from less than 100nm to around 5µm from the surface.

The size of the interaction volume depends on the electron's landing energy, the atomic number of the specimen and the specimen's density. The energy exchange between the electron beam and the sample results in the reflection of high-energy electrons by elastic scattering, emission of secondary electrons by inelastic scattering and the emission of electromagnetic radiation, each of which can be detected by specialized detectors. The beam current absorbed by the specimen can also be detected and used to create images of the distribution of specimen current. The image may be captured by digitally and displayed on a computer monitor and saved to a computer's hard disk [6,7].

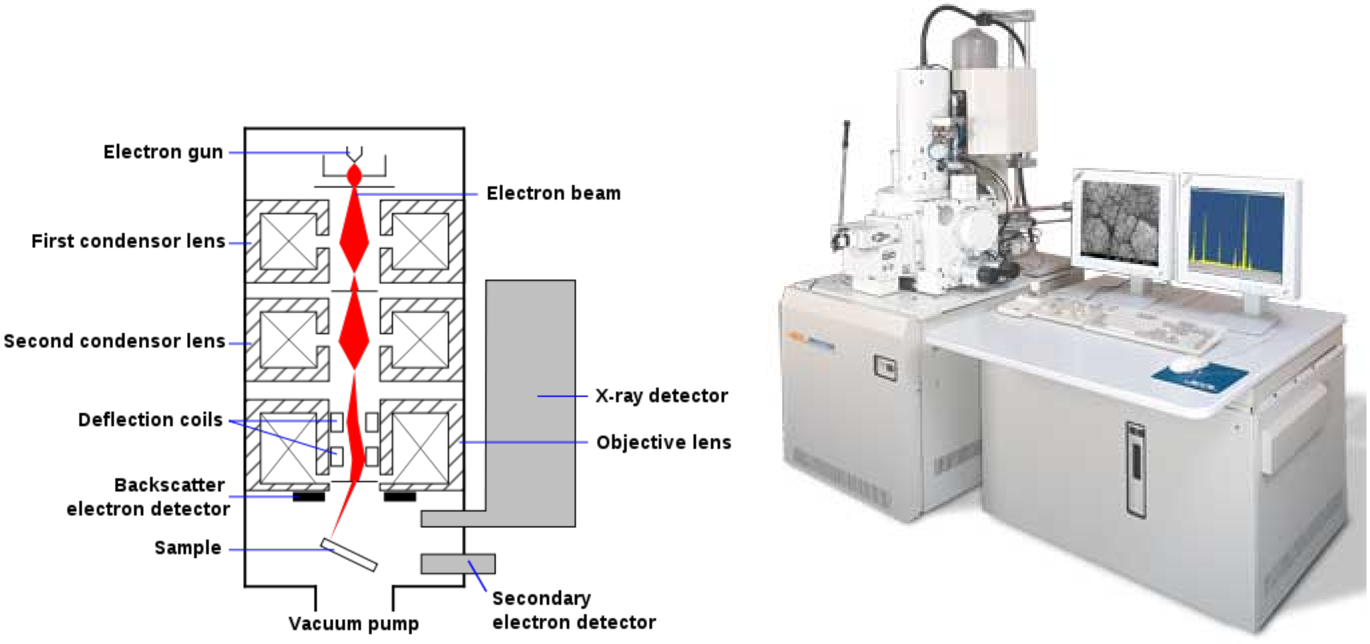

(a) (b)

Fig. 3.11 a) Schematic diagram [16] and b) Photograph of a SEM instrument [3]

iv) Energy-dispersive X-ray spectroscopy

Figure 3.12(a) presents the schematic of EDS along with detector and (b) the actual image with inner parts. EDS or EDAX is an analytical technique used for the elemental analysis or chemical characterization of a sample. It is one of the variants of X-ray fluorescence spectroscopy which relies on the investigation of a sample through interactions between electromagnetic radiation and atoms, analyzing X-rays emitted by the atoms in response to it being hit with charged particles. Its characterization capabilities are largely due to the excitation of characteristic X-rays which are specific to each element corresponding to its unique atomic structure thus permitting identification from one another.

To stimulate the emission of characteristic X-rays from a specimen, a high-energy beam of charged particles such as electrons or protons, or a beam of X-rays, is focused on the sample being studied. At rest, an atom within the sample contains electrons in the ground state (or unexcited) in discrete energy levels corresponding to different electron shells bound to the nucleus. The incident beam may excite an electron in an inner shell, ejecting it from the shell while creating an electron hole where the electron was. An electron from an outer, higher-energy shell then fills the hole, and the difference in energy between the higher-energy shell and the lower energy shell may be released in the form of an X-ray. The number and energy of the X-rays emitted from a specimen can be measured by an energy-dispersive spectrometer. As the energy of the X-rays is characteristic of the difference in energy between the two shells, and of the atomic structure of the element from which they were emitted, this allows the elemental composition of the specimen to be measured [6,7].

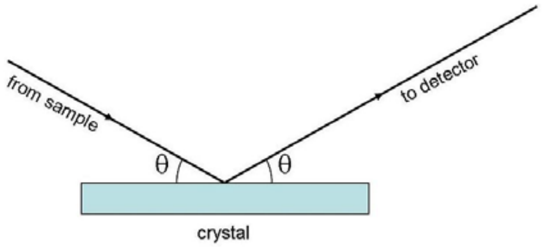

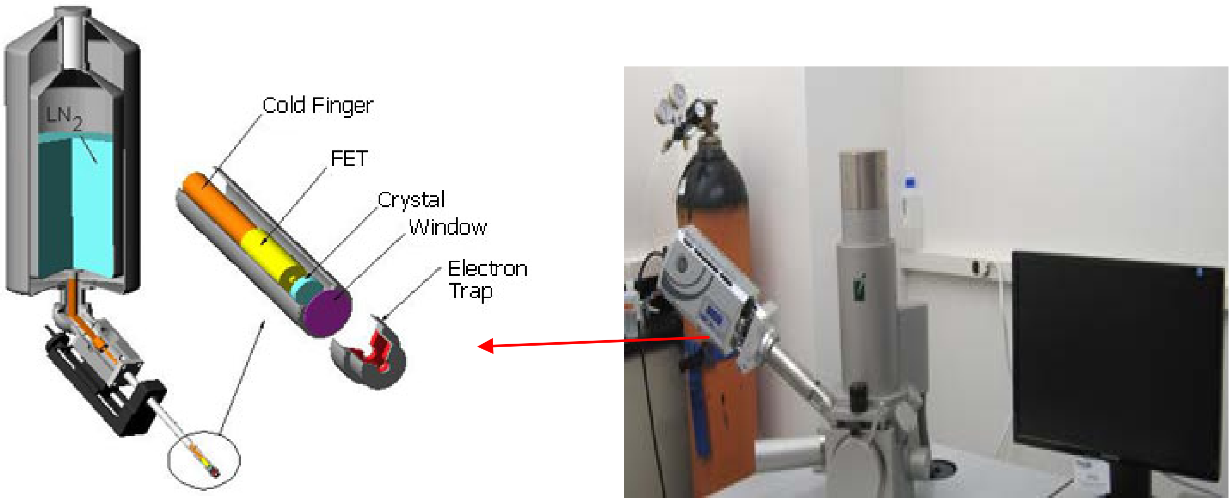

(a) (b)

Fig.3.12a) Schematic diagram along with detector [3] and b) actual equipment of EDS system [3]

v) TGA

Figure 3.13 presents the schematic of TGA. Thermogravimetric analysis is essentially to determine the changes in weight of the sample in response to a programmed temperature change in a controlled atmosphere. Such analysis relies on a high degree of precision in the measurements of weight and temperature. A derivative weight loss curve can identify the point where weight loss is most apparent [6,7].

The thermobalance used in our lab can detect change in mass as small as 0.1 μg. Only sample holder goes inside the furnace while rest of the balance must be thermally isolated from the furnace. Fig. 3.13 is a schematic diagram of our thermobalance. A change in sample mass causes a deflection of the beam, which interposes a light shutter between a lamp and one of the two photodiodes. The resulting imbalance in the photodiode current is amplified and fed into coil, which is situated between the poles of a permanent magnet. The magnetic field generated by the current in the coil restores the beam to its original position. The amplified photodiode current is monitored and transformed into mass or mass-loss information by the data-processing system. Mass versus temperature data can either be plotted in real time [6,7]. The furnace for TGA covers the range from ambient temperature to 1873K (1600^{o}C). With our earlier TGA instrument of Setaram make was used upto 2000^{o}C (2273K) for synthesis of TiB_2. Heating rate can often be selected from 0.1 to 100 K/min. Synthesis studies were carried out in 0.001Pa atmosphere and oxidation studies were carried out in air/oxygen.

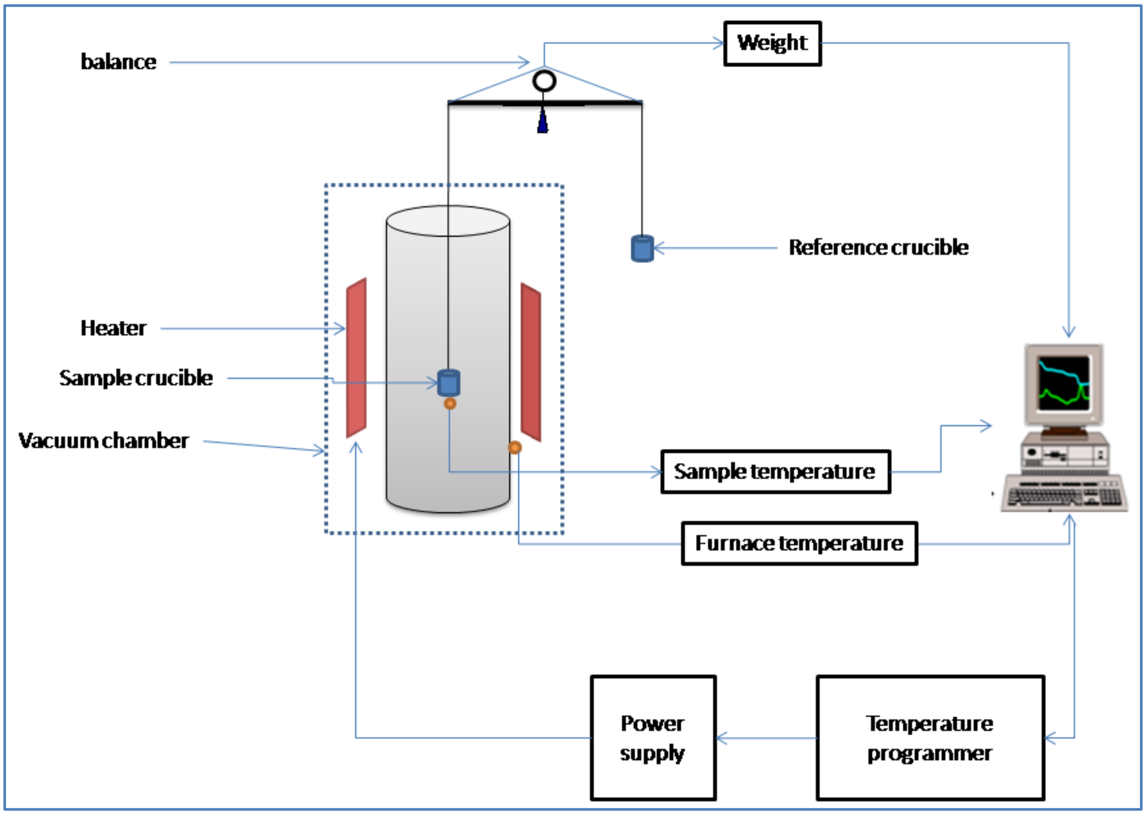

Fig.3.13 Schematic diagram of TGA system

vi) Hardness tester

Figure 3.14(a) presents the schematic of Vickers indentation [3] and (b) the actual photograph of the equipment. The Vickers test is often easier to use than other hardness tests since the required calculations are independent of the size of the indenter, and the indenter can be used for all materials irrespective of hardness. The basic principle, as with all common measures of hardness, is to observe the material's ability to resist plastic deformation from a standard source. The Vickers test can be used for all material and has one of the widest scales among hardness tests. The unit of hardness given by the test is known as the Vickers Pyramid Number (HV) or Diamond Pyramid Hardness (DPH). The hardness number can be converted into units of ‘Pa’. The hardness number is determined by the load over the surface area of the indentation [6,7]. More details on the hardness measurement of present study samples are given in section 3.4.3.3.

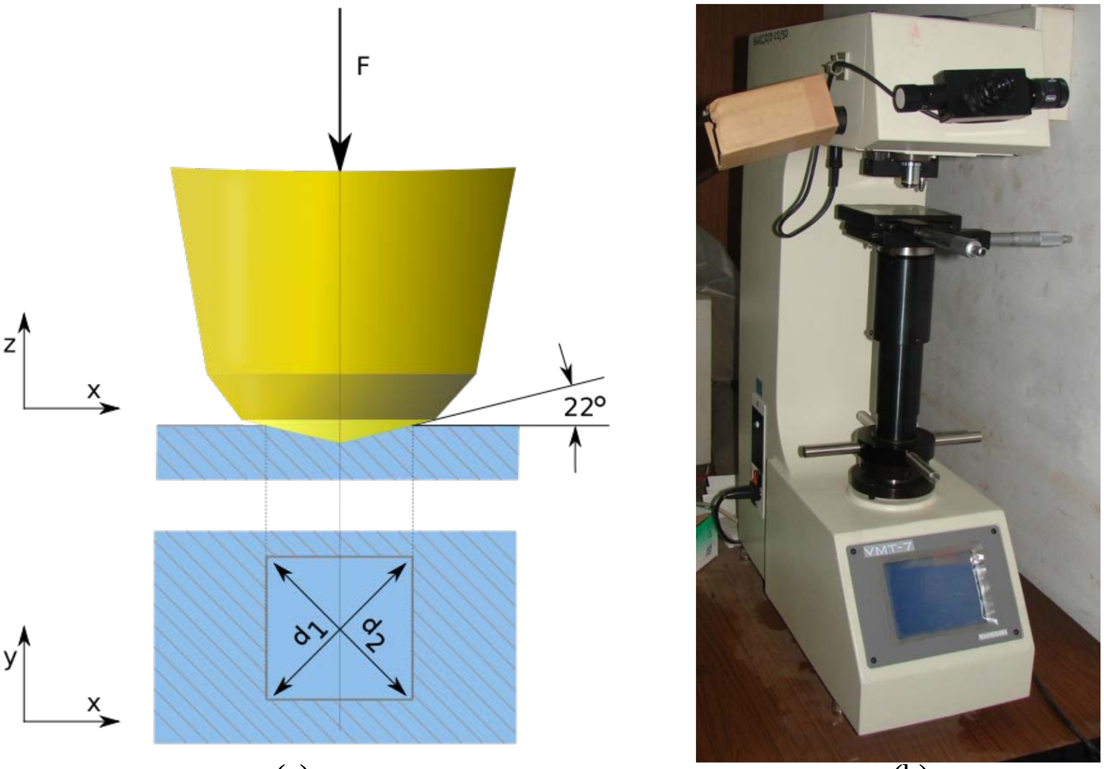

(a) (b)

Fig.3.14 a) Schematic diagram [3] and b) actual equipment of Vickers hardness tester

vii) Flexural strength (3-point bend test)

Figure 3.15(a) presents the schematic of 3-point bend test and (b) the actual equipment's photograph. The three point bending flexural test provides values for the modulus of elasticity in bending (E_f), flexural stress (σ_f), flexural strain (ε_f) and the flexural stress-strain response of the material. The main advantage of a three point flexural test is the ease of the specimen preparation and testing. However, this method has also some disadvantages: the results of the testing method are sensitive to specimen and loading geometry and strain rate [6,7]. In the present study, this equipment used for only measuring the flexural strength. Test specimens of different TiB_2 composites for 3-point bend tests were cut using EDM (ultracut S0**,** Electronica machine tools, India) and machined into bar shapes of 1.5 × 2.0 × 25 mm from hot pressed disk (50 mm) prepared under similar processing conditions. Flexural strength was measured by 3 point bend test at room temperature as per ASTM **C** 1161-02C test procedure.

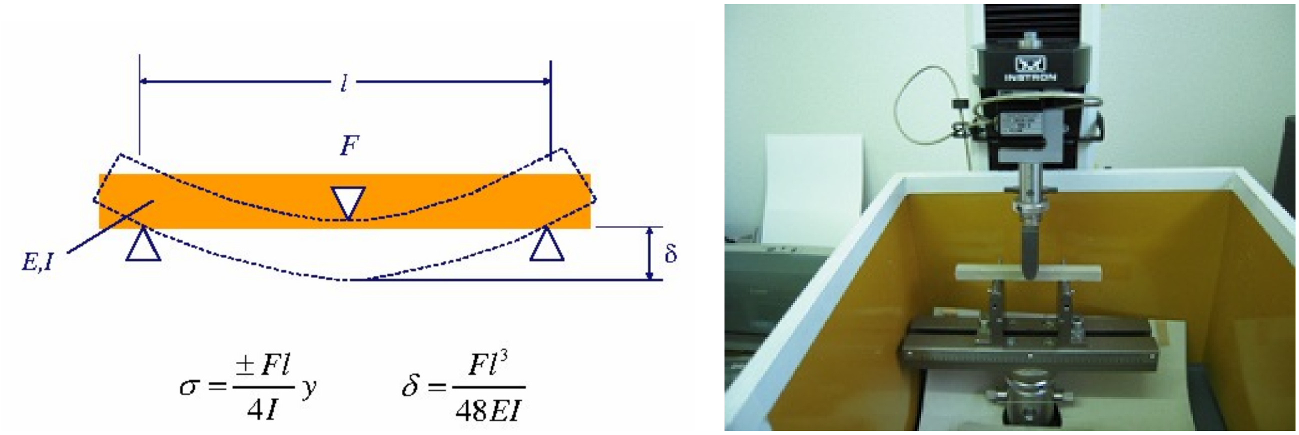

(a) (b)

Fig.3.15 a) Schematic diagram [3] and b) actual equipment of 3-point bend tester [3]

viii) Dilatometer

Figure 3.16(a) presents the schematic of dilatometer and (b) the actual equipment's photograph. The Coefficient of Linear Thermal Expansion (CLTE) is used to calculate changes in length of a sample with temperature. The sample is placed in an enclosure and is in contact with a probe leading to a displacement sensor. A small force (electromagnetic loading) is applied to keep the probe in contact with the sample. The temperature within the enclosure is raised at a rate of 5 K/minute and the expansion of the sample is measured by the displacement sensor (differential transformer) [6,7]. In the present study, dual push rod type dilatometer (horizontal model) (TD 5000S, Mcscience, Japan) was used for measuring CTE up to 900^{o}C (1173K) for the composites in inert atmosphere. Alumina sample was used as a reference. Size of the sample used in the present study is 5 mm x 5 mm cross section bar of 10 mm length.

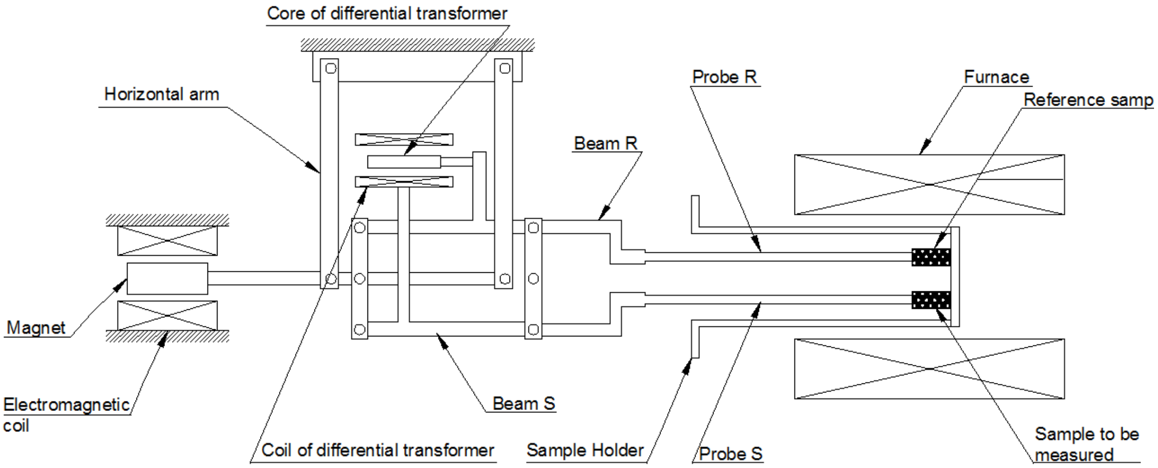

(a)

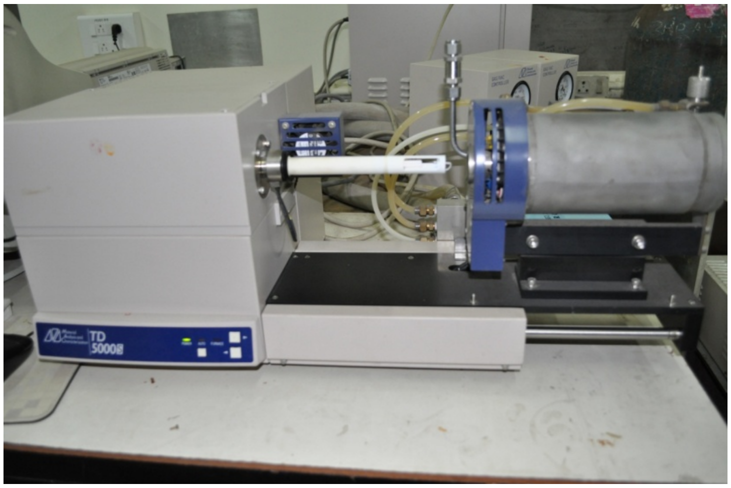

(b)

Fig.3.16 a) Schematic diagram [3] and b) actual equipment of dilatometer [3]

ix) Four probe electrical resistivity measurement unit

Figure 3.17 (a) presents the schematic of four probe electrical resistivity method and (b) the actual equipment's photograph. A four point probe is a simple apparatus for measuring the resistivity of samples. By passing a current through two outer probes and measuring the voltage through the inner probes allows the measurement of the substrate resistivity. The four-point probe station consists of a probe station (four probe tips), an ampere meter, a DC current source, and a voltmeter. The four probes are arranged in a linear fashion, where the two outer probes are connected to a current supply, and the inner probes to a voltage meter. As current flows between the outer probes, the voltage drop across the inner probes is measured [7].

In the present study, electrical conductivity was measured by using the conventional 4-probe method of all the samples from room temperature (300K) to 1273K (1000^oC). Rectangular cross section (dimensions: 5 mm width (D) x 3 mm thickness (W) x 12 mm length (A)) samples were prepared for conductivity measurement. All sides of sample were cleaned and polished. Four platinum probes were connected to the sample with the help of platinum paste. Four probes were located on the top surface of transverse direction with 3 to 4 mm (S) apart, outer most probes were connected to the programmable current source (KEITHLEY: 224) and remaining two inner probes were connected to nanovoltemeter (KEITHLEY: 2182), which recorded the output voltage when 100 mA current was passed through the sample. Electrical conductivity was calculated using the following expression:

$$\text{Conductivity} = IS/VX \qquad (3.2)$$

Where ‘I’ is current (100 mA), ‘S’ distance (mm) between two volt probes, which are connected to voltmeter, ‘V’ is recorded voltage in nanovoltemeter, ‘X’ is the cross-sectional area of the specimen (mm^2). Resistivity is an inverse of conductivity.

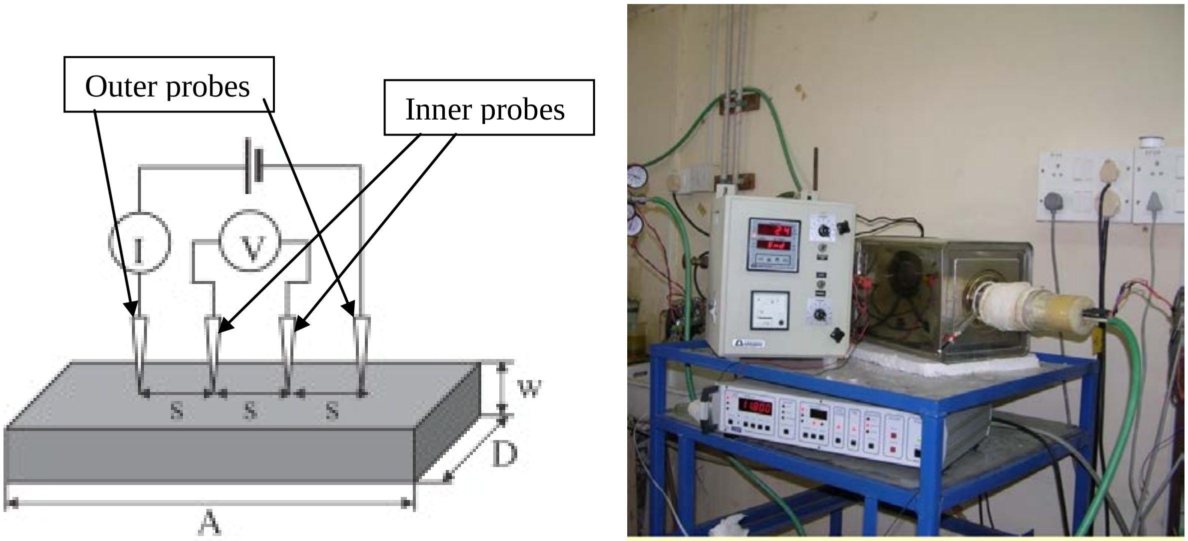

(a) (b)

Fig.3.17 a) Schematic diagram [3] and b) actual equipment of four probe resistivity unit

3.3 Synthesis of Materials

3.3.1 Titanium diboride (TiB_2)

Titanium diboride was produced by carbothermic reduction of titanium dioxide with a mixture of boron carbide and carbon.

$2TiO_2 + B_4C + 3C \rightarrow 2TiB_2 + 4CO$ (3.3)

Above reaction indicates the formation of gaseous CO and proceeds with a weight loss of the charge. Weight loss for the above reaction will be 44.4% at completion. Raw materials used were boron carbide powder (78.5 % B, 19.5% C, 6.7 µm median diameter; supplied by Boron Carbide India, Mumbai), titanium dioxide (TiO_2 - 99% purity; Merck, Germany, 0.8 µm median dia) and petroleum coke (C – 99.4 %, 18 µm median diameter; Assam carbon, India). All the raw materials were dried in an oven at 523K (250^{o}C) for 2 hours, before use to remove the moisture.

Thermograviometric study (Setaram, TAG 24) on the formation of TiB_2 by boron carbide reduction of TiO_2 was carried out up to 2273K (2000^{o}C). For regular synthesis of TiB_2, weighed quantities of titanium oxide, boron carbide and petroleum coke were mixed thoroughly using a motorized pestle and mortar for a small volume (< 150 g) and planetary ball mill for large volumes (>150 g). The powder mixture was pelletized using a hydraulic press at a pressure of 280 MPa to obtain green pellets of 20 mm diameter. In mixing and pelletizing, WC lined implements were used. The pellets were charged in a graphite crucible and heated to 2103K (1830^{o}C) in an induction furnace under a vacuum of 0.001 Pa. Temperature of the charge was measured using a thermocouple upto1273K (1000^o C) and above 1273 K by a two-color pyrometer with an accuracy of ± 10K. After completion of reaction, the furnace was cooled to room temperature in vacuum, back filled to atmospheric pressure and the product was taken out. The product was crushed and ground to fine size using jaw crusher and high energy vibratory cup grinding mill.

XRD of the final product (TiB_2) was used for phase identification. Wet chemical analysis for determination of major metallic constituents and impurities were determined by instrumental methods. Oxygen and carbon are the main impurities in TiB_2. The mean particle diameter and particle size distribution was measured using laser particle analyzer (CILAS PSA 1064L). The specific surface area was measured by BET (COULTER, SA300) method (Sorptomatic 1990, Thermoqest Italia) [1]. SEM examination of the powders was carried out to check the size and morphology. Details of raw materials and synthesized powders are given in Table 3.2. The parameters for a typical experiment are:

Charge composition:	TiO_2: 64.52 g, B_4C: 22.59 g, coke: 12.88 g
Charge weight:	100 g
Product weight:	55.08 g
Weight loss:	44.9% (Theoretical weight loss 44.4% as per reaction 3.3)
Analysis of TiB_2:	Ti-69.2%, B-29.3%,O – 0.5%, N – 0.5%, C – 0.6%
Yield:	55.1%

3.3.2 Molybdenum disilicide ($MoSi_2$)

$MoSi_2$ was synthesized from its elements by the following reaction:

$$Mo + 2Si \rightarrow MoSi_2 \tag{3.4}$$

Stoichiometric amounts of pure molybdenum (> 99.7%, Merck Germany) and silicon (> 99%, Merck Germany) were weighed and mixed using planetary mixer for 2 to 3 hours with intermittent cooling to avoid the overheat of the charge. The compacts were heated in a graphite crucible under moderate vacuum of 0.1Pa up to a temperature of 1613K (1340°C). After completion of the reaction, $MoSi_2$ product was obtained in the form of chunks, crushed by WC lined equipments: jaw crusher and fine ground to micron size by high energy vibratory cup grinding mill. Data from a typical experiment is given below:

Charge composition:	Mo – 63.2%, Si – 36.8%
Charge weight:	198.33g
Product weight:	196.77g
Weight loss:	1.56%
Analysis of $MoSi_2$:	C – 0.37%, O – 0.30%
Mean particle size (D_{50}):	1.4 μm.
Yield:	99.2%

Details of raw materials and products are given in Table 3.2.

3.3.3 Chromium diboride (CrB_2)

CrB_2 powder was prepared by carbothermic reduction of chromium oxide in the presence of boron carbide as per the following reaction:

$$Cr_2O_3 + B_4C + 2C \rightarrow 2CrB_2 + 3CO \quad (3.5)$$

Raw materials used were Cr_2O_3 (99% purity; Emerck make; 0.86 μm median diameter), boron carbide powder (78.5% B, 19.5% C, <1% O, 0.02% Fe, 0.02% Si, 5.34 μm median diameter; supplied by Boron Carbide India) and petroleum coke (C-99.4%, 13.9 μm median diameter, supplied by Assam carbon, India). All the raw materials were dried in an oven at 523K (250^{o}C) for 2 hours before use to remove moisture.

A small pellet of the reactants in Stoichiometric quantity (as per reaction 3.5) was prepared by weighing out individual components, mixing thoroughly and pelletizing. This pellet was used for thermogravimetric investigations (Setaram TAG 24) upto 1773K (1500^{o}C). For regular synthesis of CrB_2, weighed quantities of chromium oxide, boron carbide and petroleum coke in various ratios were mixed thoroughly, pelletized under 280MPa to obtain pellets of 20 mm dia. The pellets were then charged in a graphite crucible and heated in an induction furnace under a vacuum of 0.001Pa and at different temperatures of 1773, 1873 and 1973K (1500, 1600 and 1700°C) for 2 hour. Temperature of the charge was measured using a two color pyrometer. After completion of reaction, the furnace was cooled to room temperature in vacuum and the reacted pellets taken out, crushed and ground to fine size using high energy vibratory cup grinding mill.

3.3.4 Pre-alloyed titanium - chromium diboride [(TiCr)B_2]

Synthesis of (TiCr)B_2, was carried out by the carbothermic reduction of titanium and chromium oxides in the presence of boron carbide as per the reaction:

$$2TiO_2 + B_4C + Cr_2O_3 + 6C \rightarrow 2(TiCr)B_2 + 7CO \quad (3.6)$$

As the reactants consist of four solid substances, homogenization of the charge mixture is essential for completion of the reaction. Experimental procedure for synthesis of (TiCr)B_2 and grinding to fine powder is similar to other powders (TiB_2 and CrB_2) which are given above. Details of raw materials and synthesized powders are given in Table 3.2. Data on a typical experiment for synthesis of $(Ti_{0.85}Cr_{0.15})B_2$ is given below:

Charge composition:	TiO_2, B_4C, Cr_2O_3, Carbon
Charge weight (g):	TiO_2: 208.03, B_4C: 81.56, Cr_2O_3: 48.94, C: 51.76
Total charge weight:	390.29 g
Product weight:	211.79 g
Weight loss:	45.7% (Theoretical weight loss 43.08% as per reaction 3.6)
Yield:	54.3%
Analysis of $(Ti_{0.85}Cr_{0.15})B_2$:	Ti-60.9%, B-26.2%, Cr-11.6%, C-0.07%, O-0.6%, N-0.5%

Particle size distribution plots of raw materials (TiO_2, B_4C, petroleum coke, Cr_2O_3) which are used in present study for synthesis of borides are shown in Fig.3.18.

B_4C particles are showing mono-modal distribution pattern with mean particle diameter of 8.07 µm. TiO_2, petroleum coke and Cr_2O_3 are showing the bi-modal distribution patterns with mean particle diameter of 1.41, 13.90, 0.86 µm respectively.

Table 3.2 Details of raw materials and products used in the present study

Material	Source	Carbon (wt. %)	Oxygen (wt. %)	Nitrogen (wt. %)	Metallic Elements/ Impurities (wt. %)	Median particle diameter D_{50} (µm)	Surface area (m^2/g)
TiO_2	Merck, Germany	≥99% Purity			Pb≤0.005 As≤0.0005 Fe≤0.005	0.80	-
B_4C	Boron carbide India	19.50	-	-	Fe ~ 2000ppm Si~ 2000ppm	6.7	-
Cr_2O_3	Emerck	>99% purity				0.90	-
Carbon	Assam Carbon, India	99.40	-	-	-	13.9	-
Mo	Merck, Germany	>99.7% Purity					-
Silicon	Merck, Germany	>99% Purity					-
TiB_2	In-house	0.60	0.50	0.60	-	1.10	1.360
$MoSi_2$	In-house	0.37	0.30	-	-	1.40	0.389
CrB_2	In-house	0.90	0.60	-	-	4.5	-
$(Ti_{0.85}Cr_{0.15})B_2$	In-house	0.07	0.6	0.5	Ti-60.9%, B-26.2%, Cr-11.6%	5.0	-
$TiSi_2$	Sigma Aldrich	≥99.5% Purity			≤0.006%	-325#	-
$CrSi_2$		≥99.5% Purity			≤0.006%	-325#	-
WSi_2		≥99.5% Purity			≤0.006%	-325#	-

mesh

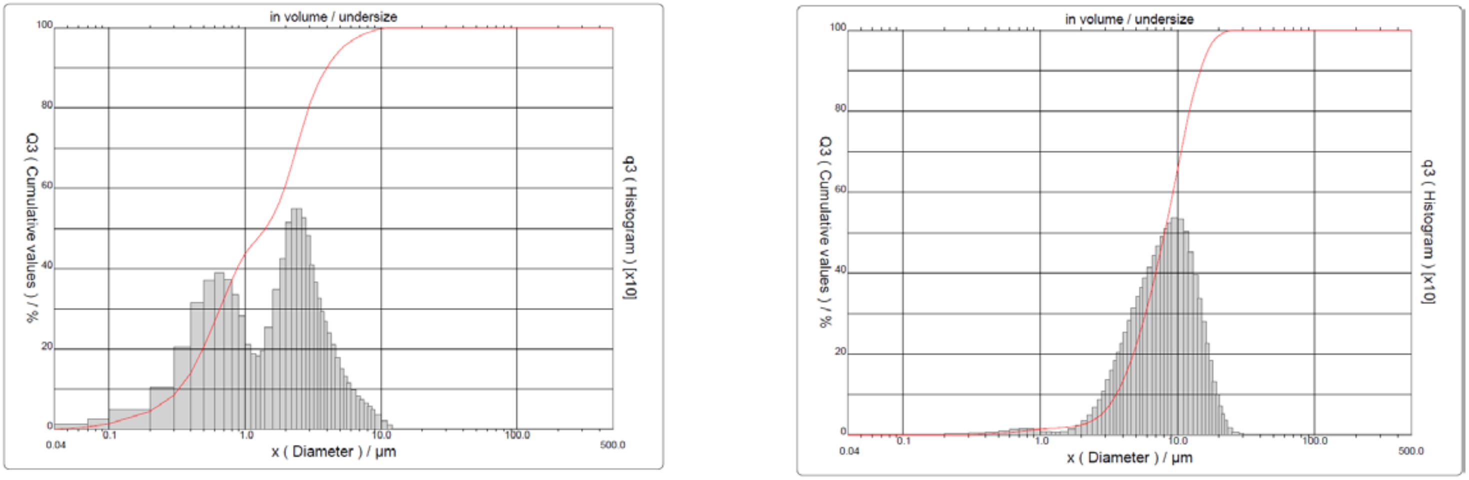

TiO_2 (D_{50}: 1.41 µm)

B_4C (D_{50}: 8.07 µm)

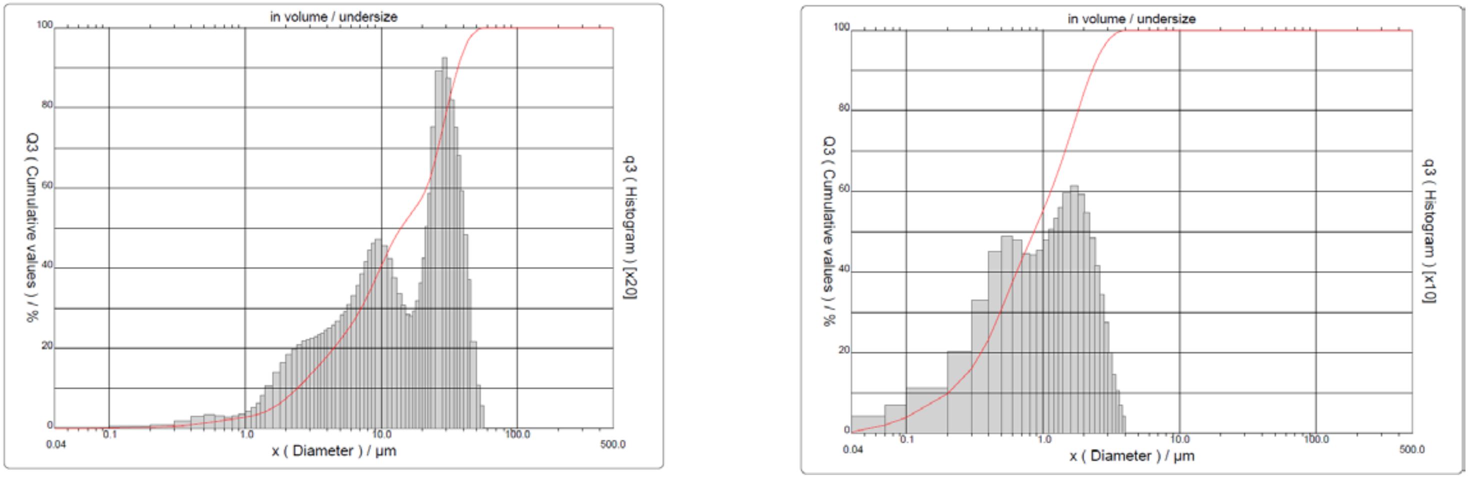

Petroleum coke (D_{50}: 13.90 µm)

Cr_2O_3 (D_{50}: 0.86 µm)

Fig. 3.18 Particle size distribution plots of raw materials

3.4 Processing and Microstructure

3.4.1Hot pressing

For hot pressing experiments, weighed quantities of TiB_2 and the selected sinter additive (2.5%, 5%, 10% and 15 wt.%) powders were mixed thoroughly using a motorized pestle and mortar in dry condition for 1h. The densification was performed by hot pressing under vacuum 0.001 Pa, using a 12 or 17 mm diameter graphite die under 15 to 35 MPa pressure. The die is filled with the mixed powder and this is kept on a vibrator to achieve good tap density for 10 minutes. The samples were hot pressed at temperatures from 1823 to 2073K (1550 to 1800^{o}C) with a heating rate of 15 K/min. Temperature was measured using a two color pyrometer with an accuracy of ± 10K. Linear variable differential transducer (LVDT) was used to measure shrinkage of the sample during the hot pressing experiment. Accuracy of the LVDT is 0.1 µm and range of measurement is 0.1 to 1500µm. After completion of hot pressing, the vacuum and die pressure were maintained till the end of cooling. The pellets were ejected from the die using manual hydraulic press. The thickness of the hot pressed pellets was between 3-5 mm.

3.4.2 Pressureless sintering

To study the feasibility of pressureless sintering, green pellets of various charge mixtures: TiB_2+ sinter additives (without organic binder) were used. The green density of the cold pressed specimens was around 60-65 % of theoretical density (TD). Graphite heating furnace was used for sintering. Green pellets were sintered at temperatures range from 1673 to 2223K (1400 to 1950^{o}C) (heating rate of 15 K/minute) for several hours (2 to 8 hours) in vacuum. After completion, the samples were cooled down to room temperature and then removed from the furnace for characterization.

3.4.3 Characterization

3.4.3.1 Density measurement and sample preparation

Hot pressed and sintered samples were thoroughly cleaned with alcohol, weighed and density determined by using Archimedes principle in distilled water. (Balance model AT 261 Delta Ra; supplier: Mettler Toledo). Density was calculated by taking the ratio of weight in air to the volume of displaced water. Open porosity was also calculated by taking the ratio of weight of absorbed water by the sample to the volume of displaced water.

Open porosity = (soaked weight – weight in air)/ (soaked weight-suspended weight) (3.7)

Since it is difficult to estimate the precise amount of secondary phases (formed due to sintering reactions) in the composites for calculating the theoretical density of materials, the image analysis technique was performed on selected multiple SEM images of the fractured samples. Relative density (RD) was calculated by determining the volume fraction of porosity of the samples. The reported density results are an average of 5 measurements that are performed on SEM micrographs of each sample by using Leica materials workstation version 3.6.6 software. Polished samples were used for phase identification, hardness measurement and microscopy.

3.4.3.2 Phase identification and microstructural characterization

The crystalline phases in the starting powders and hot pressed sample were analyzed using XRD (Diano 2000 series). XRD patterns were obtained using Cu Kα (λ = 1.5404A^o) radiation in a diffractometer. The patterns were later analyzed using latest PCPDF database with Match software. Microstructural investigation of the phase assemblage was performed by means of SEM (CAMSCAN MV2300CT) on polished surfaces and the nature of fracture was observed on fractured surfaces. The fractured surface was examined to understand the crack propagation mechanism. The detailed microstructural analysis was also performed using SED-EDS. Prior to SEM observation; the polished/fractured samples were sputter-coated with a thin Ag layer in order to obtain sufficient conductivity on the surface and to avoid charging of the surface in the SEM.

Leica materials workstation version 3.6.6 was used to measure the grain size of the densified composites.

3.4.3.3 Evaluation of mechanical properties

Micro hardness was measured at different indent loads of 50, 100 and 200N with dwell time of 5sec (VMT – 7; Matsuzawa Japan). Indentation fracture toughness (K_{IC10}) calculations were based on the crack length measurements of the radial crack pattern produced by Vickers H_{V10} indentations, according to the formula given by Anstis et al.[2]. The reported values were the average of data obtained from minimum five indentation tests. Fracture toughness values were calculated by using the Anstis empirical relation as follows [2]:

$$K_{Ic} = 0.016\ (E/H)^{1/2} \times (P/C^{3/2}) \qquad (3.8)$$

Where K_{Ic} is the fracture toughness (Mpa.m$^{1/2}$), E – Elastic modulus (GPa), H – hardness (GPa), P – load (N), 2C – full crack length (m). Elastic modulus was measured by using ultrasonic method (UT 340 pulser receiver system, UTEX Scientific Instrument Inc., Canada) as per the ASTM C 1419-99a test procedure. 15 MHz normal beam ultrasonic probe with a sampling rate of 1000 MHz was employed for velocity measurements; $(v_L/v_T)=(2T_{LT}/T_{LL})-1$, $E=\rho vL^2$, where E, ρ, v_L, v_T, T_{LL} and T_{LT} are elastic modulus (GPa), density (g/cm^3), longitudinal velocity (m/s), transverse velocity (m/s), time of flight of L–L wave (µs) and time of flight of L– T wave (µs) respectively. All the reported data points represent the average of five measured values.

Flexural strength was measured by 3 point bend test at room temperature as per ASTM **C** 1161-02C test procedure. Detailed description of test methodology was given in section 3.2

3.4.3.4 CTE measurements & Electrical conductivity

CTE (Coefficient of thermal expansion) of different TiB_2 composites were measured upto 1173K (900^{o}C) in inert atmosphere using dual push rod dilatometer (TD 5000S, Mcscience, Japan). Description of the equipment and method of measurement were given in section 3.2.

Electrical conductivity from room temperature to 1273K (1000^{o}C) was measured by using the conventional 4-probe method. Description of the equipment and method of measurement were given in section 3.2.

3.5 Oxidation studies

3.5.1 Materials

Hot pressed pellets of diameter 12 mm were sectioned into 2mm thick discs using high speed diamond wafer cutter. These discs were polished with emery papers (1/0,2/0,3/0,4/0) and finally with diamond paste up to 1/4μm finish. The polished discs were ultrasonically cleaned in alcohol for 10 minutes.

3.5.2 Experimental procedure

Mechanism and kinetics of oxidation of the composites were studied in the temperature range of 1023 to 1273K (750 to 1000^{o}C). TGA analyses of the composites were carried out up to 1273K (1000^{o}C) in 1 atmosphere oxygen with 10 K/min heating rate (ThermoSys, Setaram, France) for continuous oxidation studies.

Isothermal oxidation studies for all the composites were done at 1123K (850°C) in air at different time intervals of 0.5, 1, 2, 4, 8, 16, 32 and 64 h and in addition at 1023 and 1223K (750 and 950°C) for selected composites. Isothermal oxidation studies for selected composites were also carried out in air at 1273K (1000°C) for short duration of 2 to 4 hours only. Oxidation tests were conducted in a horizontal tubular furnace. In order to avoid oxidation during heating, the samples were directly inserted into the furnace after the furnace temperature reached the set value. Temperature was measured using a K-type (chromel–alumel) thermocouple with an accuracy of ± 1K. Samples were placed in an alumina boat and loaded in the hot zone of the furnace. The dimensions of the samples were noted using digital vernier caliper. Each sample was weighed before and after exposure, to determine the change in weight (gain) during the oxidation process. Additional experiments were also carried out for selected time intervals to check the reproducibility of the test results. In order to determine the nature of oxidation, the weight gain data was fitted in the general rate equation.

$$(\Delta w/A)^m = K_m.t \tag{3.9}$$

Where Δw- is the change in weight (kg), A- surface area of the sample (m^2), t- oxidation time (s) and K_m- rate constant. To determine the kinetics of oxidation, the data was analyzed using the parabolic law.

$$(\Delta w/A)^2 = K_p.t \tag{3.10}$$

Where K_p- parabolic rate constant ($Kg^2/m^2/s$).

3.5.3 Characterization of oxidized samples

The surfaces of the oxidized samples were characterized using X-ray diffraction (XRD) and scanning electron microscopy (SEM) with EDS. XRD patterns were obtained from the surface of the oxidized samples using Cu Kα (λ = 1.5404 A) radiation in a Rich-Seifert 2000D diffractometer. The patterns were later analyzed using latest PCPDF database with Match software.

The morphology and nature of oxide layer was observed in a scanning electron microscope. The cross sections of the selected oxidized composites (TiB_2+15%CrB_2+20%$MoSi_2$ and $(Ti_{0.85}Cr_{0.15})B_2$+20%$MoSi_2$) were examined. Elemental X-ray maps were also obtained on the cross sections of selected composites.

3.6 Summary

In this chapter, details of the various start material powders, synthesis, densification and characterization of sintered materials as well as the equipments used are described. A list of composites prepared in this work has also been presented. Experimental procedure adopted for synthesis, consolidation and characterization of the dense pellets are also described. Isothermal and continuous oxidation study methods as well as the methods of characterization of oxidized samples are also described.

3.7 References

[1] Adamson AW. Physical chemistry of surfaces, 3rd ed., New York: Wiley; 1965. p.565

[2] Anstis GR, Chantikul P, Lawn BR, Marshall DB. A Critical Evaluation of Indentation Techniques for Measuring Fracture Toughness: I, Direct Crack Measurements. J Am CeramSoc 1981;64[9]:533–538

[3] https://www.google.co.in/images

[4] http://www.insmartsystems.in/

[5] http://www.cgerhardt.co.uk/

[6] https://www.google.co.in

[7] http://www.wikipedia.org

[8] http://www.vtvacuumtech.com/

[9] http://hhv.in/

[10] http://www.britishelectricals.com

[11] http://www.metatechind.com

[12] http://www.presi.com/

[13] http://www.electronicagroup.com/

[14] http://www.struers.com

[15] http://www.cilas.com/

[16] www.wikipedia.co.in/XRF/XRD/ICP-AES/DSC/aluminothermy

[17] http://www.mettler-toledo-support.com/

[18] http://www.sciencedirect.com/science/article/pii/S0025540803001077

CHAPTER 4

CHAPTER-4

SYNTHESIS OF STARTING POWDERS

4.1 Introduction

This chapter presents the results of investigations on the synthesis of titanium diboride, chromium diboride and pre-alloyed (TiCr)B_2 by carbothermic reduction of respective oxides with carbon and boron carbide. Details of synthesis of $MoSi_2$ by direct elemental reaction are also presented. CrB_2 and $MoSi_2$ were used as sintering additives to TiB_2 and pre-alloyed (TiCr)B_2 for preparing the composites.

Thermodynamic calculations were used to check the feasibility of the formation of these borides at different temperatures. Thermogravimetric study on the formation of TiB_2 and CrB_2 by boron carbide reduction of respective oxides was carried out to obtain the conditions for reaction. Process parameters and/or charge composition was optimized to obtain the phase pure borides and silicides. The product was analyzed by XRD and chemical methods. Crushing and grinding parameters were also optimized to obtain the fine micron size and contamination free powders from as reduced mass. These powders were used further for consolidation to prepare the TiB_2 and (TiCr)B_2 composites.

4.2 Synthesis of TiB_2

Carbothermic reduction of titanium dioxide in the presence of boron carbide can be represented by the overall reaction:

$$TiO_2 + 0.5B_4C + 1.5C \rightarrow TiB_2 + 2CO \qquad (4.1)$$

Formation of TiB_2 is thermodynamically feasible at temperatures above 1200K only as ΔG for the reaction is positive at lower temperatures. Free energy data [1] for the above equation was calculated by using FactSage software version 6.3 and is presented in Fig. 4.1. High temperature favors the formation of TiB_2. The minimum temperature required and for reaction is brought down considerably by carrying out the reaction in a dynamic vacuum of 0.001Pa. The temperature required for reaction decreases by about 873K (600°C) if the reaction is carried out at 0.001Pa instead of 1 atm pressure (See Fig.4.1).

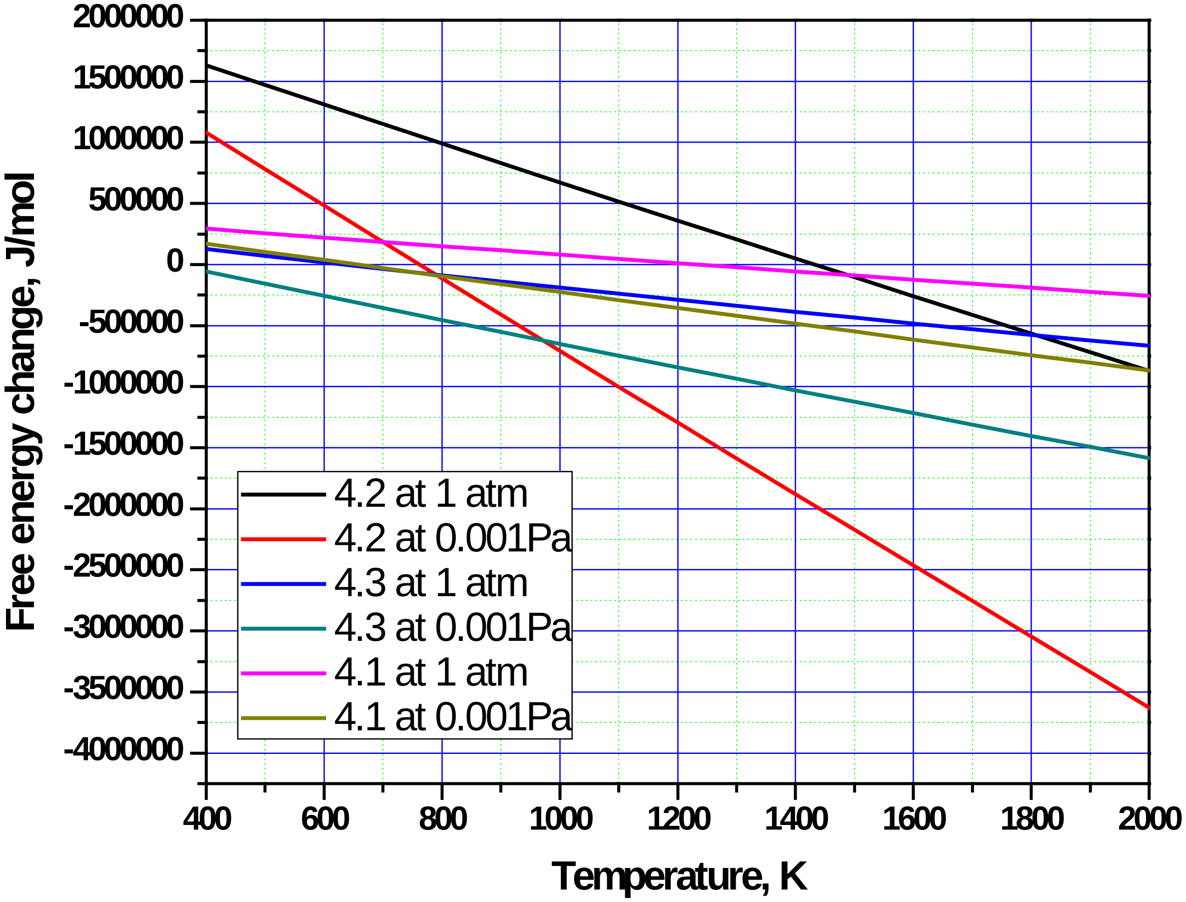

Fig. 4.1 Free energy change of various possible reactions calculated using FactSage software, version 6.3

4.2.1 Thermo gravimetric study

The TGA plot of the formation of titanium diboride is given in Fig.4.2. The start of the reaction is seen at 1365K (~1092°C) and a weight loss of 40% of the charge up to a temperature of 1603K (1330°C). The second weight loss region starts at 1753K (1480°C), with a lower rate, indicating the reaction to be probably diffusion controlled. A total weight loss of 47 wt% was recorded at the completion of the run at 2273K (2000°C), against a theoretical anticipated weight loss of 44 wt%. XRD analysis of the product showed the presence of essentially TiB_2 with minor amount of Ti_3B_4 phase (Fig.4.3).

4.2.2 Synthesis of titanium boride (batch process)

Charge composition, size, mixing and compaction details were optimized in a few preliminary experiments. Details of experiments on the optimization of process parameters such as temperature, time and final vacuum are presented in Table 4.1. These experiments were conducted in a vacuum of 0.001 Pa in induction furnace at fixed temperatures between 1473 to 2073K (1200 to 1800°C) for 60 minutes soaking each.

At the experimental temperature of 1503K (1230°C), weight loss of only 9.5% was noted and XRD of the product showed the presence of TiB_2, Ti_3B_4, TiO_2, Ti_2O_3 and graphite indicating only a partial reduction of titanium oxide. At 1633K (1360°C), weight loss was 28.5% and the phases present were TiB_2, Ti_3B_4, Ti_2O_3 and graphite. As the weight loss is higher than in the previous case and the absence of TiO_2 indicates a higher extent of reaction, but the reaction is still incomplete as Ti_2O_3 is present. At higher temperatures of 1773, 1873 and 1973K (1500, 1600, and 1700°C) the weight loss was above 40% and the product was only TiB_2. Oxygen and carbon content of these three samples were high in the range of 2 to 4% each. XRD of samples synthesized at various temperatures are presented in Fig.4.3. Only at temperatures above 2073K (1800°C) and an ultimate vacuum of <0.01 Pa, the product obtained was pure, low in carbon (<0.5 wt%) and oxygen (<0.5 wt%) and the weight loss recorded under this conditions was 44.6 to 44.9%. Details of a typical experiment are given in Table 4.1.

From the above results, it is clear that TiB_2 formation is thermodynamically feasible (in vacuum) at much lower temperatures of <1273K (<1000^oC), but in the present case, single phase TiB_2 was obtained only at or above 1773K (1500^oC). This could be due to the solid state and diffusion controlled reaction of TiB_2 formation. Usually this kind of solid state reaction takes place with intermediate steps, as a result intermediate products of Ti_3B_4 and Ti_2O_3 were observed in the present study. Possible intermediate reactions of TiB_2 formation are given follow:

$$6TiO_2 + 3/2B_4C + 15/2C \rightarrow TiB_2 + Ti_3B_4 + Ti_2O_3 + 9CO \quad (4.2)$$

$$1/5Ti_3B_4 + 3/10B_4C + 1/5Ti_2O_3 + 3/10C \rightarrow TiB_2 + 3/5CO \quad (4.3)$$

Free energy data for the above reaction (4.2) at 800K and 400K are -113.37 kJ/mol and -56.58 kJ/mol respectively (see Fig. 4.1) explains that formation of these intermediate products (Ti_3B_4 and Ti_2O_3), when synthesis was carried out at or below 1773K (1500^oC).

In the thermogravimetric run, the presence of Ti_3B_4 in the product and a weight loss of 47%, which is more than the theoretical value of 44%, indicate that some boron compound has evaporated during the process. A similar observation has not been noted in the induction furnace runs. Another notable difference is the weight loss at ~1573K (1300°C). In the thermo gravimetric run the reaction is nearly complete at 1603K (1330°C), whereas in the induction furnace run a much lower weight loss of 28.5% is recorded at 1633K (1360°C). As the temperature of reaction is increased to1773K (1500°C) the reaction is nearly complete, but the product is contaminated with higher levels of carbon and oxygen impurities (>2 wt%). Further removal of these impurities requires diffusion of the reacting species through the product layer of titanium diboride and hence the need for a much higher temperature of >2073K (1800°C) and a higher vacuum of 0.001Pa. At lower temperatures (<1673K) even extended hours of holding does not yield a pure product.

Table 4.1A typical experiment on synthesis of TiB_2

Charge composition (g): TiO_2 = 64.530; B_4C = 22.592; Coke = 12.885
Synthesis Parameters: Temperature: 2093K (1820^oC) Vacuum: 0.001 Pa; Time: 3 hour
Product: TiB_2 == 55.08 g Weight loss = 44.93% (theoretical wt. loss: 44.44% as per the reaction 4.1) Ti-68.5%, B-29.8%, O<0.5%, N<0.5%, C<0.5%, Fe<0.1%, Cl<50 ppm

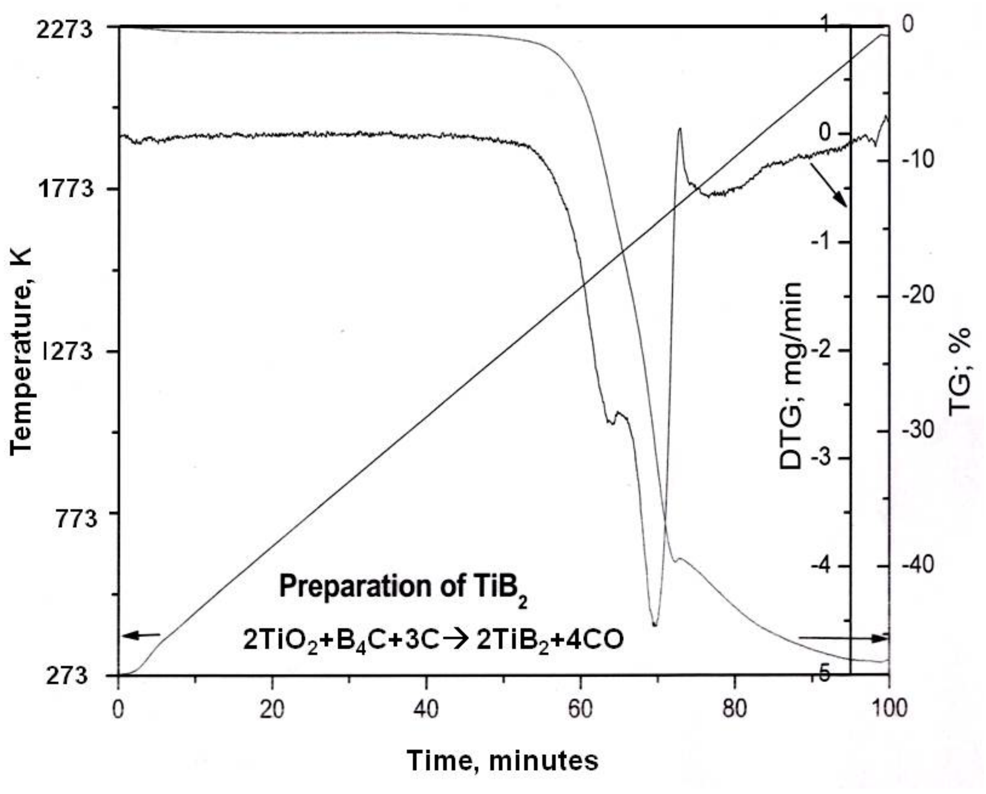

Fig.4.2 Thermogravimetric study of TiB_2 formation

The product of reduction at 2073K (1800°C) was a loosely sintered powder and could be crushed easily. Further grinding to micron size was carried out in high energy cup grinding mill.

Milling for a period of 30 minutes yielded TiB_2 of 1μm median dia. When continuously operated, the pot and the material got heated and hence the milling operations were carried out with intermittent cooling. Fig. 4.4 and 4.5 shows the particle size distribution and morphology (SEM image) of TiB_2 powders respectively.

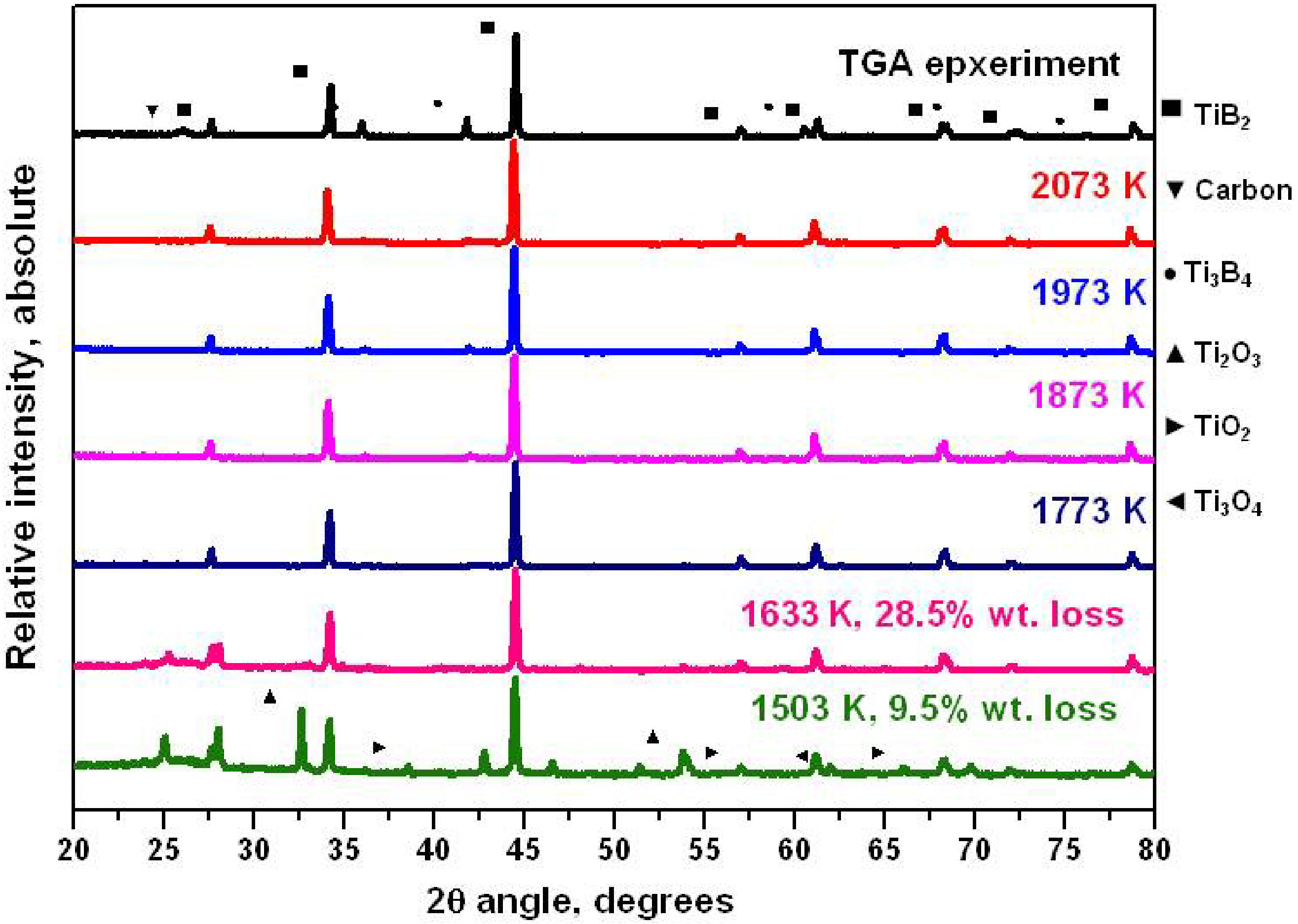

Fig.4.3 XRD of products synthesized at different temperatures

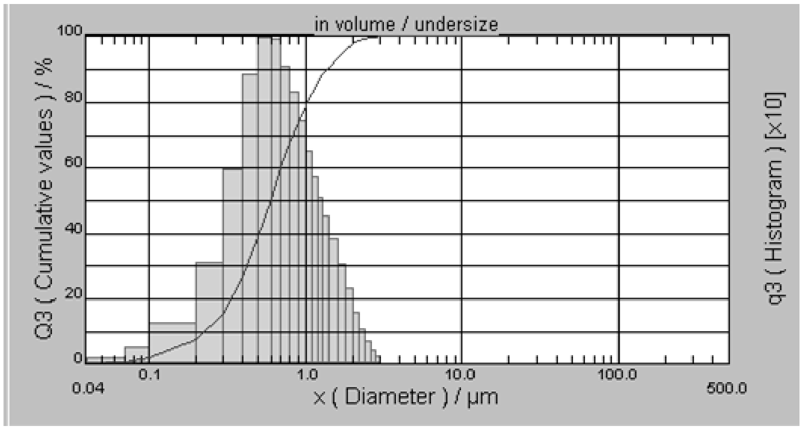

Fig. 4.4 Particle size distribution of TiB_2 powder

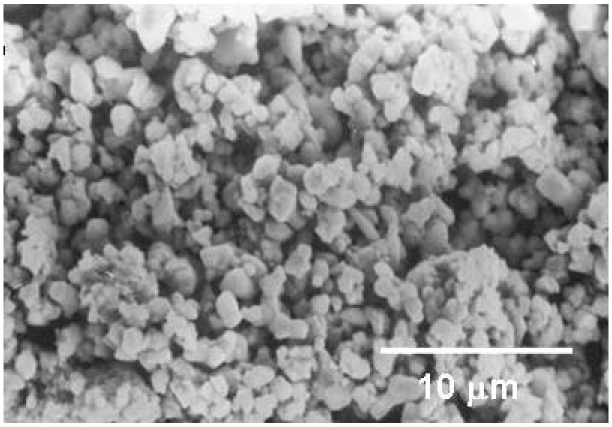

Fig.4.5 SEM image of titanium diboride powder

4.3 Synthesis of CrB_2

Synthesis of CrB_2 was carried as per the reaction (4.4). Initial experiment was carried out by TGA.

$$Cr_2O_3 + B_4C + 2C \rightarrow 2CrB_2 + 3CO \qquad (4.4)$$

Fig.4.6 shows the weight loss vs. temperature curve obtained by thermogravimetry experiment of a stoichiometric charge mixture (Cr_2O_3: B_4C: C:: 1: 1 : 2). The reaction starts at 1144K (871^{o}C) and results in a total weight loss of ~ 38.4% by 1673K (1400^{o}C). The weight loss observed is slightly (2.1%) more than the anticipated weight loss of 36.3%. This could be due to the evaporation of sub oxides of boron. The possible reactions to evaporation of sub oxides of boron are given in the next section.

Effects of temperature on synthesis of chromium boride using stoichiometric charges are presented in Table.4.2. At 1773K (1500^{o}C), though the weight loss is close to the theoretical value of 38.4%, the product is impure containing Cr_3B_4, CrB, Cr_2B_3, and graphite phases in addition to CrB_2. After reaction at 1873K (1600^{o}C) CrB and Cr_2B_3 phases are still present but these disappear after treatment at 1973K (1700^{o}C) (Fig.4.7). But presences of CrB_2, Cr_3B_4 and graphite phases are seen even after the reaction at 2073 K (1800^oC). The reasoning to explain the mechanism of reaction is presented in the following lines:

The presence of CrB phase upto1873K (1600^oC) indicates the possibility of intermediate reaction (4.5). CrB reacts with B_4C to form CrB_2 and Cr_3B_4 as per reaction (4.6). Cr_2B_3 decomposes to CrB_2 and Cr_3B_4 as per reaction (4.7). Free energy change for reaction (4.5) is negative at temperatures >700K (427^oC).

Free energy for the reaction (4.6 & 4.7) could not be computed as data for Cr_3B_4 is not available.

$Cr_2O_3 + 1/2B_4C + 5/2C \rightarrow 2CrB + 3CO$ (4.5)

$4CrB + 1/2B_4C \rightarrow CrB_2 + Cr_3B_4 + 1/2C$? (4.6)

$2Cr_2B_3 \rightarrow CrB_2 + Cr_3B_4$? (4.7)

The presence of boron deficient phase (Cr_3B_4) even after the treatment at 2073K (1800^oC) indicates the loss of boron from the charge, which could occur by following reactions:

$Cr_2O_3 + 3/2\ B_4C \rightarrow 2CrB_2 + B_2O_3\uparrow + 3/2C$ (4.8)

$Cr_2O_3 + 5/2\ B_4C \rightarrow 2CrB_2 + 3B_2O\uparrow + 5/2C$ (4.9)

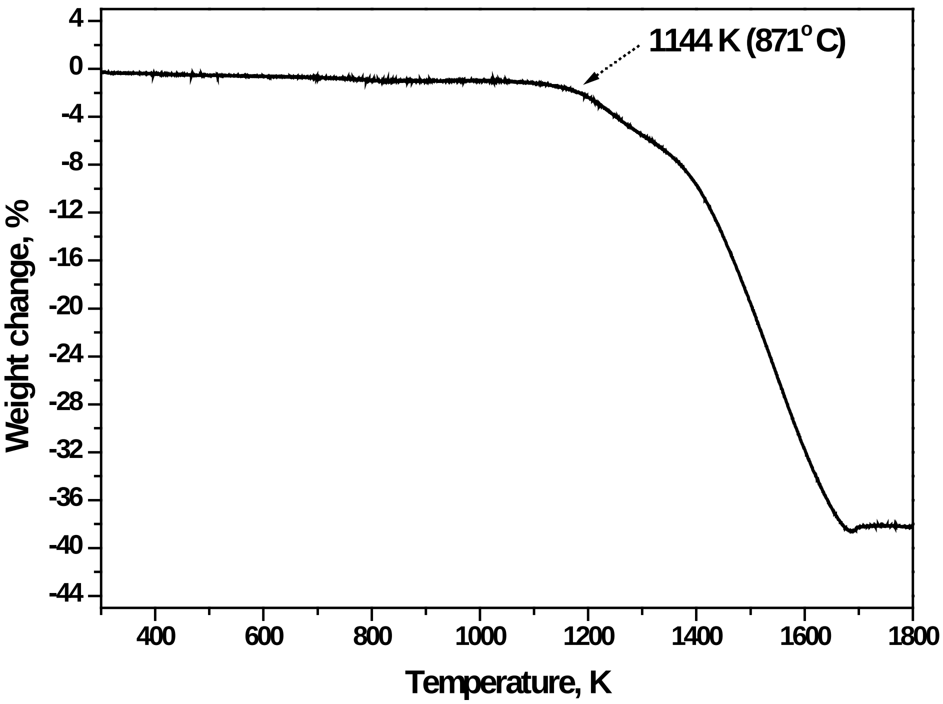

Fig.4.6 Thermograviometry study of formation of CrB_2

Table 4.2 Effect of temperature on synthesis of chromium boride using stoichiometric charge (holding time: 2 hours)

Temperature (K)	Weight loss (%)	Phases present
1773	38.65	CrB_2, Cr_3B_4,CrB, Cr_2B_3, C
1873	39.57	CrB_2, Cr_3B_4,CrB, Cr_2B_3, C
1973	38.93	CrB_2, Cr_3B_4, C
2073	39.13	CrB_2, Cr_3B_4, C

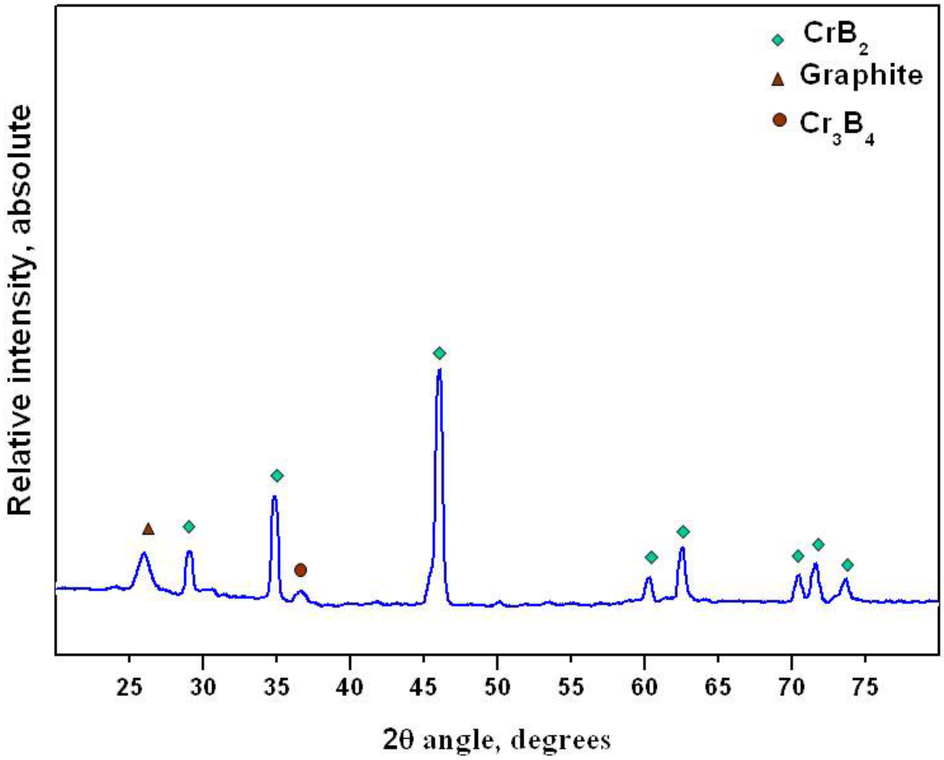

Fig.4.7 XRD pattern of chromium boride prepared by stoichiometric charge at 1973K

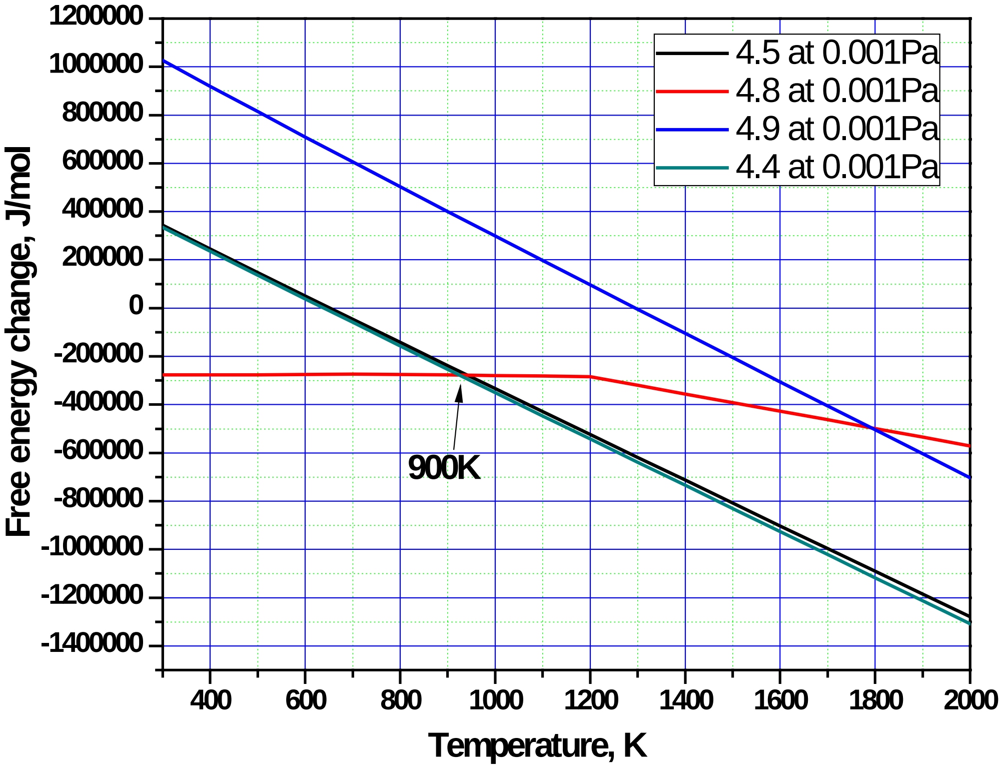

Fig.4.8 Free energy change of reactions (FactSage software version 6.3[1])

Thermodynamic calculation [1] (Fig. 4.8) indicates that both reaction (4.8) and (4.9) could take place on heating and hence boron could be lost as B_2O_3/B_2O during reaction. Vapor pressure of B_2O_3 at 1523K is 267Pa [2]. Experiments were carried out in high vacuum at 0.001Pa. Hence to obtain single-phase CrB_2 phase, it is necessary to add excess boron in the charge.

Results of experiments carried out with varying molar ratio of charge mixtures are presented in Table 4.3. The XRD patterns of product obtained by reaction of modified charge mixtures are presented in Fig.4.9. Graphite in the product is eliminated by reducing the carbon content in the charge, which can be seen in the Table 4.3 at sample no. 3 and in the Fig.4.9. With a molar ratio (Cr_2O_3: B_4C: C) of 1: 1: 1.6 a product without graphite phase was obtained but Cr_3B_4 was still present. With this reduced carbon, when boron content in the charge is increased, single phase CrB_2 was obtained (sample no.5 in Table.4.3) The molar ratio for obtaining single phase pure CrB_2 was evaluated as 1: 1.2: 1.31. CrB_2 powder prepared by such a charge was found to contain 0.9% carbon and 0.6% oxygen.

Table 4.3 Effect of charge composition on synthesis of Chromium boride
(Temperature- 1973K, holding time- 2 hours)

Sample	Molar ratio of charge (Cr_2O_3 : B_4C : C)	Phases present
1	1 : 1 : 2	CrB_2, Cr_3B_4, C
2	1 : 1 : 1.8	CrB_2, Cr_3B_4, C
3	1 : 1 : 1.6	CrB_2, Cr_3B_4
4	1 : 1.1 : 1.45	CrB_2, Cr_3B_4
5	1 : 1.2 : 1.31	CrB_2

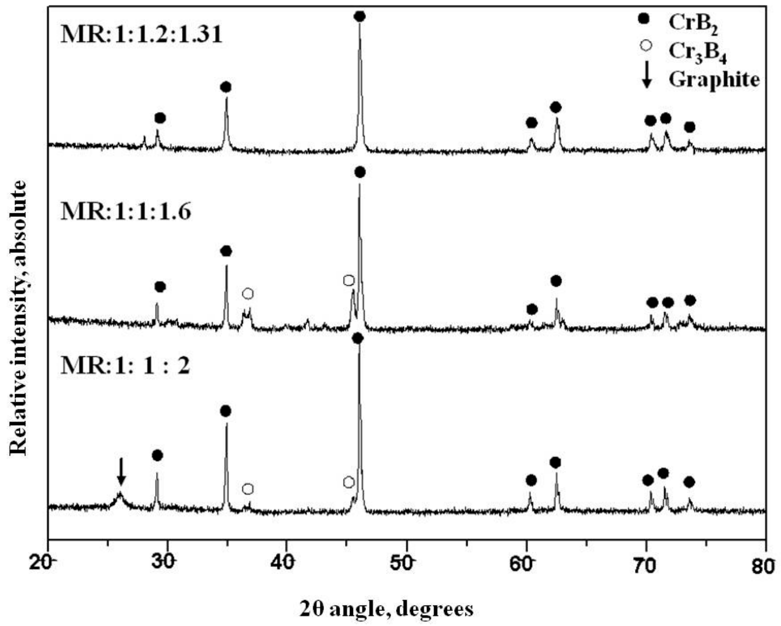

Fig.4.9 XRD pattern of the products obtained by varying charge composition (*MR: molar ratio (Cr_2O_3 :B_4C :C))

By systematic experimental studies the charge composition and the process parameters for production of single phase CrB_2 using commercial grade reactants has been arrived. The SEM image and particle size distribution of CrB_2 powder prepared in the present study are shown in Fig. 4.10 and 4.11 respectively. SEM image shows that particles are around 4-5 μm size. The particle size distribution is tri-modal in nature and the shape of the particles are irregular possibly due to grinding operations.

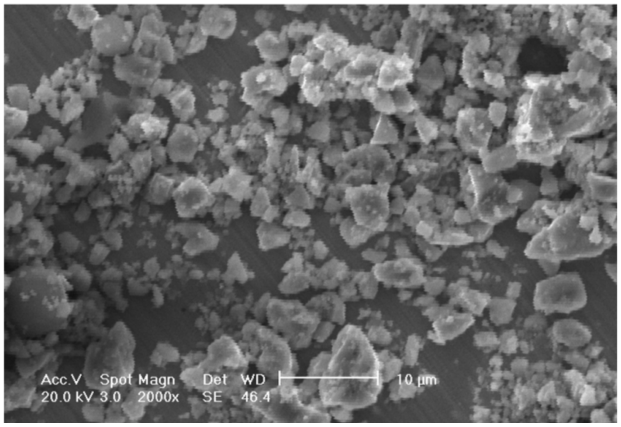

Fig. 4.10 SEM image of CrB_2 powder

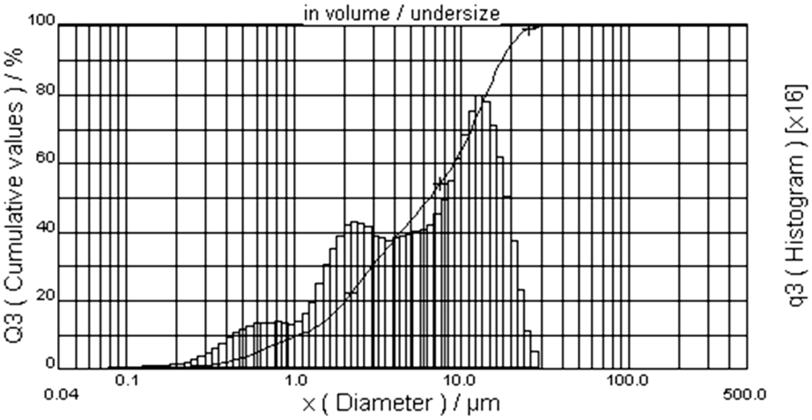

Fig. 4.11 Particle size distribution of CrB_2 powder

4.4 Synthesis of pre-alloyed $(TiCr)B_2$

The results reported earlier indicate that synthesis of TiB_2 and CrB_2 require temperatures above 1973K (1700°C) for obtaining single phase pure compounds. Synthesis of a composite boride [$(TiCr)B_2$] would be advantageous in obtaining a homogenous product with possibly improved properties. The synthesis of $(TiCr)B_2$ was attempted by the following reaction:

$$2TiO_2 + B_4C + Cr_2O_3 + 6C \rightarrow 2(TiCr)B_2 + 7CO\uparrow \quad (4.10)$$

This carbide-oxide reaction is a simple and direct method for preparation of compound, when the reactants are available in pure and finely divided form. As the reactants consist of four solid substances, homogenization of the charge mixture is essential for completion of the reaction. The product of reaction at ~1473K (1200°C) was found to be $(TiCr)B_2$ highly contaminated with carbon and oxygen, each analyzing in the range of 3-4%. As the temperature of the reaction was increased, the carbon and the oxygen contents decreased, similar to synthesis of TiB_2 and a pure product with carbon and oxygen contents below 0.5wt% each could be obtained at a temperature of 2098K (1825°C) and a final vacuum of 0.001Pa (1×10^{-5}m.bar). Particle size distribution of $(TiCr)B_2$ powder prepared in the present study is shown in Fig. 4.12. Chemical analysis of the product $(Ti_{0.85}Cr_{0.15})B_2$ is given in weight % as Ti- 60.9, Cr-11.6, B-26.2, C-0.07, O-0.6, N-0.5.

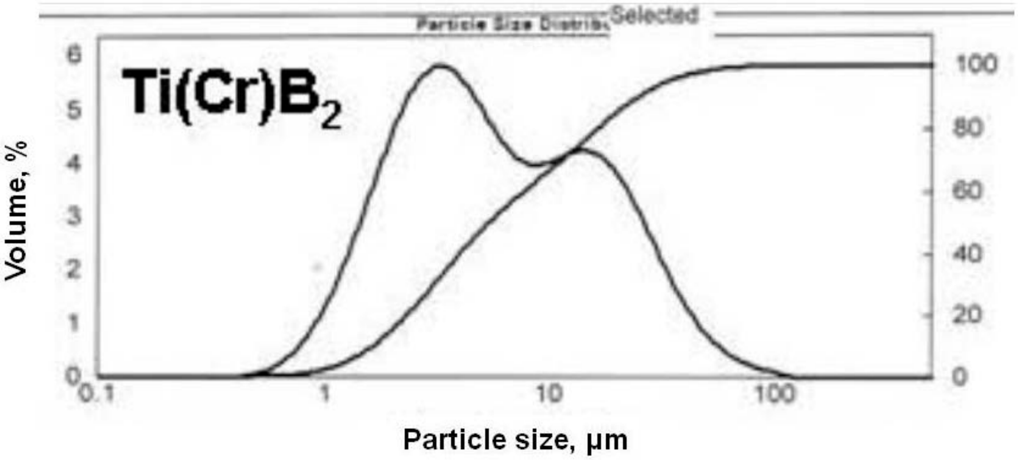

Fig. 4.12 Particle size distribution of $(Ti_{0.85}Cr_{0.15})B_2$ powder

4.5 Synthesis of $MoSi_2$

Molybdenum disilicide ($MoSi_2$) was synthesized from its elements using stoichiometric amounts of pure molybdenum (> 99.7%, Merc Germany) and silicon (>99%) as per the following reaction:

$$Mo + 2Si \rightarrow MoSi_2 \tag{4.11}$$

As the formation of $MoSi_2$ is highly exothermic (ΔH^o=-131 kJ)[1], abrupt increase in the charge temperature indicates onset of reaction. The furnace power is turned off with the onset of rise in temperature. Quantity of charge and the spacing between the pellets were adjusted such that the product $MoSi_2$ was not overheated to near melting point. A small weight loss of 1-2% was observed due to evaporation of high vapor pressure species such as SiO and MoO_3. The SEM image and particle size distribution of $MoSi_2$ powder prepared in the present study are shown in Fig. 4.13 and 4.14 respectively. SEM image shows that particles are in the range of 2-5 µm sizes. The particle size distribution is bi-model in nature and the shapes of particles are irregular due to grinding operations. Chemical analysis of impurities in synthesized $MoSi_2$ is measured in weight % as C-0.37, O-0.30, Fe-0.15.

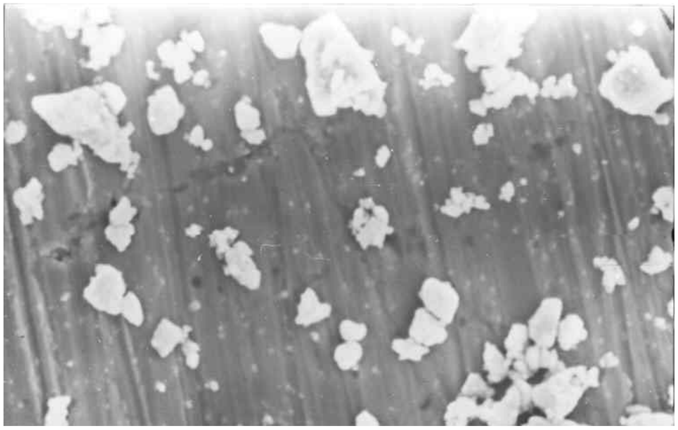

Fig. 4.13 SEM image showing the morphology of $MoSi_2$

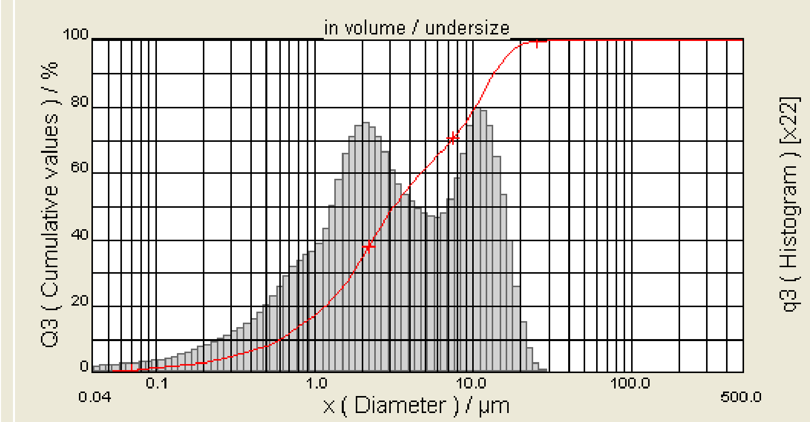

Fig. 4.14 Particle size distribution of $MoSi_2$powder

4.6 Summary

Syntheses of single-phase refractory metal borides from elemental constituents are expensive. CVD techniques are complex, generally used for coatings and not for commercial production of powders. Borothermic reduction involves loss of expensive boron in the form of boron oxides. Thus, boron carbide reduction method is a better method for the synthesis of refractory metal borides considering both start materials availability and ease of process comfort. B_4C serves both as a reducing agent (due to the presence of carbon) as well as the source of boron to form borides. Hence, the present study of synthesis of borides by carbothermic reduction in the presence of boron carbide leads to obtain a single phase refractory metal borides. By using this method, single phase TiB_2, CrB_2, $(Ti_{0.95}C_{0.05})B_2$, $(Ti_{0.90}C_{0.10})B_2$ and $(Ti_{0.85}C_{0.15})B_2$ materials were synthesized successfully in the present thesis. Important findings of the present study are given below:

a) Synthesis of titanium diboride through reduction of titanium dioxide by boron carbide and carbon was studied. Process parameters were optimized to prepare pure boride with carbon and oxygen contents of 0.5% each. Milling of the as reduced boride to a fine size of 1μm median diameter powder was achieved.

b) Charge composition and reduction conditions have been optimized to synthesize single phase chromium diboride (CrB_2) by boron carbide reduction of chromium oxide in the presence of carbon.

c) Homogenous product of pre-alloyed $(TiCr)B_2$ was prepared by carbothermic reduction of Ti and Cr oxides in the presence of boron carbide.

d) Molybdenum disilicide was synthesized from its elements using stoichiometric amounts of molybdenum and silicon.

4.7 References

[1] FactSage software version 6.3

[2] http://onlinelibrary.wiley.com/doi/10.1111/j.1151-2916.1935.tb19358.x/abstract

CHAPTER 5

CHAPTER 5

DENSIFICATION, MICROSTRUCTURE, MECHANICAL AND PHYSICAL PROPERTIES

5.1 Introduction

This chapter has been divided into three sections: section I describes densification of the composites, section II describes phase identification and microstructural characterization; and thermodynamic analysis to elucidate the densification mechanism, and section III describes the mechanical and physical properties of the composites produced, structure property relations used to explain the toughening mechanisms.

Effect of various sinter additives ($TiSi_2$, $CrSi_2$, WSi_2, CrB_2) on the densification of TiB_2 by hot pressing has been studied. Combined addition of sinter additives (CrB_2+$MoSi_2$) on densification of TiB_2 has also been studied. Dense pre-alloyed $(TiCr)B_2$ + 20% $MoSi_2$ composites were also prepared. Transition/refractory metal disilicides are selected as sintering aids for TiB_2, because they are high temperature materials in their own right in addition to their favorable thermodynamic compatibility with many borides [1-3]. Silicides are attractive for high temperature applications as they possess high melting point, retention of strength and ductility at high temperatures and excellent oxidation resistance. For example, $CrSi_2$ finds application as high temperature structural material in aerospace and energy conversion industries. $CrSi_2$ has excellent oxidation resistance, with negligible weight gain up to 1473K (1200^oC) in air and hence finds use in oxidizing environments at temperatures higher than the upper limit for Ni-base superalloys [3,4]. The oxidation resistance of $CrSi_2$ is attributed to the formation of Cr_2O_3 and amorphous SiO_2 scales. Tungsten silicide coatings have outstanding abrasive and adhesive wear resistance due to strong covalent bonds [3]. Tungsten silicides show oxidation resistance up to 2273K (2000^oC) in air due to the formation of a protective SiO_2 film [3]. $MoSi_2$ has evoked more interest for high temperature structural applications above 1273K (1000^oC), because of its high melting point (2293K), high thermal conductivity (~53 W/mK) and good oxidation resistance (up to 1973K) [1,3]. $TiSi_2$ is also of interest as a high temperature structural material, because in addition to high oxidation resistance (1473-1573K) and it also has low density (4040 kg/m^3) [2].

Densified pellets were examined by XRD, SEM-EDX, EPMA. XRD analysis confirmed that the hot pressed pellets contained in TiB_2 composites either the additives in solid solution or as reaction products. SEM microstructures present the distribution of various phases in end product. Elemental analysis of various phases of dense composites was characterized by SEM-EDS and EPMA. Spot analysis, line scan across various phases and elemental mapping over a region of phases for all elements were carried out to elucidate the interaction between matrix and sinter additives. In addition, fractography and crack propagation patterns were analyzed to explain the mode of fracture and the crack propagation mechanisms in all the composites.

Hardness and fracture toughness values of all the composites were measured. Variation of the hardness is dependent on the density, nature of second phase and its quantity in the composite. Similarly the fracture toughness also depends on the above parameters. Physical properties like coefficient of thermal expansion (CTE), electrical resistivity were also measured in the temperature range of 298 – 1273K.

Densification of TiB_2 and its composites were attempted by both pressureless sintering and hot pressing in the present study. However, required densification was not achieved by pressureless sintering even after adding sinter additives. Hence, all composites in the present study were prepared by hot pressing and hot pressed samples were used for microstructural characterization and oxidation studies. Detailed oxidation results are given in next chapter. Detailed results and discussion on densification of each of the composites is described separately in the following section.

5.2 Densification of monolithic TiB_2 and its composites

Densification of monolithic TiB_2 was attempted by pressureless sintering at 2173K (1900^{o}C) for 2 hours in an $Ar+H_2$ atmosphere. Fully dense pellets were not obtained by this method [1]. Hot pressing technique was alternatively used to densify the monolithic TiB_2 and the results are presented in Fig.5.1. In the temperature range studied, highest density of 97.5% TD was obtained only at 2073K (1800^{o}C).

5.2.1 Densification of TiB_2+TiSi_2 composites

A few pressureless sintering experiments were attempted in the temperature range of 1773-2073K (1500-1800^{o}C) with varying additions of $TiSi_2$ to TiB_2 in a vacuum induction furnace. The highest density achieved by pressureless sintering was only 82% of theoretical (TD). Hence characterization studies of pressureless sintered samples were not carried out.

Densification results of the hot pressed samples are presented in Fig.5.2. Under identical conditions of hot pressing, density of monolithic TiB_2 obtained was 82% TD, whereas that of TiB_2 with a small addition of $TiSi_2$ (2.5%) was 96% TD. Near theoretical density (~99% TD) was obtained with the increase of the sintering aid content ($TiSi_2$) to ≥5 wt%. Attainment of such a high density for TiB_2 particulate composite is attributed to the liquid phase sintering due to the low melting point (1813K) of $TiSi_2$. While hot pressing TiB_2 without any sinter additive, a higher hot pressing temperature of 2073K (1800°C) was needed to achieve 97.5 % TD [1]. In the present study, 99% TD was obtained by using sinter additive at a hot pressing temperature of 1823K (1550°C) itself. About 100K higher temperature (1923K) was reported by Raju et al.[2] for a similar densification. The applied pressure (30 MPa) is same in both the cases. The major reason for better sinterability of present samples could be due to higher purity of the starting powders, (TiB_2 having 0.5% oxygen as compared to 1.9% with Raju's samples), use of pure $TiSi_2$ (electronic grade), and the use of vacuum (0.001Pa) in the furnace in place of argon atmosphere used by Raju et.al[2]. In a high vacuum resistance heating furnace using graphite, there will always be present a partially reducing atmosphere, which helps to reduce the surface oxides of non-oxide ceramics.

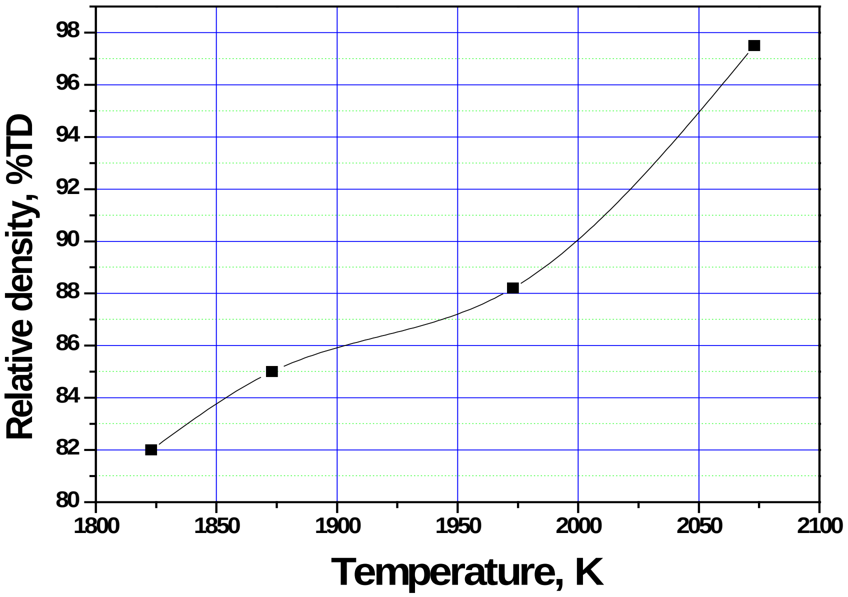

Fig. 5.1 Effect of hot pressing temperature on the densification of monolithic TiB_2
(Line joining points are for visual aid only)

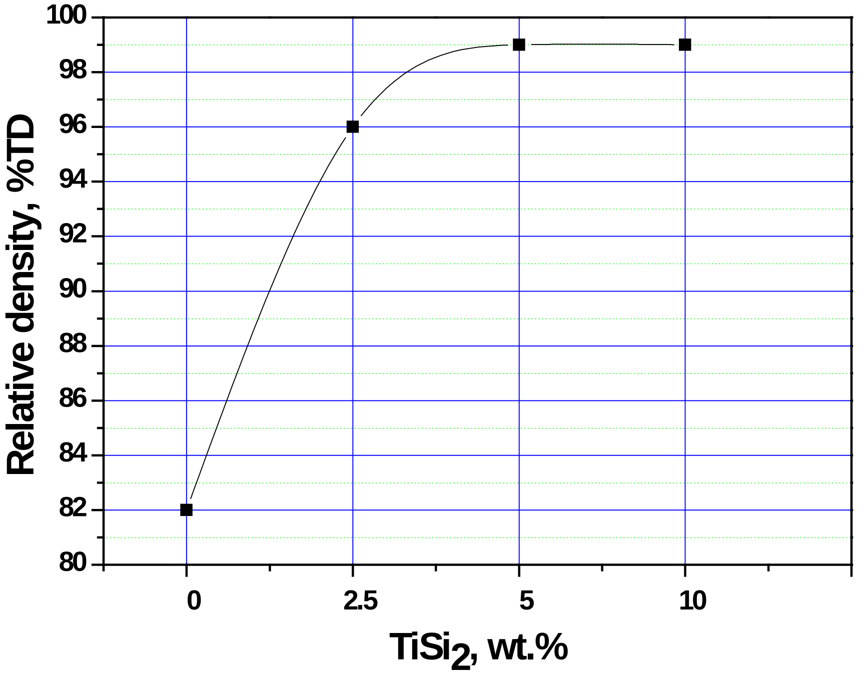

Fig. 5.2 Effect of $TiSi_2$ additive on the densification of TiB_2 by hot pressing at 1823K
(Line joining points are for visual aid only)

5.2.2 Densification of TiB_2 + $CrSi_2$ composites

Experiments were carried out on pressureless sintering of TiB_2 with varying additions of $CrSi_2$ in the temperature range of 1723-1873K (1450-1600°C) in vacuum as well as in argon for 2h. The highest density achieved was 68% TD at 1723K (1450°C) even with the addition of 10% $CrSi_2$. Hence, this approach of densification was not pursued further.

Results on the densification of hot pressed samples are presented in Table.5.1. Near theoretical density of 99.89% TD was obtained with 2.5% addition of $CrSi_2$. With further increase of sinter additive the density was found to decrease. Hot pressing of TiB_2 without any sinter additive, gave a density of 97.5% TD at a higher hot pressing temperature of 2073K (1800°C) and a pressure of 32 MPa [1]. When $CrSi_2$ is used, liquid phase sintering (MP of $CrSi_2$: 1750 K) leads to higher densification at a lower temperature (1973K) and pressure (28 MPa).

Table 5.1 Density of TiB_2 + $CrSi_2$ composites prepared by hot pressing at 1973K (1700°C) and 28 MPa pressure

Wt.% $CrSi_2$	Density (kg/m^3)	Relative Density$^{\#}$ (%TD)	Relative Density$^{\$}$ (%TD)	Open porosity$^{₹}$
2.5	4330	99.9	99.5	0.43
5	4280	98.6	98.4	0.39
10	4170	95.5	95.1	0.46
15	4060	92.3	92.4	0.41
0*	4210	97.5	-	2.34

* hot pressed at 2073K (1800°C)[1]; # calculated by using rule of mixture; $ by SEM-image analysis tool, ₹ by Archimedes principle

5.2.3 Densification of TiB_2 + WSi_2 composites

A few experiments were carried out on pressureless sintering of TiB_2 with additions of WSi_2 in the temperature range of 1873-2223K (1600-1950^{o}C) in vacuum for 2 to 4h. The highest density achieved was only 86% TD at 2223K (1950^{o}C) for 4h with the addition of 15% WSi_2. As the density obtained was low, this approach of densification was not attempted further.

Results on densification of hot pressed samples are presented in Table 5.2. To obtain a density of 97.5 %TD without any sinter additive, 2073K (1800^{o}C) and 32 MPa were needed [1]. Liquid phase sintering due to reaction products probably results in enhanced densification.

Table 5.2 Density and mechanical properties of hot pressed samples (Operating conditions: 1873K (1600^{o}C), 1 hour, 30 MPa)

Additive, wt.% WSi_2	Density, kg/m^3	Relative Density %TD	Hardness, GPa	Fracture toughness, MPa.m$^{1/2}$
0	3670	85.0	11 ± 2	-
2	3870	88.5	-	-
2.5	4360	99.5	26 ± 3	5.0 ± 1.0
5	4550	100	24 ± 3	5.9 ± 1.9
10	4640	100	26 ± 2	4.3 ± 0.9
15	4830	100	24 ± 2	4.8 ± 0.9

5.2.4 Densification of TiB_2 + CrB_2 composites

Density of the hot pressed samples is presented in Table 5.3. For monolithic TiB_2, 89% TD was obtained under the same conditions. Attainment of higher density of TiB_2 composites with CrB_2 is attributed [3,4] to the higher mobility of CrB_2 and formation of solid solution with TiB_2. While hot pressing TiB_2 and CrB_2 powders at 2023K (1750^{o}C), the microstructure has been observed to be solid sintered (Cr,Ti)B_2 clusters and particles with an unreacted base of TiB_2 with an outer layer of (Cr,Ti)B_2 [3]. The quasi binary phase diagram of CrB_2-TiB_2 system is reproduced in Fig. 5.3[3]. It shows a dotted line from 1750 to 2000^{o}C, indicating the formation of two phases of TiB_2 and (Ti,Cr)B_2 below this line. From the phase diagram, maximum CrB_2 solubility in TiB_2 does not exceed 1 mol% (1.15 wt.%) at 2073K (1800^{o}C). From the above it is clear that higher addition of CrB_2 does not contribute towards solid solution formation at the sintering temperature of 2023K (1750^{o}C) and hence no increase in density is observed for composites with CrB_2 above 2.5%. Holcombe *et al*.[5] obtained a density of 84 and 90% TD with the addition of 3% CrB_2 in pressureless sintering at 2173 and 2373K (1900 and 2100^{o}C) respectively. Konigshofer *et al*.[6] obtained 98.9% TD with the addition of 0.5% CrB_2 to TiB_2 by hot pressing at a higher temperature of 2073K (1800^{o}C) and higher pressure of 45 MPa.

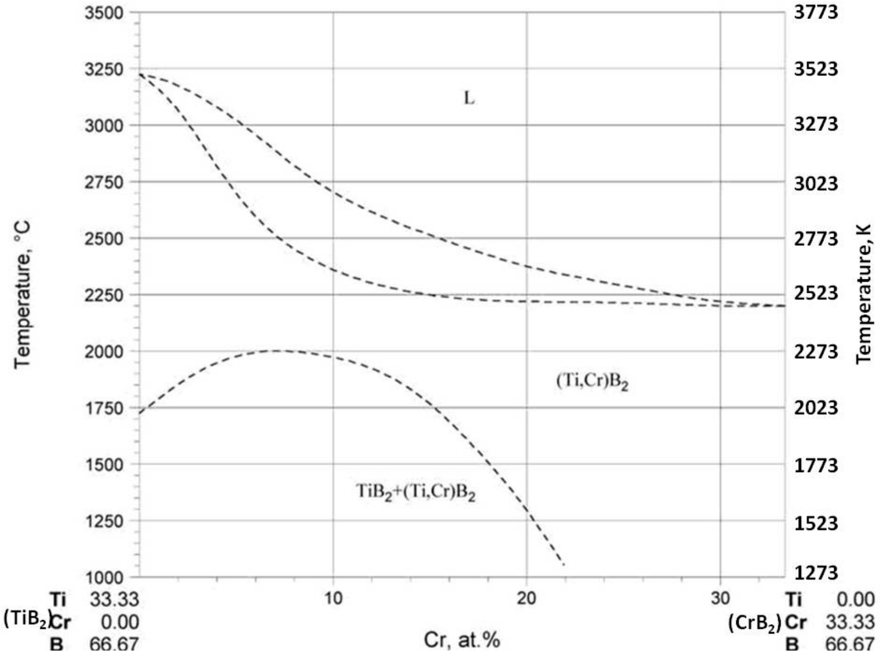

Fig.5.3 Quasi binary phase diagram of CrB_2 – TiB_2 [3]

Table.5.3 Relative density, Hardness and Fracture toughness of TiB_2+CrB_2 composite-hot pressed at 2023K (1750^{o}C), 1h, 35 MPa

CrB_2 content (%wt.)	Relative Density (%TD)	Micro hardness (GPa)	Fracture toughness K_{IC} (MPa·m$^{1/2}$)
0	89.0	-	-
2.5	96.6	23.86 ± 1.2	2.80 ± 0.1
5	94.8	23.68 ± 1.9	4.30 ± 0.3
10	94.0	23.92 ± 1.0	4.99 ± 0.9

5.2.5 Densification of TiB_2 + 20%$MoSi_2$ + CrB_2 composites

Results on densification of hot pressed samples are presented in Table 5.4. With 5% addition of CrB_2 to TiB_2+20%$MoSi_2$, 98.4% TD was obtained. As mentioned earlier, the densities obtained with 5% and 10% CrB_2 of TiB_2 were 94.8% and 94.0% TD (Table 5.3) respectively by hot pressing at 2023K (1750^{o}C) and 35 MPa. Hot pressing of TiB_2+20%$MoSi_2$ without CrB_2, resulted in a density of 98.7 %TD at a lower temperature of 1700^{o}C and 32 MPa [1]. In the present study also, $MoSi_2$ is responsible for achieving a density of >95% TD due to liquid phase sintering. Major contribution of $MoSi_2$ in densification is due to compressive deformation of $MoSi_2$ and the product of reaction between TiB_2 and $MoSi_2$, namely $TiSi_2$ also contributes in densification [1].

Table 5.4 Density, hardness and fracture toughness of TiB_2 composites; hot pressed at 2073K (1800^{o}C), 1h, 35 MPa

Sr. No.	TiB_2 Composite	Relative Density, %TD	Vickers Hardness (GPa)	Fracture toughness (MPa.m$^{1/2}$)
1	20% $MoSi_2$+5%CrB_2	98.4	24±1	3.5±0.7
2	20% $MoSi_2$+10%CrB_2	95.7	19±1	3.7±0.4
3	20% $MoSi_2$+15%CrB_2	96.4	18±1	4.1±0.3
4*	20% $MoSi_2$+0%CrB_2	98.7	25±1	5.0±0.7
5$	0% $MoSi_2$+0%CrB_2	97.5	26±1	5.1±0.7

* hot pressed at 1973K (1700^{o}C)[1];$ hot pressed at 2073K (1800^{o}C)[1]

5.2.6 Densification of $(TiCr)B_2$+20%$MoSi_2$ composites

Results on densification of hot pressed samples are presented in Table 5.5. The density of composites obtained with 5, 10 and 15% CrB_2 contained $(TiCr)B_2$+20% $MoSi_2$ composites were 96.5, 97.9 and 99.2% TD respectively.

Table 5.5 Density, hardness and fracture toughness of $(TiCr)B_2$ composites

Sr. No.	Composite	Density, kg/m^3	Relative Density* (%TD)	Micro Hardness (GPa)	Fracture toughness (MPa.$m^{1/2}$)
1	$(Ti_{0.95}Cr_{0.5})B_2$+20% $MoSi_2$	4430	96.5	25± 1	2.8 ± 0.2
2	$(Ti_{0.90}Cr_{0.10})B_2$+20% $MoSi_2$	4670	97.9	24± 1	3.5 ± 0.6
3	$(Ti_{0.85}Cr_{0.15})B_2$+20% $MoSi_2$	4810	99.2	27± 1	4.5 ± 0.5

* calculated by SEM-image analysis tool

While comparing CrB_2, $TiSi_2$, $CrSi_2$, $MoSi_2$+CrB_2, and WSi_2 as sinter additives to TiB_2, highest density values are obtained with WSi_2. But in all cases there was significant improvement in density even with a small 2.5% addition of sinter additive. With addition of $TiSi_2$ and WSi_2, there is monotonic increase in the density, whereas in other cases a decrease in density is seen beyond certain values. The mechanism of sintering is probably different in each case and the sintering temperatures also vary.

To elucidate the densification mechanism, it is necessary to identify the new phases which are formed during the course of sintering and its distribution. Following section presents results and discussion on phase identification, microstructural characterization and thermodynamic analysis of the composites studied.

5.3 Phase identification and Microstructural characterization

Densified pellets were characterized by XRD, SEM-EDAX and EPMA. XRD analysis confirmed that the hot pressed pellets of TiB_2 composites contained the additives in solid solution or as reaction products. SEM microstructures revealed the distribution of various phases in the end product. Fractured surfaces were analyzed by SEM. Fractography reveals the type of fracture (ductile/brittle/intermediate), grain growth, presence of pores and its distribution. Important findings of the individual composites are given below:

5.3.1 TiB_2+$TiSi_2$ composites

XRD pattern of the hot pressed TiB_2+10%$TiSi_2$ is shown in the Fig. 5.4. Our observations are similar to that of Raju et. al [2], showing the presence of Ti_5Si_3 in all the samples, except for the composite with $TiSi_2$ in the charge ≥10%, where both $TiSi_2$ and Ti_5Si_3 were seen. Sade et.al [7] reported the formation of SiB_6 at the interface of TiB_2 and $TiSi_2$ when annealed at 1357K (1084^{o}C). Ramos et.al [8] reported the existence of Ti_6Si_2B, a new ternary phase in the Ti-Si-B system. At 1473K (1200^{o}C) Ti_6Si_2B phase forms from the liquid through the peritectic reaction: $L + TiB + Ti_5Si_3 \Leftrightarrow Ti_6Si_2B$. In the present investigation such a ternary phase has not been identified. This could be due to the greater stability of TiB_2 phase compared to TiB in the (TiB_2+$TiSi_2$) composite.

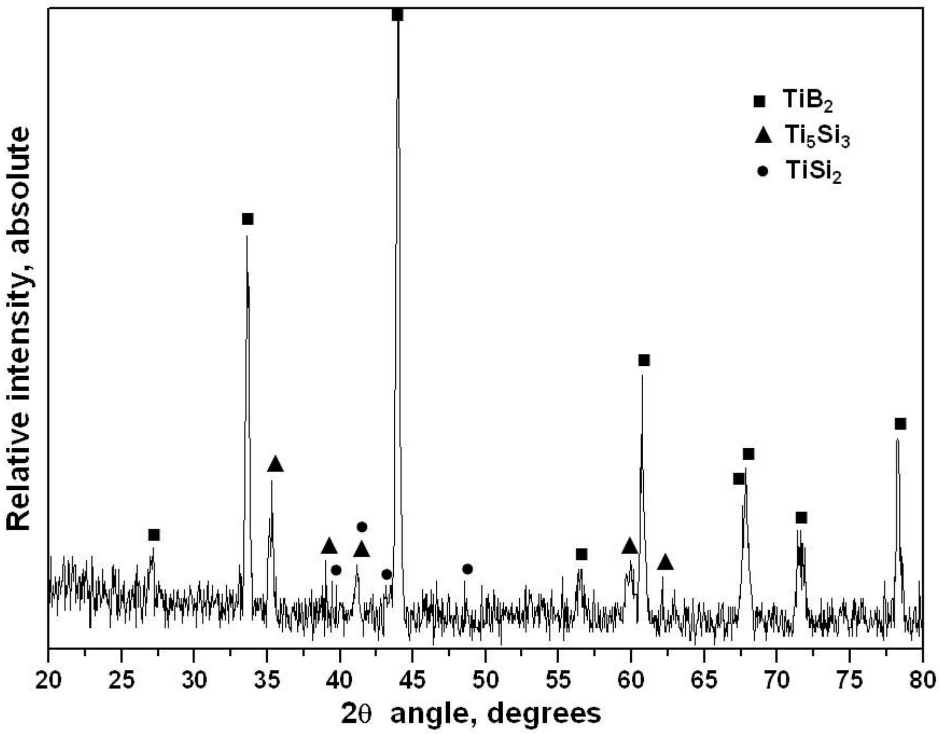

Fig. 5.4 XRD analysis of TiB_2+10%$TiSi_2$ sample

Back Scattered Electron (BSE) image of TiB_2+10%$TiSi_2$ sample is presented in Fig. 5.5. This picture shows three distinct types of regions grey matrix, black and white phase in the matrix. Elemental analysis of these regions showed the grey matrix to be of TiB_2 with ~0.22% Si, the black phases also of TiB_2 but rich in silicon (~12%) and the white phases to be rich in titanium with <1% silicon. One can see a few more areas with varying brightness. These could be reaction products with varying proportions of different phases. Fig. 5.6a presents the portion surrounding a big $TiSi_2$ particle. Elemental mapping of this portion for titanium, boron and silicon are shown in Fig. 5.6 b, c and d. Unreacted portions of $TiSi_2$ particle can be seen clearly in Fig. 5.6d as white. Fig. 5.6a and b indicate the presence of titanium surrounding the unreacted portion. Fig. 5.6c clearly shows the absence of boron in the $TiSi_2$ particle. This figure suggests that silicon from $TiSi_2$ is migrating to the matrix. TiB_2 is a more stable phase compared to $TiSi_2$ at the hot pressing temperatures [9]. EPMA analysis clearly shows traces of Si in TiB_2 phase.

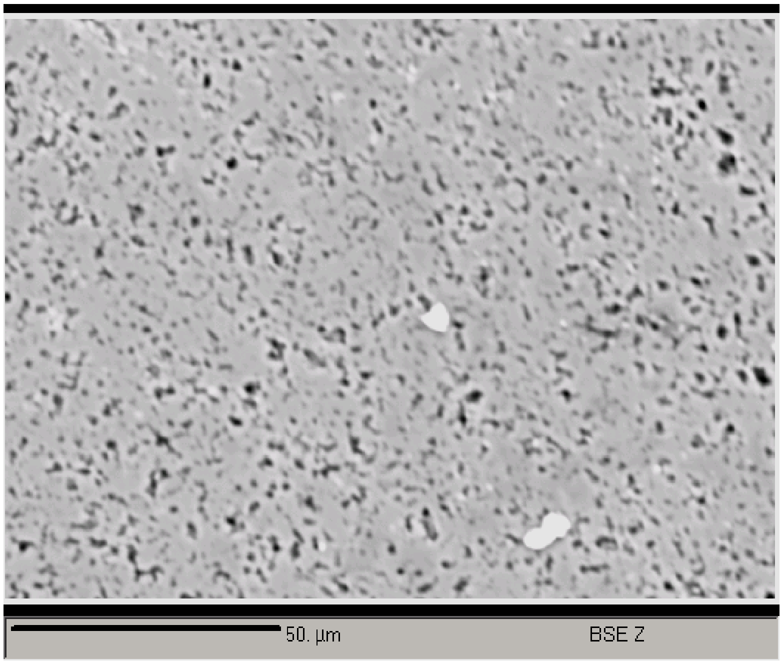

Fig. 5.5 BSE image of TiB_2+$TiSi_2$ composite

Phase analysis

Dark phase		Matrix		Bright phase	
Weight%		Weight%		Weight%	
B	26.66	B	~30	B	<0.01%
Si	12.09	Si	<0.22	Si	0.8 – 1%
Ti	61.25	Ti	~69	Ti	>98%

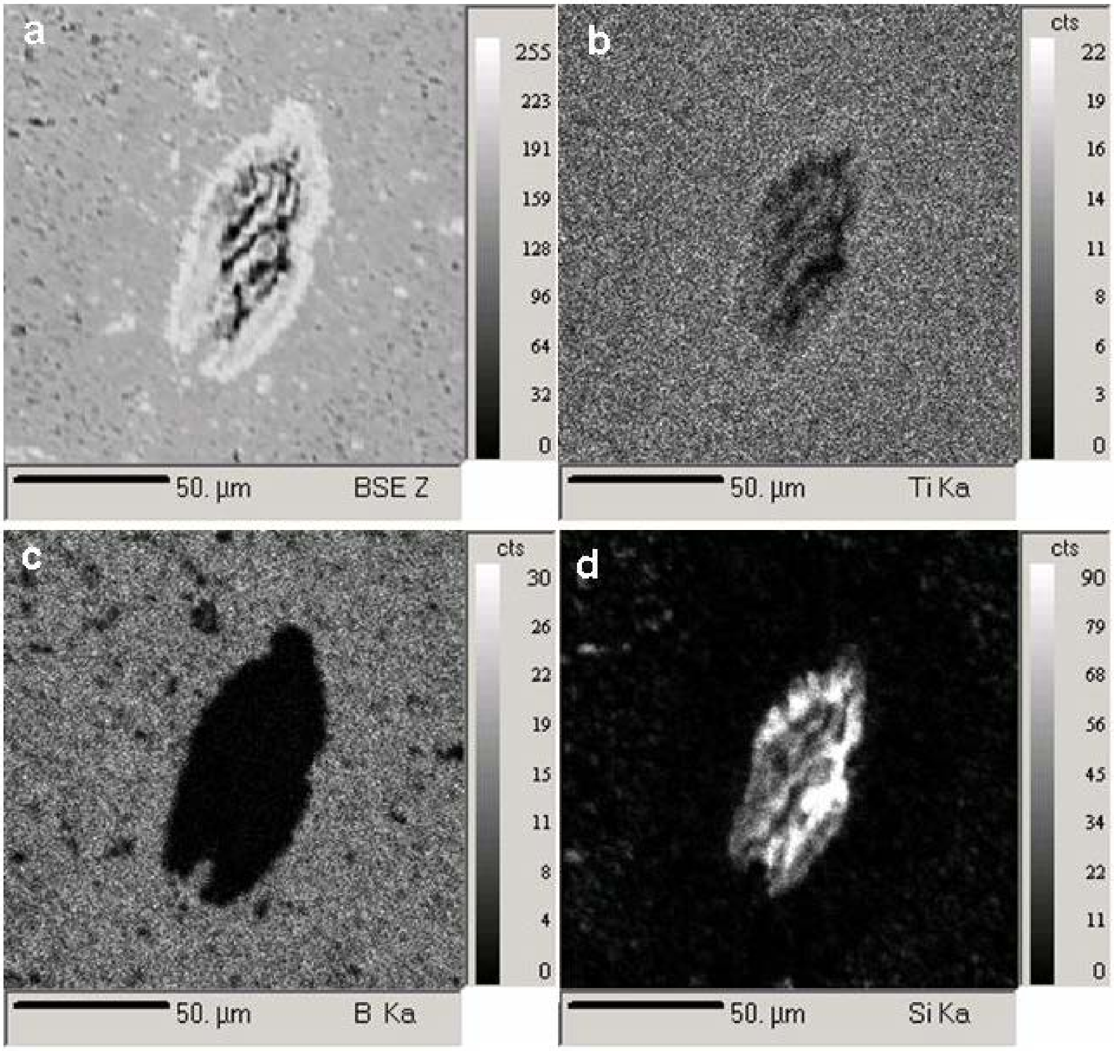

Fig. 5.6 a) BSE of a big $TiSi_2$ particle in the matrix; Elemental mapping for b) Ti, c) B and d) Si

Fractured surface of TiB_2+2.5%$TiSi_2$ and TiB_2+10%$TiSi_2$ samples taken by SEM (Secondary Electron Mode) are presented in Fig.5.7. Both the pictures show the fracture to be predominantly transgranular mode. No grain growth is observed in both the samples. Fractography of TiB_2+10%$TiSi_2$ shows the absence of pores in the fully dense structure; whereas tiny pores can be seen in the TiB_2+2.5%$TiSi_2$ which has roughly 4% porosity.

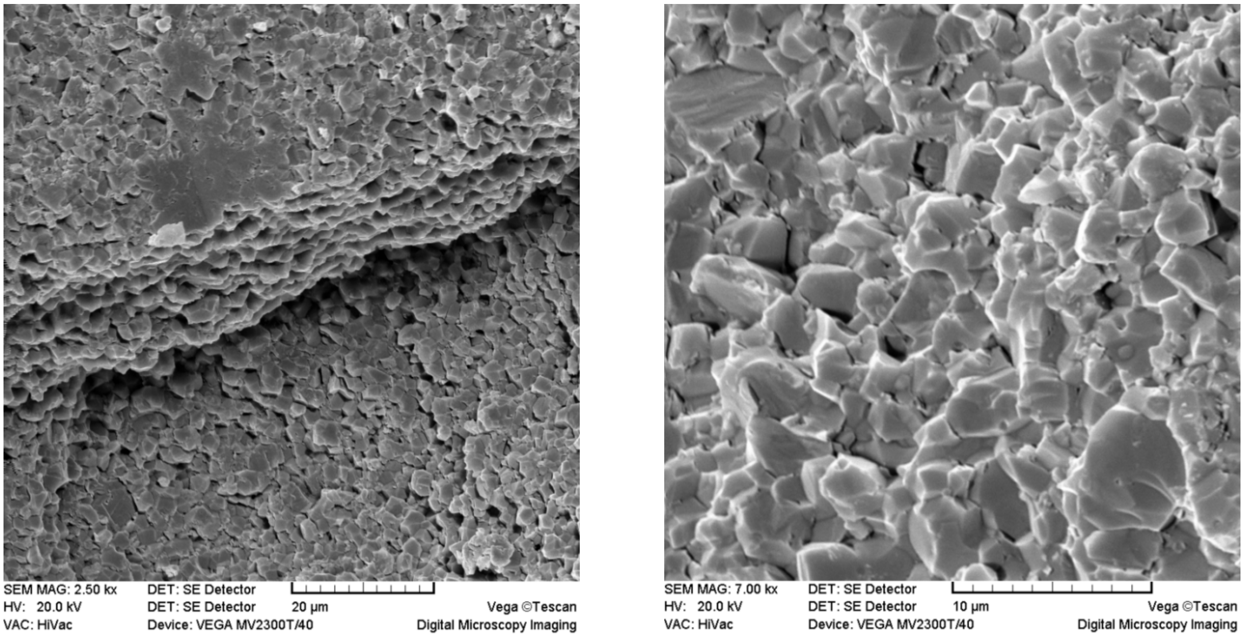

(a) **(b)**

Fig. 5.7 Fractography of a) TiB_2+2.5%$TiSi_2$ and b)TiB_2+10%$TiSi_2$ samples

5.3.2 TiB_2 + $CrSi_2$ composites

XRD patterns of the starting powder mixture and hot pressed TiB_2+10%$CrSi_2$ composite are shown in Fig.5.8. In the pellet, TiB_2 and $CrSi_2$ phases only are present indicating the absence of any reaction product. However, the intensities and number of $CrSi_2$ peaks are lower in the pellet as compared to the powder mixture. A small shift in location of TiB_2 peaks is also noticed in the pellet as compared to that of powder mixture. These observations indicate the formation of solid solution in the composite between TiB_2 and Cr. The increase in lattice parameters after hot pressing (c/a: from 1.033 to 1.066, c: from 3.158 to 3.222) also confirms the above. Origin of the Cr for the above solid solution formation is explained later.

Back Scattered Electron (BSE) image of TiB_2+10%$CrSi_2$ composite is presented in Fig. 5.9. This figure reveals three distinct phases; dark grey matrix, black and white phases.

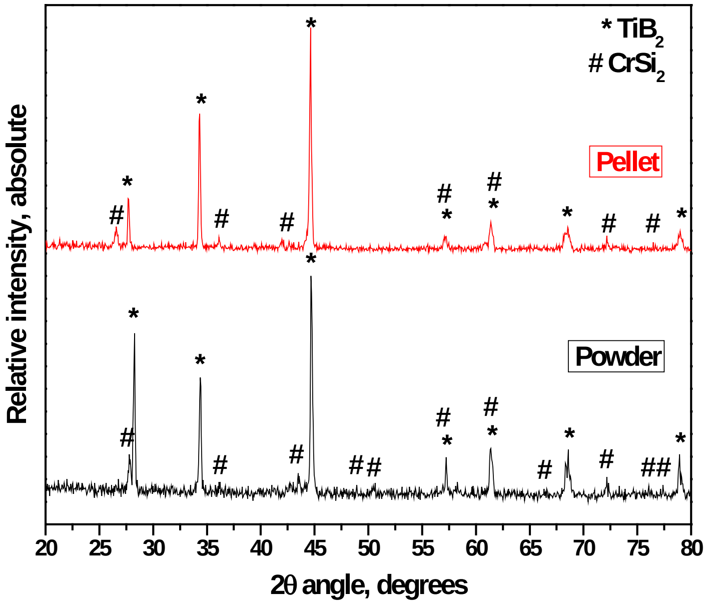

Fig. 5.8 XRD pattern of TiB_2+10%$CrSi_2$ powder and composite pellet. TiB_2 and $CrSi_2$ peaks only are seen in both

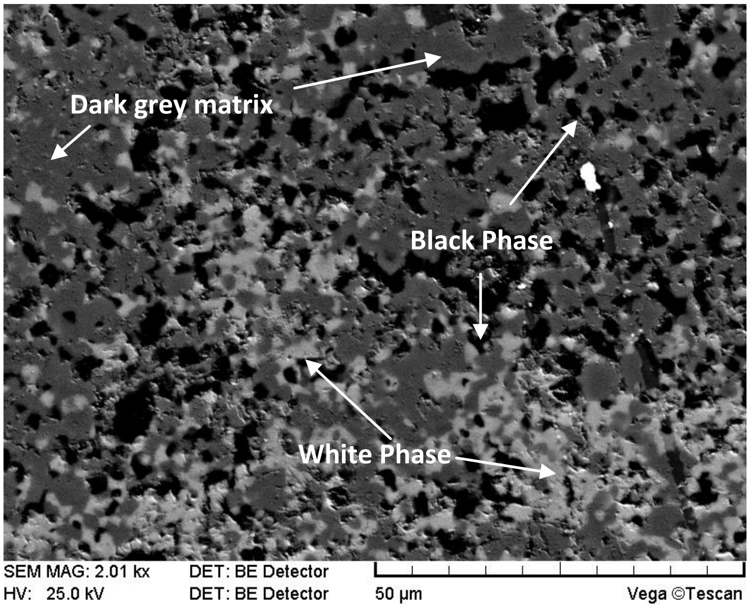

Fig. 5.9 Back Scattered Image of TiB_2+10%$CrSi_2$ composite show the presence of three different regions: dark grey matrix, white and black regions

Line scan for Ti, Si and Cr across the white and black phases are presented in Fig. 5.10. The black phase shows the presence of silicon only (Cr is absent) whereas Ti and Cr are present in white phase. BSE image and elemental mapping of all the three phases for titanium, silicon and chromium are presented in Fig. 5.11(a-d). Fig. 5.11 (b) shows the absence of Ti in the black phase, Fig. 5.11 (c) shows the presence of Si only in the black phase and Fig. 5.11 (d) uniform distribution of Cr in the whole region. The elemental distribution of Ti, Cr and Si indicate that Cr migrates to surrounding matrix leaving Si in the original position. Long streaks of black region in Fig.5.10 shows the flow of molten silicon (Melting Point of Si: 1687K), during hot pressing.

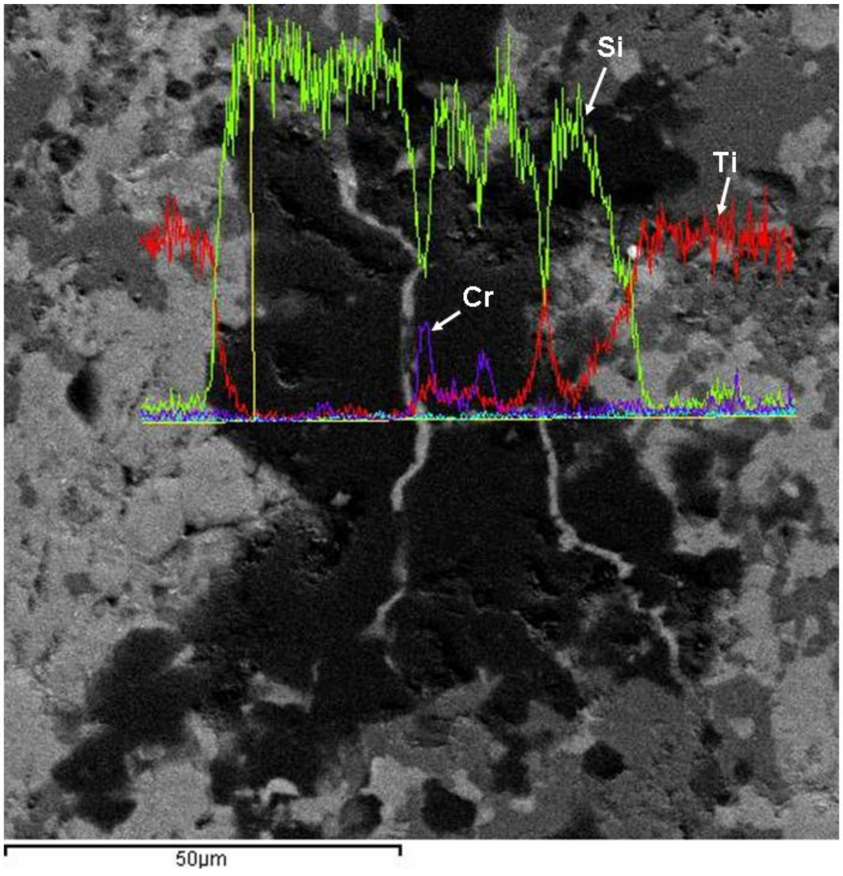

Fig. 5.10 Line scan across the white and black phases of TiB_2+10%$CrSi_2$ composite. Black phase rich in Si and white phase rich in Ti and Cr

The most probable reactions for the decomposition of $CrSi_2$ to other silicides with the formation of Si are given below and the free energy changes at 0.001 Pa for these reactions up to 2000K are presented in Fig. 5.12 [9]. All thermodynamic calculations were performed using FactSage software version 6.3 with the option of using most stable compounds data (solid/liquid/gas) at that particular temperature and pressure. For all the reactions the free energy values are more or less constant and positive till the melting point of $CrSi_2$. From the melting point free energy values are decreasing with temperature and for all the reactions becoming negative. Among all these reactions, reaction (5.1) is more negative at the hot pressing temperature of 1973K (1700^{o}C). This explains the formation of Si during hot pressing.

$CrSi_2 \rightarrow Cr + 2Si$ (5.1)

$CrSi_2 \rightarrow 1/3Cr_3Si + 5/3\ Si$ (5.2)

$CrSi_2 \rightarrow 1/5Cr_5Si_3 + 7/5\ Si$ (5.3)

$CrSi_2 \rightarrow CrSi + Si$ (5.4)

Fig. 5.13 presents the free energy of formation of CrB_2 and $CrSi_2$ with temperature. Formation of CrB_2 is more favorable compared to $CrSi_2$. This could explain the reason, why Cr from additive $CrSi_2$ is diffusing to TiB_2 matrix and confirmed by XRD analysis also.

SEM images of fractured surfaces of 5%$CrSi_2$ and 15%$CrSi_2$ composites are presented in Fig.5.14 (a & b). In 5% $CrSi_2$ composite, the major mode of fracture is seen as intergranular, whereas both intergranular and transgranular mode of fractures contribute equally in the failure of 10% $CrSi_2$ composite. No grain growth is observed in

$5\%CrSi_2$ composite (Fig. 5.14 a), whereas particle size is more in $15\%CrSi_2$ (Fig. 5.14 b), probably due to agglomeration caused by liquid Si. Both the samples show the presence of pores, more in the case of 15% composite. The formation of pores could be due to the evaporation of Si formed during the course of hot pressing, which was carried out under a vacuum of 0.001 Pa (10^{-5} m.bar). The vapor pressure of pure Si at the hot pressing temperature (1973K) is 1.01 Pa (1.01×10^{-2} m.bar) [10].

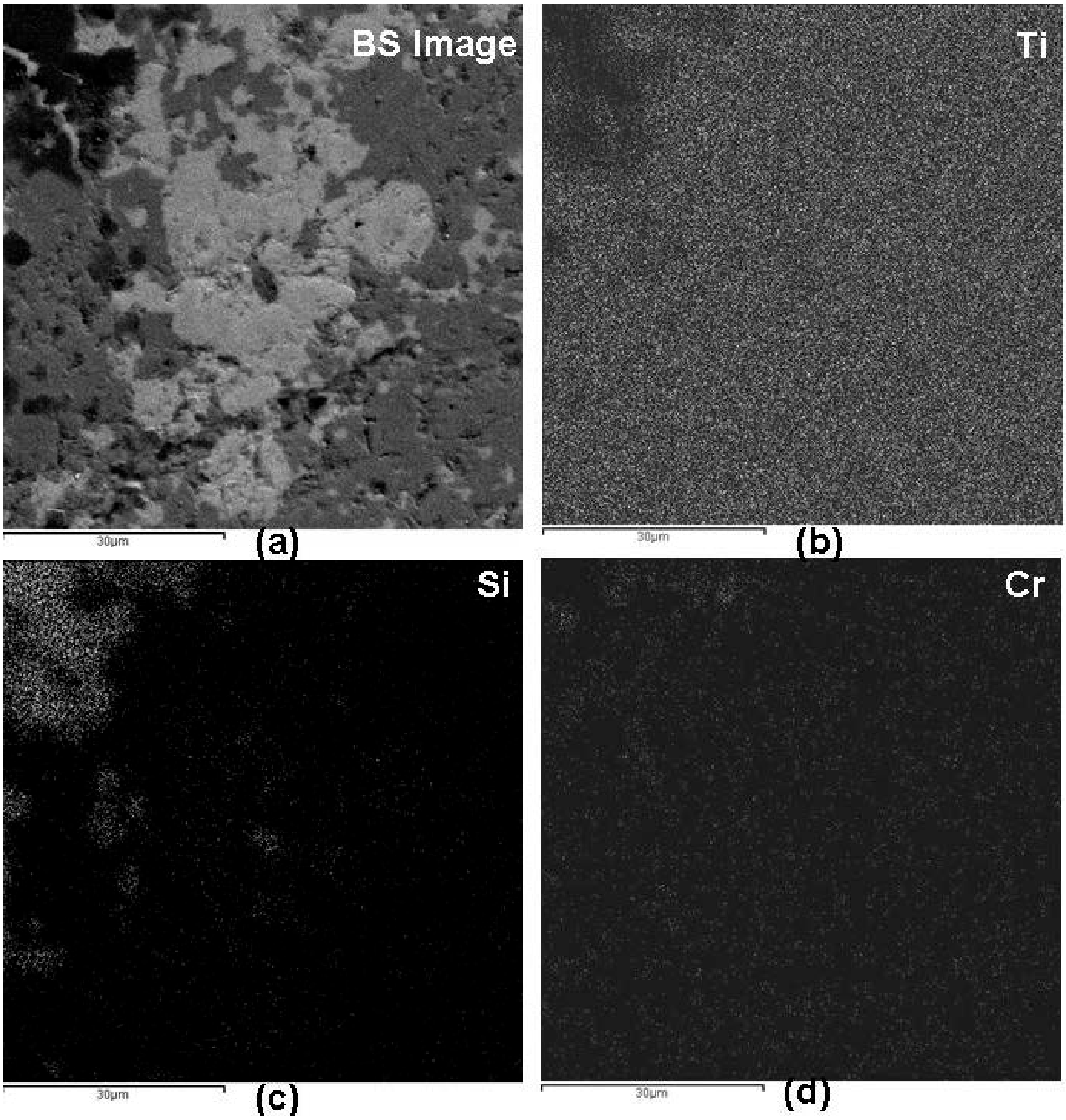

Fig. 5.11 Elemental mapping of $TiB_2+10\%CrSi_2$ composite (a) BS image and distribution of (b) Ti, (c) Si and (d) Cr in different phases

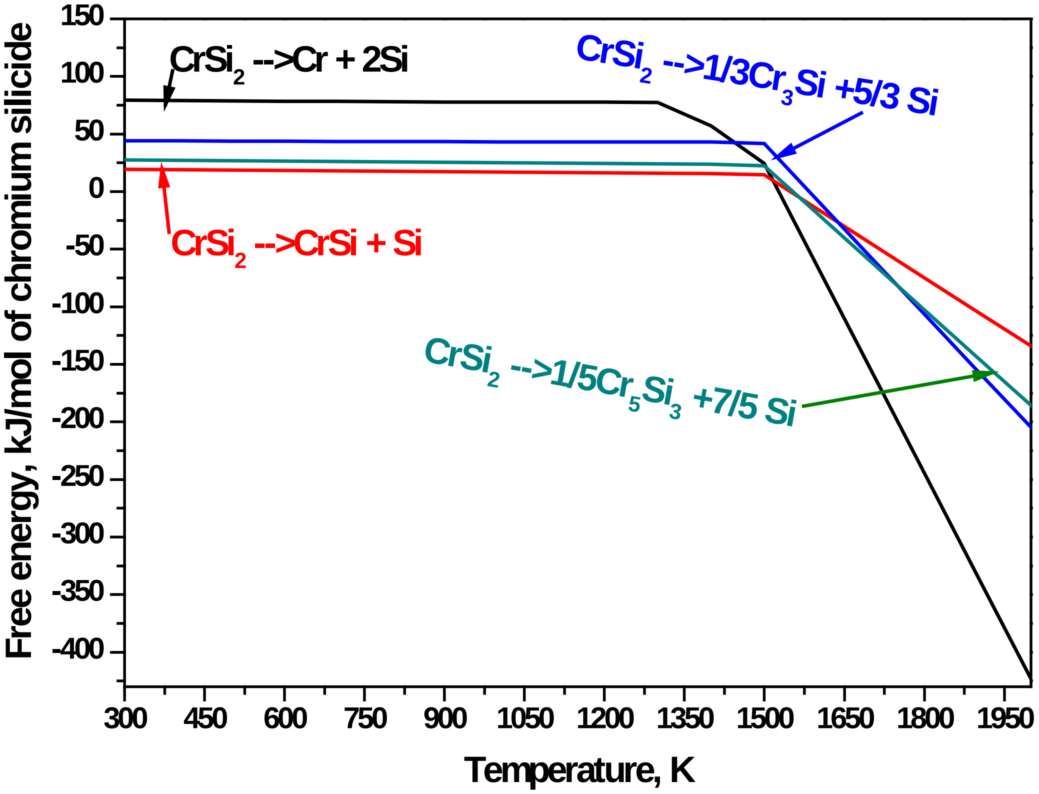

Fig. 5.12 Free energy change with temperature for $CrSi_2$ decomposition reactions with the formation of Si under 0.001Pa [9]

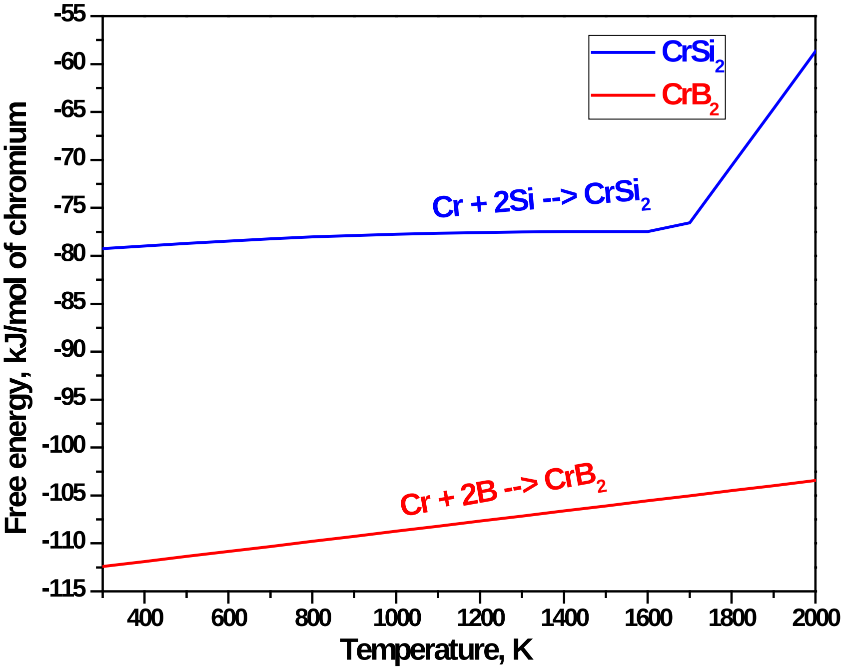

Fig. 5.13 Free energy vs. temperature curves for CrB_2 and $CrSi_2$ formation [9]

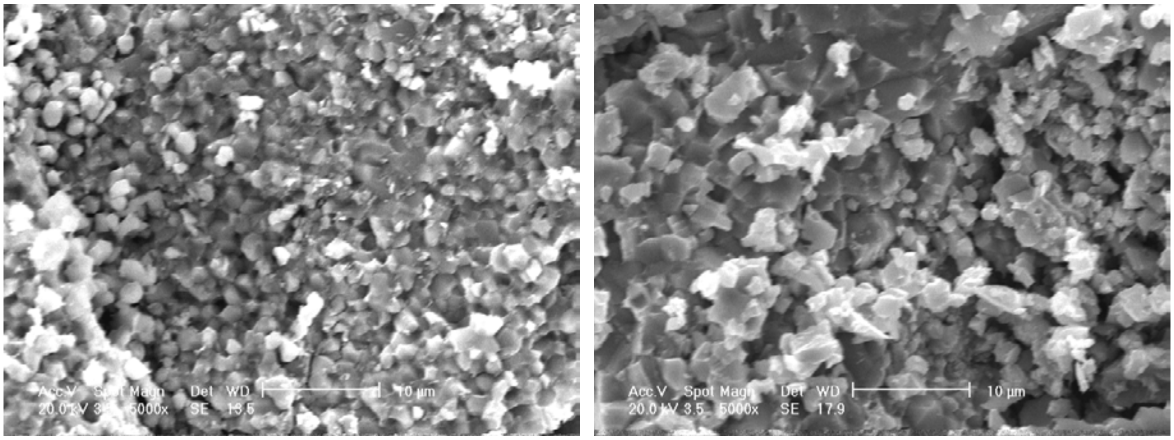

(a) **(b)**

Fig. 5.14 SEM images of fractured surface (a) TiB_2 +5% $CrSi_2$ and (b) TiB_2 +15% $CrSi_2$ composite

5.3.3 TiB_2 + WSi_2 composites

XRD patterns of the starting powder mixtures and hot pressed composites (5, 10 & 15% WSi_2) are shown in Fig.5.15. Starting powder mixtures showed the presence of Ti_6O_{11} in addition to TiB_2 and WSi_2 phases. Formation of Ti_6O_{11} could be due to the oxidation of TiB_2 while dry mixing or storage of powders. In this study, the TiB_2 powder was from the old stock; which was prepared a couple of months prior to the date of hot pressing. As a result some oxygen pick up took place during the storage due to fine size of powders. TiB_2, W_5Si_3 and SiO_2 phases are present in the densified pellet, indicating the formation of reaction products. The number of peaks and the intensity of W_5Si_3 and SiO_2 are seen to increase with increase in addition of WSi_2 from 5 to 15%. XRD results confirm the occurrence of sintering reactions, by consumption of WSi_2 phase and formation of W_5Si_3 and SiO_2 as reaction products.

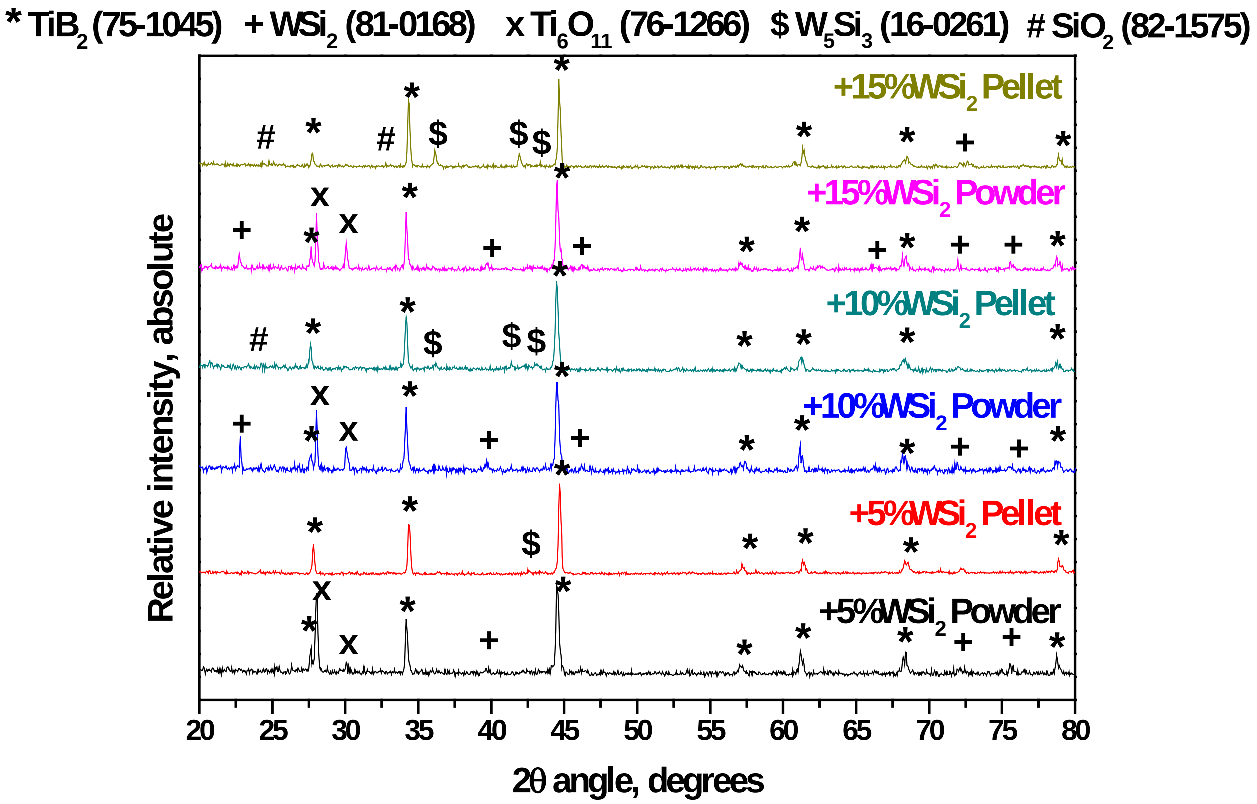

Fig.5.15 XRD patterns of staring mixtures and densified pellets of TiB$_2$+WSi$_2$ samples

Back Scattered Electron (BSE) image of TiB$_2$+10%WSi$_2$ sample is shown in Fig. 5.16a. This picture reveals two distinct phases; grey matrix and white regions. Line scan for Ti, Si and W across the grey and white phases are presented in Fig. 5.16 (b-d). The white phase shows the presence of silicon and tungsten whereas titanium in the grey phase. White, grey phases could be tungsten silicides and titanium boride respectively.

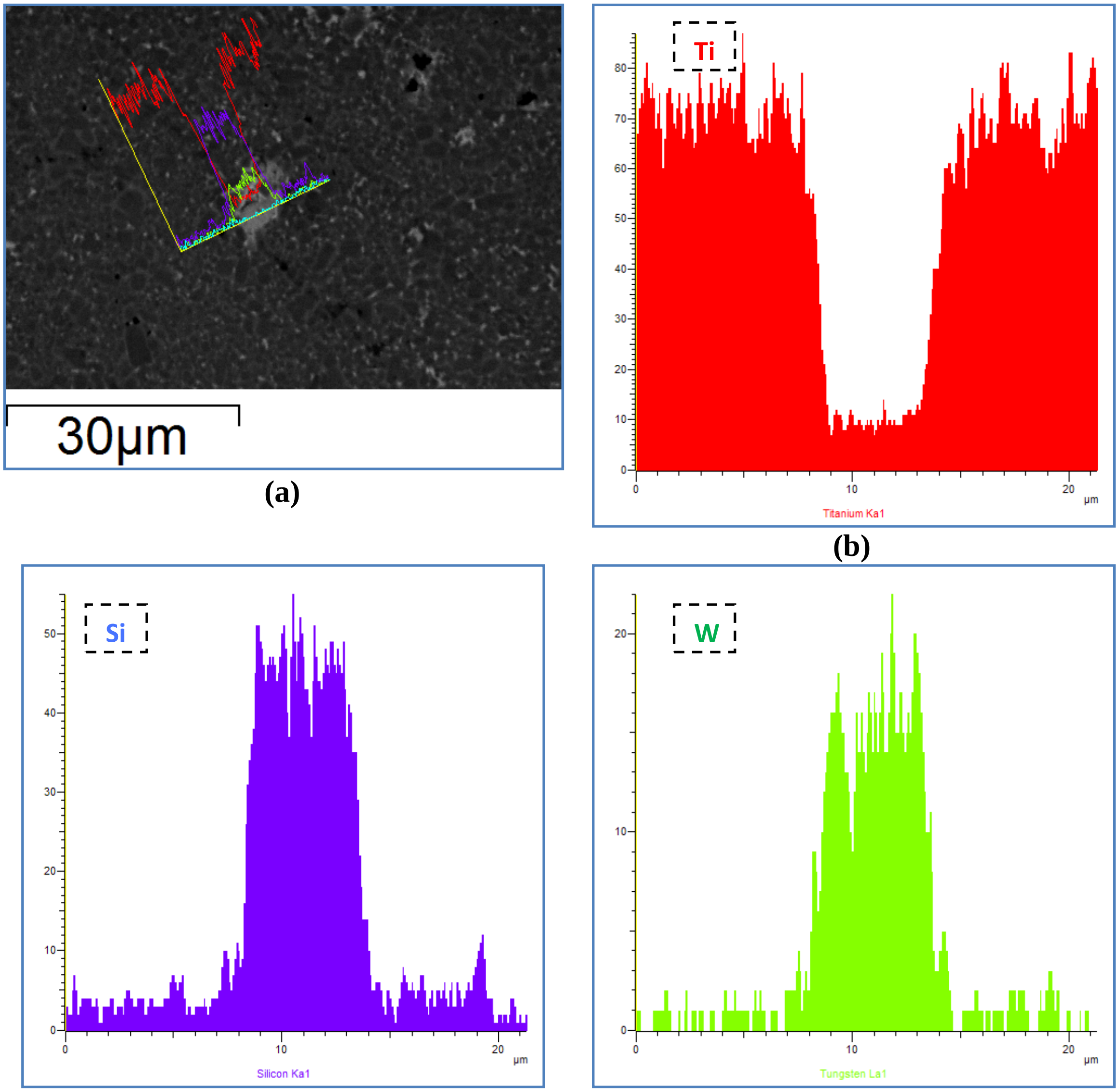

(a) **(b)**

(c) **(d)**

Fig. 5.16 a) Back Scattered Electron image of TiB_2+10%WSi_2 sample, Line scan across the white phase and matrix for different elements Ti (b), Si (c), W (d)

BSE image and elemental mapping of both phases for titanium, silicon and tungsten are presented in Fig. 5.17(a-d). Fig. 5.17 (b) shows the absence of Ti in the white phase, Fig. 5.17 (c) shows the presence of Si in the white phase and Fig. 5.17 (d) shows W in white phase.

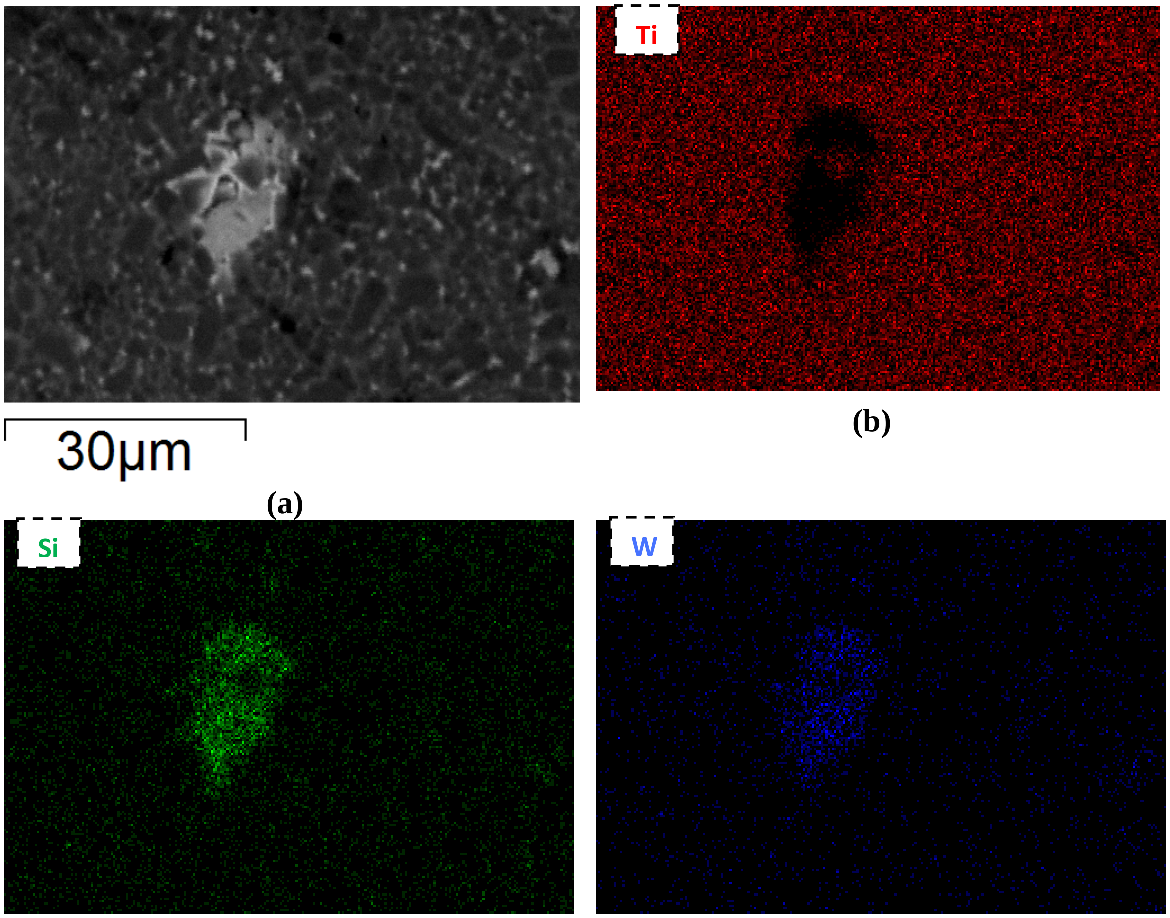

(b)

(a)

(d)

(c)

Fig. 5.17 a) Back Scattered Electron (BSE) image of TiB_2+10%WSi_2 sample, Elemental mapping of different elements Ti (b), Si (c), W (d)

The most probable reactions for the decomposition of WSi_2 and the formation of W_5Si_3 are given below. The probable reaction pathways involving different oxides (TiO_2 and B_2O_3) are also considered.

$5WSi_2 \rightarrow W_5Si_3 + 7Si$

(5.5)

$5WSi_2 + B_2O_3 + TiO_2 \rightarrow 5/2SiO_2 + TiB_2 + W_5Si_3 + 9/2Si$ (5.6)

$5WSi_2 + 7C \rightarrow W_5Si_3 + 7SiC$

(5.7)

$5WSi_2 + TiO_2 \rightarrow W_5Si_3 + SiO_2 + TiSi_2 + 4Si$

(5.8)

$5WSi_2 + 5TiO_2 + Si \rightarrow W_5Si_3 + 5SiO_2 + Ti_5Si_3$ (5.9)

$5WSi_2 + 5TiO_2 + C + 1/2Si \rightarrow W_5Si_3 + Ti_5Si_3 + 9/2SiO_2 + CO$ (5.10)

Based on the available thermodynamic data[9] on the free energy formation of different compounds, the overall free energy change (ΔG^o) for all the above reactions as written was calculated by using FactSage software version 6.3 at 0.001Pa and plotted as a function of temperature (Fig. 5.18). The data for the most stable compounds (solid/liquid/gas) at that particular temperature and pressure was used by the FactSage software. Sudden change in the slope of the lines is due to change of state of reactant/product. From the plots, it is clear that all the reactions are thermodynamically feasible at the hot pressing temperature of 1873K (1600^{o}C). Free energy change for reactions (5.6), (5.7) and (5.9) are negative and are therefore feasible even at room temperature. For example free energy change for equations (5.6), (5.7) and (5.9) at 1900K are -520.93, -146.08 and -234.26 kJ/mol respectively. Reaction (5.7) and (5.10) are also considered because TiB_2 powders contain a small amount of carbon and hot pressing is carried out in graphite dies where the powders are in direct contact with carbon. The Gibbs-free energy change of the reaction (5.10) is positive up to 1000K and becomes negative (ΔG_{10}= - 234.58 kJ/mol) above 1000K. From the above discussions, it is clear that the formation of W_5Si_3, SiO_2, Ti_5Si_3 and SiC are feasible during hot pressing. Presence of W_5Si_3 is confirmed by XRD but other phases couldn't be traced in

XRD. This could be due to either the amorphous nature of certain phases (SiO_2) or presence of these phases in small quantities. SiO_2 will exist in liquid phase at the hot pressing temperature (SiO_2 M.Pt.=1731K) of 1873K (1600° C).

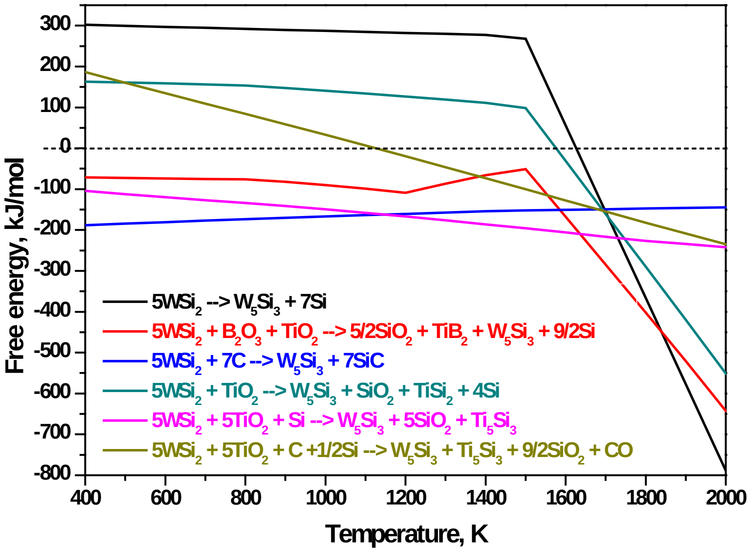

Fig.5.18 Plot showing the Gibbs free energy change of possible chemical reactions as a function of temperature at 0.001Pa [9]

SEM image of fractured surfaces of 2.5%WSi_2 and 5%WSi_2 composites are presented in Fig.5.19 (a & b). In both the composites (2.5% and 5% WSi_2), a mixed mode of fracture is seen. No grain growth is visible in 2.5%WSi_2 composite (Fig.5.19a), whereas particle size is comparatively larger in 5%WSi_2 (Fig.5.19b), probably due to agglomeration caused by liquid phases (SiO_2), which originated from reaction products. Both the samples show the absence of pores, indicating full densification.

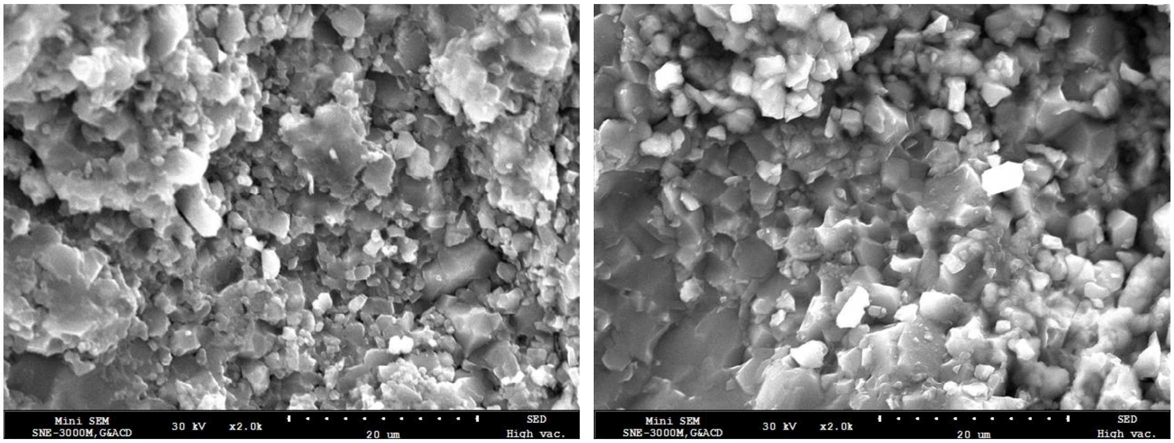

(a) **(b)**

Fig. 5.19 Fracture surfaces of TiB_2 specimens containing a) 2.5 wt% and b) 5 wt% of WSi_2

5.3.4 TiB_2 + CrB_2 composites

XRD pattern of starting powder mixture with 10%CrB_2 and hot-pressed specimen of the same composite are shown in Fig.5.20. Individual peaks of TiB_2 and CrB_2 are seen in the starting powder mixture, where as in hot pressed sample only TiB_2 peaks are visible. The disappearance of CrB_2 and a slight shift in the position of TiB_2 peaks clearly indicate the possibility of formation of solid solution.

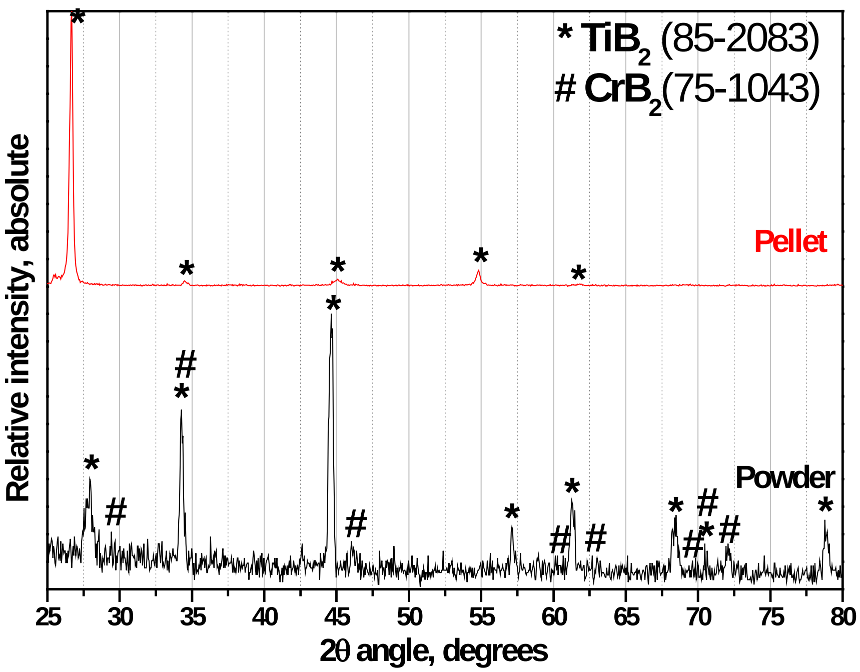

Fig .5.20 XRD of the starting powder mixture and dense pellet of TiB_2+10%CrB_2 composite

SEM image of the fractured surface of TiB_2+CrB_2 composite is shown in Fig.5.21 The average grain size of the composite is around 2-4 µm. Considering the starting particle sizes of TiB_2 (D_{50}~1.1 µm) and CrB_2 (D_{50} ~ 4.8 µm), this observation indicates the absence of grain growth. Topography of the fractured surface indicates the fracture to be a mixed mode of trans and intragranular. A few numbers of very fine pores are also visible.

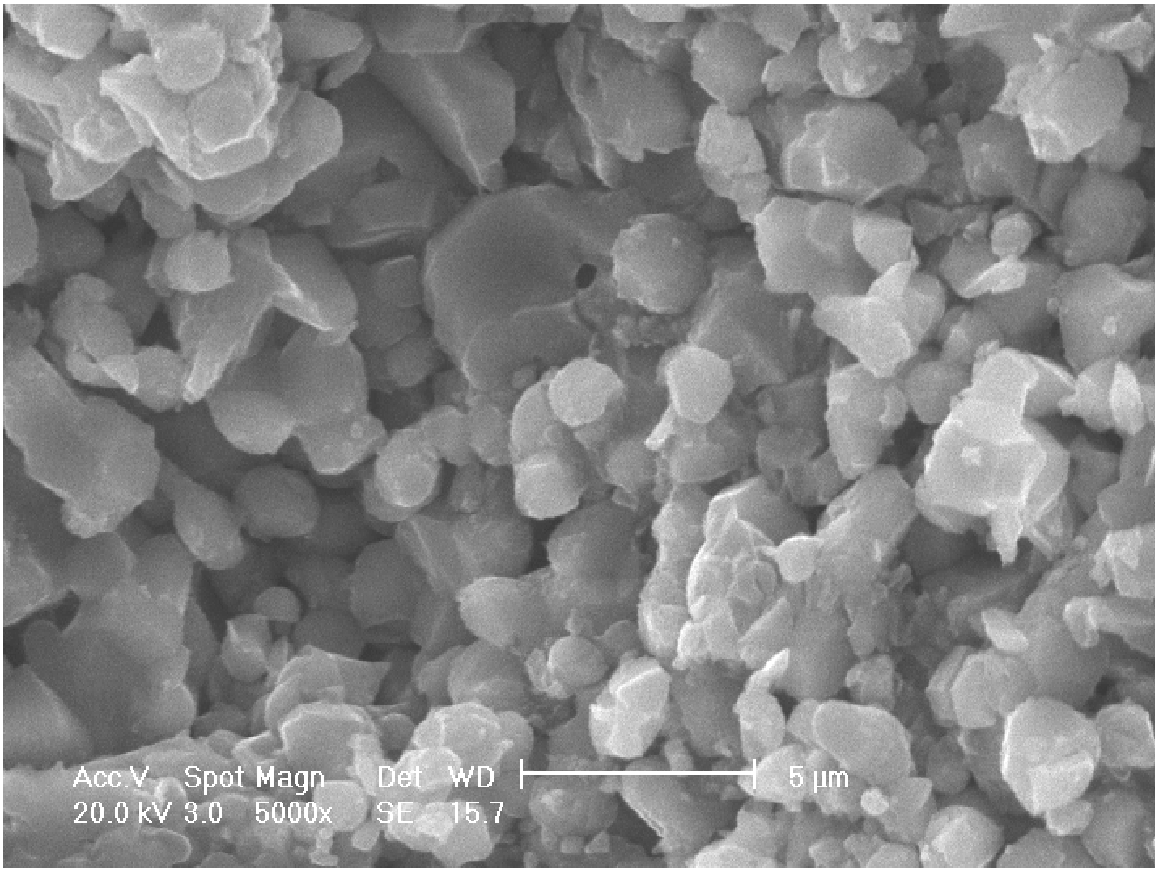

Fig.5.21 Fractography of TiB_2+10%CrB_2 composite: Fracture seen to be a combination of trans and intergranular modes

5.3.5 TiB_2 + 20%$MoSi_2$ + CrB_2 composites

XRD pattern of the hot pressed TiB_2+20%$MoSi_2$+15%CrB_2 composite is shown in Fig.5.22. TiB_2, $MoSi_2$, $Ti_5Si_3$and $TiSi_2$ phases were found in the pellet, indicating the occurrence of a reaction. CrB_2 peaks are absent in the pellet. The number and intensity of $MoSi_2$ peaks are also lower as compared to the powder mixture. A small shift in the location of TiB_2 peaks is also noticed in the pellet as compared to that of the powder mixture. These indicate the formation of solid solution of CrB_2 in TiB_2 in the composite. Formation of a similar reaction product ($TiSi_2$) has been observed in TiB_2+$MoSi_2$ composite [1,11] and formation of solid solution in the TiB_2+CrB_2 composite.

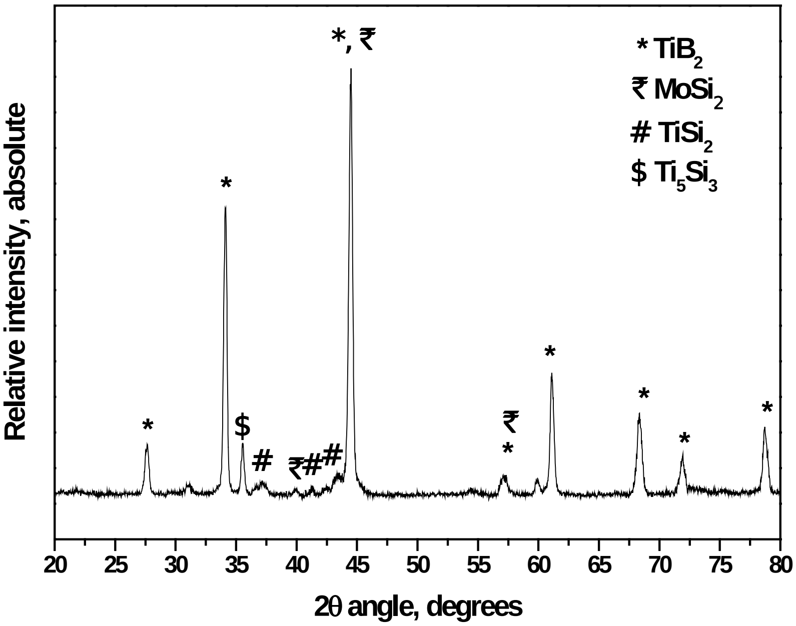

Fig. 5.22 Phase identification of hot pressed pellet of TiB_2+20%$MoSi_2$+15%CrB_2

SEM images of fractured surfaces of 5%CrB_2 and 15%CrB_2 composites are presented in Fig.5.23 (a & b). In 5% CrB_2 composite, the major mode of fracture is seen as transgranular, whereas both intergranular and transgranular modes of fractures contribute equally to the failure of 15% CrB_2 composite. No grain growth is observed in either of the composites.

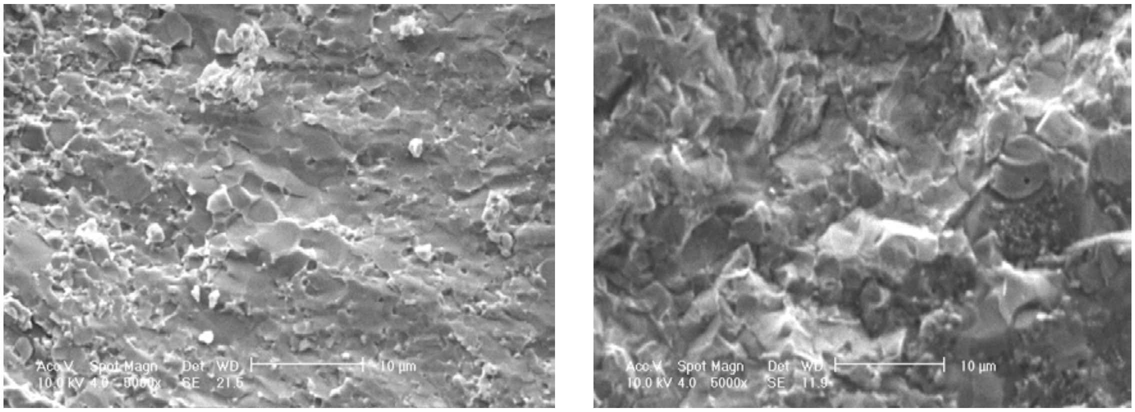

(a) **(b)**

Fig. 5.23 Fractured surfaces of a) TiB_2 + 20 wt.%$MoSi_2$ + 5 wt.%CrB_2 and b) TiB_2 + 20 wt.%$MoSi_2$ + 15 wt.%CrB_2 composites. (Fractured surfaces were obtained under an indentation load of 490N)

5.3.6 (TiCr)B_2+20%$MoSi_2$ composites

In Fig. 5.24 is presented the XRD pattern of hot pressed of $(Ti_{0.85}Cr_{0.15})B_2$ + 20%$MoSi_2$ samples. TiB_2 and $MoSi_2$ peaks are the major peaks. CrB_2 peaks were not identified in this sample. Location of CrB_2 peaks are marked in the Fig.5.24 for confirmation.

SEM images of fractured surfaces of $(Ti_{0.95}Cr_{0.05})B_2$ + 20%$MoSi_2$ and $(Ti_{0.90}Cr_{0.10})B_2$ + 20%$MoSi_2$ composites are presented in Fig.5.25 (a & b). Both intergranular and transgranular modes of fractures contribute equally in the failure of these composites. No grain growth is observed in either of the composites.

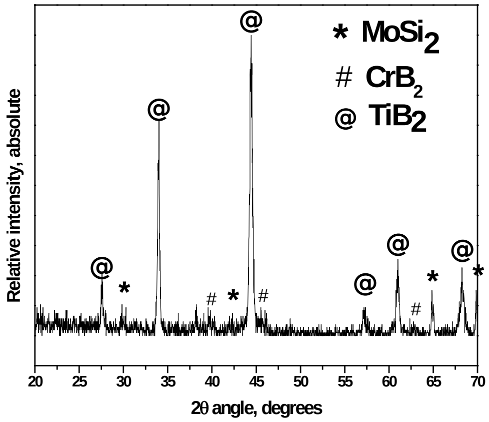

Fig. 5.24 Phase identification of hot pressed pellet of $(Ti_{0.85}Cr_{0.15})B_2$ +20%$MoSi_2$

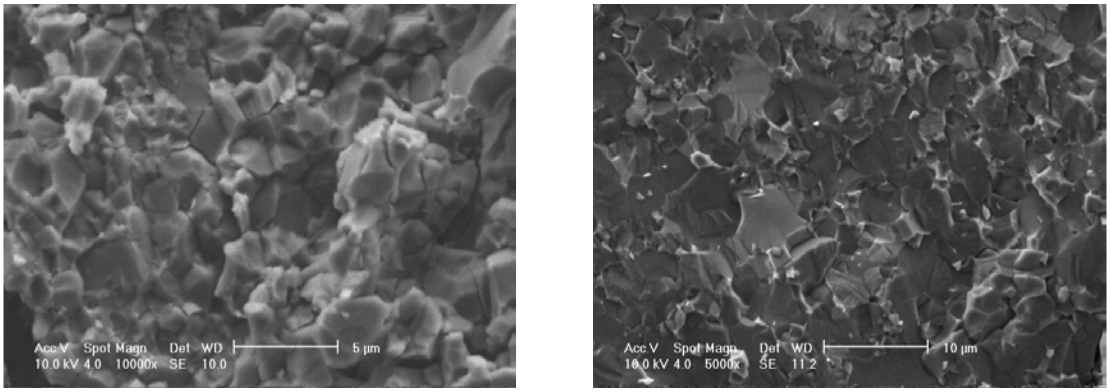

(a) **(b)**

Fig. 5.25 Fractured surfaces of a) $(Ti_{0.95}Cr_{0.05})B_2$ + 20%$MoSi_2$ and b) $(Ti_{0.90}Cr_{0.10})B_2$ + 20%$MoSi_2$ composites

$(Ti_{0.85}Cr_{0.15})B_2$+20% $MoSi_2$ composite was analyzed by EPMA. In this sample, three regions of interest were identified. They are the light grey matrix, dark grey and black phases (Fig 5.26). To identify the elements on these regions, spectrum was analyzed separately and it was found that the elements predominantly present in the matrix are Ti, Cr and B. Lighter regions contain Cr, Ti, Mo and B. Mo and Si are the only elements present in the dark patches. Quantitative analysis was done on the three identified regions to determine the chemical composition of the elements present, which are shown in Table 5.6.

Elemental mapping of the sample for Ti, Cr, Mo, B and Si and their overlay are shown in Fig. 5.27(b-g). Distribution of Ti, Cr and B in the matrix are shown in Fig.5.27 b, c and d respectively. These three elements appear to be uniformly distributed throughout the matrix. The qualitative analysis of these elements as seen by variation of brightness matches with the composition of the composite. Fig. 5.27e presents the overlay of Ti+B+Cr in the matrix, which confirms the uniform distribution of these three elements in the matrix. Fig.5.27f presents the distribution of silicon indicating that silicon is not uniformly distributed but present as clusters of 1-2 μm size in the matrix. Fig.5.27g shows the uniform distribution of Mo throughout the matrix. This clearly indicates that $MoSi_2$ has reacted with $(TiCr)B_2$. Mo has diffused and distributed in the matrix, leaving Si undisturbed. The white spots in Fig.5.27f indicate the location of original $MoSi_2$ particles. The elemental analysis of the polished surface very clearly indicates the presence of Ti, Cr, B and Mo uniformly distributed throughout the matrix and silicon was unevenly distributed and presented as clusters.

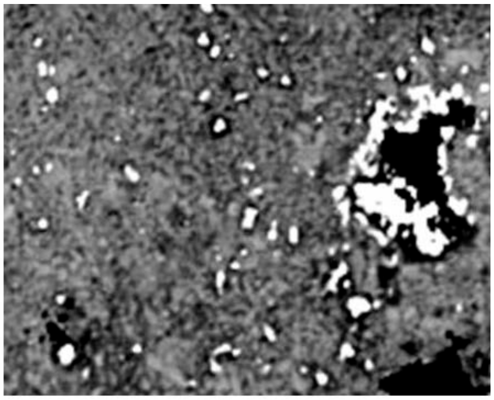

Fig. 5.26 Back scattered electron image

Table 5.6 Quantitative analysis of different phases

Element	Matrix	Light patches	Dark patches
Ti (wt.%)	59.74	3.31	0.08
B (wt.%)	33.17	17.77	0.00
Cr (wt.%)	3.68	54.48	0.82
Mo (wt.%)	3.46	26.31	61.38
Si (wt.%)	0.04	0.03	35.29

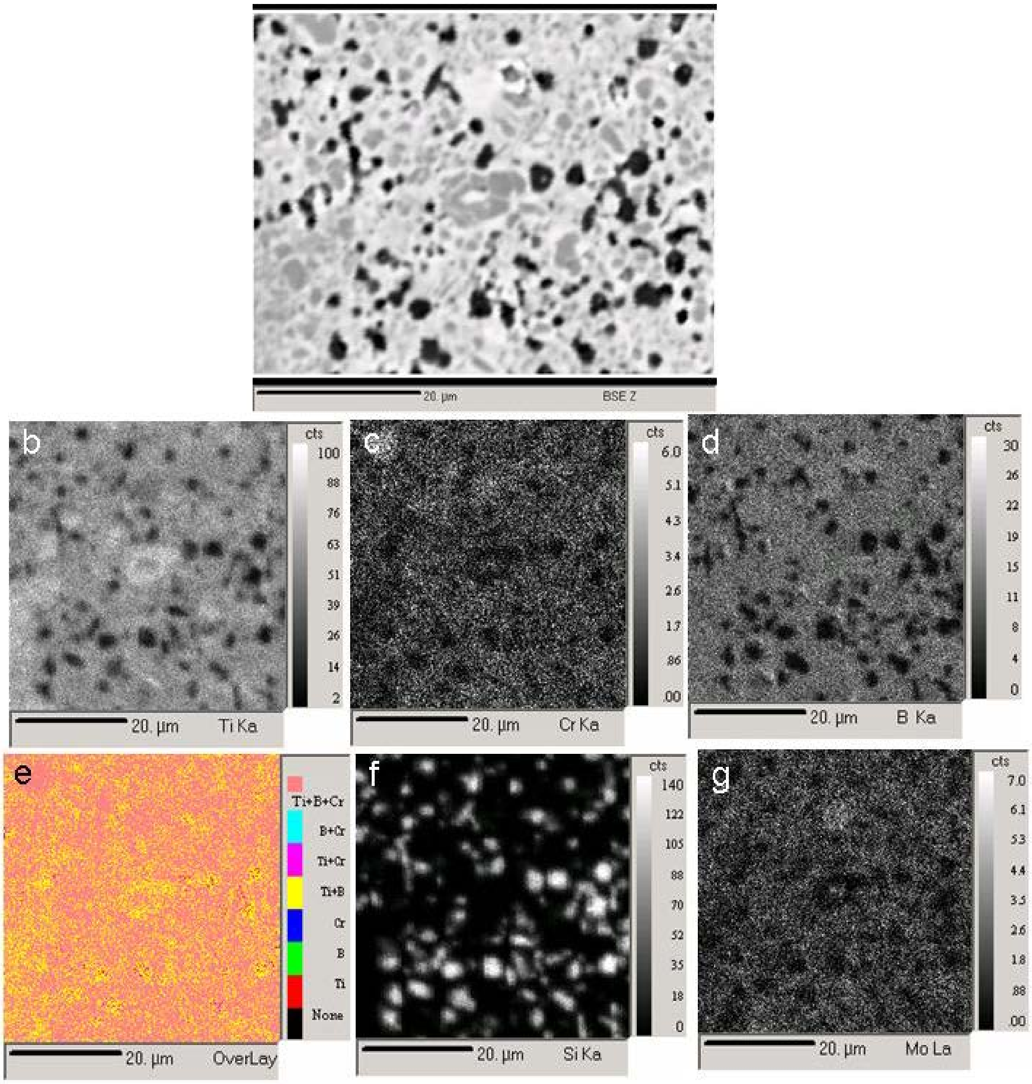

Fig. 5.27 Back scattered (BSE) image and elemental mapping of $(Ti_{0.85}Cr_{0.15})B_2$+20% $MoSi_2$

Line scan across different phases of the sample is shown in Fig. 5.28. Scan for Si indicates the non continuous presence of Si and wherever it is present the content is high. At these locations the contents of Ti, B, Cr and also Mo are comparatively low. Otherwise concentrations of these four elements are more or less constant throughout the region of line scan. Line scan analysis is in full agreement with the results of elemental mapping.

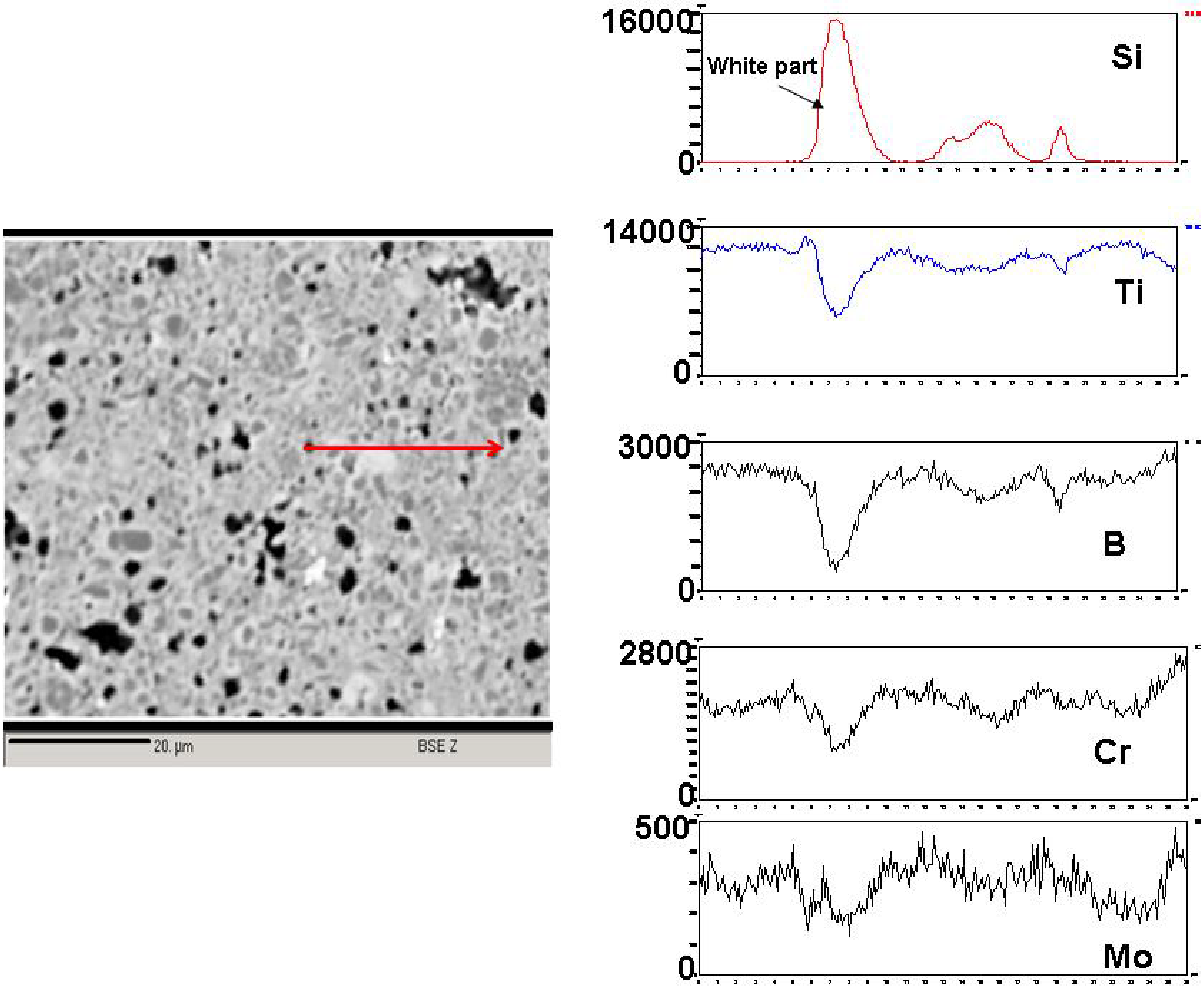

Fig. 5.28 Line scans across different phases of $(Ti_{0.85}Cr_{0.15})B_2$+20% $MoSi_2$

5.4 Mechanical and Physical Properties

Many of the composites in the present study are not reported in the open literature. Evaluation of mechanical and physical properties of these composite are very essential to know their potential for applications. Hardness and fracture toughness of all the composites were measured. The hardness is dependent on the density, nature of second phase and its quantity in the composite. Similarly the fracture toughness also depends on the above cited parameters. Physical properties like coefficient of thermal expansion (CTE), electrical resistivity were also measured in the temperature range of RT – 1273K (1000^{o}C). Important findings of the individual composites are given below:

5.4.1 TiB_2+$TiSi_2$ composites

Table 5.7 presents the hardness and fracture toughness of hot pressed samples. Increase in hardness with increase in density is as expected. With increased addition of $TiSi_2$ by 10wt%, (99% ρ_{th}) hardness is found to decrease to a value of 20.3±2.6 GPa. This decrease could be due to the presence of increased amounts of Ti_5Si_3 and $TiSi_2$ which have lower hardness values, in the range of 8-10 GPa.

Flexural strength of TiB_2+2.5%$TiSi_2$ was measured as 390±40 MPa at room temperature, which is in good agreement with that reported (~380 MPa) by Raju et.al [2]. Indentation fracture toughness of monolithic TiB_2 was calculated as 3.8 ± 1.5MPa.m$^{1/2}$, and those with the addition of $TiSi_2$ in the range of 4-6 MPa.m$^{1/2}$. Raju *et al*. [2] also have reported similar fracture toughness values for TiB_2+$TiSi_2$ composites. Fracture toughness of TiB_2 composite with $MoSi_2$ [1] is reported in the range of 4-5 MPa.m$^{1/2}$. The improvement of strength by the incorporation of particles of another phase is usually accompanied by an increase in fracture toughness due to crack deflection, microcracking and crack impediment [12]. Fig.5.29 presents the picture of TiB_2+$TiSi_2$ composite with clear crack deflection and crack branching mechanisms developed under an indentation load of 196 N (20 kg). These mechanisms are responsible for the marginally higher toughness (4-6 MPa.$m^{1/2}$) values recorded for TiB_2+$TiSi_2$ composites compared to monolithic TiB_2.

Table 5.7 Relative density, Hardness and fracture toughness of TiB_2+$TiSi_2$ composite

% $TiSi_2$	Relative Density (%)	Hardness Vickers, GPa	K_{IC}, MPa.$m^{1/2}$
2.5	96	18.1 ± 2.4	5.3 ± 1.5
5	99	25.1 ± 2.5	4.7 ± 1.1
10	99	20.3 ± 2.6	6.3 ± 0.6
0*	98	26.0 ± 1.0	5.1 ± 0.7

* hot pressed at 2073K (1800^{o}C)[1]

Variation of CTE with increasing temperature upto 1073K (800^{o}C) is plotted in Fig.5.30. Coefficient of thermal expansion (CTE) of TiB_2+2.5%$TiSi_2$ composite was measured as 6.9 x 10^{-6} K^{-1} in the temperature range of 298 to 1073K. Theoretical CTE values of monolithic TiB_2, $TiSi_2$ and Ti_5Si_3 are 7.3, 10.4 and 10.8 x 10^{-6} K^{-1} respectively in the temperature range of 298 to 1273K. In the present TiB_2+2.5%$TiSi_2$ composite's CTE value closely matches with the CTE of monolithic TiB_2.

Electrical resistivity of TiB_2 + 2.5 %$TiSi_2$ composite up to 1273K (1000^{o}C) is shown in Fig.5.31. The value of resistivity is measured as 20.69, 62.14 and 100.84 μΩ–cm at room temperature (RT), 773 and 1273K (500 and 1000^{o}C) respectively. Raju *et.a*l[2] have reported a value of 10.96 μΩ–cm at room temperature for similar composite. Electrical resistivity of the monolithic TiB_2 has been reported to be in the range of 7 to 15 μΩ–cm at RT depending on the purity and method of preparation [13-15]. Lower density (96% TD) of our sample and finer grain size could be the reasons for higher electrical resistivity value in the TiB_2 + 2.5 %$TiSi_2$ composite.

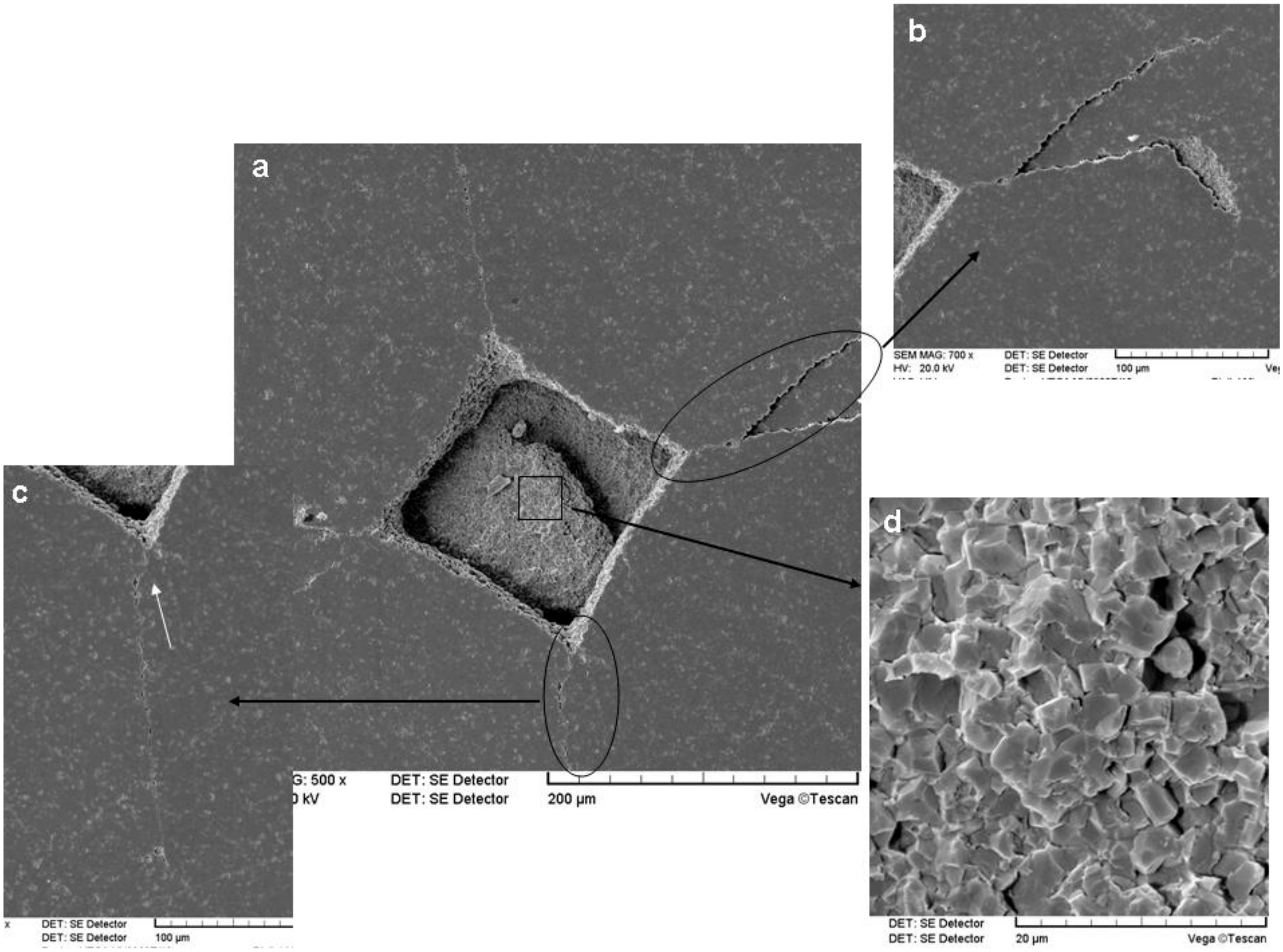

Fig. 5.29 Crack deflection and crack branching observed in TiB_2+$TiSi_2$ composite a) Overview of vickers indentation pattern with edge cracks, b & c) crack propagation pattern, d) fractography

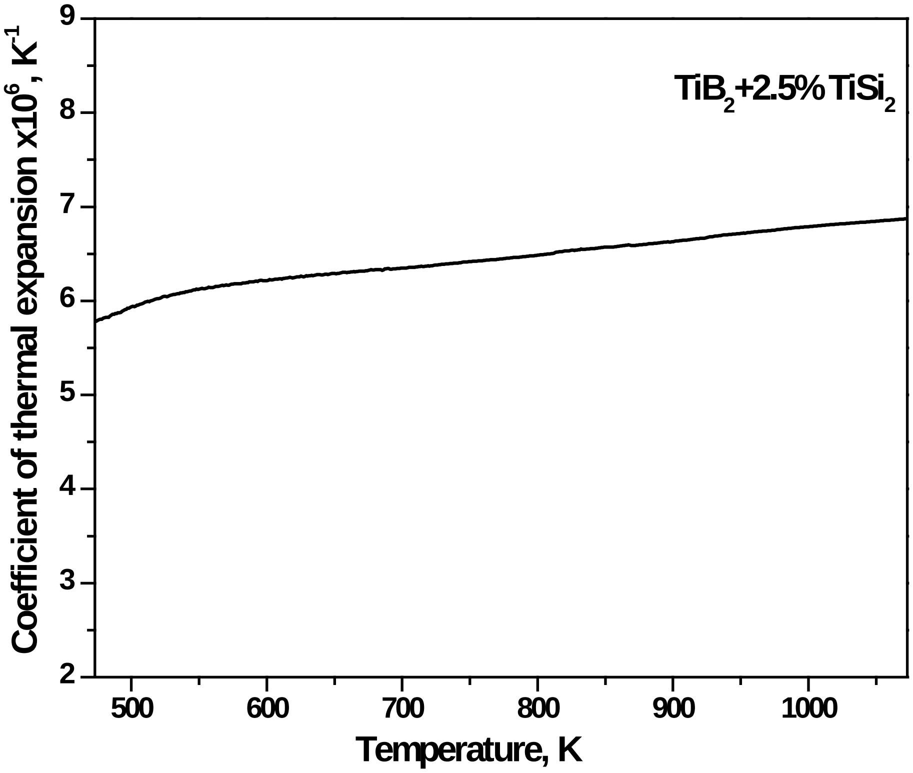

Fig. 5.30 Coefficient of thermal expansion with temperature

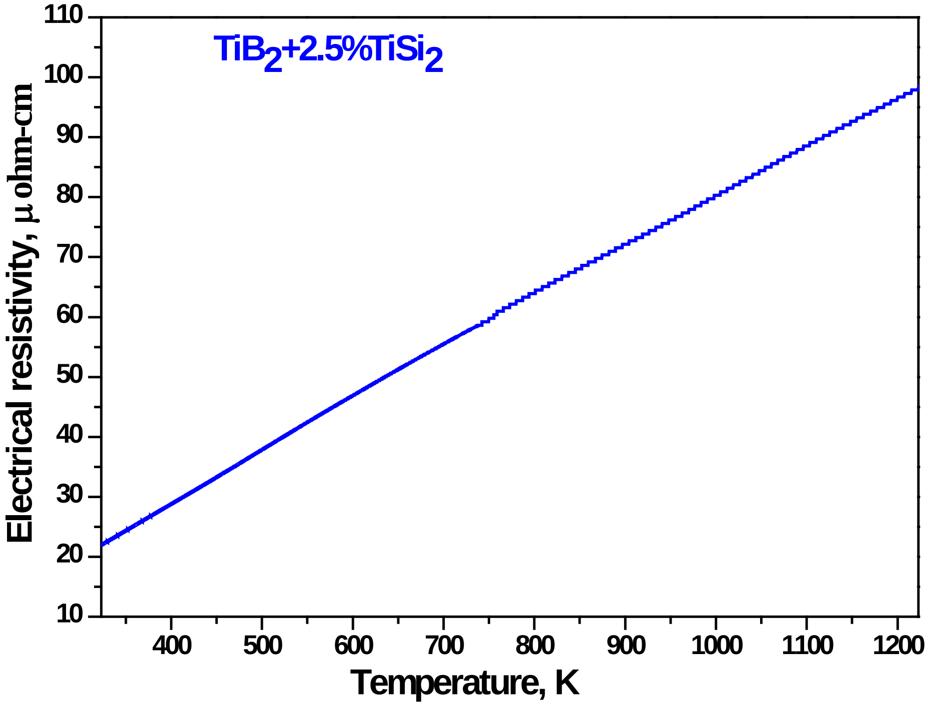

Fig. 5.31 Electrical resistivity of TiB_2 + 2.5 %$TiSi_2$ composite with temperature

5 4.2 TiB_2 + $CrSi_2$ composites

Hardness and fracture toughness of hot pressed samples are presented in Table 5.1. Variation of density, hardness and fracture toughness of TiB_2 composite with $CrSi_2$ are also presented in Fig 5.32. The micro hardness value of composite with 2.5% $CrSi_2$ (99.89% TD) was 29±2 GPa. With increased addition of $CrSi_2$ the hardness decreased linearly and the hardness of composites with 5%, 10% and 15% $CrSi_2$ were measured as 28 ± 3, 26 ±2 and 22±3 GPa respectively. This decrease in hardness is due to the decrease in density and also the presence of increased amount of $CrSi_2$ and Si, both are having lower hardness value of ~11 GPa. Flexural strength of TiB_2+5%$CrSi_2$ was measured as 200±50 MPa which is much lower compared to that of TiB_2 (300 to 600 MPa). Indentation fracture toughness of TiB_2 +2.5% $CrSi_2$ was calculated as 5.97 ± 0.61 $MPa.m^{1/2}$, which decreased to 3.41±0.94 $MPa.m^{1/2}$ with increased addition of 15% $CrSi_2$.

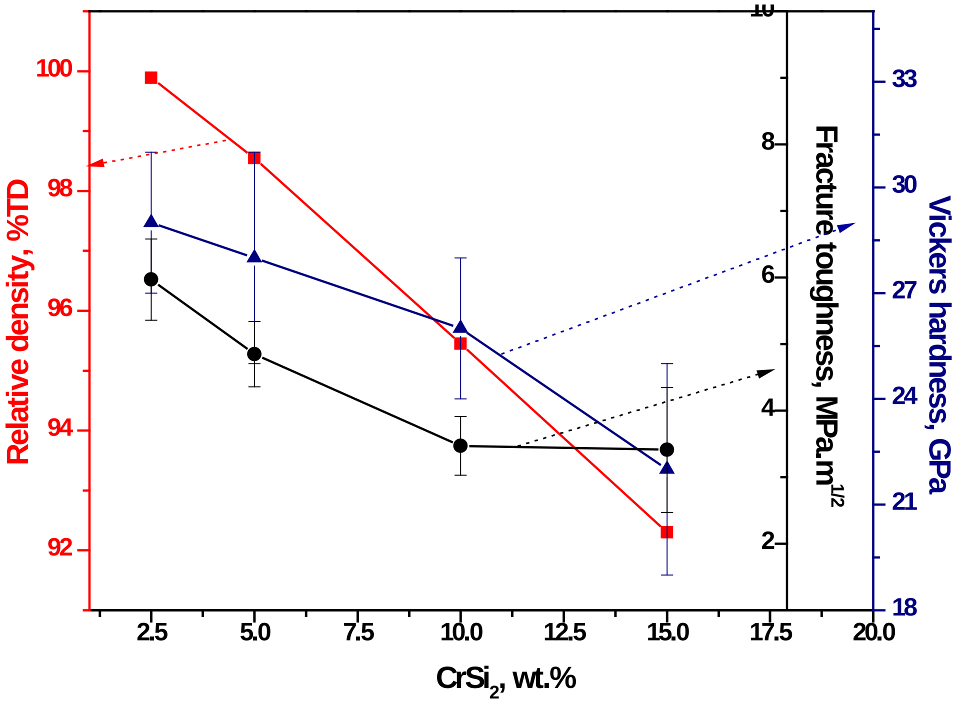

Fig. 5.32 Variation of density, hardness and fracture toughness of TiB_2 + $CrSi_2$composite (line joining points are for visual aid only)

Fig.5.33(a & b) presents the image of TiB_2+2.5%$CrSi_2$ composite indicating clear crack branching, deflection and bridging mechanisms developed under an indentation load of 196 N (20 kg). These mechanisms are responsible for the observed higher toughness (5.97 ± 0.61 $MPa.m^{1/2}$) value of this composite.

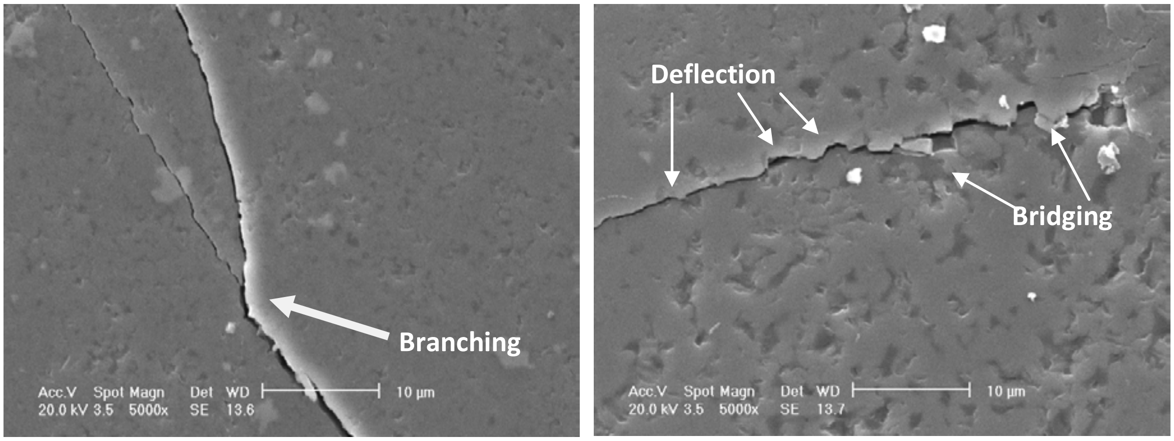

(a) (b)

Fig.5.33 SEM image of TiB_2 + 2.5% $CrSi_2$ composite showing a) Crack branching and b) Deflection and bridging

Variation of CTE and electrical resistivity of TiB_2 + 5% $CrSi_2$ composite with temperature up to 1173K (900^{o}C) are plotted in Fig. 5.34. CTE value was measured as 7.1 x 10^{-6} K^{-1} in the range of RT to 1173K. These values are slightly lower than theoretical values of monolithic TiB_2 (7.3 x 10^{-6} K^{-1}) and $CrSi_2$ (8.6 x 10^{-6} K^{-1}), which could be due to the presence of Si phase which has a low CTE value of 4.19 x 10^{-6} K^{-1} [16]. Electrical resistivity of the composite was measured as 47.45, 84.8 and 133 $\mu\Omega\cdot$cm at 473, 773 and 1173K (200, 500 and 900^{o}C) respectively. It is observed that coefficient of resistivity is increasing linearly with the increase of temperature. Electrical resistivity of the monolithic TiB_2 has been reported to be in the range of 7 to 15 $\mu\Omega\cdot$cm at RT depending on the purity and method of preparation[13,15]. Resistivity of polycrystalline

TiB_2 varies between 10 to 40 μΩ·cm at room temperature and up to 40 - 80 μΩ·cm at 1173K (900°C)[14]. Lower density (98% TD) and finer grain size of our sample could be the reasons for higher electrical resistivity value. Grain boundaries and pores will be the barriers/obstacles for free flow of electrons.

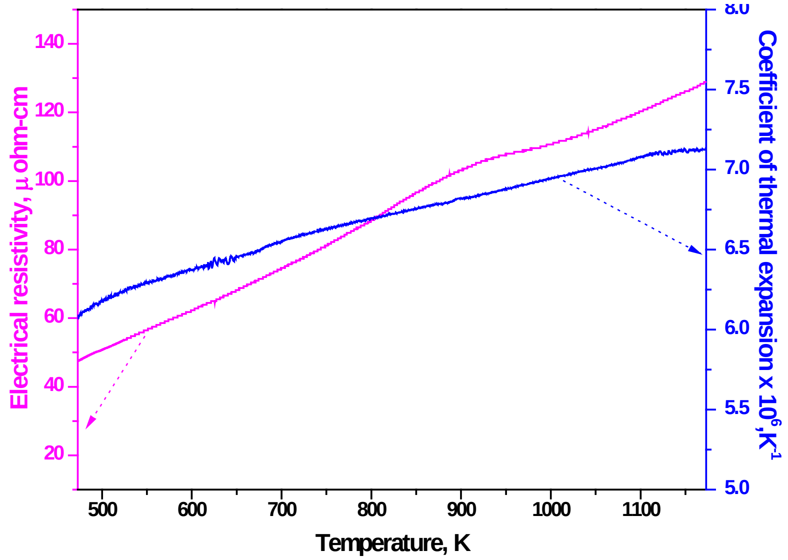

Fig. 5.34 Electrical resistivity and coefficient of thermal expansion of TiB_2 + 5% $CrSi_2$ composite measured in inert (argon) atmosphere

5.4.3 TiB_2 + WSi_2 composites

Micros hardness and fracture toughness of hot pressed samples are presented in Table 5.2. Micro hardness values of the composite with varying WSi_2 were measured to be in the range of 24-26 GPa. Fracture toughness was moderately higher in the range of 4-6 $MPa.m^{1/2}$ compared to 3-4 $MPa.m^{1/2}$ for monolithic TiB_2. Fig. 5.35 presents the image of TiB_2+10%WSi_2 composite indicating clear crack bridging and slight deflection mechanisms developed under an indentation load of 196 N (20 kg). These mechanisms are responsible for the recorded higher toughness value of this composite.

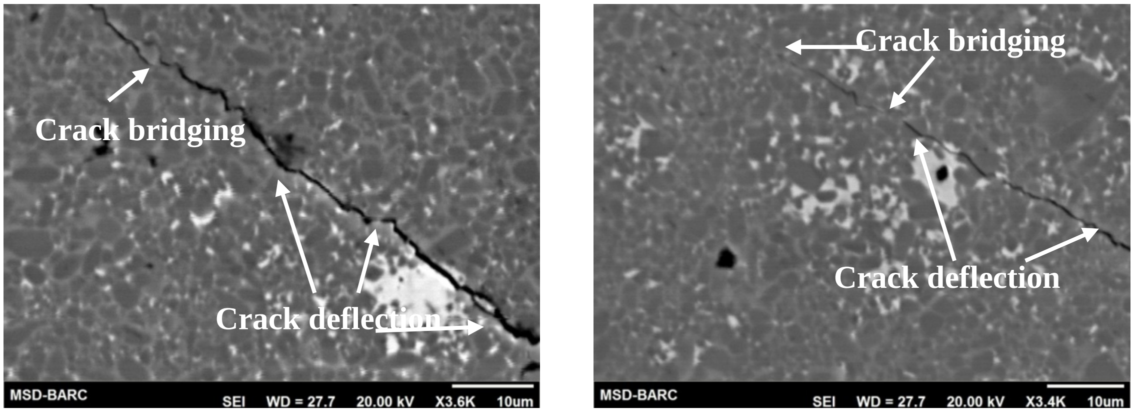

(a) **(b)**

Fig. 5.35 Crack propagation patterns of TiB_2+10%WSi_2 composites a&b) crack bridging & deflections

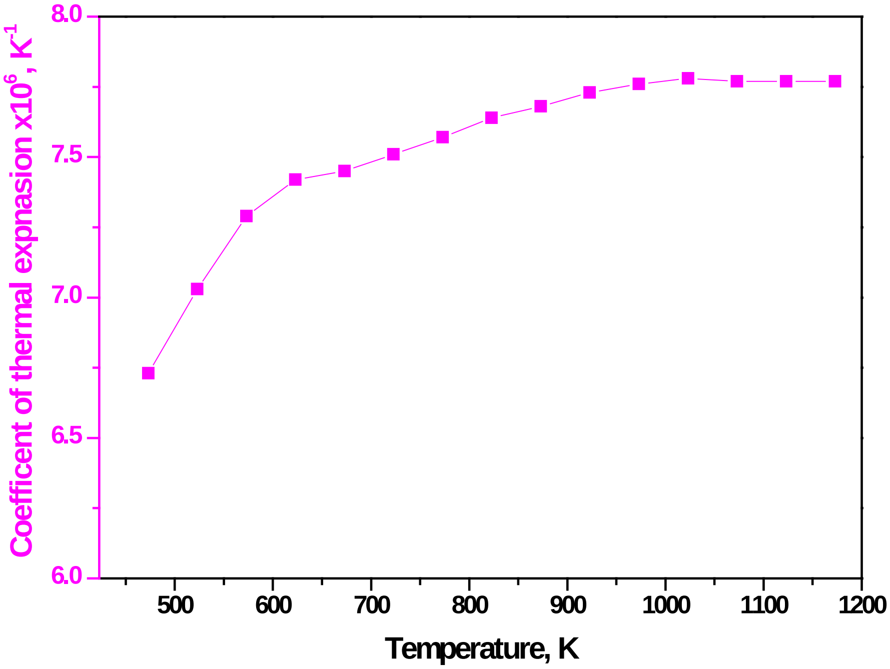

Fig. 5.36 CTE vs. temperature plot of TiB_2+15%WSi_2 composite, measured in inert atmosphere (line joining points are for visual aid only)

Variation of CTE of TiB_2 +15 %WSi_2 composite with temperature up to 1173K (900°C) is plotted in Fig. 5.36. CTE value was measured as 7.7 x 10^{-6} K^{-1} in the range of RT to 1173K. These values are in between the theoretical values of monolithic TiB_2 (7.3 x 10^{-6} K^{-1}) and WSi_2 (8.5 x 10^{-6} K^{-1}).

5.4.4 $TiB_2 + CrB_2$ composites

Table 5.3 presents the hardness and indentation fracture toughness values of the hot pressed samples. Hardness values of all the composites are close to 24 GPa. This value is marginally lower as compared to that reported by Holcombe *et al* [5]. They had obtained a value of 28.9 and 27.0 GPa for TiB_2 with 3% CrB_2, with a density of >95% prepared by microwave sintering at higher temperatures of 2173K (1900^{o}C) and 2373K (2100^{o}C) respectively. Konigshofer *et al.*[6] have reported a higher micro hardness of 35 GPa for a TiB_2 composite with 0.5% CrB_2, with a density of 99% TD prepared by hot pressing at 2073K (1800^{o}C) and 45MPa pressure. Average indentation fracture toughness of 2.5, 5 and 10% composites were measured as 2.80±0.13, 4.30±0.38 and 4.99±0.99 $MPa \cdot m^{1/2}$ respectively. Holcombe et al.[5] have reported a toughness value of 6.24 $MPa \cdot m^{1/2}$ (using Evans method). The reason for lower hardness and fracture toughness of our samples are given below. The samples in the present investigation were prepared at a lower temperature of 1973K (1700^{o}C) compared to others. The hot pressing pressure used in the present study also is lower at 30 MPa compared to 45 MPa by Konigshofer *et al* [6]. Holcombe *et al.*[5] have used microwave heating for densification, by which enhanced densification and finer microstructures can be obtained due to uniform and rapid heating, as the energy is directly coupled into the specimen rather than being conducted from an external heat source.

Vickers indentation with crack pattern of TiB_2 + 2.5% CrB_2 composite and the crack propagation are presented in Fig. 5.37. The crack line appears to be fairly straight, indicating low fracture toughness of the material. Flexural strength (3-point) of TiB_2 +

10% CrB_2 was measured as 275±20, 315±15 and 255±10 MPa respectively at room temperature, 773 and 1273K (500 and 1000^{o}C). These values are lower than that of monolithic TiB_2 and the composite (99% TD) with 0.5% CrB_2 [6]. Room temperature flexural strength of hot pressed CrB_2 is only 207 MPa [17]. Lower density (~95% TD) and higher amount of CrB_2 (10%) could be the reasons for lower value of flexural strength of this composite. It is known that pores lead to initiation of cracks and this degrades the strength [18]. A small increase in flexural strength value from room temperature to 773K (500^{o}C) and retention of strength at 1273K (1000^{o}C) could be attributed to the relief of internal stresses, which arise from the anisotropic thermal expansion of microstructural constituents [18]. However, at 1273K (1000^{o}C), oxidation of the sample could be the reason for lowering of strength.

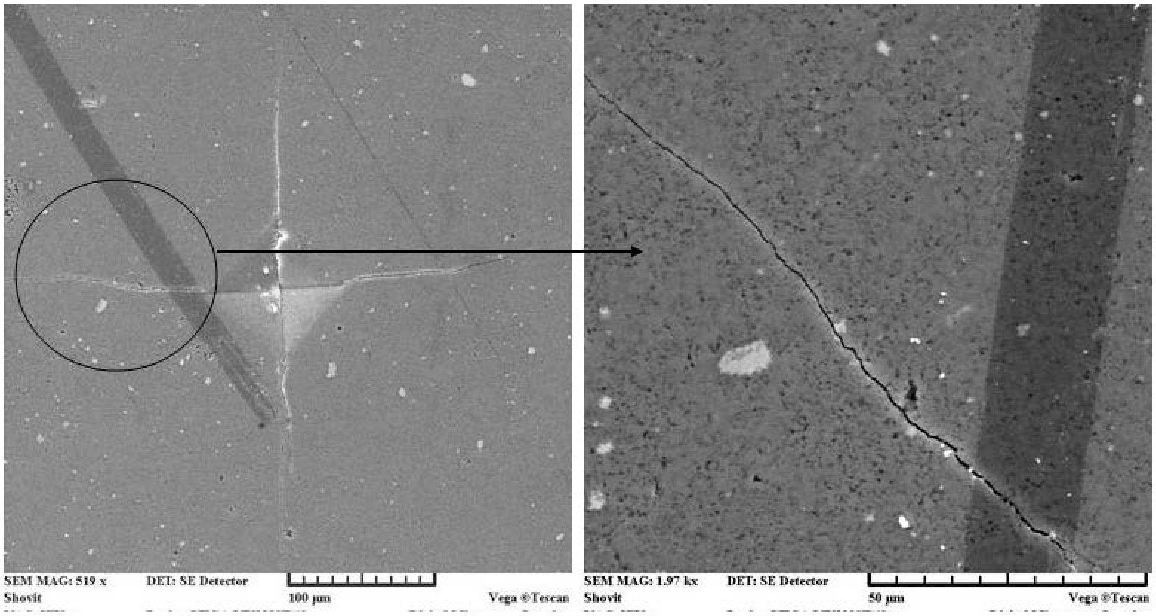

(a) (b)

Fig. 5.37 (a) Vickers indentation with crack pattern and (b) crack propagation line of TiB_2+ 2.5%CrB_2 composite

Variation of CTE with temperature upto 1273K (1000°C) is plotted in Fig.5.38 for TiB_2 + 10% CrB_2 composite. The CTE value in the range of RT to 1273K was 7.4 x 10^{-6} K^{-1}. These values are close to the theoretical values of monolithic TiB_2 (7.3 x 10^{-6} K^{-1}) and CrB_2 (7.0 x 10^{-6} K^{-1}). Electrical resistivity of TiB_2 + 10% CrB_2 composite up to 1173K (900°C) measured in argon atmosphere is presented in Fig. 5.38. It is observed that resistivity is increasing linearly with increase of temperature. The value of resistivity is measured as 32.83, 75.97 and 120 μΩ-cm at RT, 773 and 1173K (500 and 900°C) respectively. Konigshofer et al.[15] measured the resistivity at 292K (19°C) as 10 μΩ-cm for 0.5% CrB_2 contained sample (>99%TD). Electrical resistivity of monolithic TiB_2 and CrB_2 have been reported in the range of 7 to 30 μΩ-cm respectively at RT depending on the purity and method of preparation [13-15,19]. Resistivity of polycrystalline TiB_2 varies between 10 to 40 μΩ-cm at room temperature and up to 40 - 80 μΩ-cm at 1173K (900°C) [14]. Lower density (95% TD) and finer grain size of our sample could be the reasons for slightly higher electrical resistivity value. Similar observations are noticed in TiB_2+$TiSi_2$ and TiB_2+$CrSi_2$ composites also (Fig 5.31 and Fig. 5.34).

5.4.5 TiB_2 + 20%$MoSi_2$ + CrB_2 composites

Table 5.4 presents the micro hardness and indentation fracture toughness values of the hot pressed samples. Hardness values of the composites decrease from 24 to 18 GPa with increasing CrB_2 content from 5 to 15%. The possible reasons for decrease in hardness with increasing in CrB_2 content are due to the presence of higher amount of CrB_2 (which has a lower hardness) and decrease in the density with increasing the addition of CrB_2. Average indentation fracture toughness of 5, 10 and 15% composites were measured as 3.5±0.7, 3.7±0.4 and 4.1±0.3 MPa·$m^{1/2}$ respectively.

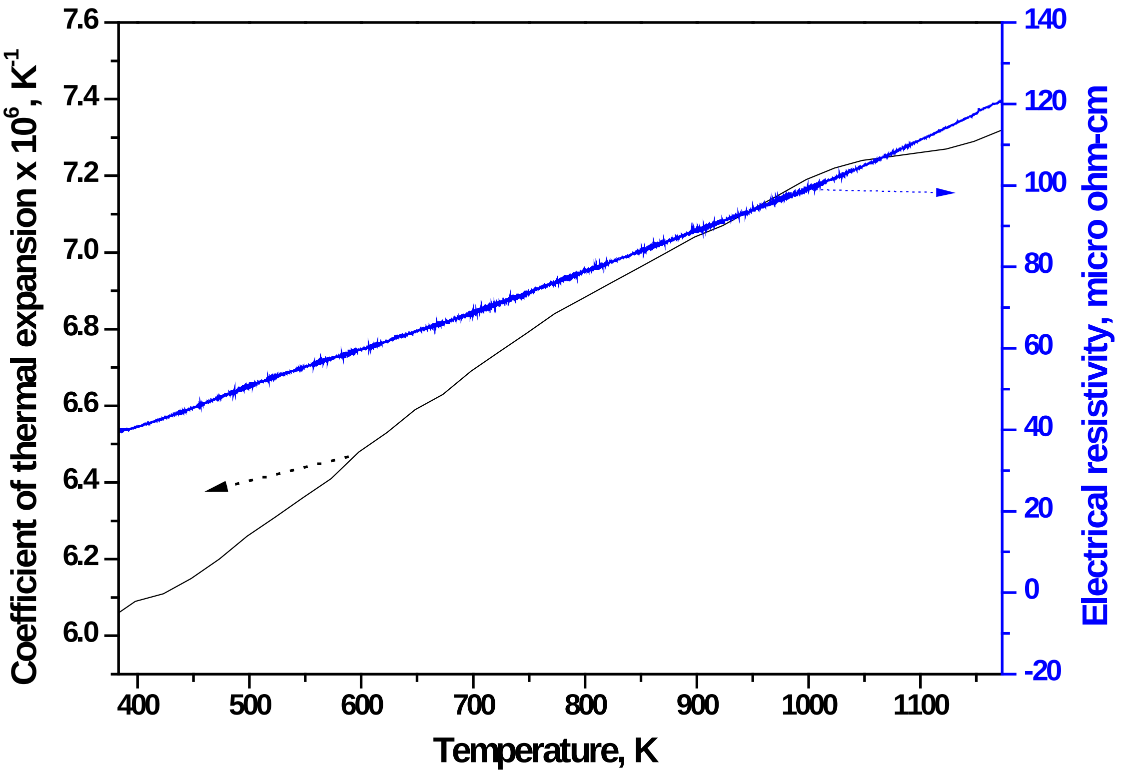

Fig.5.38 Coefficient of thermal expansion and electrical resistivity of TiB_2 + 10% CrB_2 composite in inert atmosphere

Vickers indentation with crack pattern of all the composites and the crack propagation path are presented in Fig. 5.39 and 5.40. The crack line appears to be fairly straight with a few crack deflections, indicating low fracture toughness of the composite with 5% CrB_2 (Fig. 5.39). With increasing amount of CrB_2 content to 10%, fracture toughness was found to increase. In the microstructure also more crack deflections and crack bridging mechanisms are seen (Figure 5.40), which are responsible for moderate improvement in the fracture toughness.

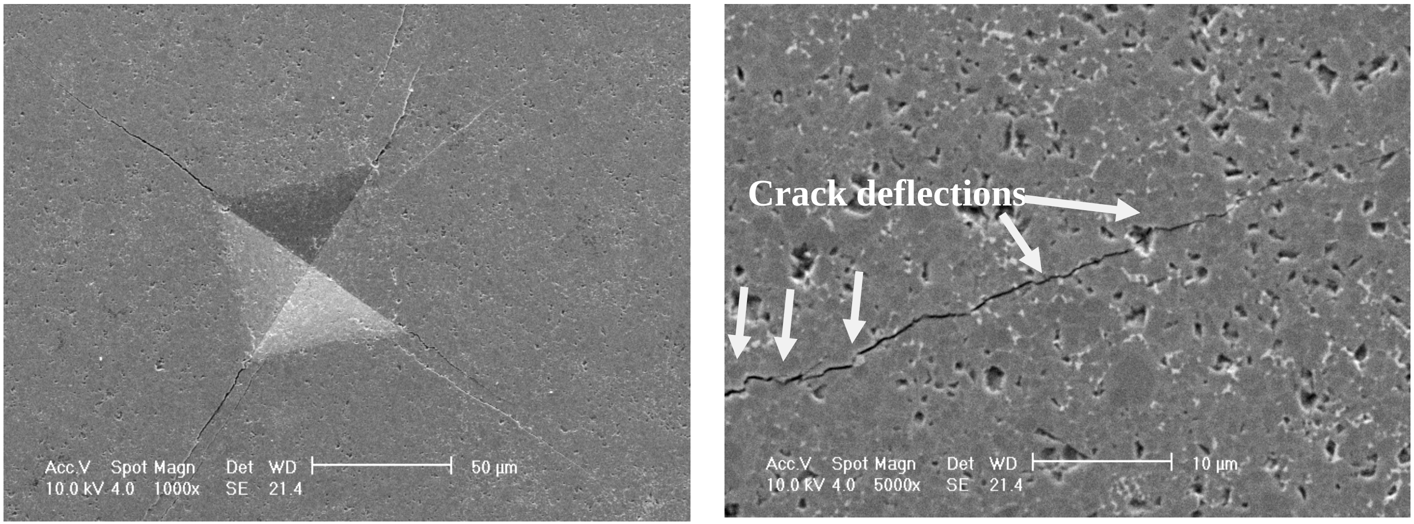

(a) (b)

Fig. 5.39 Vickers indentation (a) with crack propagation pattern (b) of TiB_2 + 20% $MoSi_2$ + 5% CrB_2 composite

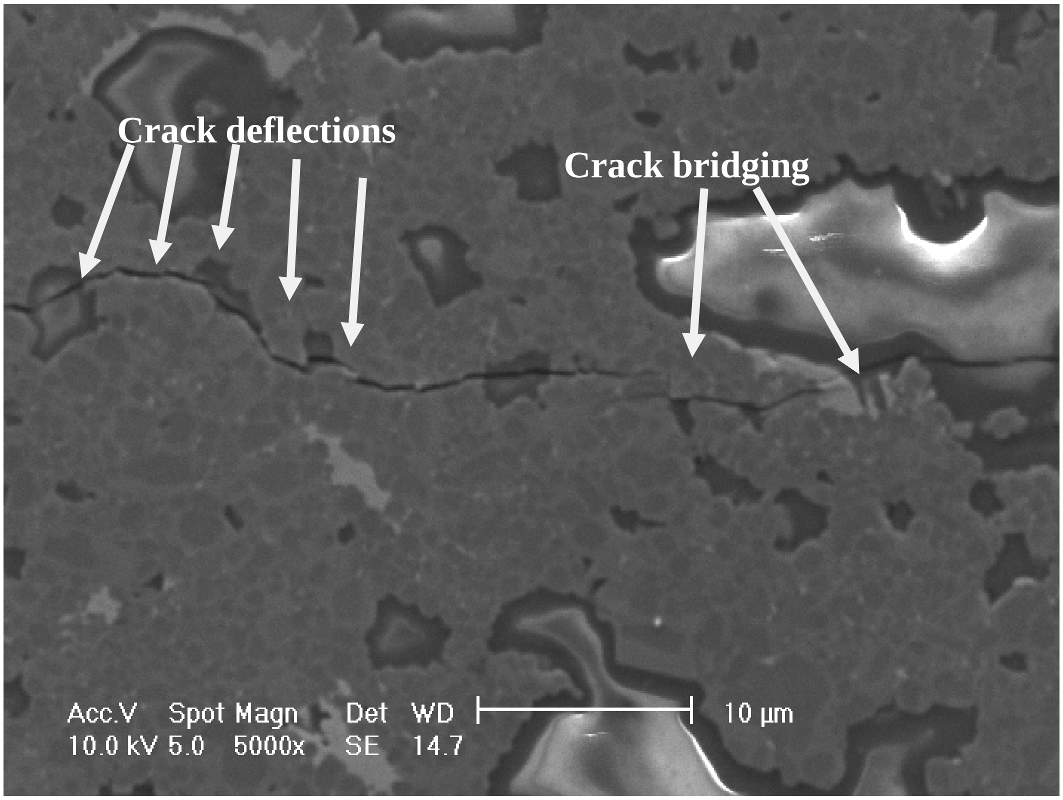

Fig. 5.40 Crack propagation pattern in the TiB_2 + 20% $MoSi_2$ + 10% CrB_2 composite

5.4.6 $(TiCr)B_2$+20%$MoSi_2$ composites

Table 5.5 presents the hardness and indentation fracture toughness values of the hot pressed $(TiCr)B_2$+20%$MoSi_2$ composites. Micro hardness values of all the composites are in the range of 24 to 27 GPa. Average indentation fracture toughness of $(Ti_{0.95}Cr_{0.05})B_2$, $(Ti_{0.90}Cr_{0.10})B_2$ and $(Ti_{0.85}Cr_{0.15})B_2$+20% $MoSi_2$ composites were measured as 2.8±0.2, 3.5±0.6 and 4.5±0.5 $MPa\cdot m^{1/2}$ respectively. Hardness of $(Ti_{0.85}Cr_{0.15})B_2$+20% $MoSi_2$ sample from RT upto 1273K (1000^{o}C) with an interval 100K was measured using diamond indenter and the values are presented Fig. 5.41. As expected, with increase in temperature, decrease in hardness values was noted. Drastic decrease in the hardness value from 30 to 16 GPa was observed from RT to 573K (300^{o}C). Flexural strength was measured at RT, 773 and 1173K (500 and 900^{o}C) for $(Ti_{0.85}Cr_{0.15})B_2$+20% $MoSi_2$ sample and the data is also presented in Fig.5.41. Three samples were tested at each temperature and the average values were 320, 295 and 285 MPa respectively. Similar to hot hardness, decrease in flexural strength values with increase in temperature was noticed. However, decrease in strength is not significant, indicating the retention of strength at elevated temperatures.

Microstructures of $(TiCr)B_2$+20%$MoSi_2$ indentations with edge cracks are shown in Fig.5.42(a & b). More crack deflections were observed in $(Ti_{0.95}Cr_{0.05})B_2$+20% $MoSi_2$ composite, where as both crack deflections and bridging mechanisms were observed in $(Ti_{0.90}Cr_{0.10})B_2$+20% $MoSi_2$ composites. These mechanisms are responsible for moderate improvement of the fracture toughness.

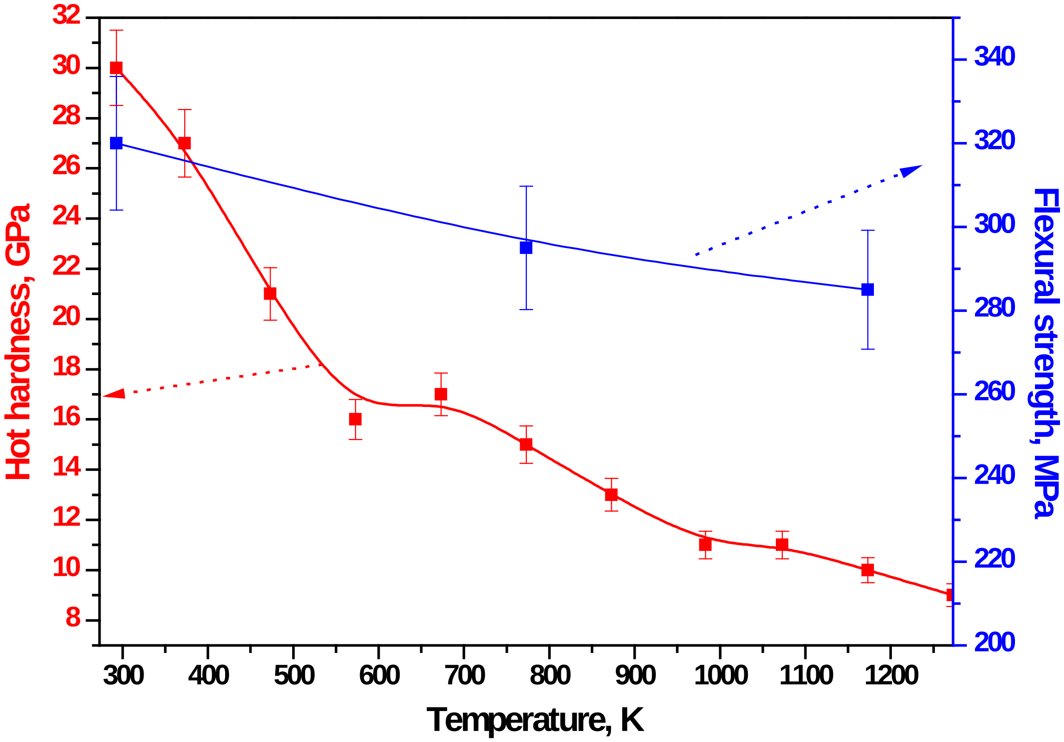

Fig. 5.41 Hot hardness and flexural strength values of $(Ti_{0.85}Cr_{0.15})B_2$+20% $MoSi_2$ composite

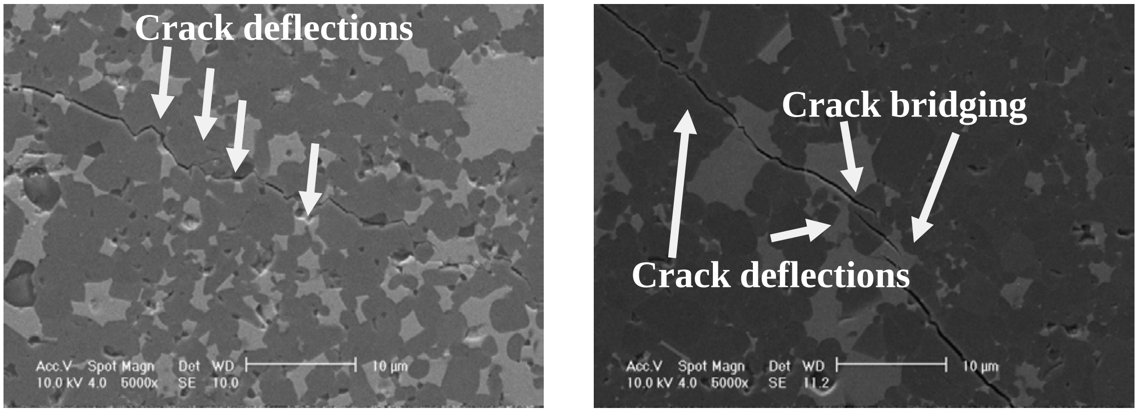

(a) (b)

Fig. 5.42 Crack propagation patterns of a) $(Ti_{0.95}Cr_{0.05})B_2$+20% $MoSi_2$ (crack deflections) b) $(Ti_{0.90}Cr_{0.10})B_2$+20% $MoSi_2$ (crack bridging) composites

CTE and electrical resistivity of $(Ti_{0.85}Cr_{0.15})B_2$+20% $MoSi_2$ composite was measured in inert atmosphere and the data is presented in Fig.5.43. CTE value was 7.54 x 10^{-6} K^{-1} in the temperature range of RT to 1073K.

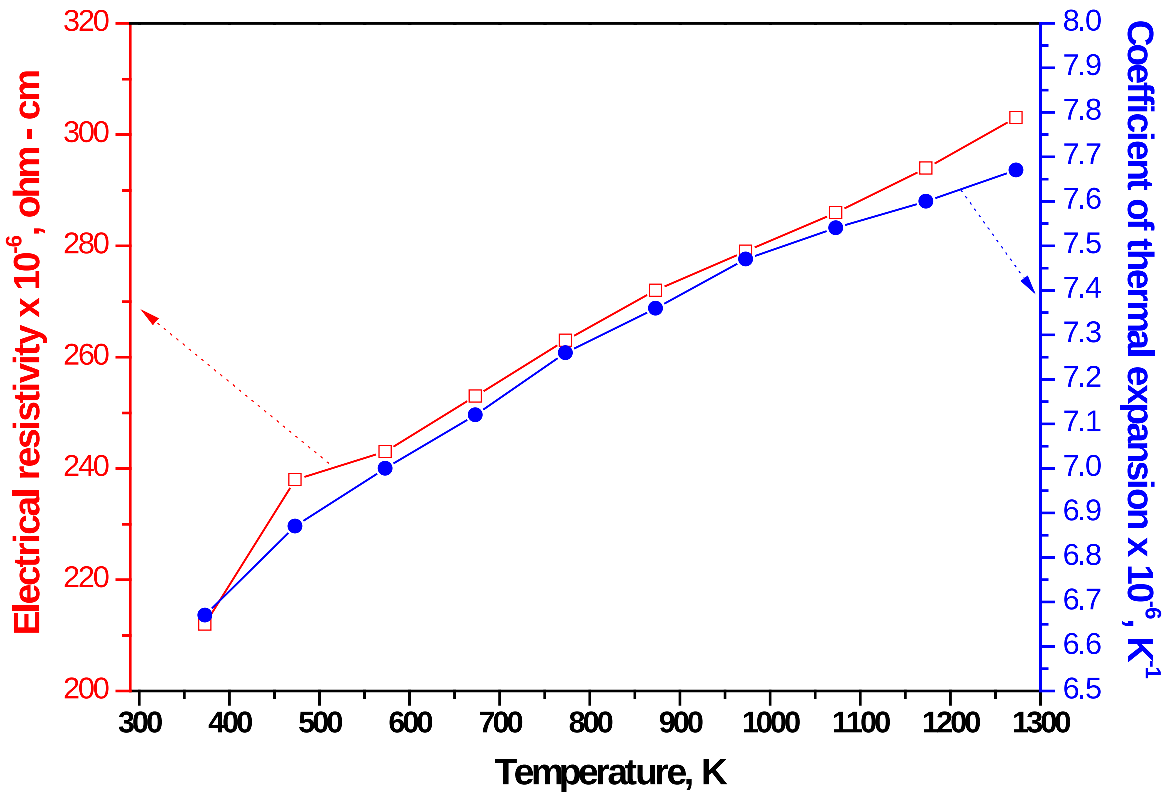

Fig. 5.43 Coefficient of thermal expansion and electrical resistivity data of $(Ti_{0.85}Cr_{0.15})B_2$+20% $MoSi_2$ composite evaluated in inert atmosphere

A Comprehensive plot on densification of all TiB_2 composites is shown in Fig.5.44. Hot pressing temperature, relative density, mechanical and physical properties of all the composites is compared in Table 5.8 & 5.9. Hot pressing conditions are also indicated in the Figure 5.44 and Table 5.9 for better comparison. Highest density of only 97.5% TD was obtained without any sinter additives to TiB_2 at 2073K (1800^{o}C) under a pressure of 35 MPa. From the data it is clear that near theoretical density was obtained with the addition of 5wt% WSi_2 to TiB_2 as compared to all the other additives. With increasing amount of sinter additive decreasing trend in density was observed in CrB_2 and $CrSi_2$ contained TiB_2 composites. However the density remained constant with further increase of WSi_2 and $TiSi_2$ content in TiB_2. Combined addition of CrB_2 and $MoSi_2$ to TiB_2 also improved the density to ≥95% TD.

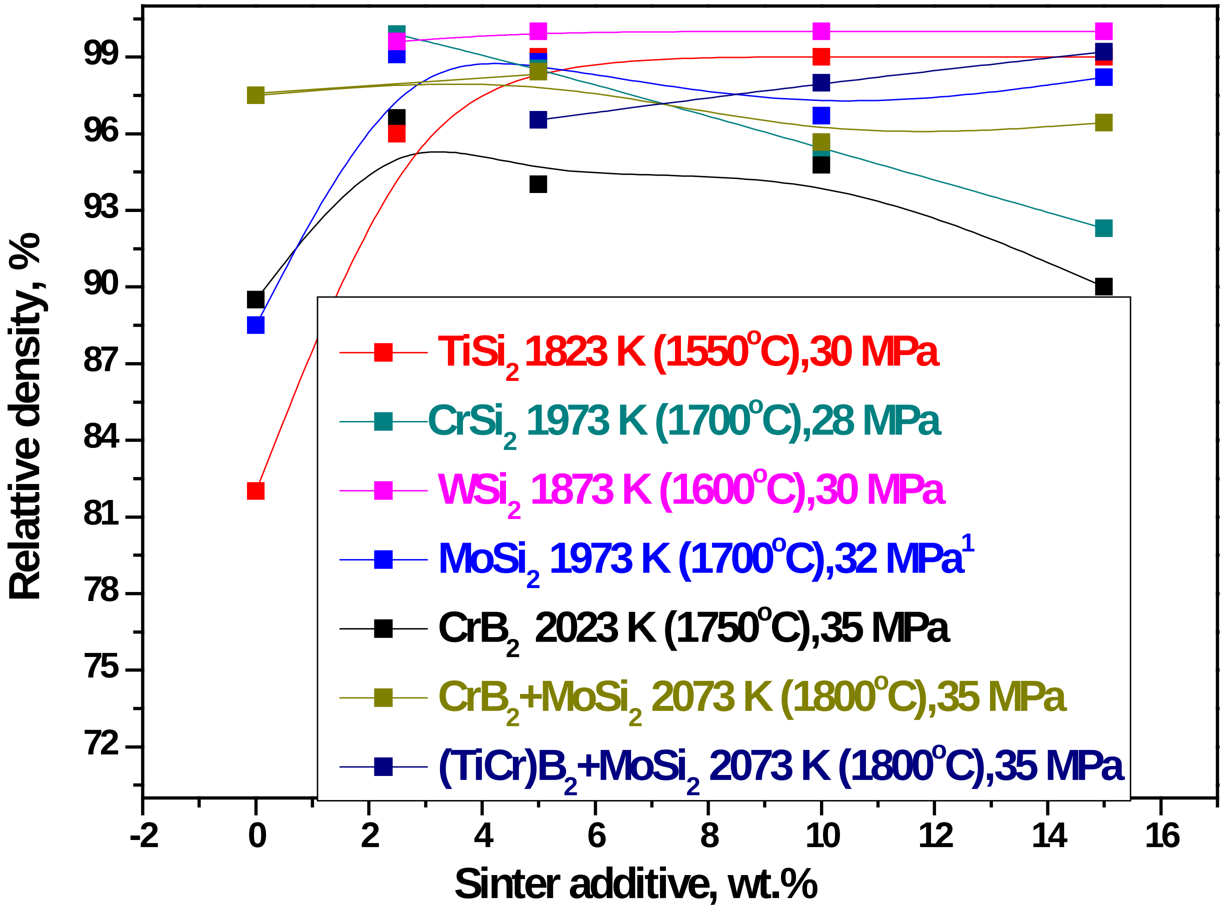

Fig.5.44 Effect of various sinter additives on densification of TiB_2 (line joining points are for visual aid only)

Table 5.8 Physical properties of TiB_2 composites

Composite	CTE @ 1073K (800°C), x 10^6 K^{-1}	Electrical resistivity @ 1273K (1000°C), μΩ-cm
TiB_2 + $TiSi_2$	6.9	100
TiB_2 + $CrSi_2$	7.0	136
TiB_2 + WSi_2	7.7	-
TiB_2 + CrB_2	7.3	125
$(Ti_{0.85}Cr_{0.15})B_2$ +20% $MoSi_2$	7.5	300

Table 5.9 Relative density and mechanical properties of TiB_2 composites

Sample	% additive (x.%)	Hot pressing conditions	Relative Density, %TD	Hardness (GPa)	Fracture toughness ($MPa.m^{1/2}$)
TiB_2 + x%$TiSi_2$	2.5	1550°C, 30MPa,1h	96.00	18 ± 2	5.3 ± 1.5
	5		98.50	25 ± 2	4.6 ± 1.1
	10		98.50	20 ± 2	6.3 ± 0.6
TiB_2 + x%$CrSi_2$	2.5	1700°C, 28MPa,1h	99.89	29 ± 2	5.9 ± 0.6
	5		98.55	28 ± 3	4.8 ± 0.4
	10		95.45	26 ± 2	3.4 ± 0.4
	15		92.30	22 ± 3	3.4 ± 0.9
TiB_2 + x%WSi_2	0	1600°C, 30MPa,1h	85.00	11 ± 2	-
	2		88.50	-	-
	2.5		99.50	26 ± 3	5.0 ± 1.0
	5		~100	24 ± 3	5.9 ± 1.9
	10		~100	26 ± 2	4.3 ± 0.9
	15		~100	24 ± 2	4.8 ± 0.9
TiB_2 + x%CrB_2	2.5	1750°C, 35MPa,1h	96.61	23 ± 1	2.8 ± 0.1
	5		94.77	23 ± 1	4.3 ± 0.3
	10		94.01	23 ± 1	4.9 ± 0.9
TiB_2 + x%CrB_2 (+20% $MoSi_2$)	5	1800°C, 35MPa,1h	98.43	24 ± 1	3.5 ± 0.7
	10		95.66	19 ± 1	3.7 ± 0.4
	15		96.43	18 ± 1	4.1 ± 0.3
$(Ti_{1-x}Cr_x)B_2$ (+20% $MoSi_2$)	0.05		96.54	21 ± 1	2.8 ± 0.2
	0.10		97.99	21 ± 1	3.5 ± 0.6
	0.15		99.20	22 ± 1	4.5 ± 0.5

5.5 Discussion on Results of densification studies

In the present study, transition/refractory metal silicides ($TiSi_2$, $CrSi_2$, WSi_2, $MoSi_2$) and CrB_2 were used as sinter additives. Reason for the choice of these additives is listed out in Table 3.1. Six different TiB_2 composites were studied to understand the densification mechanism of each composite.

1) TiB_2 + x%$TiSi_2$ (x=2.5, 5, 10 and 15)
2) TiB_2 + x%$CrSi_2$ (x=2.5, 5, 10 and 15)
3) TiB_2 + x%WSi_2 (x=2.5, 5, 10 and 15)
4) TiB_2 + x%CrB_2 (x=2.5, 5, 10 and 15)
5) TiB_2 + x%CrB_2+20%$MoSi_2$ (x=5, 10 and 15)
6) $(Ti_{1-x}Cr_x)B_2$+20%$MoSi_2$ (x=0.5, 0.10 and 0.15)

(Quantities of sinter additives are given in weight percent.)

The use of sintering aid enhances the sinterability of TiB_2 [20]. A number of earlier studies have also reported on this effect[3]. Processing and properties of TiB_2 are sensitive to microstructural details and sinter-additive content. Majority of the research investigations relate to effects on room temperature properties as well as microstructural characteristics. Basu et. al. [3, 21] reported the high temperature and tribological properties of TiB_2 + $MoSi_2$ and TiB_2 + $TiSi_2$ composites. However, very few studies on TiB_2 have focused on relating processing, microstructure and properties in particular including high temperature properties (oxidation studies) of TiB_2. Although TiB_2 has potential for a range of high temperature applications like sharp leading edge of hypersonic re-entry vehicles, cutting tools, molten metal crucibles, control rod materials, armour materials; very few reports are available on the physical, mechanical and high temperature properties of these materials. When available, these investigations are limited to monolithic TiB_2 without any sinter additive.

An earlier study revealed that $MoSi_2$ aids in the densification of TiB_2 via liquid phase sintering by the formation of a reaction product $TiSi_2$, when hot pressed at 1973K (1700^{o}C) for 1h in vacuum [1,11]. TEM analysis of a hot pressed TiB_2+20 wt% $MoSi_2$

composite revealed traces of $TiSi_2$ at grain boundary triple pockets [11]. Since the reported melting point of $TiSi_2$ is ~1813K (~1540^oC), liquid phase sintering was noticed as dominant sintering mechanism for TiB_2+$MoSi_2$ composites containing up to 20wt% $MoSi_2$. The above observation was the motivation for the present work using $TiSi_2$ and other transition/refractory metal silicides as sintering aids for consolidation of TiB_2.

The transition/refractory metal disilicides are selected as sintering aids for TiB_2, because of their ability to be selected as high temperature materials in their own right in addition to their favorable thermodynamic compatibility with many borides [20]. The densification mechanisms involved in the formation of a composite with each specific additive are identified in the following sections:

5.5.1 Densification of TiB_2 with $TiSi_2$ additions

Experimental investigations were pursued with the following objectives;

i) Does $TiSi_2$ addition provide the densification at lower hot pressing temperature as compared to that for $MoSi_2$ addition?

ii) What is the likely densification mechanism for $TiSi_2$ addition?

iii) Are TiB_2 and $TiSi_2$ thermo chemically compatible (stability at the application temperatures)?

iv) How the mechanical properties and oxidation resistance of TiB_2+$TiSi_2$ composite compare with respect to composite formed by addition of other sinter additives?

An improvement in densification of TiB_2 is observed with the additions of $TiSi_2$ as sintering additive, when hot pressed at 1823K (1550^oC) for 1h (Fig.5.2). XRD analysis indicates the presence of Ti_5Si_3 phase. As the hot pressing is performed above the melting point of $TiSi_2$ (1813K), the primary densification mechanism appears to be liquid phase sintering (LPS). From the phenomenological point of view, LPS involves the rearrangement of the TiB_2 particles. The liquid phase that is formed during sintering wets the TiB_2 grains, fills the pores of the compact and causes densification by mass transfer. The presence of Ti_5Si_3 indicates that $TiSi_2$ reacts with TiO_2 present on the surface of TiB_2 particles. The formation of Ti_5Si_3, has been described by two thermodynamically favorable reactions [2]:

$$7TiO_2 + 8TiSi_2 = 3Ti_5Si_3 + 7SiO_2 \tag{5.11}$$

$$5TiO_2 + 5TiSi_2 + 2C = 2Ti_5Si_3 + 4SiO_2 + 2CO(g) \tag{5.12}$$

Reaction (5.12) is considered since TiB_2 powders contain some amount of carbon and hot pressing was carried out in graphite dies. The above phenomenon appears to be feasible as non-oxide ceramic powders are covered by a thin oxide layer [24,25]. Li et al.[26] reported that Si_3N_4 and SiC were effective in improving the sinterability of TiB_2 by eliminating the oxide layer of TiB_2 and with the formation of an amorphous SiO_2 phase during sintering. It needs to be mentioned here that the sintering reactions clearly indicate the existence of SiO_2 along with Ti_5Si_3 as other major product phase; but the existence of SiO_2 could not be identified from XRD analysis in the composites. It could be due to the amorphous nature of SiO_2 or its quantity may be below the instrument limit.

It can be thus said that $TiSi_2$ is an effective sintering aid in hot pressing of TiB_2 in achieving high density at lower hot pressing temperature through the formation of Ti_5Si_3. Ti_5Si_3, also exhibits better mechanical properties compared to $TiSi_2$ and can retain strength beyond 1473K (1200^oC) [23].

5.5.2 Densification of TiB_2 with $CrSi_2$ additions

Experimental investigations were carried for the composite. When Si, Cr and Al based additives were added to TiB_2, oxidation resistance was enhanced due to formation of SiO_2, Cr_2O_3 or Al_2O_3 on the surface [20,26]. $CrSi_2$ has both the elements Cr and Si, which are known to improve the oxidation resistance. In this composite of the present study $CrSi_2$ was used as sintering aid in view of its excellent oxidation resistance by formation of Cr_2O_3 and amorphous SiO_2 scale.

Near theoretical density of 99.89% TD was obtained with 2.5% addition of $CrSi_2$ when hot pressed at 1973K (1700^oC) for 1h (Fig.5.44). With increasing amount of sinter additive the density was found to decrease. The density of composites obtained with 5%, 10% and 15% $CrSi_2$ were 98.55%, 95.45% and 92.30% TD respectively. As the hot pressing is performed above the melting point of $CrSi_2$ (1750K), liquid phase sintering (LPS) mechanism appears to be important. Solution-diffusion process leads to the decomposition of $CrSi_2$ to other silicides with different ratio of Cr : Si accompanied with the formation of free Si (Melting point: 1687K). The presence of Si is clearly noticed in SEM-EDS analysis (Fig.5.10). The most probable reactions for the decomposition of $CrSi_2$ to other silicides with the formation of Si are given in section 5.3.2 and the free energy changes at 0.001 Pa for these reactions up to 2000K are presented in Fig. 5.12 [9]. For all the reactions the free energy values are more or less constant and positive till the melting point of $CrSi_2$. From the melting point the ΔG decreases with temperature and for all the reactions becoming more and more negative. Among all these reactions, reaction (5.1) is more negative at the hot pressing temperature of 1973K (1700^oC). This explains the formation of Si during hot pressing.

Samples containing higher amounts of $CrSi_2$ (≥10%) show the presence of closed pores, as evident in the case of composite containing 15wt% $CrSi_2$. The formation of pores could be due to the evaporation of Si formed during the course of hot pressing, which was carried out under a vacuum of >0.001 Pa (10^{-5} m.bar). The vapor pressure of pure Si at the hot pressing temperature (1973K) is 1.01 Pa (1.01×10^{-2} m.bar) [10]. Therefore with increased addition of $CrSi_2$, decrease in density is observed due to formation of higher amounts of Si. Existence of material in the gaseous phase during sintering is not desirable, as it leads to poor densification. The measured closed porosity in these samples clearly supports the above phenomenon. Whereas in other hot pressed composites; for eg. TiB_2+$TiSi_2$, TiB_2+WSi_2 mainly open porosity is observed with negligible amounts of closed pores in all the samples.

Small addition (2.5%) of $CrSi_2$ has been found to be an effective sinter additive to TiB_2. Compacts with near theoretical density were prepared with the addition of 2.5% $CrSi_2$ by hot pressing at 1973K (1700°C), 28 MPa. Higher additions of $CrSi_2$ led to decrease in the density of the product.

5.5.3 Densification of TiB_2 with WSi_2 additions

Tungsten silicide coatings have outstanding abrasive and adhesive wear resistance due to its strong covalent bonds and high hardness [3]. Tungsten silicides show protective nature in oxidation up to 2273K (2000°C) in air by formation of a protective SiO_2 film [3]. WSi_2 was accordingly selected as a sinter additive.

WSi_2 was found to be an effective sinter additive to TiB_2. Compacts with near theoretical density were prepared with the addition of ≥5% WSi_2 by hot pressing at 1873K (1600°C), 30 MPa. XRD results confirm the occurrence of chemical reactions during hot pressing, consumption of WSi_2 phase and formation of W_5Si_3 and SiO_2 as reaction products. The probable reactions for the decomposition of WSi_2 and the formation of W_5Si_3 are given section 5.3.3. The probable reaction pathways involving different oxides (TiO_2 and B_2O_3) are also considered, as these oxides are usually present on surface of TiB_2 powders [25,26].

Based on the available thermodynamic data [9] on the free energy of formation of different compounds, the overall free energy change (ΔG) for all the above reactions to occur from left to right was calculated by using FactSage software version 6.3 at 0.001Pa and plotted as a function of temperature (Fig. 5.18). From the plots, it is clear that all the reactions are thermodynamically feasible at the hot pressing temperature of 1873K (1600^oC). Free energy change for reactions (5.6), (5.7) and (5.9) are negative and are therefore feasible even at room temperature. For example free energy change for equations (5.6), (5.7) and (5.9) at 1900K are -520.93, -146.08 and -234.26 kJ/mol respectively. Reaction (5.7) and (5.10) are also considered since TiB_2 powders contain small amounts of carbon and hot pressing was carried out in graphite dies where the powders are in direct contact with carbon. The Gibbs-free energy change of the reaction (5.10) is positive up to 1000K and becomes negative (ΔG_{10}= - 234.58 kJ/mol). From the above discussions, it is evident that the formations of W_5Si_3, SiO_2, Ti_5Si_3 and SiC are feasible during hot pressing. Presence of W_5Si_3 is confirmed by XRD but other phases couldn’t be traced by XRD. This could be due either to the amorphous nature of certain phases (SiO_2) or their presence in small quantities. SiO_2 is likely to exist in liquid phase at the hot pressing temperature (SiO_2 M.Pt.=1731K) of 1873K (1600^oC). The formation of SiO_2 appears to be feasible because of the oxide coating that is always present on the surface of non-oxide powders [24,25].

The present experimental results suggest that the chemical reactions at the sintering temperature play an important role in determining the densification behavior and material properties of the non-oxide ceramics. WSi_2 has therefore been found to be an effective sinter additive to TiB_2.

5.5.4 Densification of TiB_2 with CrB_2 additions

Though some work has been reported earlier with the addition of CrB_2 in pressureless/ microwave sintering and hot pressing of prealloyed composite, detailed studies on the preparation and characterization of TiB_2+CrB_2 composite have not been reported so far. The present work reports on the densification behaviour of TiB_2 using CrB_2 as sinter additive.

With the addition of 2.5% CrB_2 to TiB_2, a composite of density >96% TD was obtained by hot pressing at 2023K (1750^{o}C) and a pressure of 35 MPa. Addition of CrB_2 was found to aid in sintering and inhibit particle coarsening during densification. Solid solution formation of TiB_2 and CrB_2 were confirmed by XRD (Fig. 5.20 shows shift in the peaks). Attainment of higher density of TiB_2 composites with CrB_2 is attributed to the higher mobility of CrB_2 and formation of solid solution with TiB_2 [3,4]. In addition, the application of high pressure for consolidation contributes to particle rearrangement and leads to high stresses at the particle contact points. This stress gradient at the contact points acts as a driving force for mass transport which aids sintering [27]. Atomic movement with simultaneous application of high pressure facilitates material transport resulting in high dense TiB_2+CrB_2 composites. No trace of liquid phase was seen in the microstructures of TiB_2+CrB_2 composite.

While hot pressing TiB_2 and CrB_2 powders at 2023K (1750°C), the microstructure has been observed to be solid sintered $(Cr,Ti)B_2$ clusters and particles with an unreacted base of TiB_2 with an outer layer of $(Cr,Ti)B_2$.[3] The phase diagram of CrB_2-TiB_2 system shows a complete solid solubility above a temperature of 2273K (2000°C) (Fig.5.3)[3]. As per the phase diagram, maximum CrB_2 solubility in TiB_2 does not exceed 1 mol% (1.15 wt%) at 2073K (1800°C). From the above it is clear that higher addition of CrB_2 does not contribute towards solid solution formation at the sintering temperature of 2023K (1750°C) and hence no increase in density is observed for composites with CrB_2 above 2.5%. Holcombe *et al.*[5] have obtained a density of 84 and 90% TD with the addition of 3% CrB_2 in pressureless sintering at 2173 and 2373K respectively. Konigshofer *et al.*[6] obtained a density of 98.9% TD with the addition of 0.5% CrB_2 to TiB_2 by hot pressing at a higher temperature of 2073K (1800°C) and higher pressure of 45MPa. With the small addition of 2.5% CrB_2 to TiB_2, a composite of density >96% TD was obtained by hot pressing. Addition of 2.5% CrB_2 was found to aid in sintering and inhibit particle coarsening during densification. Further addition above 5% CrB_2 has not helped to improve the densification.

5.5.5 Densification of TiB_2 with combined additions of CrB_2 and $MoSi_2$

In continuation of the present study, composite of TiB_2 with combined addition of CrB_2 and $MoSi_2$ was prepared. Combined additions of different sinter additives many times may be beneficial in enhancing the densification and the desired properties. For example, simultaneous addition of 0.5 wt% Cr and Fe was found to enhance the densification of TiB_2 up to 98.8% of theoretical [28].

In previous reported work $MoSi_2$, and in the present work CrB_2 were separately used as additive to TiB_2 to improve the densification and oxidation behavior [1,29]. With $MoSi_2$, additions improvement in densification was achieved but the oxidation resistance was poor [1,29]. On the other hand, addition of CrB_2 resulted in improvement in the oxidation behavior without improvement in density. This observation provided the motivation for the present study on combined addition of CrB_2 and $MoSi_2$ on the densification as well as oxidation behavior of TiB_2.

High density composites (>96% TD) of TiB_2 were prepared by combined addition of CrB_2 and $MoSi_2$. TiB_2, $MoSi_2$, Ti_5Si_3 and $TiSi_2$ phases were identified by the XRD analysis, indicating the occurrence of a reaction. Similar reaction product of $TiSi_2$ phase was identified in previous studies when $MoSi_2$ was used as a sintering aid [1,11]. CrB_2 peaks were absent in the XRD and the number & intensity of $MoSi_2$ peaks is also lower as compared to the initial powder mixture. A small shift in the location of TiB_2 peaks is also noticed in the pellet as compared to that of the powder mixture. These indicate the formation of solid solution of CrB_2 in TiB_2 in the composite. Similar observations were also noticed in TiB_2+CrB_2 composites.

From the above results, it is evident that the densification mechanisms were similar in TiB_2+$MoSi_2$ [1] and TiB_2+CrB_2 composites. In previous study [1,11] investigated that $MoSi_2$ aids in the densification of TiB_2 via liquid phase sintering by the formation of a reaction product of $TiSi_2$. Attainment of higher density of TiB_2 composites with CrB_2 is attributed to the higher mobility of CrB_2 and formation of solid solution with

TiB_2. High dense composites (>96% TD) of TiB_2 were prepared by combined addition of CrB_2 and $MoSi_2$.

5.5.6 Densification of $(TiCr)B_2$+20%$MoSi_2$

The objective of the present investigation has been to prepare a fully dense TiB_2 with favorable resistance to oxidation and thermal shock. In order to improve resistance to thermal shock, the formation of a solid solution in preference to a two phase microstructure is desirable. Further, more uniform distribution at the atomic level of secondary phase elements can be seen in solid solution instead of particulate composites. In this regard, studies on the synthesis of starting powders and densification of pre-alloyed $(TiCr)B_2$ using $MoSi_2$ as sinter additive were carried out. Densified compacts were evaluated for mechanical (hardness, fracture toughness, flexural strength, hot hardness) and physical properties (CTE, electrical resistivity). Phase identification and microstructural characterizations were carried out. Detailed oxidation and thermal cycle studies were also carried out and compared with other developed composites.

High density composites (>97%) of pre-alloyed $(TiCr)B_2$+20%$MoSi_2$ were prepared by hot pressing. TiB_2 and $MoSi_2$ peaks were seen as major peaks in XRD analysis. CrB_2 peaks were not identified in the sample, however slight shift in TiB_2 peaks were seen. Detailed EPMA results revealed three regions of interesting. These are the light grey matrix, dark grey and black phases (Fig 5.26). To identify the elements on these regions, spectrum was analyzed separately and it was found that the elements predominantly present in the matrix are Ti, Cr and boron. Lighter regions contain Cr, Ti, Mo and B. Mo and Si are the only elements present in the dark phases. Quantitative analysis was done on the three identified regions to determine the chemical composition of the elements present, which are shown in Table 5.6. Elemental mapping of the sample shows the distribution of Ti, Cr and B in the matrix. These three elements appear to be uniformly distributed throughout the matrix. The qualitative analysis of these elements as seen by variation of brightness matches with the composition of the composite. Fig. 5.27e presents the overlay of Ti+B+Cr in the matrix, which confirms the uniform distribution of these three elements in the matrix. Fig.5.27f presents the distribution of silicon indicating that silicon is not uniformly distributed but present as clusters of 1-2 μm size in the matrix. Fig.5.27g shows the uniform distribution of Mo throughout the matrix. This clearly indicates that a reaction has occurred between $MoSi_2$ and $(TiCr)B_2$. Mo is seen to have diffused and distributed in the matrix, leaving Si undisturbed. The white spots in Fig.5.27f indicate the location of original $MoSi_2$ particles. The elemental analysis of the polished surface indicates the presence of Ti, Cr, B and Mo uniformly distributed throughout the matrix and silicon as a second phase precipitate in the matrix. Further line scanning across different phases was carried out to confirm these results. Scan for Si indicates the non continuous presence of Si in the form of clusters. At these locations the contents of Ti, B, Cr and also Mo are comparatively low. Otherwise concentrations of these four elements are more or less constant throughout the region of line scan. Line scan analysis is in full agreement with the results of elemental mapping. High dense composite (>99%) of pre-alloyed $(Ti_{0.85}Cr_{0.15})B_2$+20%$MoSi_2$ was prepared.

It may be worthwhile here to compare the densification results of all composites prepared in this work using TiB_2 of same origin. Density of TiB_2 composites with varying

$MoSi_2$ [1], $TiSi_2$, WSi_2, $CrSi_2$, CrB_2 and composites of $(TiCr)B_2$+20%$MoSi_2$ are presented in Fig.5.44. In all cases, one can see a significant improvement in density with a small addition of 2.5% sinter additive. With higher additions in the case of $TiSi_2$, WSi_2 and CrB_2 content in $(TiCr)B_2$+20%$MoSi_2$ an increase in the density is observed, whereas in other cases a decrease in density is seen. The mechanism of sintering is different in each case and the sintering temperatures also vary as explained above. In the case of sintering with $TiSi_2$ or WSi_2 it is liquid phase sintering. In case of $MoSi_2$, the major contribution in densification is due to compressive deformation of $MoSi_2$ in addition to the formation of liquid reaction product of $TiSi_2$ [1,11]. Whereas during additions of $CrSi_2$, formation of a reaction product of Si was mainly observed, which leads to deteriorate the densification due to its existence in the gaseous phase at the hot pressing temperature under vacuum of 0.001Pa (10^{-5} m.bar). Near theoretical density TiB_2+CrB_2 composites were not obtained due to the absence of liquid phase sintering. At the same time, high dense composites (>96% TD) of TiB_2 were obtained by combined additions of CrB_2 and $MoSi_2$. Dual mechanism of sintering was observed in TiB_2+CrB_2+$MoSi_2$ composites namely: reactive liquid phase sintering and solid solution formation of $(Ti,Cr)B_2$. High dense composite (>99%) of pre-alloyed $(Ti_{0.85}Cr_{0.15})B_2$+20%$MoSi_2$ were also obtained.

From the above discussion, it is clear that additions of silicides to TiB_2 helps to enhance the density by liquid phase sintering and/or activated sintering. When CrB_2 is added to TiB_2 liquid phase sintering was not seen. However, improvement in densification was seen due to the higher mobility of CrB_2 and formation of solid solution with TiB_2. Mechanical and physical properties were evaluated and presented in the results section.

5.6 Summary

Consolidation of TiB_2 is a challenge due to its high melting point; covalent nature requires high temperatures for sintering. However, borides undergo an abnormal grain growth at high temperatures. The occurrence of microcracking at the grain boundaries is also promoted with the increase in grain size. Thus, it is very difficult to achieve crack free dense borides by the conventional cold compaction and sintering, as no shape accommodation occurs without an external pressure and large pores tend to coarsen during high temperature sintering. A thin oxygen rich layer (mainly TiO_2 and B_2O_3) is usually present on the surface of TiB_2 powder, irrespective of synthesis route. The presence of oxygen finally results in increase in grain size and coarsening of pores because the presence of oxides increases the surface diffusivity. In order to overcome the above issues it is very essential to add a suitable sinter additive. Choice of sinter additive is a challenge to obtain a density without losing its (TiB_2) inherent properties. In literature, various metallic/non metallic additives were used to lower the densification temperature. Although metallic additives helps to lower the densification temperature, from the perspective of high temperature applications, the presence of metallic binder is not desirable, the low melting point of either sintering liquid or metallic additives leads to incipient fusion and consequent degradation of high temperature properties. The principal objective of non-metallic additives is therefore to improve sinterability of TiB_2 without promoting grain growth thus circumventing limitations of metallic additives. Silicides have not been used extensively in the past for densification of TiB_2. Silicides have attracted considerable interest due to their compatibility with borides to densify at lower temperatures. In the present investigations, various silicides were used to densify the TiB_2

by hot pressing. Silicides not only lowered the densification temperature, but also helped to improve the toughness and oxidation resistance. Reactive sintering and liquid phase sintering were the main densification mechanism in all the cases. Silicon in the silicides helped to reduce the surface oxides of TiB_2, which is advantageous as mentioned above. Presence of reaction product/second phase helped to improve the fracture toughness by crack deflection or bridging mechanisms. However, presence of silicon also helped to improve the oxidation resistance by formation of a thin glassy layer on the surface. Effect of various silicides and its quantity on the densification, properties and oxidation behavior was mainly studied in this thesis. Important findings w.r.t. densification and mechanical/physical properties are listed below:

a) Composite (TiB_2 + ≥5% $TiSi_2$) pellets of 99% TD were prepared by hot pressing at 1823K (1550^{o}C) and 30 MPa pressure in a vacuum environment for 1h. Compacts with near theoretical density were prepared with the addition of 2.5% $CrSi_2$ by hot pressing at 1973K (1700^{o}C), 28 MPa, ≥5% WSi_2 by hot pressing at 1873K (1600^{o}C), 30 MPa. With the small addition of 2.5% CrB_2 to TiB_2, a composite of density >96% TD was obtained by hot pressing at 2023K (1750^{o}C) and a pressure of 35 MPa. High dense composites (>96% TD) of TiB_2 were prepared by combined addition of CrB_2 and $MoSi_2$. High dense composite (>99%) of pre-alloyed $(Ti_{0.85}Cr_{0.15})B_2$+20%$MoSi_2$ were obtained by hot pressing at 2073K (1800^{o}C) under a pressure of 35 MPa.

b) Ti_5Si_3 was observed as a reaction product of TiB_2 and $TiSi_2$ during hot pressing. W_5Si_3 phase was identified as a reaction product of TiB_2 + WSi_2 composite. Solid solution formation of TiB_2 and CrB_2 were confirmed, when CrB_2 is added to TiB_2.

c) Microstructural characterization results are summarized here for all the composites. EPMA studies of TiB_2 + $TiSi_2$ showed the presence of three distinct phases namely matrix (TiB_2), dark spot (Ti-61.2%, B-26.6%, Si-12.1%) and white spot (Ti->98%, Si-0.8 to 1.0%). Elemental analysis of the reaction site revealed the migration of silicon from $TiSi_2$ to the matrix. SEM of the fractured surface of the same composite revealed the absence of particle coarsening during densification and the mode of fracture to be predominantly intergranular. In TiB_2 + $CrSi_2$ composites three distinct regions namely a) dark grey matrix of TiB_2, b) black region, rich in Si and c) white phase, Cr laden TiB_2 were seen on the polished surface. Presence of free silicon (black phase) has been observed, which increases in quantity with the increased addition of $CrSi_2$. No grain growth was observed up to 5% $CrSi_2$ addition, whereas due to coagulation of Si, large particles were observed when $CrSi_2$ content was high. The failure analysis showed that the contribution by transgranular mode increases with increasing $CrSi_2$ content. No grain growth was observed up to 2.5% WSi_2 addition, to TiB_2 whereas due to coagulation of liquid/product phases, large particles were observed when WSi_2 content was high. The failure analysis showed the mixed mode of fracture. With increased CrB_2 (5 to 15%) content, failure of this composite was found to change from predominantly transgranular to a mixed (trans and intergranular) mode.

d) Hardness (20-25GPa), fracture (indentation) toughness (4.6-6.3MPa. $m^{1/2}$) and flexural strength (390 MPa) of TiB_2 + $TiSi_2$ composite is found to match with that of monolithic TiB_2 of similar density. Hardness and fracture toughness of TiB_2 +

$CrSi_2$ composite were 29± 2 GPa and 5.97± 0.6 MPa.m$^{1/2}$ respectively. With the increase in sinter additive, mechanical properties were found to decrease for TiB_2 + $CrSi_2$ composite like in the density. Hardness and fracture toughness of TiB_2 + WSi_2 composite were 25± 1 GPa and 5.0 ± 1.0 MPa.m$^{1/2}$ respectively. Crack deflection and bridging mechanisms were apparently responsible for high fracture toughness in TiB_2 + $TiSi_2$ and TiB_2 + WSi_2 composites. Hardness of TiB_2 composites containing 2.5, 5 and 10% CrB_2 are close to 24 GPa and fracture toughness values in the range of 3-5 MPa·m$^{1/2}$. Failure of this composite has been found to be through a mixed (trans and intergranular) mode of fracture. Moderate hardness in the range of 18- 24 GPa and fracture toughness values in the range of 3-4 MPa·m$^{1/2}$ were recorded for combined addition of CrB_2 and $MoSi_2$ to TiB_2. In pre-alloyed $(TiCr)B_2$+20%$MoSi_2$ composites, hardness values are recorded in the range of 24-27 GPa. With increase in CrB_2 content from 5 to 15%, fracture toughness values were found to increase from 2.8 to 4.5 MPa.m$^{1/2}$ in pre-alloyed composites.

e) Coefficient of thermal expansion (CTE) of TiB_2 + $TiSi_2$ composite is found to be close to that of TiB_2 and found to increase marginally with temperature upto 1073K (800^{o}C) (5.8 x 10^{-6} K^{-1} at 473K to 6.9 x 10^{-6} K^{-1} at 1073K). Electrical resistivity increases linearly with temperature upto 1273K (1000^{o}C) and the room temperature value of TiB_2 + $TiSi_2$ composite is slightly higher than that of TiB_2 as the specimen tested was of only 96% TD. CTE and electrical resistivity of TiB_2 + 5% $CrSi_2$ composites are comparable to that of monolithic TiB_2. CTE of TiB_2 + 15% WSi_2 composites are comparable to that of monolithic TiB_2. Coefficient of thermal expansion of TiB_2+10%CrB_2 (6.21-7.43 x 10^{-6} K^{-1} from RT to 1273K) is close to that of TiB_2 and CrB_2. Electrical resistivity of TiB_2+10%CrB_2 was measured to be 32.83, 75.97 and 116.96 μΩ-cm at RT, 773 and 1273K respectively. These values are slightly higher than that of monolithic TiB_2 but are in the same order. In the present, studied composite's properties are not in linear combination of individual components. This could be due to the formation of a reaction products or the difference in the interfacial energies.

5.7 References

[1] T. S. R. Ch. Murthy, B. Basu, R. Balasubramaniam, A. K. Suri, C. Subramonian, and R. K. Fotedar, Processing and Properties of TiB_2 With $MoSi_2$ Sinter- Additive: A First Report, J. Am. Ceram. Soc., 2006;89[1]:131–138

[2] G.B.Raju, and B.Basu, Densification, Sintering Reactions, and Properties of Titanium Diboride with Titanium Disilicide as a sintering Aid, J. Am. Ceram. Soc. 2007;90[11]:3415-3423

[3] a) G. Effenberg editors. Red book. ASM international, 1993;38:927-929; b) http://books.google.co.in; c) V.I Zmii, N.V Kovtun, P.I Glushko, S.G Ruden'kii. Stability and heat resistance of silicide coatings on tungstem and molybdenum at 1500-2000°C. Powder Metallurgy and Metal Ceramics 2003;42(1-2):50-53.

[4] B. Post, F.W. Glaser, Moskovitz D. Transition metal diborides. Acta Metallurgica 1954;2:20–25

[5] C.E Holcombe, N.L Dykes. Microwave sintering of titanium diboride. J Mater Sci 1991;26[14]:3730–3738

[6] R. Konigshofer, S. Furnsinn, P. Steinkellner, W. Lengauer, R. Haas, K. Rabitsch, M. Scheerer. Solid-state properties of hot-pressed TiB_2 ceramics. Int J Ref Met & Hard Mater 2005;23[4-6]:350-357

[7] G.Sade, J.Pelleg, V.Ezersky, Titanium silicide formation in $TiSi_2$ /TiB_2 bilayer barrier structure, Microelectronic Engineering, 1997;33:317-323

[8] A.S. Ramos, C.A.Nunes, G.Rodrigues, P.A. Suzuki, G.C.Coelho, A.Grytsiv, P.Rogl, Ti_6Si_2B, a new ternary phase in the Ti-Si-B system, Intermetallics, 2004;12:487-491

[9] FactSage software Version 6.3 and Barin I, Thermochemical data of pure substances, vol. 1&2, third ed., VCH, Weinheim, 1995

[10] E.H Richard, A.K Dean.”Vapor Pressure Curves of the Elements" 1969;Radio Corporation of America

[11] K. Biswas, B. Basu, A.K. Suri, K. Chattopadhyay. A TEM study on TiB_2-20%$MoSi_2$ composite: Microstructure development and densification mechanism. Scripta Materialia, 2006;54:1363-1368

[12] R.Telle, G.Petzow, “Strengthening and toughening of boride and carbide hard material composites”, Materials Science and Engineering, 1988;A 105/106:97-104

[13] C.Subramanian, T.S.R.Ch.Murthy, and A.K.Suri, Synthesis and consolidation of titanium diboride, Int. J. Ref. Met. & Hard Mat. 2007;25:345-350

[14] A.D. Mcleod, J.S. Haggerty, D.R. Sadoway, Electrical resistivities of monocrystalline and polycrystalline TiB_2, J Am Ceram Soc. 1984;67[11]:705–708

[15] R. Konigshofer, S. Furnsinn, P. Steinkellner, W.Lengauer, R. Haas, K. Rabitsch, Solid-state properties of hot-pressed TiB_2 ceramics, Int J Refract Met Hard Mater., 2005;23:350–357

[16] www.vriginiasemi.com

[17] M.L Emiliani. Characterization and oxidation resistance of hot pressed chromium diboride. Mater Sci Eng A 1993;172:111-124

[18] G.B Raju, B Basu, N.H Tak, S.J Cho. Temperature dependent hardness and strength properties of TiB_2 and $TiSi_2$ sinter-aid. J Eur Ceram Soc 2009;29[10]:2119-2128

[19] M. Rahman, C.C Wang, W Chen, S.A Akbar. Electrical resistivity of titanium diboride and zirconium diboride. J Am Ceram Soc 1995;78[5]:1380-82

[20] B. Basu, G.B. Raju, A.K. Suri. Processing and properties of monolithic TiB_2 based materials. Int Mater Rev 2006;51[6]:354-374

[21] G.B Raju, B Basu Wear Mechanisms of TiB_2 and TiB_2-$TiSi_2$ at fretting contacts with steel and WC-6wt% Co. Int. J. Appl. Ceram. Technol., 2010;7[1]:89-103

[22] T.S.R.Ch.Murthy, B. Basu, A. Shrivastava, R. Balasubramaniam, and A. K. Suri; "Tribological Properties of TiB_2 and TiB_2-$MoSi_2$ Ceramic composites", Journal J. Eur. Ceram. Soc., 2006;26:1293-1300

[23] C.L.Yeh, W.H.Chen, C.C. Hsu, "Formation of titanium silicides Ti_5Si_3 and $TiSi_2$ by self-propagating combustion synthesis", J. Alloys and compounds, 2007;432:90-95

[24] W. Wang, Z. Fu, H. Wang and R. Yuan, "Influence of hot pressing temperature and time on microstructure and mechanical properties of TiB_2 ceramics," J. Eur. Ceram. Soc., 2002;22:1045-1049

[25] S. Baik and P. F. Becher, "Effect of oxygen contamination of densification of TiB_2," J. Am. Ceram. Soc., 1987;70:527-530.

[26] L. H. Li, H. E. Kim, E. S. Kang, "Sintering and mechanical properties of titanium diboride with aluminum nitride as a sintering aid," J. Eur. Ceram. Soc., 2002;22: 973-977.

[27] P Larsson, N Axen, S Hogmark., Improvements of the microstructure and erosion resistance of boron carbide with additives. J. Mater. Sci., 2000; **35**: 3433-3440.

[28] S. H. Kang and D. J. Kim, E. S. Kang and S. S. Baek: J. Am. Ceram. S oc. , 2001;84[4]:893–895

[29] T.S.R.Ch Murthy, R Balasubramaniam, B Basu, A.K. Suri, M.N. Mungole. Oxidation of Monolithic TiB_2 and TiB_2-20 wt% $MoSi_2$ Composite at 850^o C. J. Eur. Ceram. Soc. 2006;26:187-192.

CHAPTER 6

CHAPTER 6

OXIDATION STUDIES

6.1 Introduction

This chapter covers the non isothermal and isothermal oxidation of TiB_2 composites. Mechanism of oxidation was evaluated from the weight change data. Specific weight gain vs. time plots were fitted to parabolic and general rate equations to calculate the rate constants and to determine the slope of the oxidation curve. Important findings are given in this chapter.

Non isothermal oxidation studies were carried out in oxygen and air to determine the start and severity of oxidation and the effect of sinter additives by using TG-DTA. Morphology of the oxidized surfaces was investigated by SEM.

Isothermal oxidation studies were carried out in air by measuring the weight change to elucidate the nature of oxidation with respect to sinter additives. Morphology and phases of the oxidized surfaces were investigated by SEM-EDS, XRD and XPS. Cross section of the oxidized surface after 256h was characterized by SEM-EDS for the most oxidation resistant composites. Effect of various sinter additives ($TiSi_2$/$CrSi_2$/CrB_2/WSi_2) on the oxidation behavior of TiB_2 is analyzed. Effect of the combined addition of CrB_2 and $MoSi_2$ to TiB_2 on the oxidation behavior is also investigated and compared with the results of pre-alloyed $(TiCr)B_2$+20%$MoSi_2$ composite. Discussion on the oxidation behavior of all the composites is presented.

6.2 Continuous oxidation (non-isothermal)

TGA analysis of the composite was carried out up to 1273K (1000^{o}C) in 1 atmosphere oxygen and air with 10 K/min heating rate. TGA plot in 1 atm oxygen (O_2) flow is given in Fig.6.1. Three different stages of weight gain are observed for each of the composites, (i) no change in sample weight up to 673 – 873K (400-600^{o}C), (ii) a gradual weight gain between 873 to 1073K (600 to 800^{o}C)/ sudden increase in weight gain and (iii) a steep weight gain above 1073K (800^{o}C). In all composites (except TiB_2+CrB_2 composites) the total specific weight gain was less than 30x10^{-3} kg/m^{2} and the rates of weight gain were similar. Detailed investigations were carried out for TiB_2+CrB_2 composites using TG-DTA.

TG-DTA plot of TiB_2 + 5% CrB_2 and TiB_2 + 10% CrB_2 composites are given in Fig.6.2. Two DTA peaks were seen: one starting at 693K (420^{o}C) and the second at 933K (660^{o}C). The first peak indicating the start of oxidation of TiB_2 is more pronounced than the other. The second (minor) peak indicates the start of oxidation of CrB_2. Specific weight gain of the samples indicated by TGA plot shows that the sample with higher CrB_2 content is less prone to oxidation.

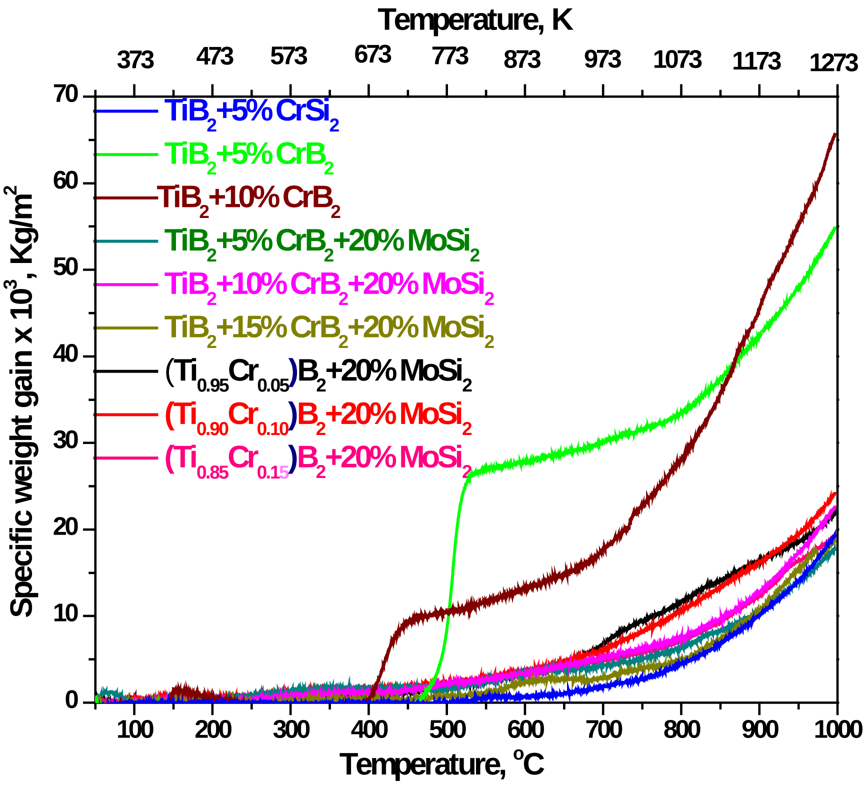

Fig.6.1 TGA plot on continuous oxidation of TiB_2 composites in oxygen.

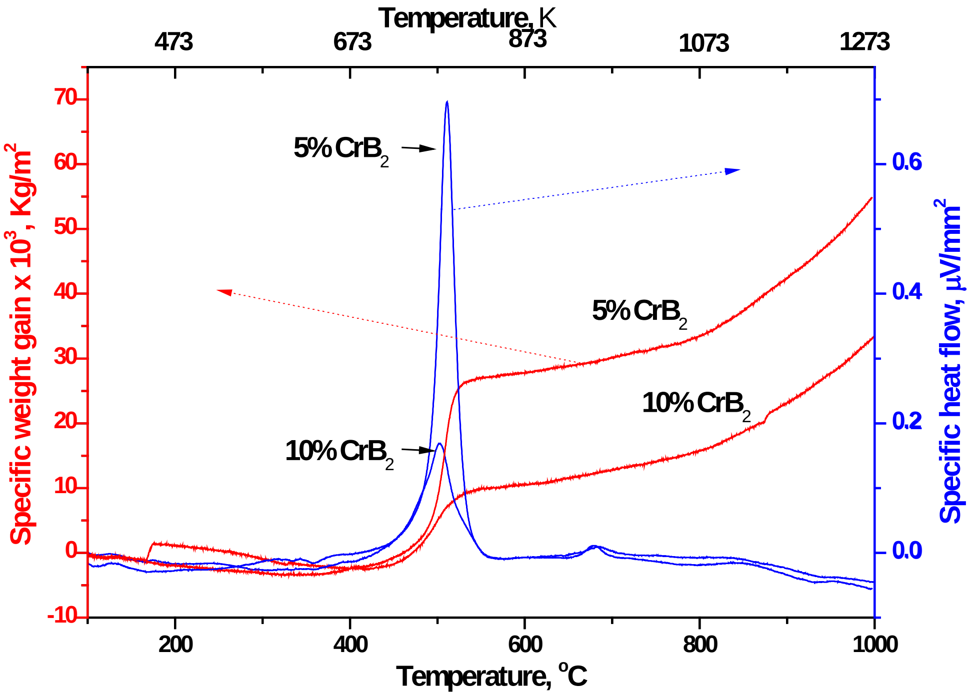

Fig. 6.2 TG-DTA analysis of TiB_2 + CrB_2 composites in oxygen

TGA plot on the continuous oxidation of the composites of TiB_2 + x% CrB_2 (x=5,10,15) + 20% $MoSi_2$ in one atmosphere oxygen pressure are given in Fig.6.1 and in air in Fig.6.3. These results are compared with that of TiB_2 composite with 5% CrB_2. In all the composites, total specific weight gain recorded was in the range of 10-15 x 10^{-3} kg/m^2 at 1173K (900^{o}C). When these composites were oxidized in air, the TGA plot (Fig. 6.3) showed two stages of weight gain, (i) no change in the sample weight up to 773K (500^{o}C) and (ii) a gradual weight gain from 773 to 1173K (500 to 900^{o}C). As expected, the specific weight gain recorded in the range of 5 -10 x 10^{-3} kg/m^2 in air is low due to lower oxygen content as compared to pure oxygen. However, TiB_2 composites containing $MoSi_2$ in addition to CrB_2 show low specific weight gain compared with composites containing only CrB_2. This could be due to the availability of Si, which forms protective layer.

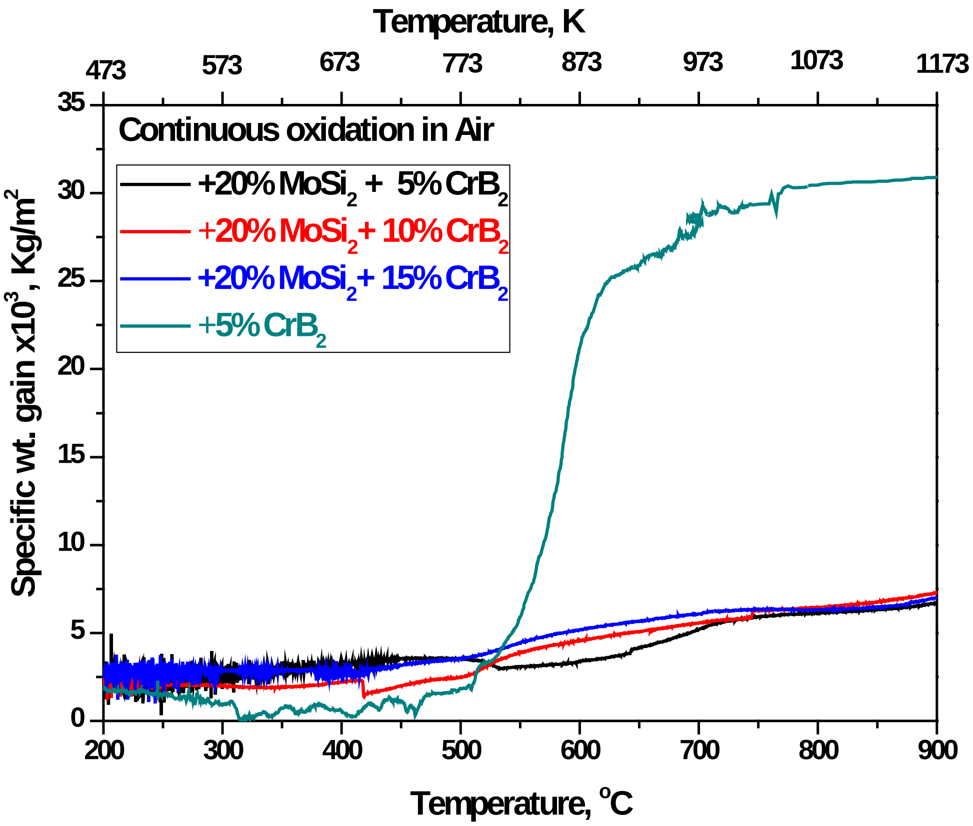

Fig.6.3 Specific wt. gain vs. temperature plot of TiB_2 composites oxidized in air by TGA

SEM images of oxidized surfaces of all composites (5, 10 and 15% CrB_2) up to 1273K (1000^{o}C) after continuous oxidation (TGA) in oxygen are presented in Fig.6.4a-c.These surfaces show the formation of a thick and continuous glassy layer. The surface morphology of composite with 15% CrB_2 is free of cracks (Fig. 6.4c), whereas in the other two samples (5 and 10% CrB_2) cracks are visible (Fig. 6.4 a and b). This shows the effectiveness of CrB_2 content on the formation of a crack free and continuous oxide layer. Morphology of the oxidized surface of $(TiCr)B_2$+$MoSi_2$ samples after continuous oxidation up to 1273K (1000^{o}C), (TGA) in oxygen are presented in Fig. 6.5a-f. These surfaces also show the formation of a thick and continuous glassy layer.

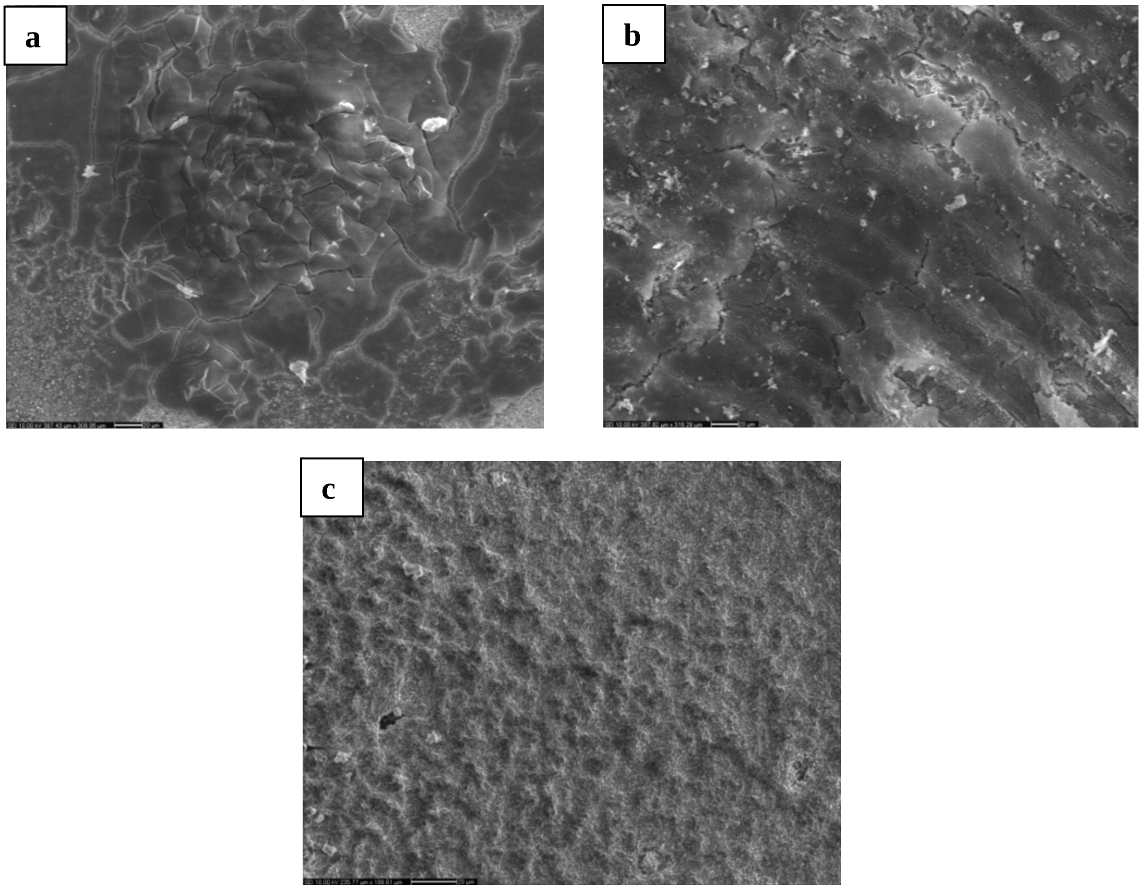

Fig. 6.4 SEM images of oxidized surfaces of (a) 5, (b) 10 and (c) 15%CrB_2 contained TiB_2 + 20% $MoSi_2$ composites after oxidation at 1273K (1000^{o}C) in one atmosphere oxygen pressure (TGA sample).

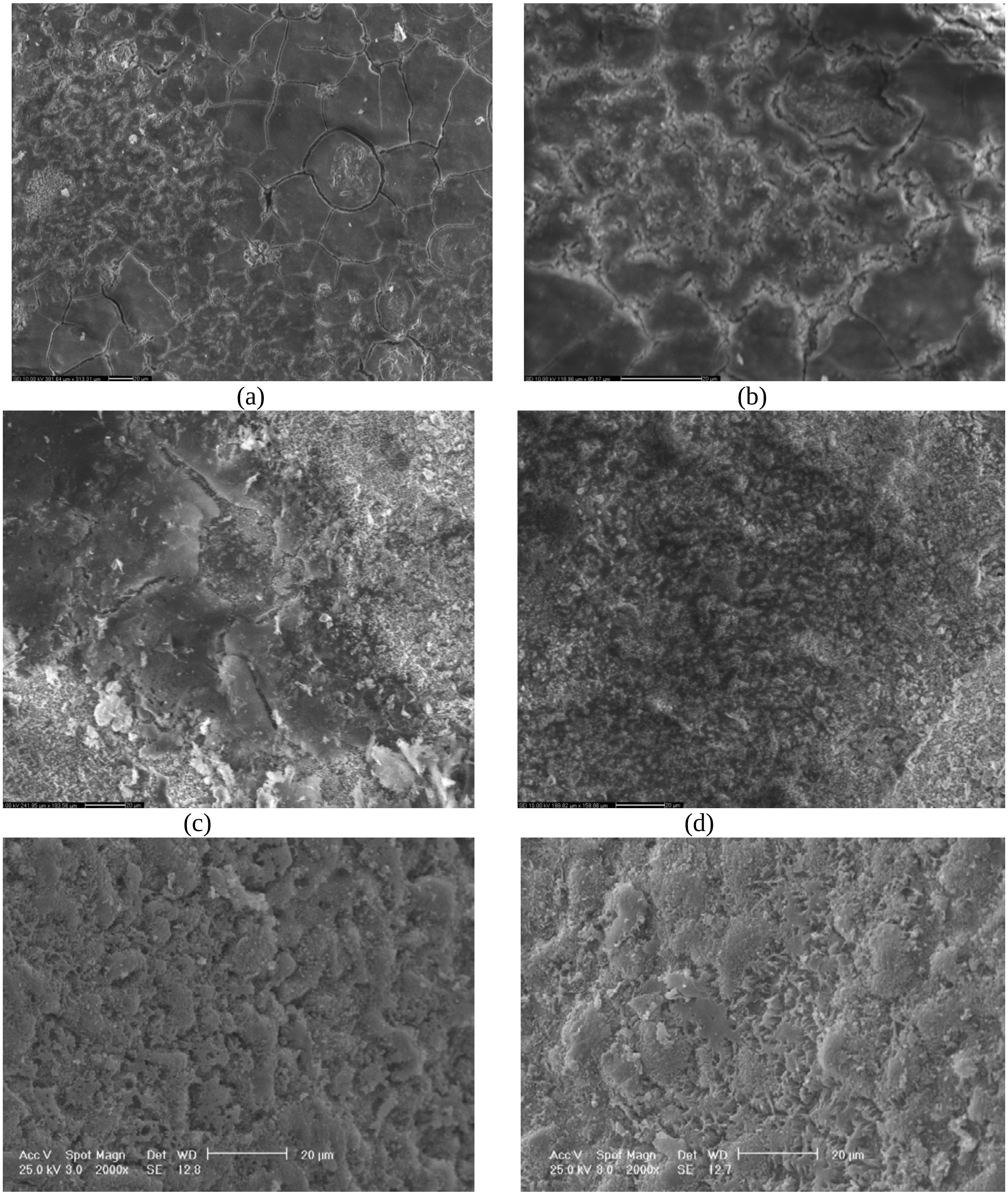

(a) (b)

(c) (d)

(e) (f)

Fig. 6.5 Morphology of the oxidized surface of a&b) $(Ti_{0.95}Cr_{0.05})B_2$+20% $MoSi_2$, c&d) $(Ti_{0.90}Cr_{0.10})B_2$+20% $MoSi_2$ and e&f) $(Ti_{0.85}Cr_{0.15})B_2$+20% $MoSi_2$ composites after continuous oxidation up to 1273K (1000°C), in oxygen (TGA samples)

6.3 Isothermal oxidation

This section presents the results on isothermal oxidation studies. Specific weight gain vs. time plots were drawn at different temperatures. Isothermal oxidation studies for all the composites were done at 1123K (850^{o}C) in air at different time intervals of 0.5, 1, 2, 4, 8, 16, 32 and 64h and in addition at 1023 and 1223K (750 and 950^{o}C) for selected composites. This data is fitted in general rate and parabolic rate equations. Many of the composites are not following the complete parabolic behavior; still the data is fitted in parabolic rate law for comparison purpose. Mechanism of oxidation was understood from the kinetics data. XRD and SEM analysis were used to identify the oxidized products and their morphology. Important findings are given below.

6.3.1 Oxidation studies of TiB_2+$TiSi_2$ composites

Weight gain of the TiB_2+$TiSi_2$ samples during oxidation at 1123K (850^{o}C) as a function of time is presented in Fig. 6.6 and Table 6.1. An increase in weight with time occurs. The recorded values of specific weight gain after oxidation for 64h at 1123K (850^{o}C) were 59.83, 12.92 and 4.84 $x10^{-3}$ kg/m^2 for 2.5, 5 and 10% composites respectively. In order to understand the nature of oxidation, the data were fitted in the general rate equation.

$$(\Delta w/A)^m = K_m.t \qquad (6.1)$$

Where Δw- is the change in weight, A- surface area of the sample, t- oxidation time and K_m- rate constant. K_m and m values are presented in Table 6.1. The nature of oxidation appears to be near parabolic for 2.5% $TiSi_2$ sample as seen by the slope of the curve (1.789). To understand the kinetics of oxidation, the data was analyzed using the parabolic law.

$(\Delta w/A)^2 = K_p.t$

(6.2)

Where K_p- parabolic rate constant. K_p of TiB_2+2.5%$TiSi_2$ are presented in Table 6.1.

XRD pattern of surface oxide layer of 2.5% $TiSi_2$ sample after 1, 4, 16 and 64 hours are shown in Fig. 6.7. The phases seen are TiO_2 (PCPDF 88-1172) and SiO_2 (PCPDF 89-1667) in all the samples.

Table 6.1 Specific weight gain and rate constants after 64h of oxidation

Material	Sp.wt. gain, kg/m^2 x 10^3	$^*K_p$ ($Kg^2\ m^{-4}\ s^{-1}$)	$^\$K_m$	$^\#m$
TiB_2+2.5%$TiSi_2$	59.83	1.377×10^{-7}	2.280×10^{-7}	1.789
TiB_2+5%$TiSi_2$	12.95	6.11×10^{-8}	-	1.990
TiB_2+10%$TiSi_2$	4.84	1.25×10^{-8}	-	2.012

($^*K_p$ – Parabolic rate constant, $^\$K_m$ – Rate constant of general rate equation, $^\#$m- Slope of general rate equation)

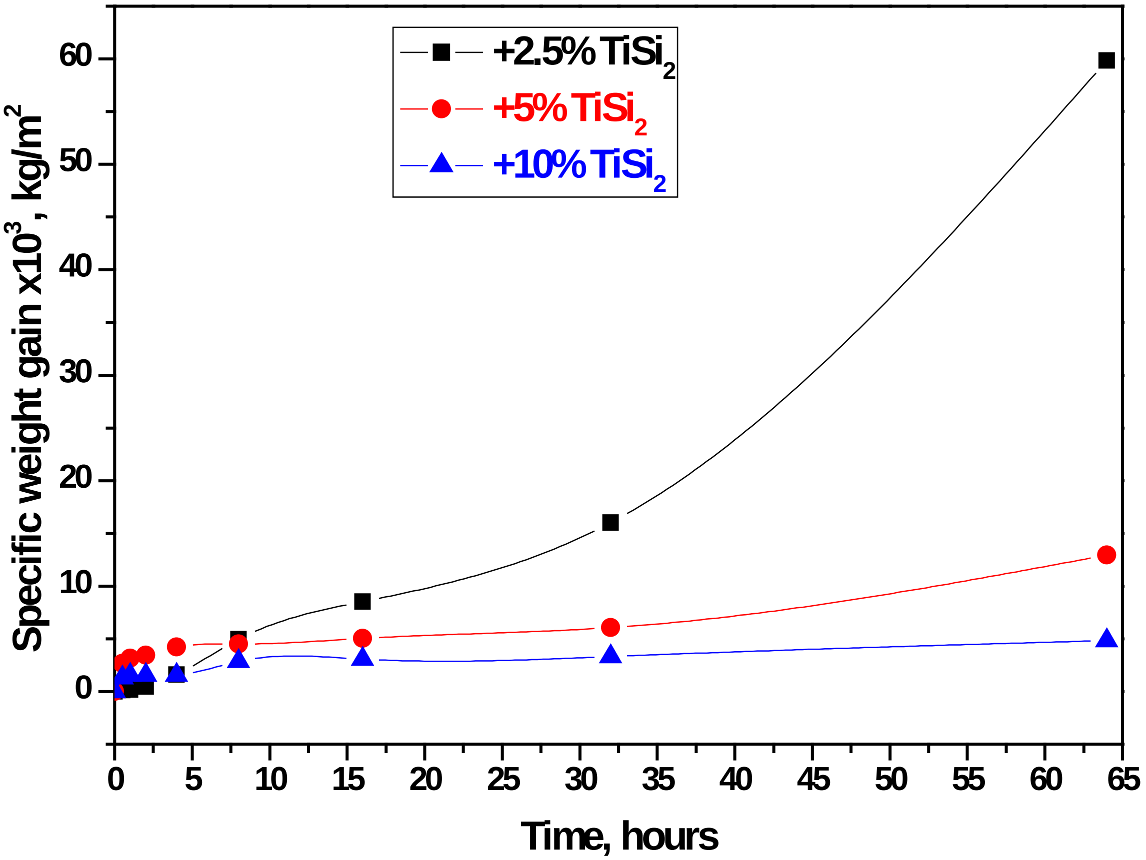

Fig. 6.6 Specific weight gain of the TiB_2+TiSi_2 samples during oxidation at 1123K in air

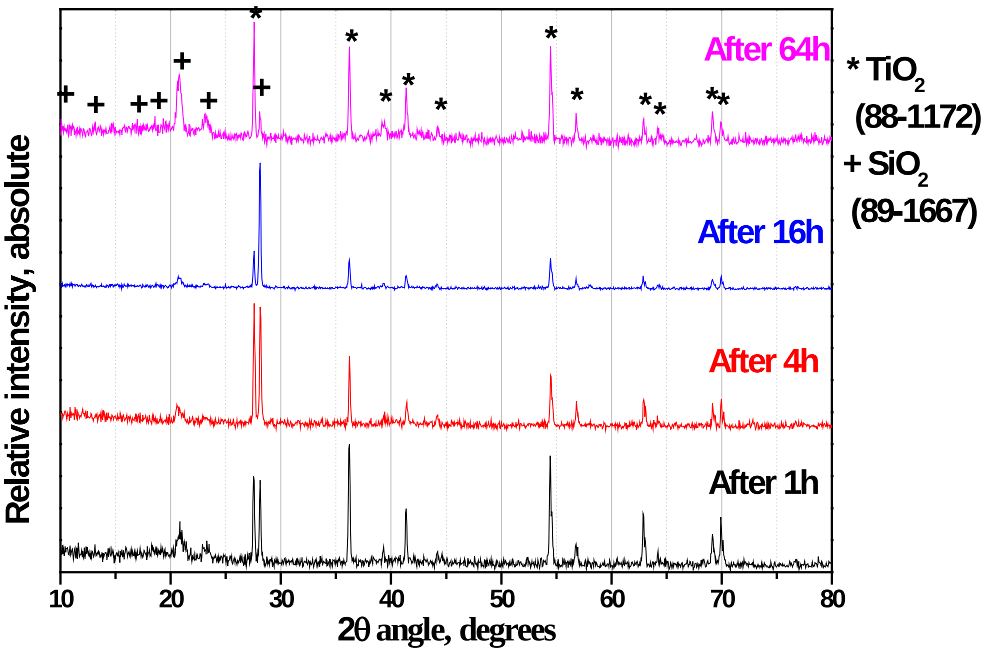

Fig. 6.7 XRD pattern of the oxidized surfaces of TiB_2+2.5%$TiSi_2$ samples at different time intervals

Scanning electron micrographs of the surface oxide scales after oxidation at 1123K (850^{o}C) for 64h are presented in Fig.6.8.The oxidized surface appears to be continuous and crack free with stable SiO_2 layer and spherical crystalline TiO_2.

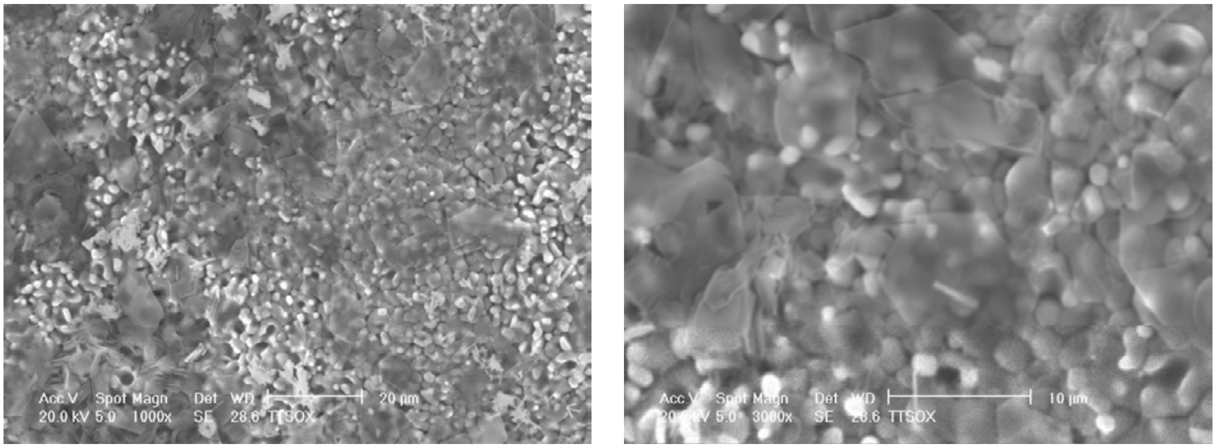

(a) (b)

Fig. 6.8 SEM image of the Oxidized surface of TiB_2+2.5%$TiSi_2$ after 64h of oxidation at 1123K

Murthy *et al*.[1] while characterizing the oxidized surface of TiB_2 and TiB_2+$MoSi_2$ composites under similar oxidizing conditions, have seen the major phase as TiO_2 only on the oxidized surface by XRD analysis, but SEM-EDS showed the presence of boron oxide and silicon oxide in addition to TiO_2. Pugach et al. [2] have reported the presence of TiO_2, SiO_2 and B_2O_3 on the surface of oxidized TiB_2 + 20 %$TiSi_2$ in the range of 1273-1473K (1000- 1200^{o}C). Koh *et al*. [3] have reported a parabolic weight gain and the formation of $TiO_2(s)$ and $B_2O_3(l)$ on the oxidized surface of TiB_2 at temperatures below 1273K (1000^{o}C). Graziani *et al*. [4] reported the kinetics of oxidation of TiB_2+20%B_4C in air to be parabolic upto 1173K (900^{o}C) and the oxide scale containing TiO_2, B_2O_3 and traces of $TiBO_3$. Kulpa *et al*. [5] have found the formation of $TiBO_3$ while heating TiB_2 in low partial pressures of oxygen up to a temperature of

1273K (1000^{o}C). For TiB_2+2.5wt% Si_3N_4 composite, at temperature below 1273K (1000^{o}C), parabolic weight gain was observed [7]. Formation of SiO_2 layer on the oxidized surface of TiB_2+$TiSi_2$ appears to be responsible for the better oxidation resistance of this composite compared with TiB_2+$MoSi_2$ sample [1].

Oxidation of TiB_2+$TiSi_2$ samples may be represented by the following overall reactions.

$$2/5TiB_2 + O_{2(air)} \rightarrow 2/5TiO_2 + 2/5B_2O_3 \qquad (6.3)$$

$$1/3TiSi_2 + O_{2(air)} \rightarrow 1/3TiO_2 + 2/3SiO_2 \qquad (6.4)$$

$$1/8Ti_5Si_3 + O_{2(air)} \rightarrow 5/8TiO_2 + 3/8SiO_2 \qquad (6.5)$$

Free energy of formation for the above reactions is calculated for 0.21 atm partial pressure of oxygen by using FactSage software version 6.3 [6] and presented in Fig. 6.9. All these reactions are thermodynamically possible. Among these, reaction 6.4 ($TiSi_2$) has more negative free energy compared with reactions 6.3 and 6.5 (TiB_2 and Ti_5Si_3).

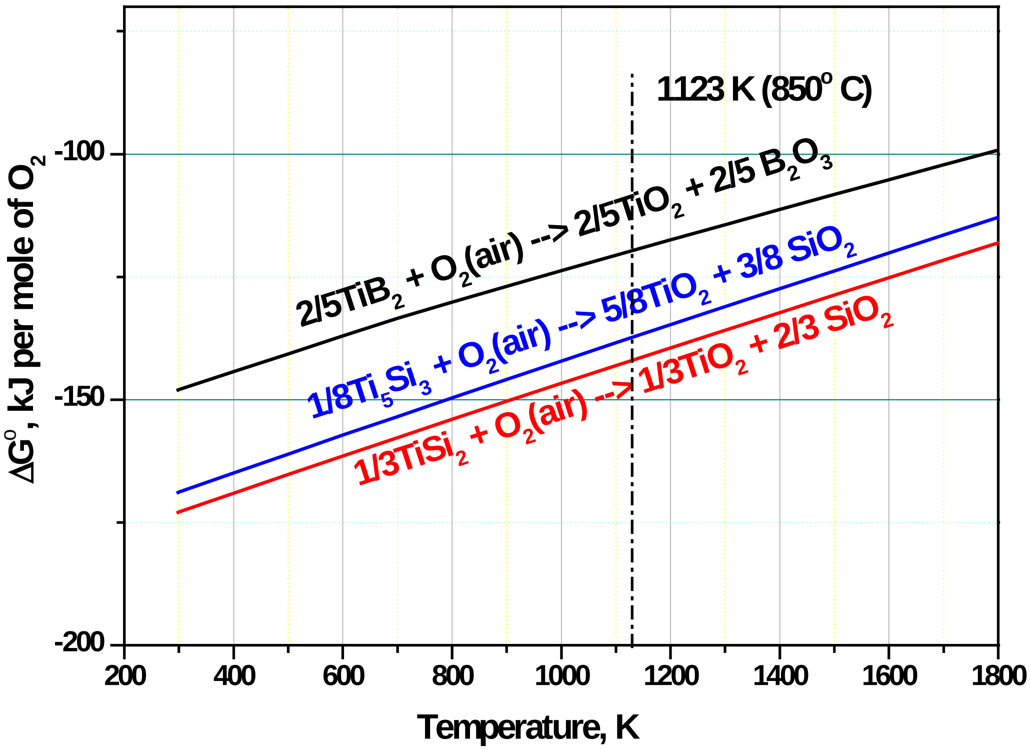

Fig. 6.9 Free energy data for the formation of oxides at 0.21 atm partial pressure of oxygen

6.3.2 Oxidation studies of TiB_2+$CrSi_2$ composites

The weight gain data obtained during isothermal oxidation at 1123K (850°C) as a function of time for 2.5%, 5%, 10% and 15% $CrSi_2$ composites are presented in Fig.6.10. Continuous weight gain with time is observed in all the samples. With increasing $CrSi_2$ content, decrease in weight gain rate is seen. The recorded values of specific weight gain after oxidation for 64h at 1123K (850°C) were 0.150, 0.123, 0.113 and 0.058 kg/m^2 for 2.5, 5, 10 and 15% composites respectively.

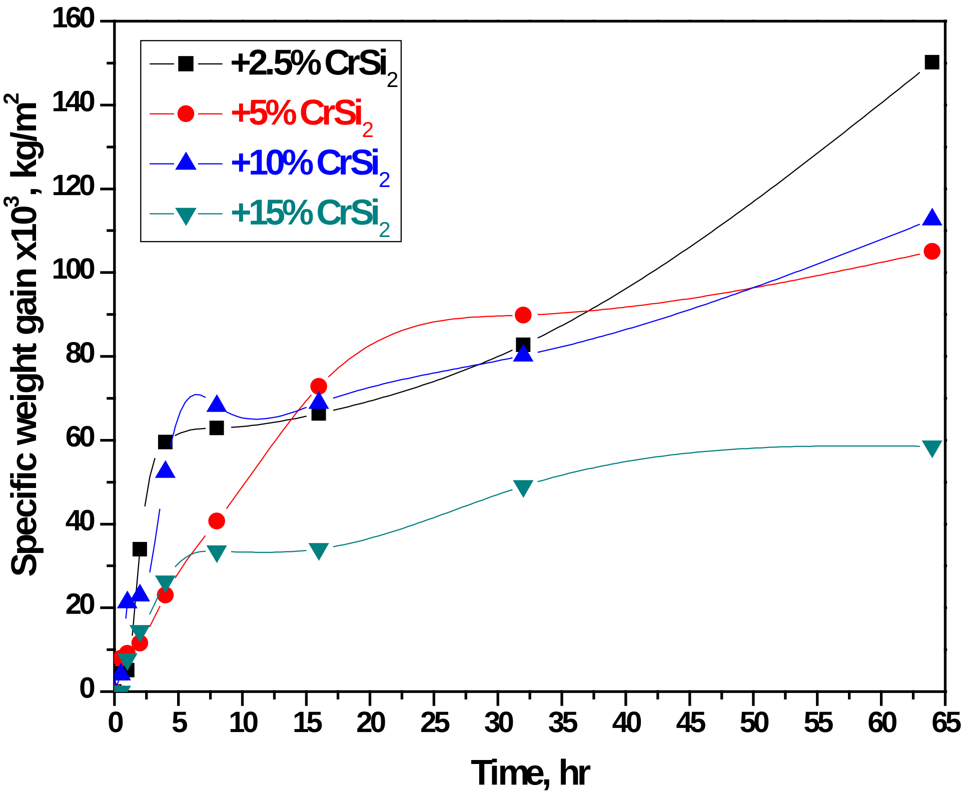

Fig. 6.10 Specific wt. gain vs. Time during oxidation of TiB_2+$CrSi_2$ composites at 1123K (850°C) in air

Calculated K_p, K_m and m values of all the composites are presented in Table 6.2. The nature of oxidation appears to be parabolic (m=1.99 to 2.71) for all the composites. Parabolic rate constants of all three composites (2.5, 5 and 10%) are in the same order (6 to 9 x 10^{-8} kg^2 m^{-4} s^{-1}) indicating the mechanism of oxidation to be similar. The value of parabolic rate constant is found to decrease with increase of $CrSi_2$ content, indicating the effectiveness of $CrSi_2$ addition in improving the oxidation resistance.

To measure the kinetics, oxidation of TiB_2+5% $CrSi_2$ was carried out at five different temperatures 1023, 1073, 1123, 1173 and 1223K (750, 800, 850, 900 and 950°C) up to 64h. Specific weight gain vs. time plots are presented in Fig.6.11. The weight gain measured was least at the lowest oxidation temperature of 1023K (750°C). At 1123 and 1223K (850 and 950°C) the weight gain plot is parabolic up to 16h and linear afterwards. Up to 16h, the weight gain of the sample oxidized at 1123K (850^{o}C) is lower than at 1223K (950^{o}C). However, a reversal in weight gain is noted after 16h. This could be due to the evaporation of sub oxides of boron and/or Cr at 1223K after 16h of holding. Specific weight gain recorded after 64h of oxidation was 0.008, 0.123 and 0.103 kg/m^2 at 1023, 1123 and 1223K (750, 850 and 950^{o}C) respectively.

Table 6.2 Rate constants of isothermal oxidation kinetics of TiB_2 composites at 1123K (850^{o}C) in air up to 64h

Sinter additive	Kp* (Kg^2 m^{-4} s^{-1})x10^8	Km$^{\$}$ x 10^8	m$^{\#}$
2.5% $CrSi_2$	8.94	6.67	2.129
5% $CrSi_2$	6.91	7.05	1.992
10% $CrSi_2$	6.73	1.17	2.716
15% $CrSi_2$	1.91	0.37	2.540

($^{*}K_p$ – parabolic rate constant, $^{\$}K_m$ – rate constant of general rate equation, $^{\#}$m- slope of general rate equation)

The oxidation data up to 16h was fitted in an Arrhenius equation (6.6) and the plot is shown in Fig.6.12.

$$Kp = Ko \exp(-Q/RT) \tag{6.6}$$

where, Q is the activation energy, R is the gas constant, T is temperature in K. The value of activation energy obtained was 114.9 kJ/mol in the temperature range of 1023 to 1223K (750 to 950^{o}C). Tampieri and Bellosi [8] have reported an activation energy of 230 kJ/mol (T: 673 to 1173K) and 40 kJ/mol (T: 1173 to 1373K) for monolithic TiB_2. The vast difference in the value of activation energy for TiB_2 oxidation with temperature is due to change in mechanism caused by the evaporation of B_2O_3 at higher temperatures [8].

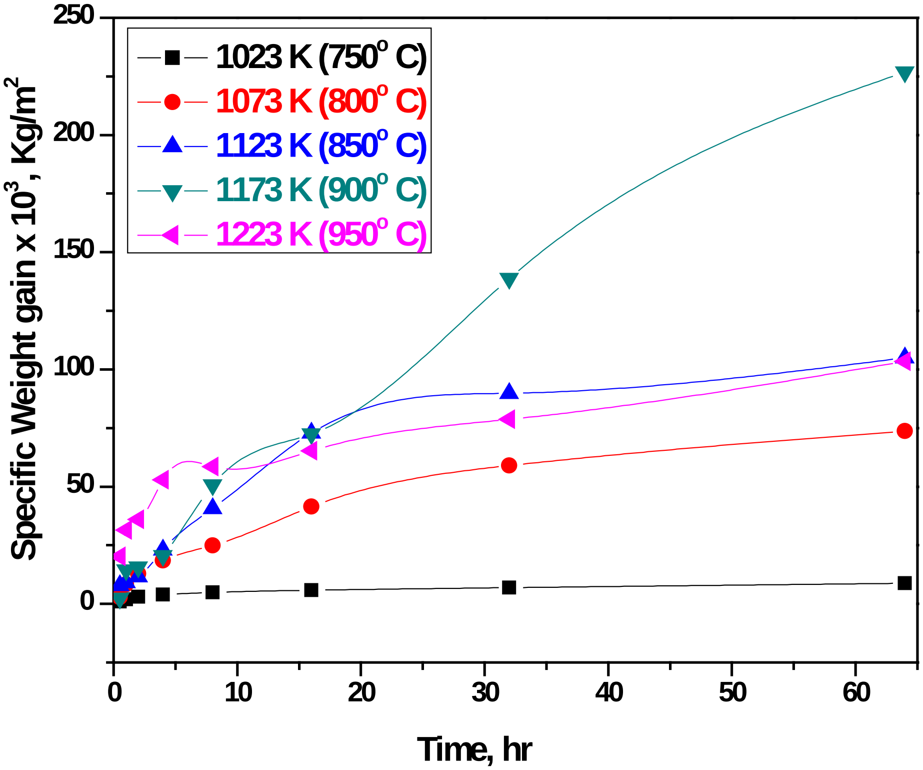

Fig. 6.11 Specific weight gain vs. time plot of TiB_2+5%$CrSi_2$ composite at 1023, 1073, 1123, 1173 and 1223K (750, 800, 850, 900 and 950°C)in air

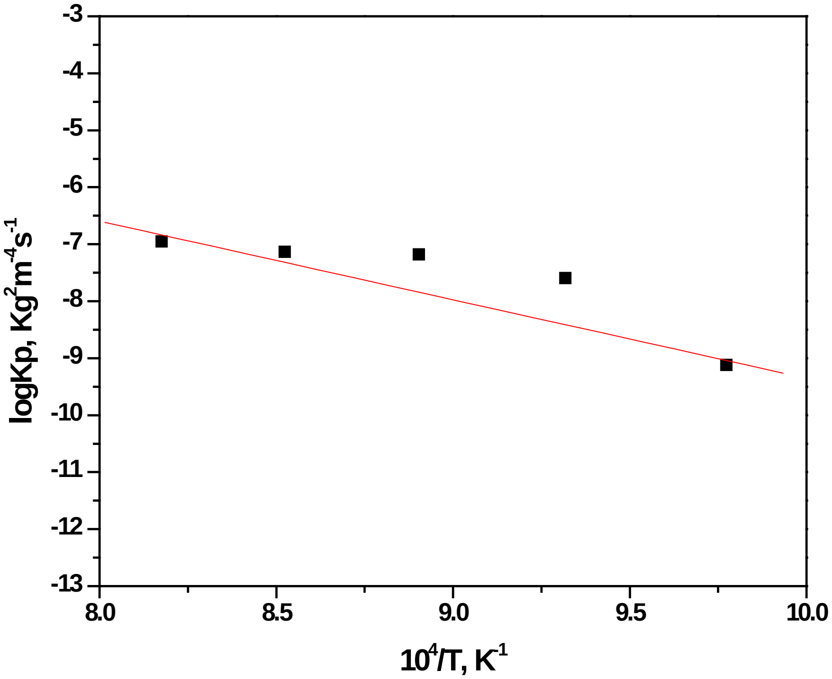

Fig. 6.12 Arrhenius plot of log K_p vs 1/T for TiB_2+5%$CrSi_2$ composite (Activation energy = 114.9 kJ/mol)

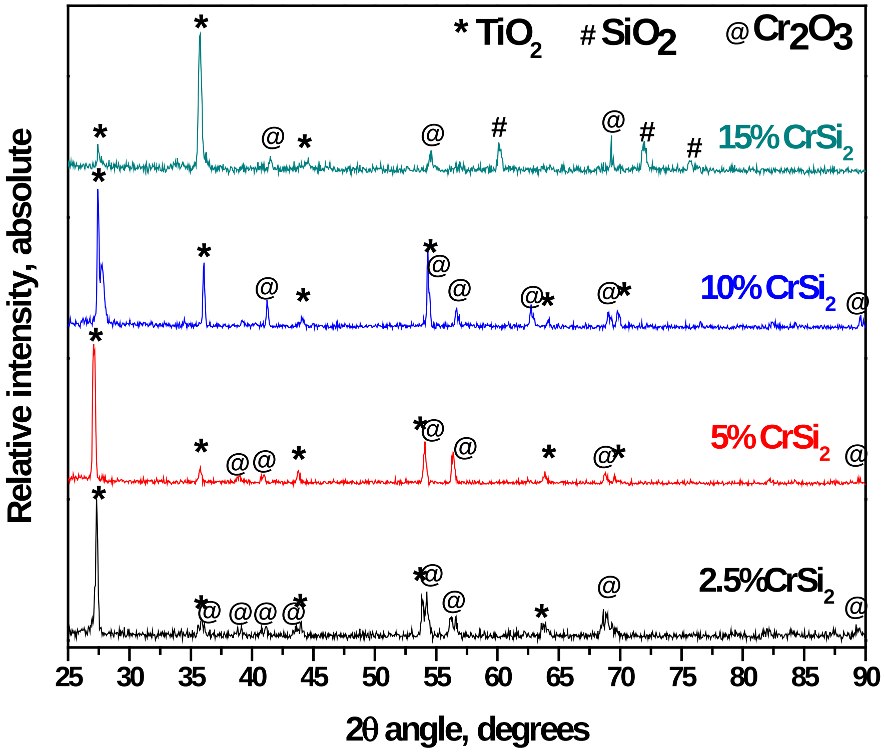

Fig. 6.13 XRD pattern of the oxidized surfaces of TiB$_2$+CrSi$_2$ composites after oxidation at 1123K (850^{o}C) for 64h in air

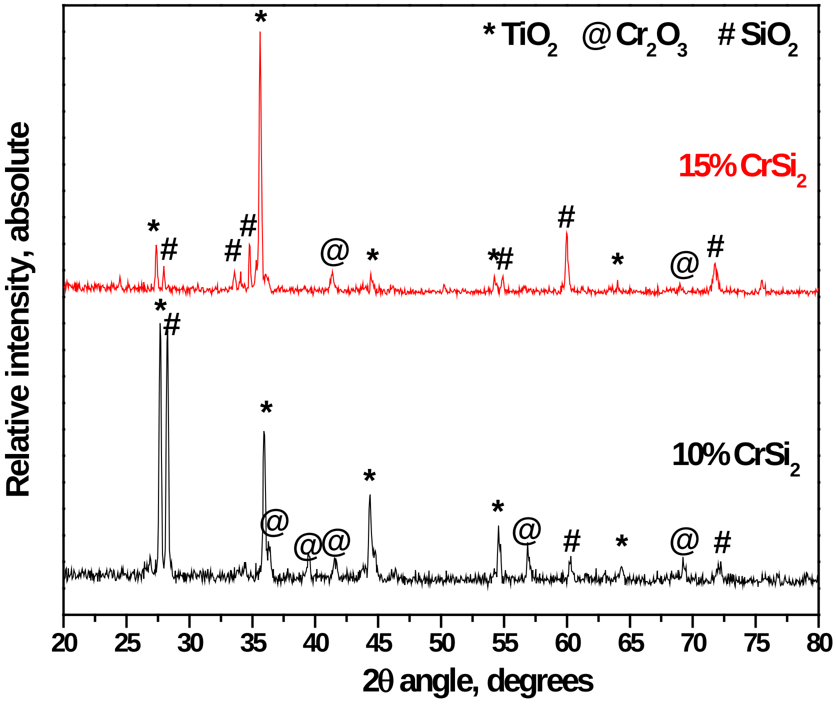

Fig. 6.14 XRD pattern of oxidized surfaces of TiB$_2$ composites after oxidation at 1273K (1000^{o}C) for 4 h in air

The activation energy obtained in the present study with the addition of $CrSi_2$ to TiB_2 lies in between the values obtained by the above authors (Tampieri and Bellosi [8]). Graziani et al. [4] have reported activation energy of 220 kJ/mol for TiB_2+20vol%B_4C composite in the temperature range of 973 to 1173K (700 to 900^oC).

XRD patterns of surface layer of all the composites oxidized at 1123K (850^oC) for 64 hours are shown in Fig. 6.13. TiO_2 and Cr_2O_3 phases were identified in all the composites. In addition, SiO_2 peaks were observed in 15% $CrSi_2$ composite. The surface oxide layer obtained at a higher temperature of 1273K (1000^oC) for 4 h showed the presence of all the phases (TiO_2, Cr_2O_3 and SiO_2) (Fig. 6.14).

Oxidation of TiB_2+$CrSi_2$ composite may be represented by the following overall reactions:

$$2/5TiB_2(s) + O_2(air) \rightarrow 2/5TiO_2(s) + 2/5B_2O_3(l) \quad (6.7)$$

$$4/11CrSi_2(s) + O_2(air) \rightarrow 2/11Cr_2O_3(s) + 8/11SiO_2(s) \quad (6.8)$$

$$2/7CrSi_2(s) + O_2(air) \rightarrow 2/7CrO_3(g) + 4/7SiO_2(s) \quad (6.9)$$

$$1/3CrSi_2(s) + O_2(air) \rightarrow 1/3CrO_2(g) + 2/3SiO_2(s) \quad (6.10)$$

For the system $CrSi_2$-O_2, the thermodynamic probability of reactions taking place resulting in the formation of gaseous SiO is small [9] and hence not considered. Free energy of formation for the above reactions in 0.21 atm partial pressure of O_2 is calculated by using FactSage software version 6.3 [6] and presented in Fig.6.15. It is clear that all these equations are thermodynamically feasible. Oxidation of TiB_2 is more favorable compared to $CrSi_2$. Although formation of gaseous CrO_3 (ΔG^o=-93 kJ/mol) and CrO_2 (ΔG^o=-101 kJ/mol) are thermodynamically more favorable compared to Cr_2O_3(ΔG^o=-80 kJ/mol), weight gain of the sample during oxidation and the XRD results indicate the formation of Cr_2O_3 only (CrO_3 and CrO_2 are in gaseous state) in the present investigation. During oxidation of the composite, B_2O_3 is formed first which increases in thickness due to the high mobility of small sized boron atom and this liquid layer of B_2O_3 controls further oxidation [10,11]. As oxygen ions have to diffuse through this liquid layer, rate of oxidation decreases further. With the available of limited oxygen beneath the liquid layer, lower oxide of chromium (Cr_2O_3) is more stable.

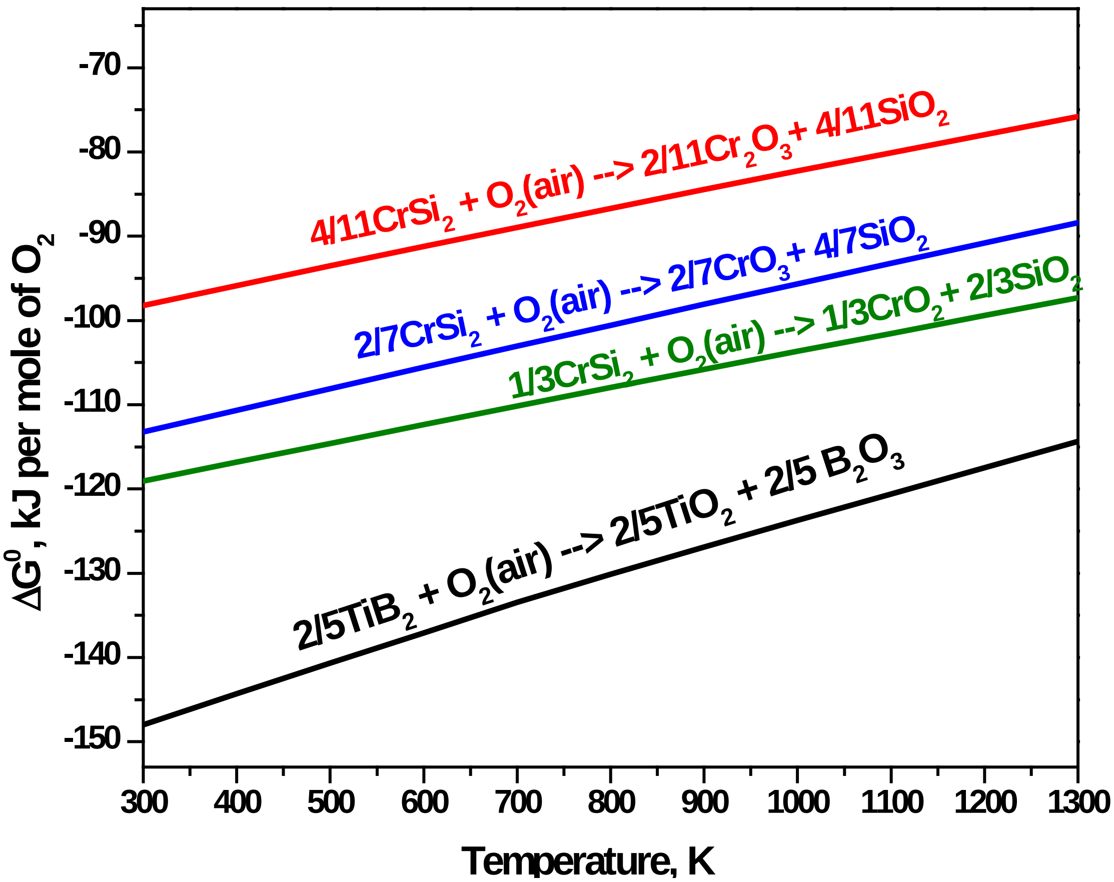

Fig. 6.15 Free energy data for the formation of oxides at 0.21 atm partial pressure of oxygen[6].

Crystalline B_2O_3 and TiO_2 were found on the oxidized surfaces of TiB_2 at 973 and 1073K (700 and 800^oC) [8]. The large volume expansion that occurs during the oxidation of

TiB_2 to TiO_2 subsequently causes cracking of the oxide layer, resulting in an increase in the active area for further oxidation [12,13]. Dasgupta et al [14] have reported good oxidation resistance of $CrSi_2$ powder up to 873K (600°C) in air. Ma et al. [15] have found that oxidation of $CrSi_2$ starts at 1089K (816°C) and a weight gain of only about 8.6 wt% of the sample on oxidation up to 1273K (1000°C), due to a protective oxide layer (crystalline Cr_2O_3 and amorphous SiO_2) formation on the surface. Gang et al. [16] observed the formation of Cr_2O_3 and SiO_2 phases on oxidation of $CrSi_2$ at 1773K (1500°C) for 34h in air. Cr_2O_3 is nonvolatile, insoluble in SiO_2 and helps to form a protective layer on the surface [9]. Naoyuki et al. [18] have reported excellent oxidation resistance of $CrSi_2$ upto 1373K (1100°C) due to the formation of a thin and dense SiO_2 layer. Shishido et al.[19] has not observed any weight gain of the $CrSi_2$ during heating up to 1473K (1200°C) in air. Both SiO_2 and TiO_2 are soluble in molten B_2O_3[20,21]. In fact eutectic reaction of SiO_2 with B_2O_3 is seen at 724K (451°C) at 5% SiO_2 composition.

SEM images of oxidized surfaces (5% $CrSi_2$ composite) at 1023, 1123 and 1223K (750, 850 and 950°C) for 64h is shown in Fig.6.16 (a-c). All the surfaces appear to be crack free. Globules of oxidized particles are seen on oxidation at 1023K (750°C) (Fig 6.16 a). At 1123K (850°C), the oxidized particles are elongated, acicular and a few bunches of particles are joined together (Fig.6.16b). At 1223K (950°C), the size of the particles has increased due to coagulation (Fig.6.16c). These images clearly present the early stage of oxidation, growth of oxide crystals and coagulation with temperature. SEM images of oxidized surfaces of 2.5, 5, 10 and 15% $CrSi_2$ at 1123K (850°C) for 64h are presented in Fig.6.17(a-d). In 2.5% $CrSi_2$ composite, the start of coagulation of liquid formed by oxidation (Fig.6.17a) is seen. With increasing $CrSi_2$ content, coagulation increases to give a protective and continuous oxide layer. In the 15% $CrSi_2$

composite, the size of the coagulated particles is bigger and formation of a near complete protective layer is seen (Fig.6.17d). SEM images of samples (2.5, 5, 10 and 15% $CrSi_2$ composites) oxidized at 1273K (1000^oC) for a shorter duration of 4h are shown in Fig.6.18 (a-d). Here also all the surfaces appear to be crack free. The morphology of oxide layer appears to be different for different composites. In 2.5% $CrSi_2$ samples, one could see fine crystals of oxide particles fusing together to form a glassy looking phase. The image for 5% $CrSi_2$ shows the surface covered with bigger size crystalline layer (Fig.6.18b). In this image also the crystals appear to be fused and joined together.

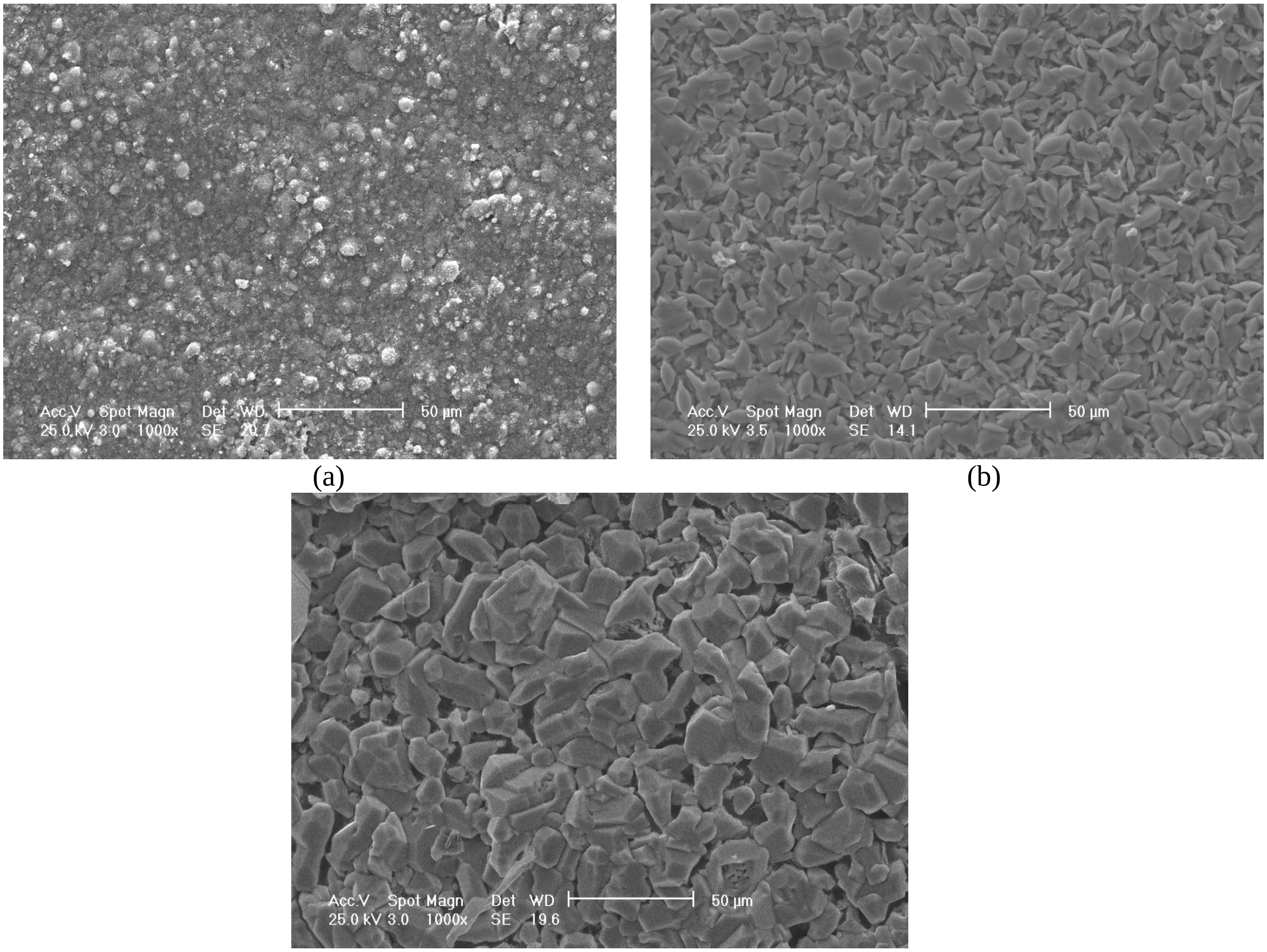

(a) (b)

(c)

Fig.6.16 SEM images of oxidized surface of 5% $CrSi_2$ composite at a) 1023, b) 1123 and c) 1223K after 64 h in air

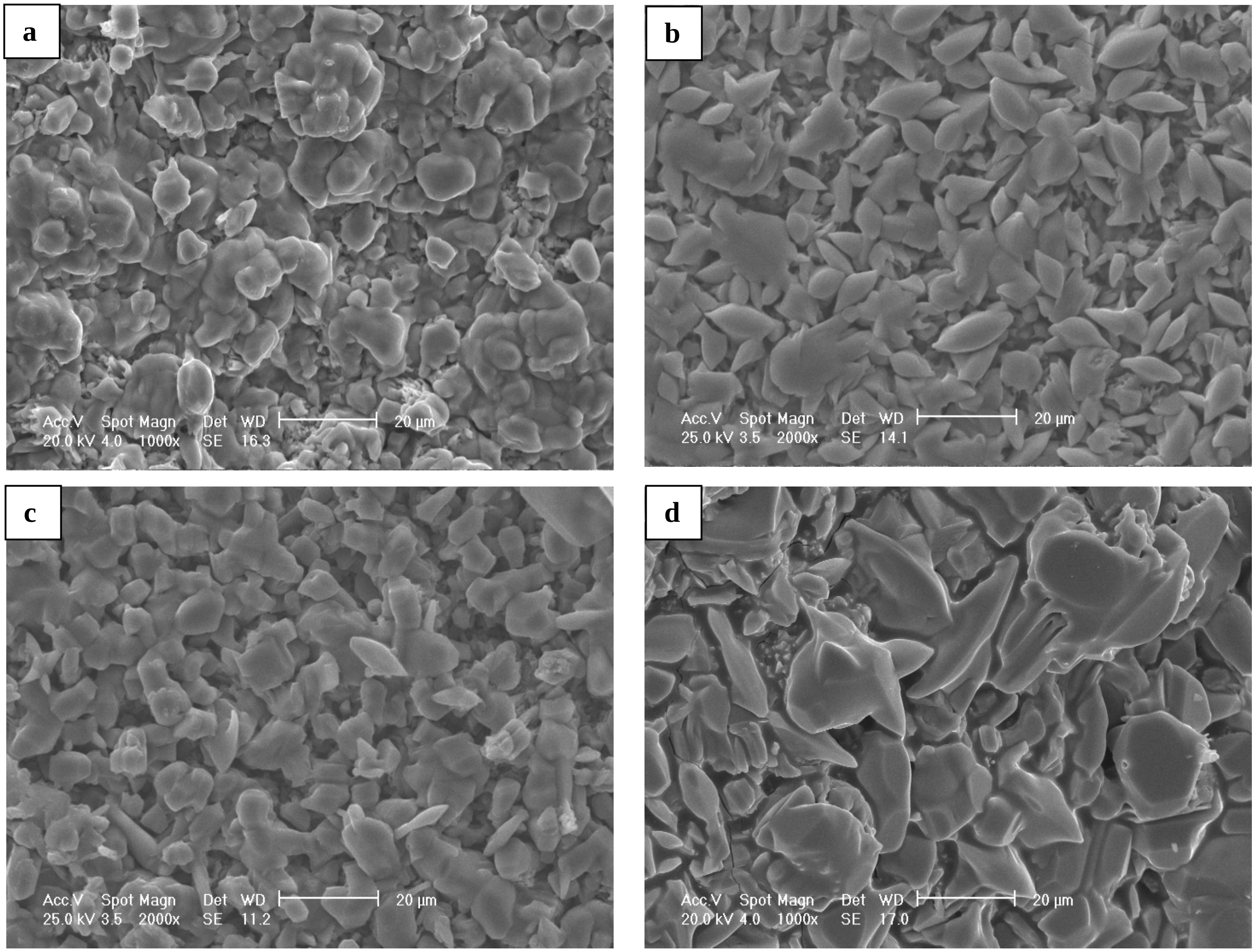

Fig. 6.17 SEM images of oxidized surfaces of TiB_2 +$CrSi_2$ composites with (a) 2.5% (b) 5 % (c) 10% and (d) 15% $CrSi_2$ after oxidation at 1123K (850°C) for 64h in air

Appearances of crystals with morphology similar to that observed presently was reported by Koh et al. [7] and Tampieri & Bellosi [8]. The latter group also reported the formation of a continuous needle like TiO_2 oxide scale at temperatures above 1173K (900°C). In 10% $CrSi_2$

composite more area of the surface is covered by the glassy phase and the needle like structure has disappeared (Fig.6.18c).

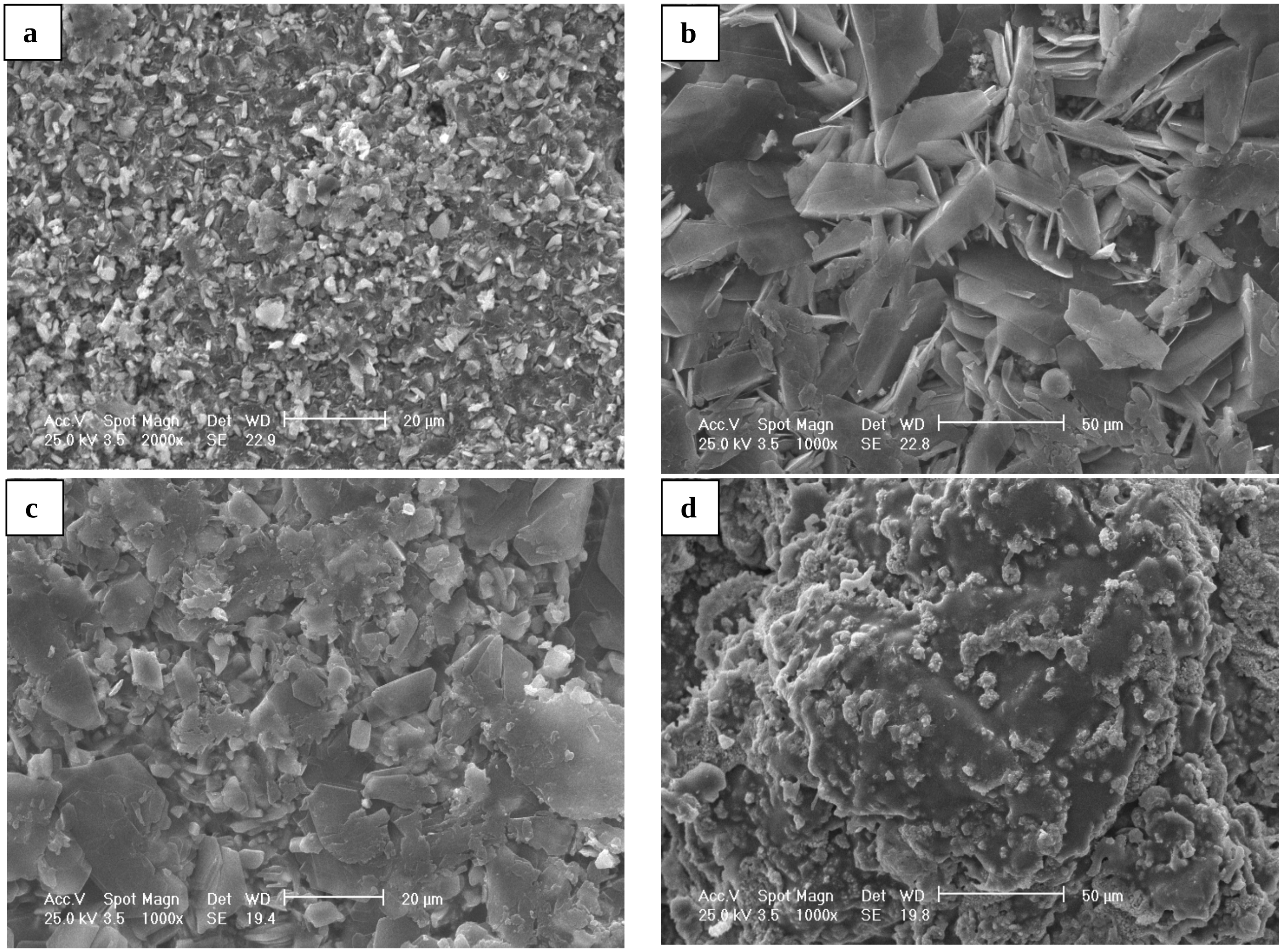

Fig. 6.18 SEM images of oxidized surfaces of TiB_2 +$CrSi_2$ composites with (a) 2.5% (b) 5% (c) 10% (d) 15% $CrSi_2$ after oxidation at 1273K (1000^oC) for 4 h in air.

The surface is fully covered by glassy layer in the 15% $CrSi_2$ composite (Fig.6.18d). From the above it is clear that both temperature of oxidation and the amount of $CrSi_2$ determine the formation of a protective glassy phase. Though the formation of protective glassy layer was observed with 5% $CrSi_2$ sample at 1223K (950°C) after 64h and with 15% $CrSi_2$ at 1123K (850°C) after 64h, a continuous fully covered glassy layer is formed with 15% $CrSi_2$ at 1273K (1000°C) after 4h.

Measurement of electrical resistivity of TiB_2 + 5%$CrSi_2$ sample in air (Fig.6.19) has shown very interesting results. Y-axis of this Figure is in Ohm-cm, whereas that of Figure 5.32 (Electrical resistivity in inert atmosphere) is in micro Ohm-cm. A steep raise in electrical resistivity at 1103K (830°C) and continuous decrease above 1233K (960°C) was observed (Fig.6.19). The increase in resistivity is about 5 orders higher compared to that measured in an inert atmosphere, which is probably due to the formation of non-conducting oxides such as $TiO_{2,}$ Cr_2O_3 and B_2O_3. At higher temperatures (above 1233K) formation of liquid/glass phases like $B_2O_{3,}$ borosilicate, eutectics/mixtures of B_2O_3-TiO_2 and B_2O_3-SiO_2 are responsible for the enhanced electrical conductivity. Electrical resistivity of glasses will decrease with increase of temperature. The ion mobility of glasses increases with increasing temperature [28,29]. For example, 13 orders of lower electrical resistivity was reported for silica (SiO_2) by heating it to 1073K (800°C) from 293K (20°C) [29].

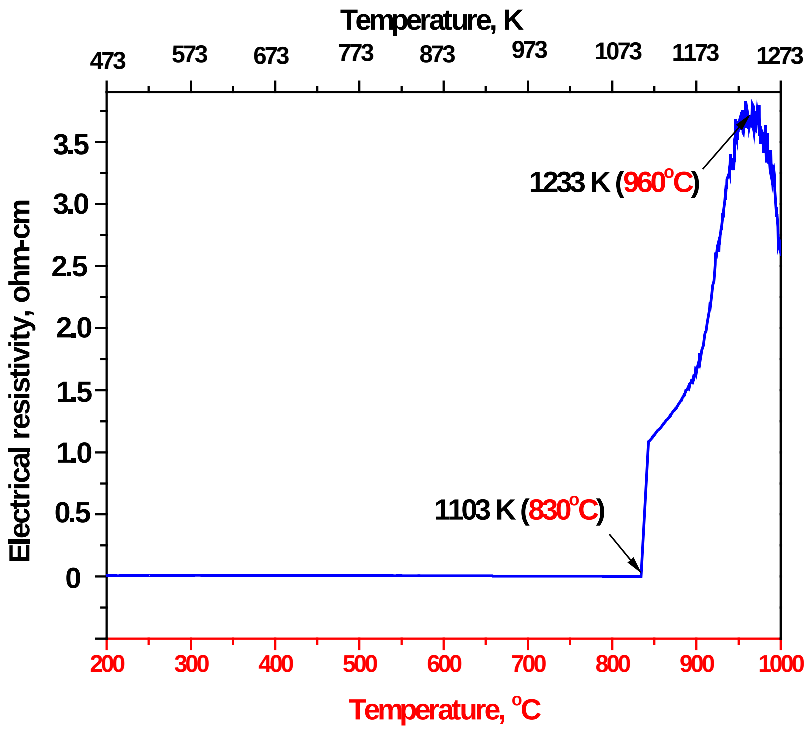

Fig. 6.19 Electrical resistivity vs. temperature of TiB_2+5%$CrSi_2$ composite in air

6.3.3 Oxidation studies of TiB_2+WSi_2 composites

The weight gain data obtained during isothermal oxidation at 1123K (850°C) as a function of time for 2.5%, 5%, 10% and 15% WSi_2 composites are presented in Fig.6.20. Continuous weight gain with time is observed in all the samples. With increasing WSi_2 content, decrease in weight gain rate is seen. The recorded values of specific weight gain after oxidation for 64h at 1123K (850°C) were 0.130, 0.047, 0.063 and 0.038 kg/m^2 for 2.5, 5, 10 and 15% composites respectively.

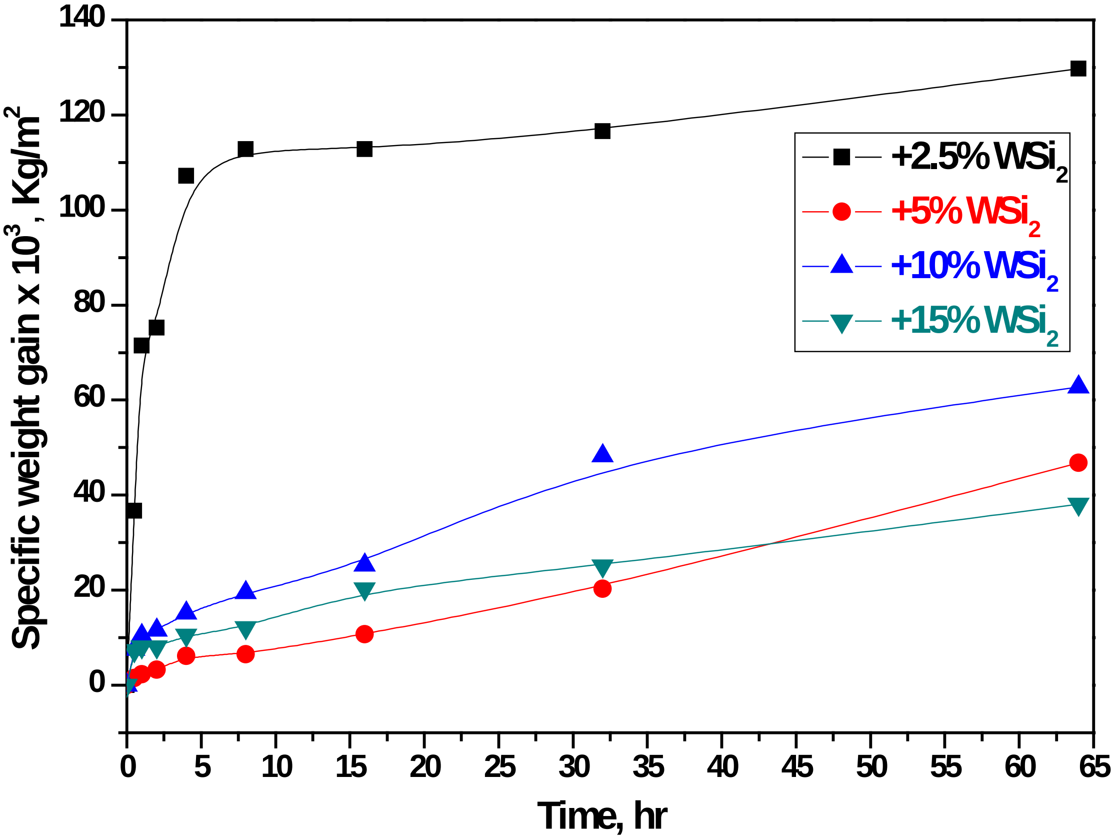

Fig. 6.20 Specific weight gain vs. time plot of isothermal oxidation at 1123K (850^{o}C) for 64h

K_p, K_m and m values of all the composites are presented in Table 6.3. A drastic decrease in the K_m value is noted with addition of WSi_2, from 255.2 x 10^{-8} for 2.5% composite to 19.93, 2.51 and 0.22 x10^{-8} for 5, 10 and 15% WSi_2 respectively. The nature of oxidation appears to be linear and para-linear for 2.5% (m<1.0) and 5% (m=1.5) composites respectively, close to parabolic (m=1.86) and complete parabolic for 10% and 15% (m=2.297) composites respectively. Parabolic rate constants (Table 6.3) of all three composites (5, 10 and 15%) are in the same order (0.55 to 1.62 x 10^{-8} kg^2 m^{-4} s^{-1}) indicating similar mechanism of oxidation. The value of parabolic rate constant is found to increase one order (14.22 x 10^{-8}) when the addition of WSi_2 is low at 2.5%.

Table 6.3 Specific weight gain, rate constants and slope of isothermal oxidation of TiB_2 + WSi_2 composites at 1123K (850°C) in air after 64h

Sinter additive	Specific weight gain, Kg/m^2 x 10^3	Kp^* ($Kg^2 m^{-4} s^{-1}$)x10^8	$Km^\$$ x 10^8	$m^\#$
2.5% WSi_2	129.72	14.22	255.2	<1.0
5% WSi_2	46.76	0.55	19.93	1.500
5%WSi_2 (80%TD)	393.05	74.21	29.40	<1.0
10% WSi_2	62.76	1.62	2.51	1.860
15% WSi_2	38.10	0.63	0.22	2.297

(*K_p – Parabolic rate constant, \$$K_m$ – Rate constant of general rate equation, #m- Slope of general rate equation)

XRD patterns of surface layer of all the composites (2.5, 5 & 10%) oxidized at 1123K (850°C) for 64 hours are shown in Fig. 6.21. TiO_2 and SiO_2 phases were identified in all the composites. Number of SiO_2 peaks and their intensity increase with the increase of WSi_2 addition.

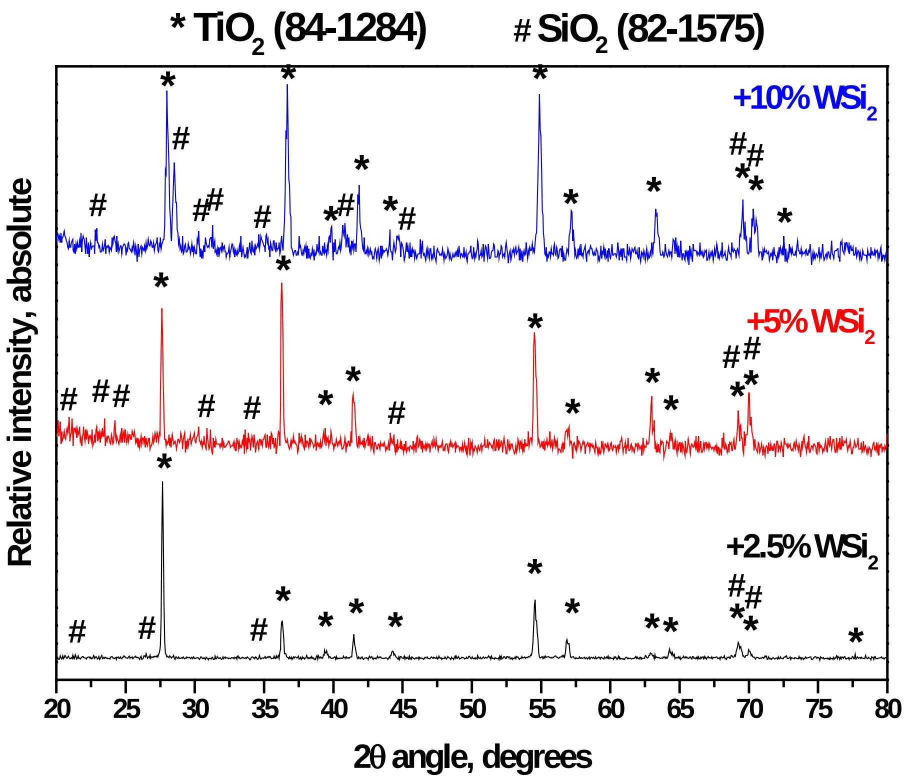

Fig.6.21: XRD patterns of TiB_2+WSi_2 oxidized samples at 1123K (850°C) in air for 64h

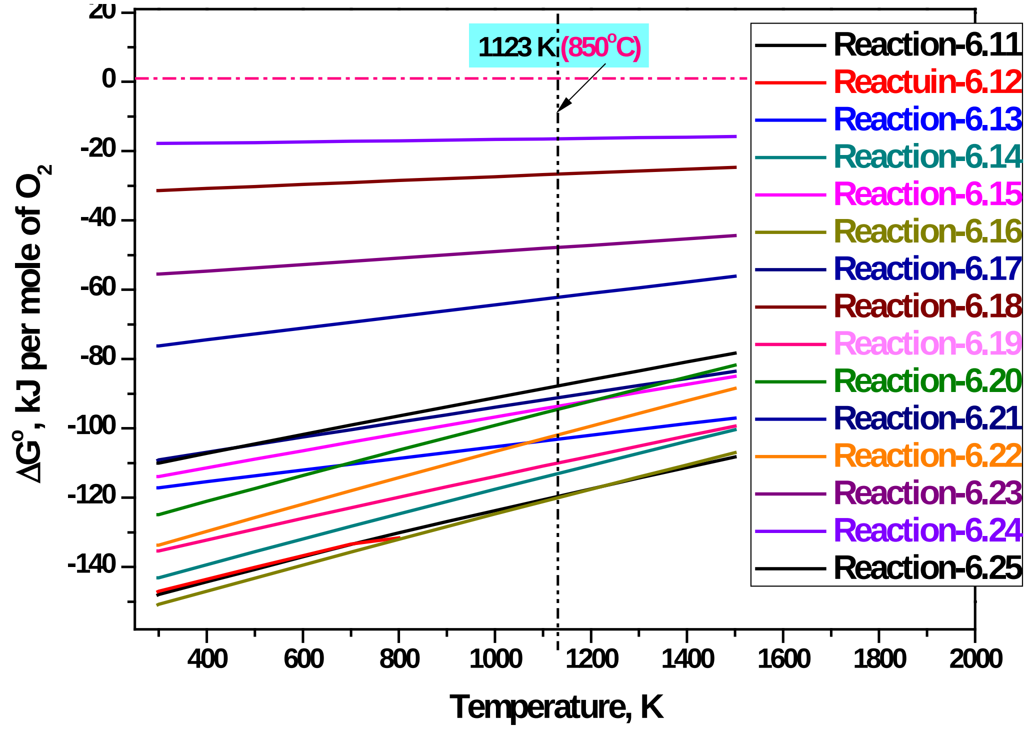

Fig. 6.22 Plot showing the Gibbs free energy change of oxidation reactions (6.11-6.25) as a function of temperature for 0.21 atm partial pressure of oxygen

Oxidation of TiB_2+WSi_2 composite may be represented by the following overall reactions. W_5Si_3 is also considered as one of the possible oxidation product in the reactions as the presence of this phase in the composites was confirmed by XRD results (Fig.5.13).

$$2/5TiB_2(s) + O_2(air) \rightarrow 2/5TiO_2(s) + 2/5B_2O_3(s) \tag{6.11}$$

$$2/5TiB_2(s) + O_2(air) \rightarrow 2/5TiO_2(s) + 2/5B_2O_3(glass) \tag{6.12}$$

$$2/5TiB_2(s) + O_2(air) \rightarrow 2/5TiO_2(s) + 2/5B_2O_3(g) \tag{6.13}$$

$$2/7WSi_2(s) + O_2(air) \rightarrow 2/7WO_3(s) + 4/7SiO_2(s) \tag{6.14}$$

$$2/7WSi_2(s) + O_2(air) \rightarrow 2/7WO_3(g) + 4/7SiO_2(s) \tag{6.15}$$

$$1/3WSi_2(s) + O_2(air) \rightarrow 1/3WO_2(s) + 2/3SiO_2(s) \tag{6.16}$$

$$1/3WSi_2(s) + O_2(air) \rightarrow 1/3WO_2(g) + 2/3SiO_2(s) \tag{6.17}$$

$$2/5WSi_2(s) + O_2(air) \rightarrow 2/5\,WO(g) + 2/5\,SiO_2(s) \tag{6.18}$$

$$3/10WSi_2(s) + O_2(air) \rightarrow 1/10W_3O_8(g) + 3/5SiO_2(s) \tag{6.19}$$

$$2/21W_5Si_3(s) + O_2(air) \rightarrow 10/21\,WO_3(s) + 6/21SiO_2(s) \tag{6.20}$$

$$2/21W_5Si_3(s) + O_2(air) \rightarrow 10/21\,WO_3(g) + 6/21SiO_2(s) \tag{6.21}$$

$$1/8W_5Si_3(s) + O_2(air) \rightarrow 5/8WO_2(s) + 3/8SiO_2(s) \tag{6.22}$$

$$1/8W_5Si_3(s) + O_2(air) \rightarrow 5/8WO_2(g) + 3/8SiO_2(s) \tag{6.23}$$

$$2/11W_5Si_3(s) + O_2(air) \rightarrow 10/11WO(g) + 6/11SiO_2(s) \tag{6.24}$$

$$3/29W_5Si_3(s) + O_2(air) \rightarrow 5/29W_3O_8(g) + 9/29SiO_2(s) \tag{6.25}$$

Free energy change (ΔG^o) for each of the above reactions, was calculated for 0.21 atm partial pressure of O_2 by using FactSage software version 6.3 and plotted as a function of temperature (up to 1500K) [6] and presented in Fig.6.22. All these reactions are thermodynamically feasible. Oxidation of TiB_2 (reactions -6.11 &6.12) and WSi_2 (reaction-6.16) are more favorable compared to oxidation of W_5Si_3. Formation of sub oxides of W [g] (WO, WO_3, WO_2, W_3O_8) and B_2O_3[g] are thermodynamically favorable as the change of free energy is negative for all reactions. But formation of B_2O_3(glass), B_2O_3(s), WO_3(s), WO_2(s) are more favorable compared to formation of gaseous phases due to large negative free energy change. Formation of above solid/glass phases are confirmed by the weight gain data of the samples during oxidation. B_2O_3 and SiO_2 are formed initially during oxidation of the composite which increases in thickness due to the high mobility of small size boron atom and this liquid/glassy layer of B_2O_3/SiO_2 controls further oxidation [10,11].

Crystalline B_2O_3 and TiO_2 were found on the surfaces of TiB_2 oxidized at 973 and 1073K (700 and 800^{o}C) [8]. The large volume expansion that occurs during the oxidation of TiB_2 to TiO_2 causes cracking of the oxide layer, resulting in an increase in the active area for further oxidation [12,13]. SiO_2 and WO_3 have been reported on the surfaces of WSi_2 oxidized at 1373K (1100^{o}C) and only SiO_2 at 1573K (1300^{o}C) [22]. A similar observation has been reported for oxidation of WSi_2 films, where the formation of SiO_2 and WO_3 were reported [23]. Both SiO_2 and TiO_2 are soluble in molten B_2O_3[20,21].

Porosity in the material is known to increase the oxidation rate due to increased surface area available for the reaction. In the present study, effect of porosity on oxidation of TiB_2+5wt% WSi_2 composite was studied using two samples with porosity and the other with full density (~100% TD). Porous sample was prepared at lower hot pressing temperature and pressure. Specific weight gain vs. time plot of these two samples are presented in Fig.6.23. The weight gain after 8 h of oxidation is recorded as 175.92 x $10^{-3}$and 6.49 x 10^{-3} kg/m^2 for porous and near 100% TD samples respectively. The values after 64h of oxidation are recorded as 393.06 x 10^{-3} and 46.76 x 10^{-3} kg/m^2. The oxidation behavior changed from linear (m<1.0) to para-linear (m=1.5) and the parabolic rate constant decreased from 7.4 x 10^{-7} to 5.5 x 10^{-9} Kg^2 m^{-4} s^{-1} with increase in density of the composite.

SEM images of surfaces of porous (80% TD) composite oxidized at 1123K (850^{o}C) for 64h are presented in Fig. 6.24(a & b). Though continuous oxide layer has formed, some portions are severely damaged and cracks also have appeared (Fig. 6.24a). Similar features are seen at different locations and at higher magnification (Fig. 6.24b). The surface of sample with 2.5% WSi_2 (Fig. 6.25) appears to be crack free continuous oxide layer. Two SEM images of different magnifications of 5% WSi_2 oxidized sample are presented in Fig. 6.26(a & b). The surface layer appears similar to 2.5% sample but with a number of cuboids shaped particles, which were confirmed to be TiO_2 by EDAX. Appearances of highly textured crystals with similar morphology have been reported by Koh et al. [7] and Tampieri & Bellosi [8]. SEM images of oxidized surfaces of 10 & 15% WSi_2 composites are presented in Fig. 6.27 & 6.28 respectively. These surfaces appear similar to that of 2.5% sample but with more amount of glassy phase. With the increased addition of WSi_2, quantity of borosilicate glass formed would be higher during oxidation, which explains the absence of TiO_2 cuboids. As both boron and silicon atoms are smaller in size, they could easily diffuse out to the surface [10,11]. Samples with 10 & 15% WSi_2 after long duration of 128h oxidation showed some unique features on the surface. SEM images of these features are presented in Fig. 6.29 & 6.30. A thick non porous glassy layer can be seen on the surface with flakes like transparent objects. These flakes appear to be detached from the surface during cooling after oxidation.

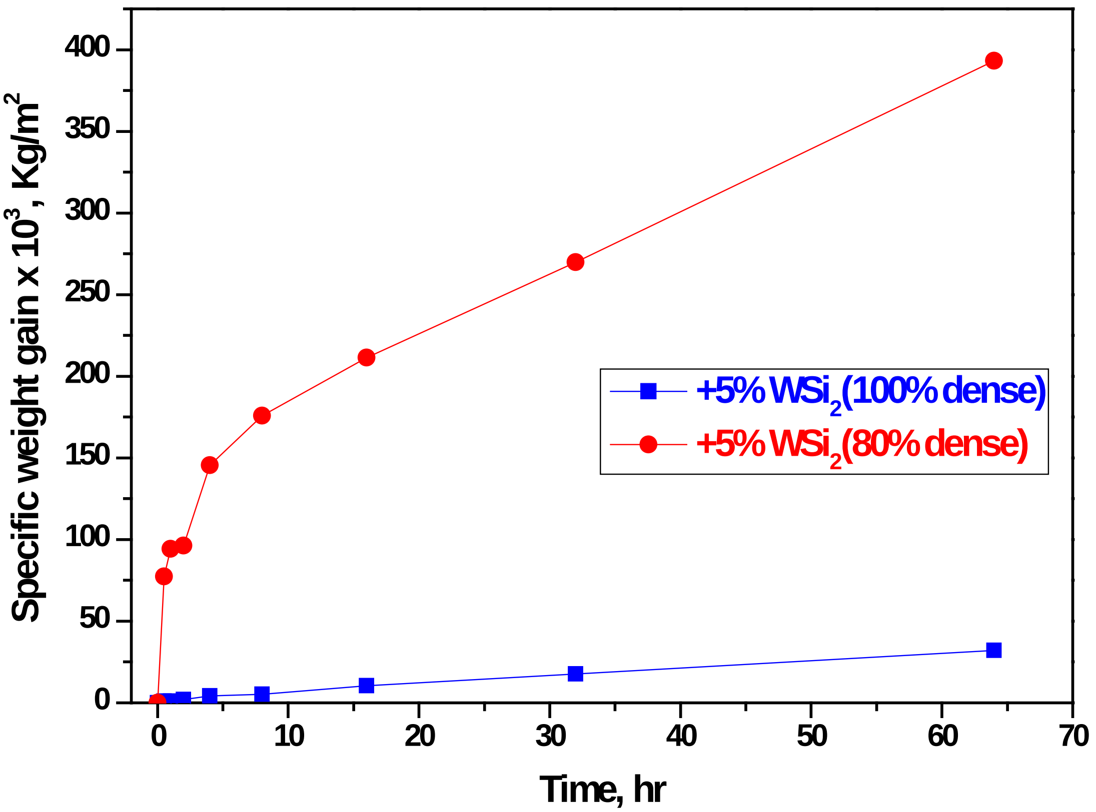

Fig. 6.23 Specific weight gain vs. time plot of porous (80%) and near 100% TD TiB_2+5%WSi_2 oxidized samples at 1123K (850°C) in air

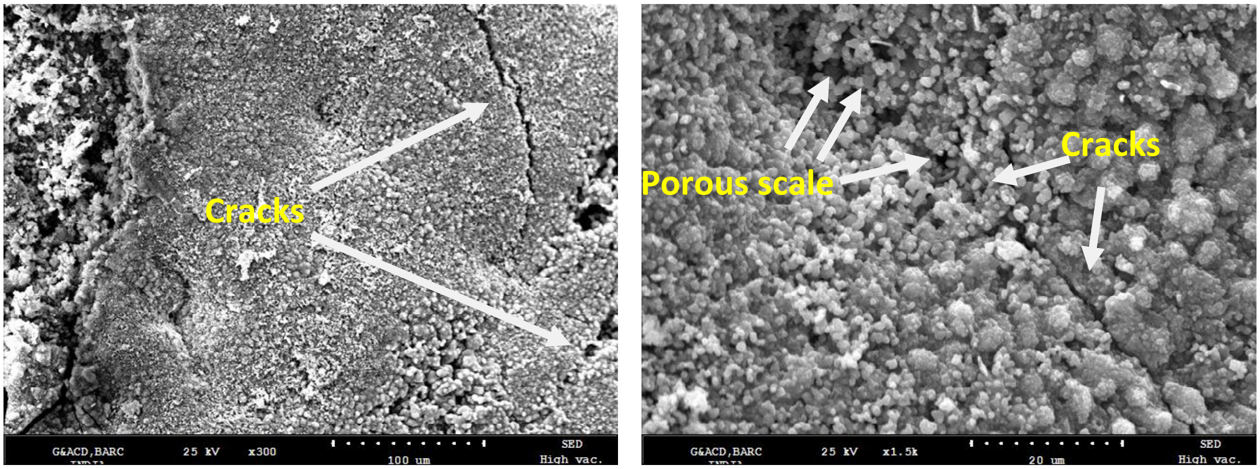

(a) **(b)**

Fig. 6.24 SEM images of surfaces of 80% TD (5% WSi_2) composite oxidized at 1123K (850°C) for 64h at different magnifications

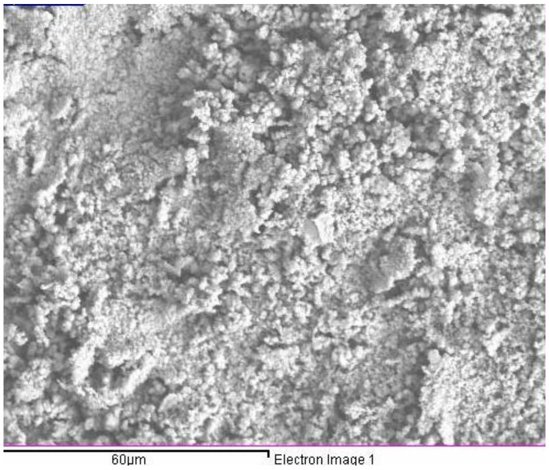

Fig. 6.25 SEM images of surface of 2.5% WSi_2 composite oxidized at 1123K (850^{o}C) for 64h

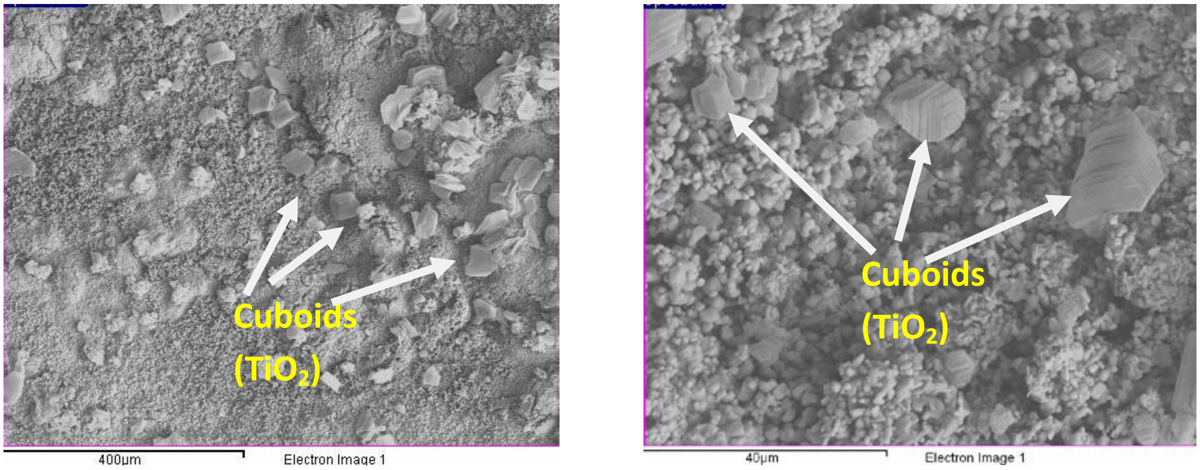

(a) (b)

Fig. 6.26 SEM images (a & b) of different magnifications of 5% WSi_2 oxidized sample at 1123K (850^{o}C) for 64h

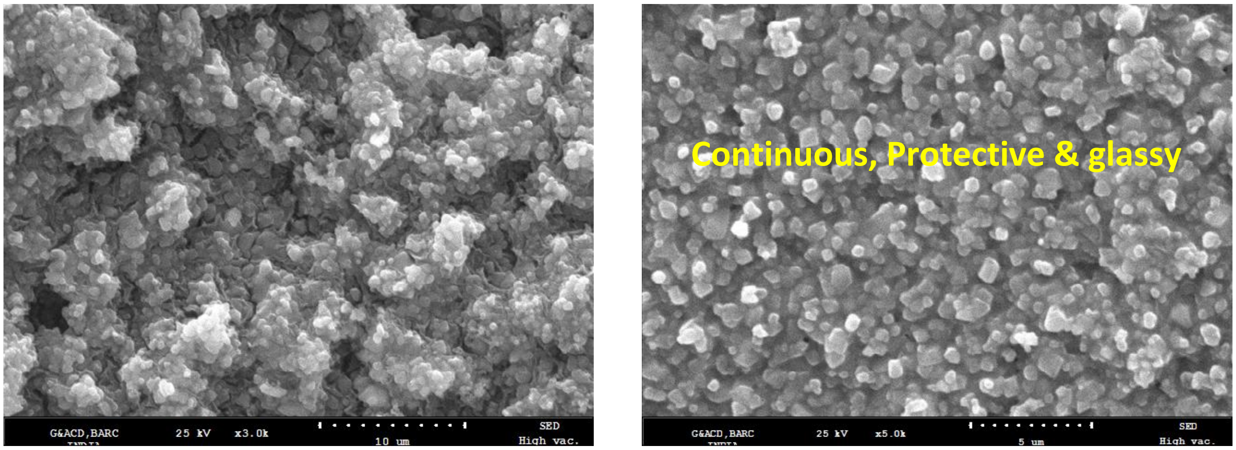

(a) (b)

Fig. 6.27 SEM images of oxidized surface of 10% WSi_2 composites (a & b) at 1123K for 64h

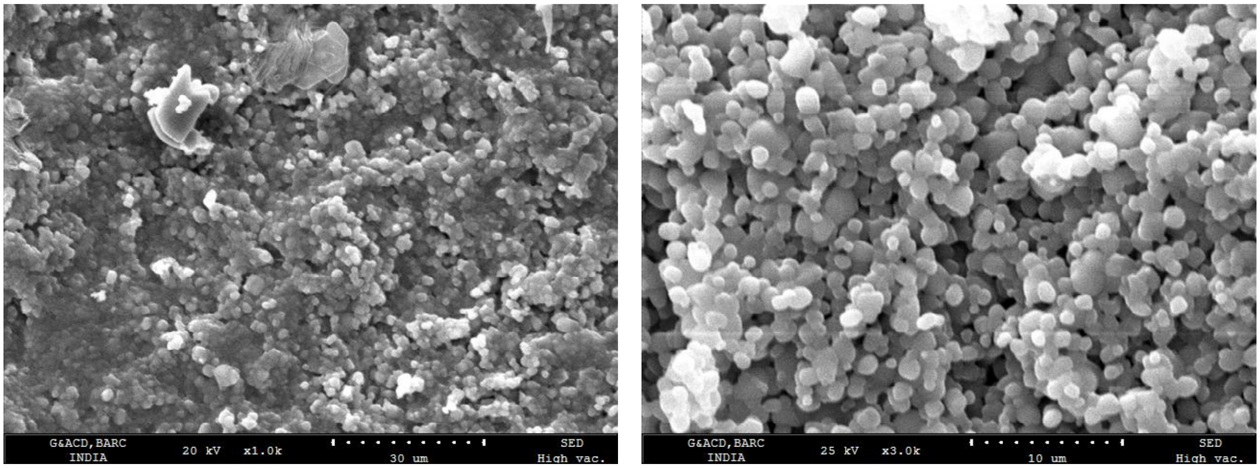

(a) (b)

Fig. 6.28 SEM images of oxidized surface of 15% WSi_2 composites (a&b) at 1123K for 64h

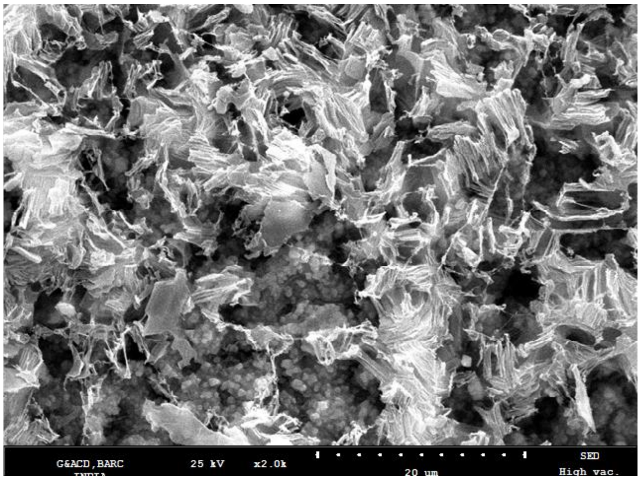

Fig. 6.29 SEM images of surfaces oxidized at 1123K for a very long duration of 128h (10% WSi_2)

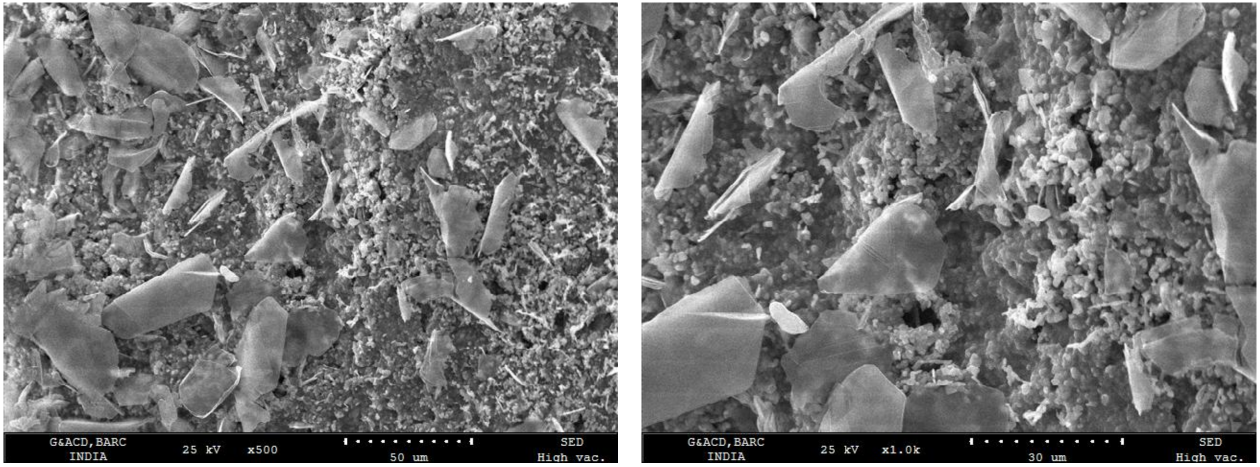

(a) (b)

Fig. 6.30 SEM images of surfaces oxidized at 1123K (850^{o}C) for a long duration of 128h (15% WSi_2)

6.3.4 Oxidation studies of TiB_2+CrB_2 composites

The weight gain data obtained during oxidation at 1123K (850^{o}C) as a function of time for 2.5%, 5% and 10% CrB_2 contained TiB_2 composites are presented in Fig.6.31. Continuous weight gain with time is observed in all the samples. With increasing CrB_2 content, increase in the weight gain also is recorded upto 32 hours. At 64 hours the weight gain for 5% and 10% samples are almost equal. K_p, K_m and m values are presented in Table 6.4. The nature of oxidation near parabolic (m=1.901) for 2.5% and (m=1.908) 5% CrB_2 samples, with complete parabolic nature (m= 2.5) for TiB_2+10%CrB_2 composite. Parabolic rate constants of all three composites are in the same order (4-13 x10^{-8} Kg^{2}m^{-4}s^{-1}) indicating the mechanism of oxidation to be similar.

Short duration oxidation studies were carried out at different temperatures of 873, 1073 and 1273K (600, 800 and 1000^{o}C) for 10% CrB_2 samples. Oxidized surfaces were analyzed by XRD and SEM. XRD plots of samples which underwent short duration oxidation experiments are presented in Fig.6.32. At 873K (600^{o}C), oxidation has just started, indicated by a few faint peaks of $TiO_{2.}$ After oxidation at 1073 and 1273K (800 and 1000^{o}C), TiO_2 and $CrBO_3$ peaks are identified on the surface. SEM images of the oxidized surfaces are presented in Fig.6.33(a-d). After oxidation at 873K (600^{o}C), there is no visible change in the appearance of the surface (Fig.6.33a). After oxidation at 1073K (800^{o}C), multiple nuclei of liquid droplets are observed (Fig.6.33b). One can see the coagulation of liquid droplets on the surface after oxidation at 1273K (1000^{o}C) (Fig.6.33c). At higher magnification, the same surface shows patches of glassy film (Fig.6.33d).

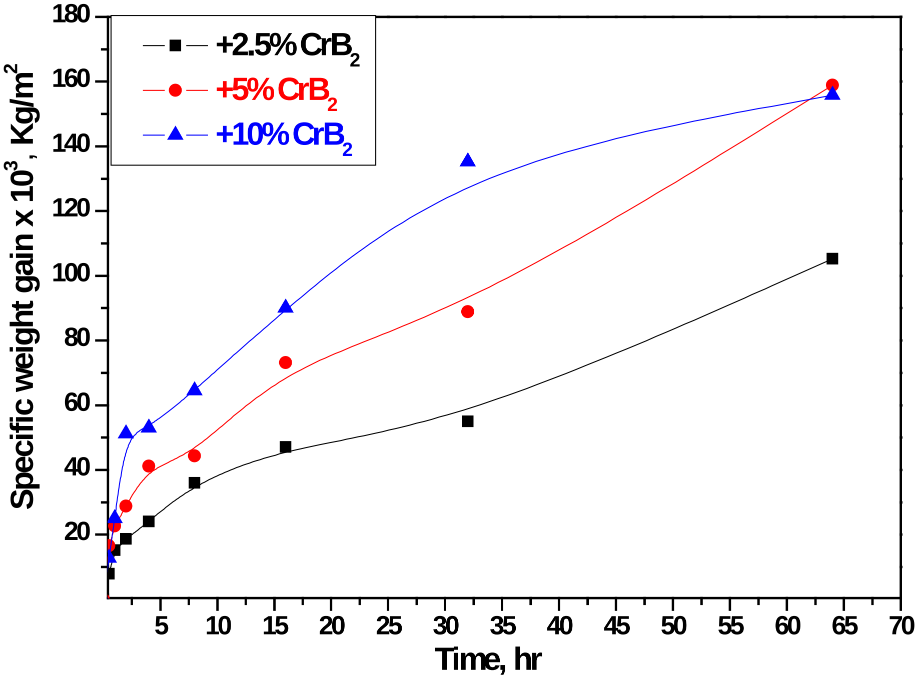

Fig.6.31 Weight gain with time of TiB_2+CrB_2 composites during oxidation at 1123K (850°C)

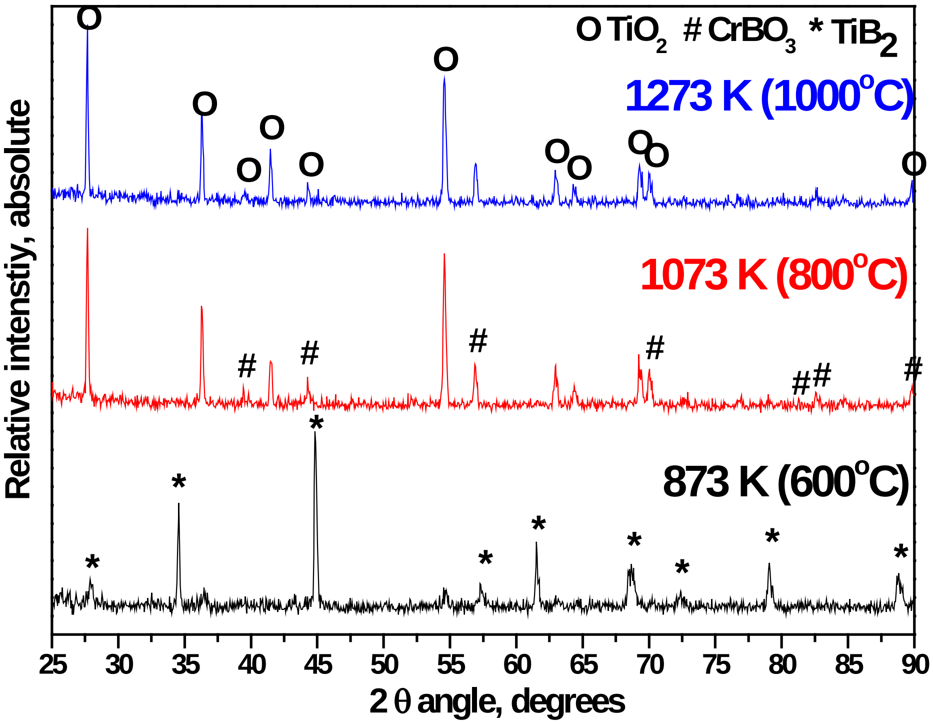

Fig. 6.32 XRD patterns of the surface of TiB_2+10%CrB_2 composite oxidized at 873, 1073 and 1273K (600, 800 and 1000°C)

Table.6.4 Isothermal oxidation kinetics of TiB_2 and composites at 1123K (850°C)

Material	Kp^* ($Kg^2\ m^{-4}\ s^{-1}$)x10^8	$Km^\$$ x 10^8	$m^\#$
TiB_2 + 2.5% CrB_2	4.05	5.26	1.901
TiB_2 + 5% CrB_2	9.43	11.60	1.908
TiB_2 + 10% CrB_2	13.08	5.01	2.456

$^*K_p$ – parabolic rate constant, $^\$K_m$ – rate constant of general rate equation, $^\#$m- slope of the general rate equation

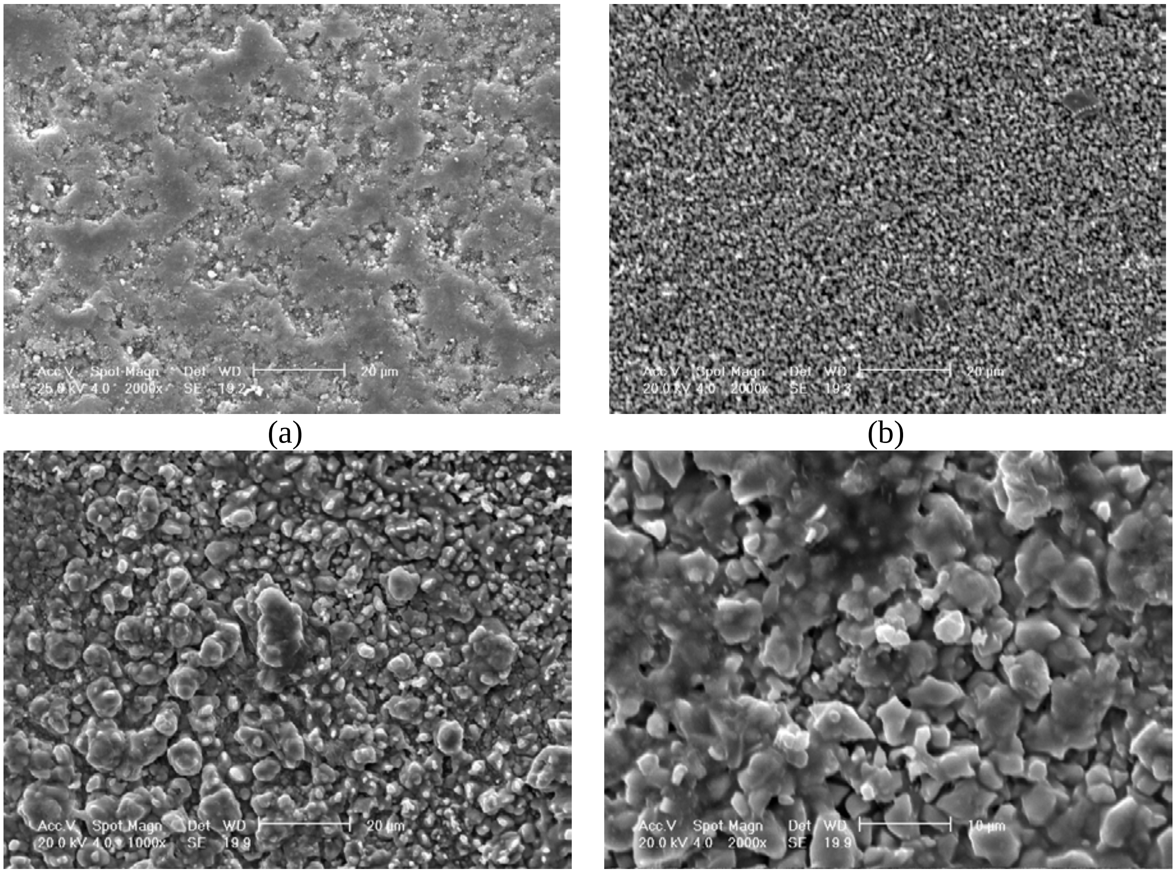

(a) (b)

(c) (d)

Fig. 6.33 SEM images of the oxidized surface of TiB_2+10%CrB_2 at (a) 873K, (b) 1073K and (c&d) 1273K

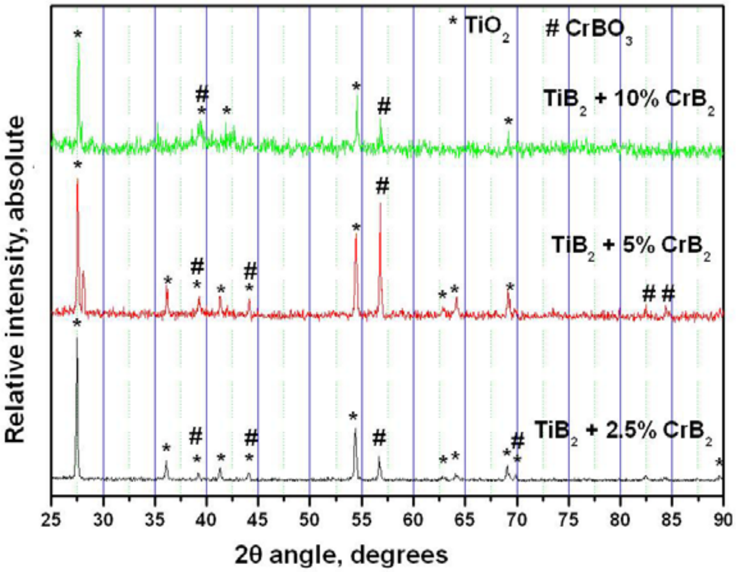

Fig.6.34 XRD patterns of oxidized surface of TiB_2+CrB_2 composites after 64 h at 1123K

XRD pattern of surface oxide layer of the composites after 64 hours are shown in Fig.6.34. TiO_2 and $CrBO_3$ phases were identified in all the composites. SEM of the surface after oxidation at 1123K (850^oC) for 64h is shown in Fig.6.35a-c. The surface is crack free in all the composites. In 2.5% composite, the start of formation of an oxide layer (Fig.6.35a) can be seen. With increasing CrB_2 content, more flow of liquid and disappearance of individual particles (Fig.6.35b) occur. With 10% $CrB_{2,}$ a continuous protective layer is formed on the surface (Fig.6.35c). As the availability of Cr_2O_3 increases with increased CrB_2 content in the composite, a thick protective layer of $CrBO_3$ is formed. Increase in CrB_2 content in the sample also increases B_2O_3, a glassy phase, indicated by the absence of clear/definite peaks and the disturbance noticed in the XRD pattern (Fig.6.34).

Okada *et al.*[24] have studied the oxidation behavior of CrB_2 single crystal and reported that, oxidation begins at 997K (740^oC) resulting in the formation of Cr_2O_3 and $CrBO_3$ phases. Emiliani[25] have reported that oxidation of hot pressed CrB_2 at 1373K (1100^oC), a massive chromium borate ($CrBO_3$) scale gets formed which results in weight gain. Tombs *et al.* [26] have identified the formation of a stable compound $CrBO_3$, by reaction of Cr_2O_3 and B_2O_3 in a melt containing excess B_2O_3. Samsanov *et al.* [27] have reported the formation of a fairly tenacious oxide film consisting of B_2O_3 and $CrBO_3$ on oxidation of CrB_2 at 1173-1273K (900-1000^oC). In the present study also identified the formation of $CrBO_3$ phase.

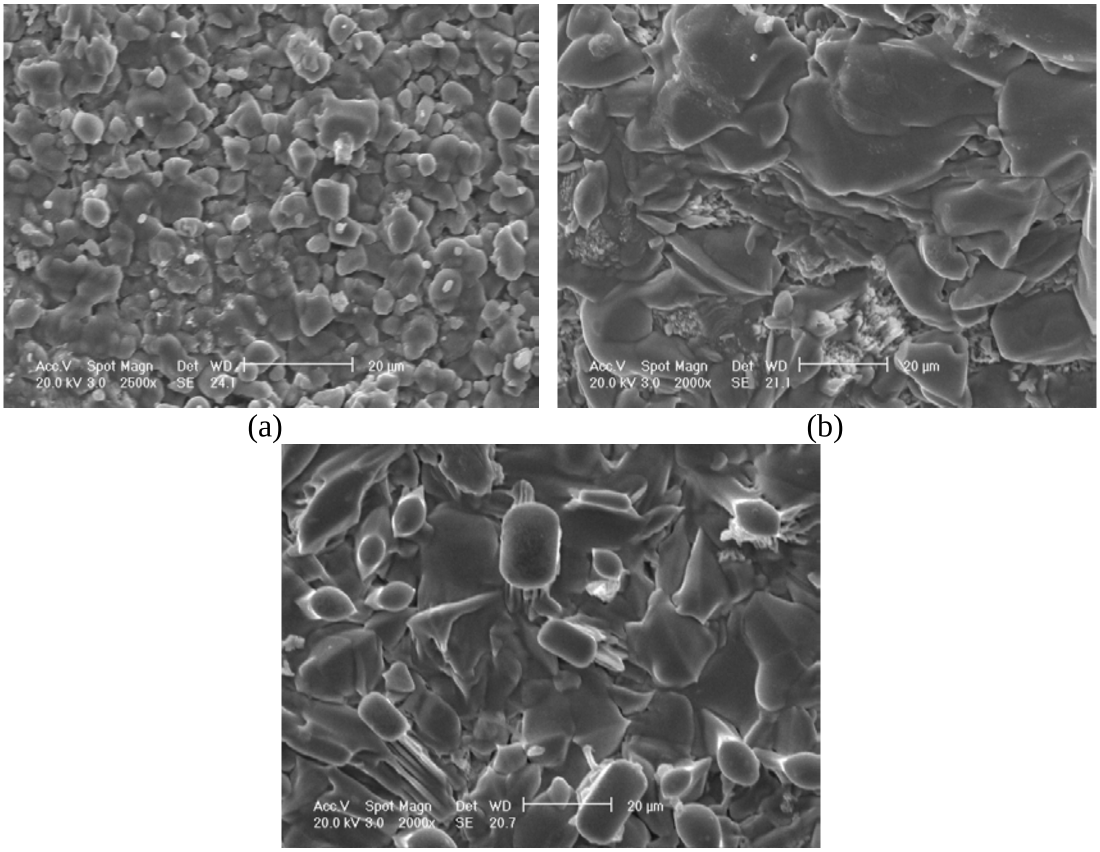

(a) (b)

(c)

Fig 6.35 SEM of the oxidized surface of TiB_2 composite with (a) 2.5%CrB_2, (b) 5%CrB_2 and (c) 10%CrB_2 after 64 h at 1123K (850^oC)

Oxidation of TiB_2+CrB_2 samples may be represented by the following overall reactions:

$$2/5TiB_2(s) + O_2(air) \rightarrow 2/5TiO_2(s) + 2/5B_2O_3(l) \tag{6.26}$$

$$4/9CrB_2(s) + O_2(air) \rightarrow 2/9Cr_2O_3(s) + 4/9B_2O_3(l) \tag{6.27}$$

$$2/5CrB_2(s) + O_2(air) \rightarrow 2/5CrO_2(g) + 2/5B_2O_3(l) \tag{6.28}$$

$1/3CrB_2\,(s) + O_2(air) \rightarrow 1/3CrO_3(g) + 1/3B_2O_3\,(l)$ (6.29)

$Cr_2O_3(s) + B_2O_3\,(l) \rightarrow 2CrBO_3\,(s)$ (?) (6.30)

Though B_2O_3 starts evaporating above 1273K (1000°C), $CrBO_3$ is stable up to 1473K (1200°C) and at higher temperatures decomposes in the presence of oxygen to Cr_2O_3 and B_2O_3. Free energy change of formation for the above reactions except (6.30) is calculated for 0.21 atm partial pressure of oxygen by using FactSage software version 6.3 [6] and presented in Fig.6.36. Free energy of formation of $CrBO_3$ data is not available. However, $CrBO_3$ formation was confirmed in XRD. It is clear that all these reactions (6.26 to 6.29) are thermodynamically possible. Oxidation of CrB_2 is more favorable compared to TiB_2 as seen from the Fig.6.36. This could be the reason for the higher weight gain of the samples on oxidation with increased CrB_2 content. Reaction 6.26, 6.27 and 6.30 results in weight gain whereas reactions 6.28 and 6.29 result in weight loss due to the gaseous nature of CrO_2 and CrO_3 at 1123K (850°C). The overall weight gain observed in oxidation experiments indicate that reactions leading to weight gain are predominant.

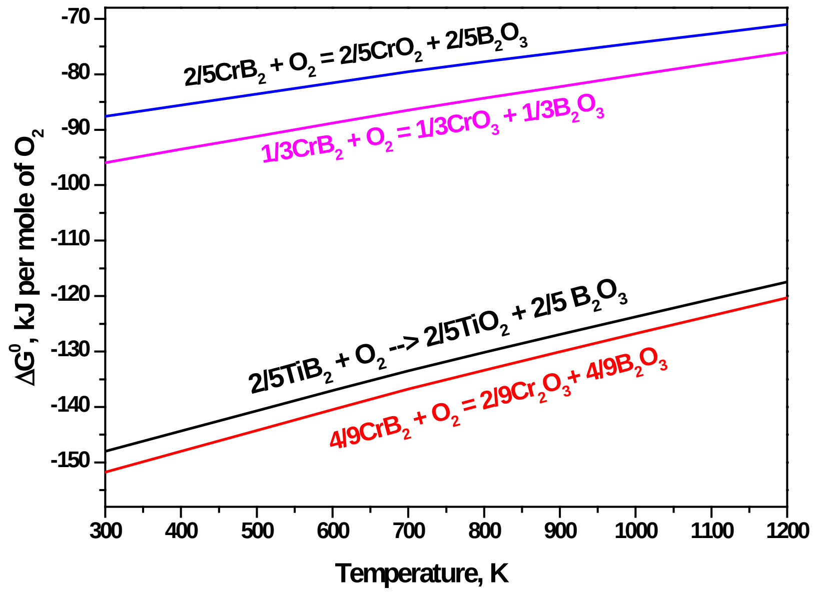

Fig. 6.36 Free energy data for the formation of oxides at 0.21 atm partial pressure of oxygen

Measurement of electrical resistivity of TiB_2 + 10 wt% CrB_2 sample in air (Fig.6.37) has shown very interesting results. At 933K (660°C) a sudden raise of electrical resistivity and above 1158K (885°C), continuous decrease of resistivity is observed. The increase in resistivity is about 14 times higher compared to that measured in inert atmosphere. The increase in resistivity could be due to the formation of non-conducting oxide layers of TiO_2 and B_2O_3. At higher temperatures (above 1158K) formation of liquid phases (probably B_2O_3, and $CrBO_3$) is responsible for the enhanced electrical conductivity. Similar observations have been noted in the case of TiB_2 + $CrSi_2$ composite also.

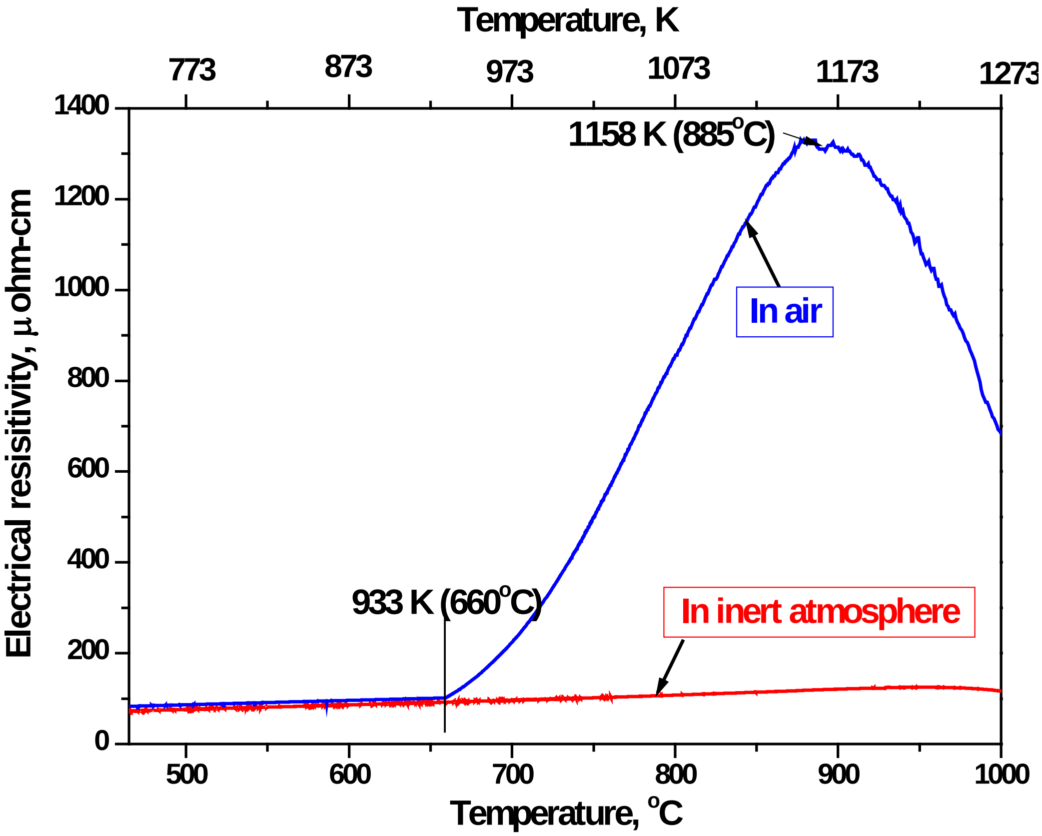

Fig. 6.37 Electrical resistivity of TiB_2+10%CrB_2 measured by 4-probe method in inert atmosphere and air

6.3.5 Oxidation studies of TiB_2+CrB_2 +20%$MoSi_2$ composites

The weight gain data obtained during isothermal oxidation at 1023, 1123 and 1223K (750, 850 and 950°C) as a function of time for TiB_2+20%$MoSi_2$+x%CrB_2 **(**x=5,10,15) composites are shown in Fig.6.38a, b and c respectively. Continuous weight gain with time is observed in all the samples and at all temperatures. However the rate of weight gain is different for different samples and temperatures. With increasing CrB_2 content, decrease in weight gain rate is seen at 1023 and 1123K (750 and 850°C).

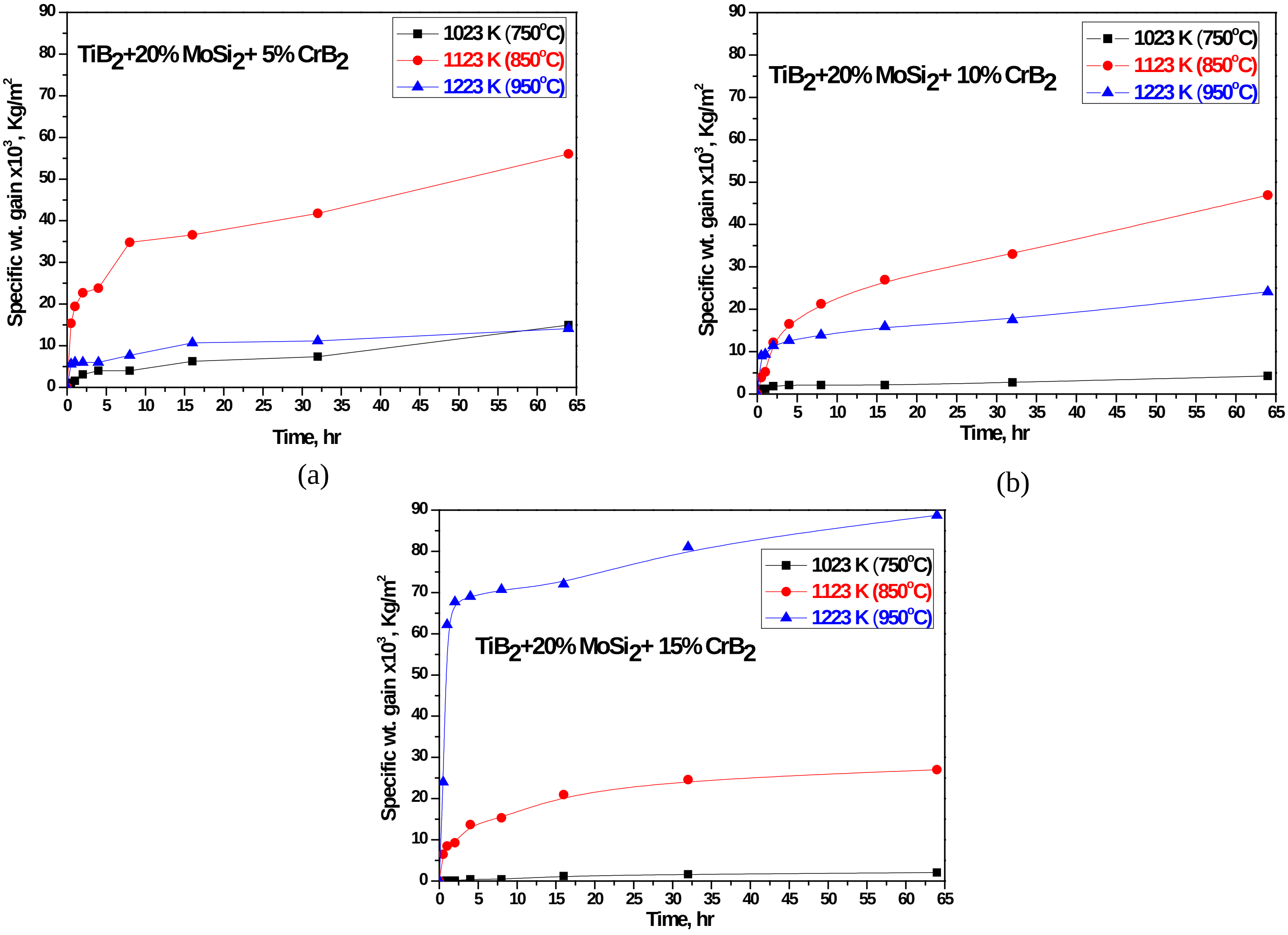

(a) (b)

(c)

Fig. 6.38 Specific weight gain vs. time plots of TiB_2+20%$MoSi_2$composites of a) 5% b) 10% and c) 15% CrB_2 oxidized at different temperatures

The recorded values of specific weight gain after oxidation for 64h at 1023K (750°C) were 14.97, 4.26 and 2.06 x 10^{-3} kg/m^2 for 5, 10 and 15% CrB_2 composites respectively (Fig. 6.38). The recorded values of specific weight gain after oxidation for 64h at 1123K (850°C) were 56.03, 46.94 and 27.02 x 10^{-3} kg/m^2 for the same composites (Fig. 6.38). The recorded values of specific weight gain after oxidation for 64h at 1223K (950°C) were 14.14, 24.10 and 88.76 x10^{-3} kg/m^2 for the same composites (Fig. 6.38). Comparing the weight gain between 1023 and 1123K (750 and 850°C), it is noticed that weight gain increases with temperatures for all the composites. But at 1223K (950°C) a low specific weight gain was observed for 5 and 10% CrB_2 composites compared to that oxidized at 1123K (850°C). This could be due to the evaporation of oxides that have high vapor pressure such as B_2O_3, MoO_3 from the sample at higher temperature [1,17]. But in the case of 15% CrB_2 composite, specific weight gain recorded was higher compared to that at 1123K (850°C). This could probably be due to the formation of thick oxide layer which might have prevented the evaporation of MoO_3 and B_2O_3. Specific weight gain of TiB_2+CrB_2 composites was higher at all time intervals compared with TiB_2+20%$MoSi_2$+x%CrB_2 (x=5,10,15) samples. TiB_2 composites with 20%$MoSi_2$ have also been reported to record very high weight gain which is about 3 orders of magnitude higher (34790 x10^{-3} kg/m^2) as compared to the present study [1]. From the above, it can be inferred that the composite with combined addition of CrB_2 and $MoSi_2$ has low specific weight gain during oxidation compared to TiB_2 composites that were formed either with CrB_2 or with $MoSi_2$ alone.

K_p, K_m and m values at different temperatures are listed in Table 6.5. The nature of oxidation appears to be near parabolic (m=1.6 to 2.0) at 1023K (750°C) for all the composites, which alters to cubic (m>3) at 1123K (850°C). Nature of oxidation at 1223K (950°C) is not predictable, as these values will not be representative due to evaporation of MoO_3/B_2O_3.

Parabolic rate constant of 5, 10 and 15% CrB_2 composites are measured as 7.73 $x10^{-10}$, 0.91 $x10^{-10}$, $0.19x10^{-10}$ $kgm^{-4}s^{-1}$ respectively at 1023K (750°C). Two orders higher parabolic rate constants are measured for the same composites at 1123K (850°C) in the range of 0.5 $x10^{-8}$ to $1.8x10^{-8}$ $kgm^{-4}s^{-1}$. The above parabolic rate constant values at 1023 and 1123K (750 and 850°C) indicate that mechanism of oxidation to be diffusion controlled. The value of parabolic rate constant is found to decrease with increase of CrB_2 content from 5 to 15%, indicating the effectiveness of CrB_2 addition in improving the oxidation resistance. Lower order parabolic rate constant value was observed in TiB_2 composite containing both $MoSi_2$ and 15% CrB_2 (Table 6.5) as compared to the composite containing either CrB_2 or $MoSi_2$ alone during oxidation at 1123K (850°C).

XRD patterns of surface layer of all the composites oxidized at 1123K (850°C) for 64 hours are shown in Fig. 6.39. TiO_2, Cr_2O_3 and SiO_2 phases were identified in all the composites. XPS analysis of oxidized surfaces was carried out to understand the presence of amorphous/glassy phases. Results are presented in the Fig. 6.40(a & b) for 5% and 15% CrB_2 samples. Similar to XRD results, TiO_2, Cr_2O_3 and SiO_2 phases were observed in both the composites. In addition MoO_3 and B_2O_3 phases were identified in 5% CrB_2 samples. Unidentified peaks are due to the conductive coating material used for sample preparation. From the above it is clear that higher content of CrB_2 ($\geq$10%) forms a protective coating and prevents the escape of boron and molybdenum species as suboxides.

Table 6.5 Specific weight gain and rate constants after 64h of oxidation at different temperatures

Sample	Wt. % CrB_2	Sp.wt. gain, $Kg/m^2 \times 10^3$	$Kp^*(Kg^2m^{-4}\ s^{-1})$	$Km^\$$	$m^\#$
At 1023K (750 °C)					
(TiB_2 +20% $MoSi_2$) + CrB_2	5	14.97	7.73×10^{-10}	1.84×10^{-9}	1.812
	10	4.26	9.13×10^{-11}	1.47×10^{-15}	3.906
	15	2.06	1.86×10^{-11}	1.67×10^{-10}	1.661
At 1123K (850 °C)					
TiB_2 + CrB_2	2.5	105.25	4.05×10^{-8}	5.26×10^{-8}	1.901
	5	158.86	9.43×10^{-8}	11.60×10^{-8}	1.908
	10	155.84	13.08×10^{-8}	5.01×10^{-8}	2.456
(TiB_2 +20% $MoSi_2$) + CrB_2	0^1	34789.7	5992	33490	1.423
	5	46.94	1.06×10^{-8}	2.80×10^{-9}	2.396
	10	56.03	1.84×10^{-8}	5.23×10^{-11}	3.876
	15	27.02	4.91×10^{-9}	1.73×10^{-11}	3.495
TiB_2 [1]	0	305238.6	6.0×10^{-8}	-	-
At 1223K (950 °C)					
(TiB_2 +20% $MoSi_2$) + CrB_2	5	14.14	1.26×10^{-9}	2.43×10^{-14}	4.422
	10	24.10	3.50×10^{-9}	4.71×10^{-14}	4.821
	15	88.76	6.63×10^{-8}	8.49×10^{-14}	7.403

($^*K_p$ – Parabolic rate constant, $^\$K_m$ – Rate constant of general rate equation, $^\#$m- Slope of general rate equation)

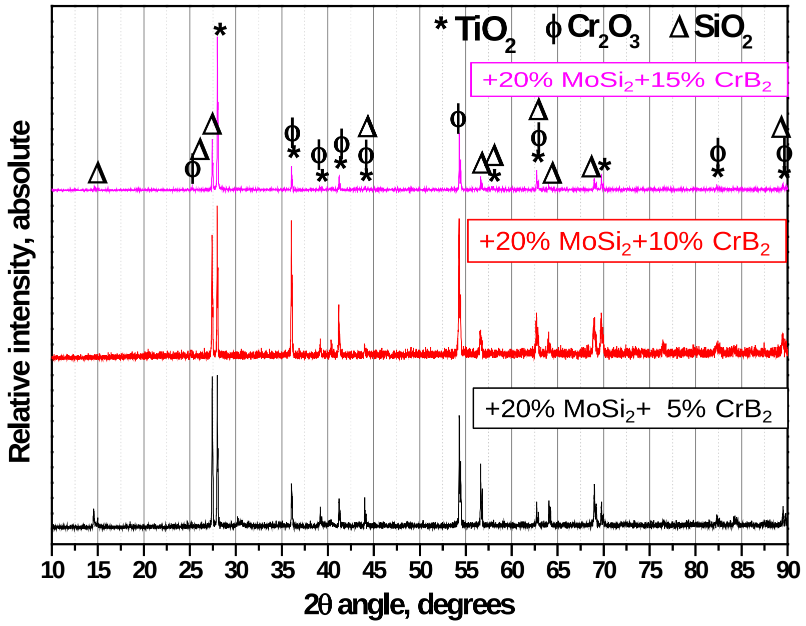

Fig. 6.39 XRD patterns of surface of 5, 10 and 15% CrB_2 composites oxidized at 1123K

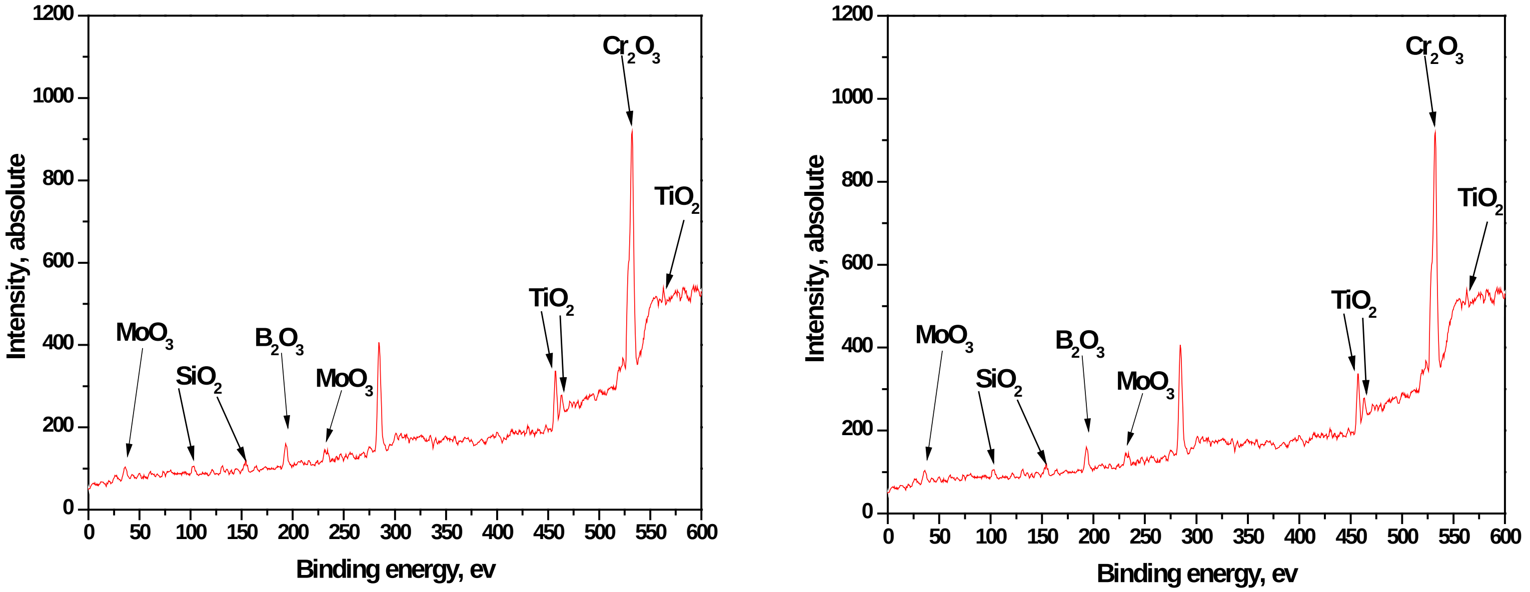

(a) (b)

Fig.6.40 XPS analysis of oxidized surface of (a) 5% and (b)15% CrB_2 composite after isothermal oxidation at 1123K (850^{o}C) for 64h in air

Oxidation of TiB_2+$MoSi_2$+CrB_2 composite may be represented by the following overall reactions:

$2/5TiB_2(s) + O_2(air) \rightarrow 2/5TiO_2(s) + 2/5B_2O_3(s)$ (6.31)

$2/5TiB_2(s) + O_2(air) \rightarrow 2/5TiO_2(s) + 2/5B_2O_3(glass)$ (6.32)

$2/5TiB_2(s) + O_2(air) \rightarrow 2/5TiO_2(s) + 2/5B_2O_3(g)$ (6.33)

$4/9CrB_2(s) + O_2(air) \rightarrow 2/9Cr_2O_3(s) + 4/9B_2O_3(l)$ (6.34)

$2/5CrB_2(s) + O_2(air) \rightarrow 2/5CrO_2(g) + 2/5B_2O_3(l)$ (6.35)

$1/3CrB_2(s) + O_2(air) \rightarrow 1/3CrO_3(g) + 1/3B_2O_3(l)$ (6.36)

$2/7MoSi_2 + O_2(air) \rightarrow 4/7SiO_2 + 2/7MoO_3(s)$ (6.37)

$2/7MoSi_2 + O_2(air) \rightarrow 4/7SiO_2 + 2/7MoO_3(g)$ (6.38)

Free energy change (ΔG^o) for each of the above reactions was calculated for 0.21 atm partial pressure of O_2 by using FactSage software version 6.3 and plotted as a function of temperature up to 1200K (927°C) (for reaction – 6.32 up to 800K) in Fig.6.41 [6]. It is clear that reactions (6.31)-(6.37) are thermodynamically feasible as the change in free energy is negative. Oxidation of CrB_2 (reaction 6.34) is more favorable compared to TiB_2 and $MoSi_2$. Formation of gaseous sub oxides of chromium (CrO_3, CrO_2), MoO_3[g] and B_2O_3[g] are thermodynamically favorable as the change of free energy is negative for all reactions. But the reactions for the formation of B_2O_3(glass), Cr_2O_3(s), MoO_3(s) have more negative free energy change compared to reactions leading to gaseous product phases. Formation of the solid/glass phases as indicated above was confirmed by the weight gain data and XRD analysis of the samples during oxidation.

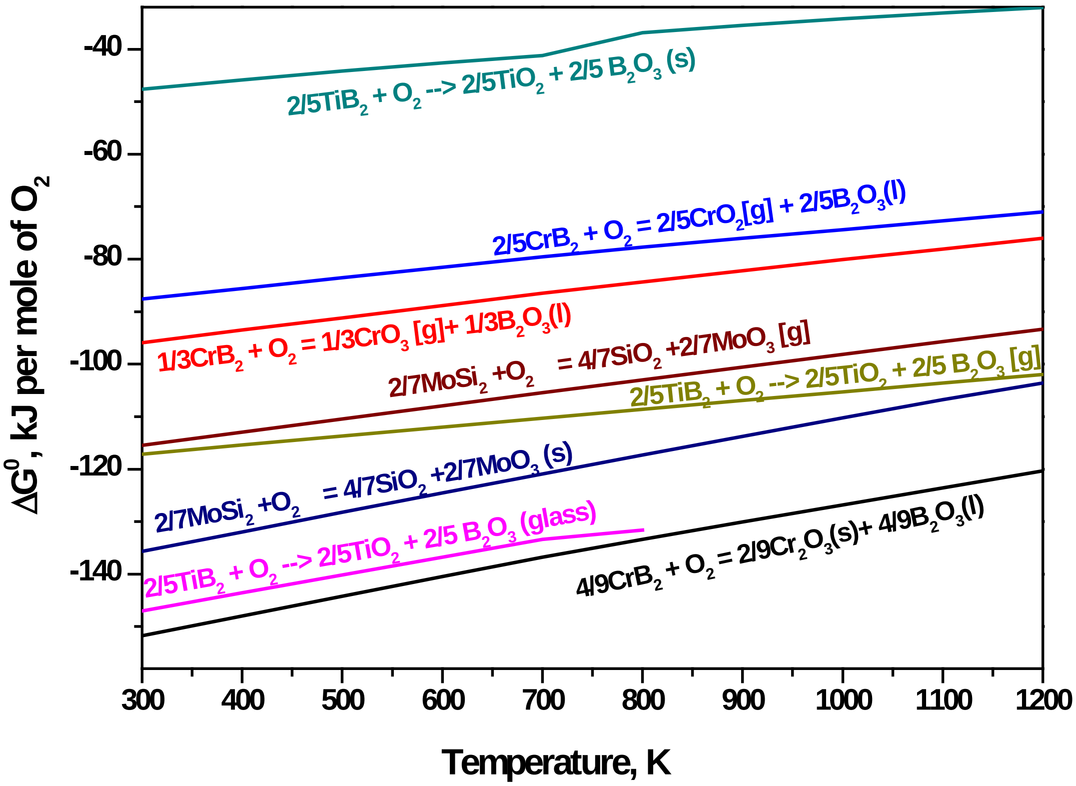

Fig. 6.41 Free energy formation data of various possible oxidation reactions for 0.21 atm partial pressure of O_2 [6]

B_2O_3 and SiO_2 are formed initially during oxidation of the composite which increases in thickness due to the high mobility of small sized boron atom and this liquid/glassy layer of B_2O_3/SiO_2 controls further oxidation [10,11]. In fact, eutectic reaction of SiO_2 with B_2O_3 is seen at 724K (451^oC) at 5% SiO_2 composition. Both SiO_2 and TiO_2 are soluble in molten B_2O_3[20,21]. Crystalline B_2O_3 and TiO_2 were found on the oxidized surfaces of TiB_2 at 973 and 1073K (700 and 800^oC) [8]. The large volume expansion that occurs during the oxidation of TiB_2 to TiO_2 (7 vol%) causes cracking of the oxide layer, resulting in an increase in the active area for further oxidation [12,13]. $CrBO_3$ phase has been identified on oxidation of CrB_2 [24,25,27]. This particular compound was not identified on the oxidized surface of the TiB_2 + 20%$MoSi_2$ + x%CrB_2 **(**x=5,10,15) composites. It is well-established that the excellent oxidation resistance of $MoSi_2$ at high temperatures is attributed to the formation of a self-healing, glassy silica (SiO_2) layer. But during low temperature (673-873 K) oxidation, it exhibits pest behavior. 'Pest' means disintegration of the material (the disintegrated $MoSi_2$ results in powdery products) [1].

SEM images of oxidized surfaces of all composites (5, 10 and 15% CrB_2) at 1123 and 1223K (850 and 950^oC) for 64h are presented in Fig.6.42(a-f). At 1123K (850^oC), the oxidized surface of 5% CrB_2 composite shows the formation of glassy phase partially covering the surface (Fig. 6.42a). At 1223K (950^oC) the glassy layer completely covered the surface (Fig. 6.42b). Though the weight gain data shows that evaporation is more at higher temperature for this composite, the higher temperature has also helped in the formation of liquid glassy phase. With 10% CrB_2 composite globules of oxidized particles are seen covered with the glassy layer (Fig. 6.42c) at 1123K (850^oC). At the higher temperature, the glassy layer appears to be punctured by the evaporating species (Fig. 6.42d) and the oxide crystals appear to be bigger in size. This is in conformity with the results of weight gain data on oxidation. With further increase in CrB_2 (15%) the oxidized surface appears to be crack free, continuous and with cuboid shaped crystalline particles after oxidation at 1123K (850^{o}C) (Fig 6.42e). After oxidation at 1223K (950^{o}C) the surface of the same composite appears fully covered with a wavy pattern (Fig. 6.42f). This feature goes well with the weight gain pattern shown by this composite at 1223K (950^{o}C) with lower evaporation and higher weight gain.

To understand the role of various elements during oxidation of TiB_2 composites extended oxidation was carried out at 1123K (850^{o}C) for 256h. Cross section of the TiB_2+15%CrB_2+20%$MoSi_2$ oxidized surface after 256h was characterized by SEM-EDS and presented in Fig.6.43. The thickness of the oxide layer is ~100 μm and the elemental distribution of this layer for Si, Ti, B, Mo, Cr and O is also presented. Outer most layer of oxidized surface is boron oxide. Boron content decreases drastically up to 20 μm and then gradually increases up to 100 μm from the outer most layer of oxidized surface. Beyond 100 μm, the boron content is uniform. This clearly shows the migration of boron towards the outer surface. The next inner layer is silicon oxide. Higher silicon content is seen from 5 to 60 μm from the outer layer. This shows that silicon also migrates to the outer surface. It has also been reported that due to the small radius of the boron atom, it can diffuse easily to the surface during oxidation of TiB_2[1]. Both silicon and boron have very high affinity for oxygen, which also aid the migration. Qualitative analysis of this oxide layer shows that boron migrates towards the surface layer. Silicon combined with oxygen forms the barrier layer for further diffusion of oxygen ions.

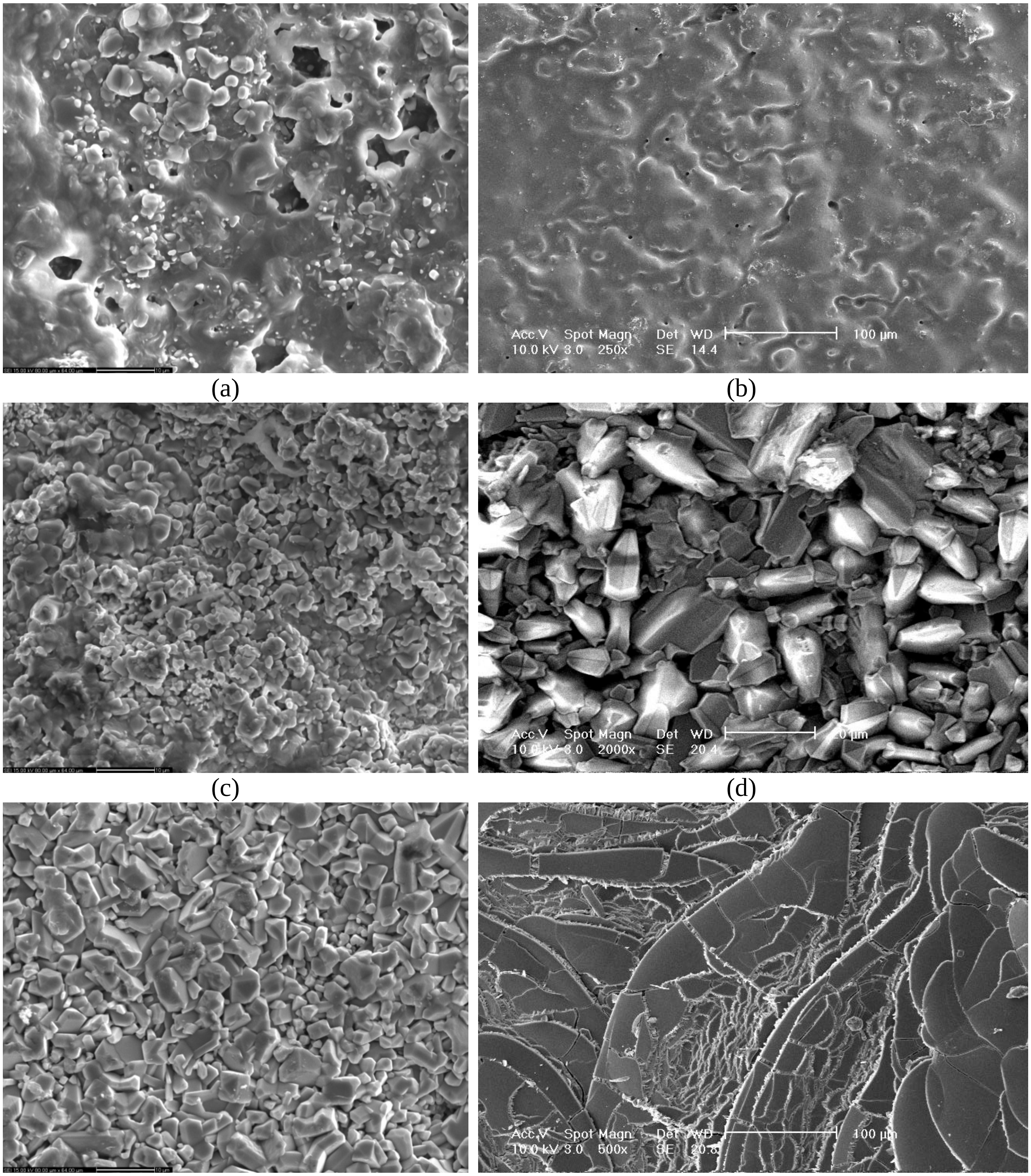

(a) (b)

(c) (d)

(e) (f)

Fig. 6.42 SEM images of oxidized surfaces of 5, 10 and 15%CrB_2 composites at 1123K (850^{o}C) (a,c,e) and the same composites at 1223K (950^{o}C) (b,d, f) for 64h

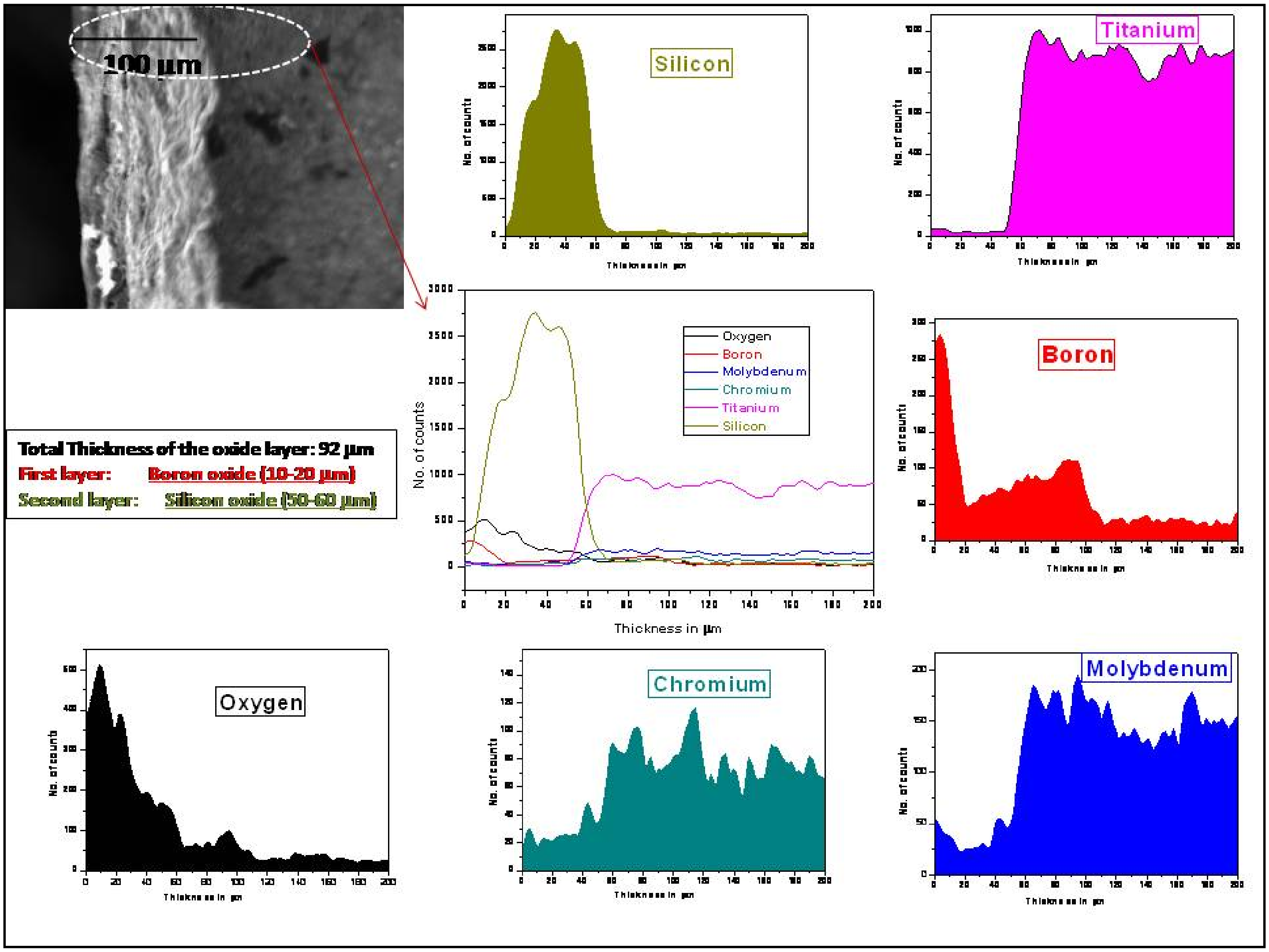

Fig. 6.43 SEM - EDS analysis of cross section of the composite TiB_2 + 20 wt.%$MoSi_2$ +15 wt. %CrB_2 oxidized at 1123K (850°C) for 256h

6.3.6 Oxidation studies of (TiCr)B_2 +20%$MoSi_2$ composites

The weight gain data obtained during isothermal oxidation at 1023, 1123 and 1223K (750, 850 and 950°C) as a function of time for all the composites are presented in Fig. 6.44(a-c). Continuous weight gain with time is observed in all the samples and at all temperatures. However the rate of weight gain is different for different samples and temperatures. With increasing CrB_2 content, decrease in weight gain rate is seen at all temperatures. The recorded values of specific weight gain after oxidation for 64h at 1023K (750^oC) were 4.73, 2.32 and 3.07 x 10^{-3} kg/m^2 for $(Ti_{0.95}Cr_{0.05})B_2$, $(Ti_{0.90}Cr_{0.10})B_2$ and $(Ti_{0.85}Cr_{0.15})B_2$+20% $MoSi_2$ composites respectively (Fig. 6.44). The recorded values of specific weight gain after oxidation for 64h at 1123K (850^oC) were 34.62, 26.07 and 8.17 x 10^{-3} kg/m^2 for the same composites (Fig. 6.44). The recorded values of specific weight gain after oxidation for 64h at 1223K (950^oC) were 57.32, 39.58 and 4.58 x10^{-3} kg/m^2 for the same composites (Fig. 6.44). Comparing the weight gain between 1023 and 1223K (750 and 950^oC), it is noticed that weight gain increases with temperatures for all the composites. But at 1223K (950^oC) a low specific weight gain was observed for $(Ti_{0.85}Cr_{0.15})B_2$+20% $MoSi_2$ composites compared to that oxidized at 1123K (850^oC). Specific weight gain of TiB_2+CrB_2+20%$MoSi_2$ composites was higher at all time intervals compared with the $(TiCr)B_2$ +20%$MoSi_2$ samples. From the above, it can be inferred that the composite with pre-alloyed $(TiCr)B_2$ with addition of 20%$MoSi_2$ has low specific weight gain during oxidation compared to TiB_2 composites that were formed without pre-alloyed (TiB_2 + CrB_2).

K_p, K_m and m values at different temperatures are presented in Table 6.6. The nature of oxidation appears to be complete parabolic (m=2.1 to 2.6) for 5 and 10%CrB_2 composites and cubic (m>3) for $(Ti_{0.85}Cr_{0.15})B_2$+20% $MoSi_2$ composite at 1023K (750^oC). Parabolic rate constant of $(Ti_{0.95}Cr_{0.05})B_2$, $(Ti_{0.90}Cr_{0.10})B_2$ and $(Ti_{0.85}Cr_{0.15})B_2$+20% $MoSi_2$ composites are measured as 1.25, 0.23, 0.53 x 10^{-10} kg m^{-4} s^{-1} respectively at 1023K (750^oC). One order higher parabolic rate constants are measured for the same composites at 1123K (850^oC) in the range of 3 to 5 x 10^{-9} kgm^{-4}s^{-1}. The above parabolic rate constant values at 1023 and 1123K (750 and

850°C) indicate that mechanism of oxidation to be diffusion controlled. The value of parabolic rate constant is found to decrease with increase of CrB_2 content from 5 to 15%, indicating the effectiveness of CrB_2 addition in improving the oxidation resistance.

Table 6.6 Specific weight gain and rate constants after 64h of oxidation at different temperatures

Sample	Sp.wt. gain, $Kg/m^2 \times 10^3$	Kp^* ($Kg^2m^{-4}s^{-1}$)	$Km^\$$	$m^\#$
At 1023 K (750°C)				
$(Ti_{0.95}Cr_{0.05})B_2$+20% $MoSi_2$	4.73	1.25×10^{-10}	2.69×10^{-12}	2.687
$(Ti_{0.90}Cr_{0.10})B_2$+20% $MoSi_2$	2.32	2.32×10^{-11}	8.50×10^{-12}	2.156
$(Ti_{0.85}Cr_{0.15})B_2$+20% $MoSi_2$	3.06	5.26×10^{-11}	3.49×10^{-15}	3.590
At 1123 K (850°C)				
$(Ti_{0.95}Cr_{0.05})B_2$+20% $MoSi_2$	34.62	5.24×10^{-9}	1.55×10^{-9}	2.327
$(Ti_{0.90}Cr_{0.10})B_2$+20% $MoSi_2$	26.07	3.72×10^{-9}	3.57×10^{-10}	2.602
$(Ti_{0.85}Cr_{0.15})B_2$+20% $MoSi_2$	8.17	1.75×10^{-9}	6.80×10^{-14}	4.359
At 1223 K (950°C)				
$(Ti_{0.95}Cr_{0.05})B_2$+20% $MoSi_2$	57.32	1.46×10^{-8}	2.69×10^{-8}	1.807
$(Ti_{0.90}Cr_{0.10})B_2$+20% $MoSi_2$	39.58	9.96×10^{-9}	8.01×10^{-11}	3.410
$(Ti_{0.85}Cr_{0.15})B_2$+20% $MoSi_2$	4.58	2.14×10^{-10}	2.43×10^{-31}	10.953

(${}^*K_p$ – Parabolic rate constant, ${}^\$K_m$ – Rate constant of general rate equation, ${}^\#m$- Slope of general rate equation)

XRD patterns of surface layer of all the composites oxidized at 1023, 1123 and 1223K (750, 850 and 950°C) for 64 hours are shown in Fig. 6.45(a-c). TiO_2, Cr_2O_3 and SiO_2 phases were identified in all the composites after oxidation at 1023 and 1123K (750 and 850°C). TiO_2, CrO_3, B_2-SiO_5 phases were identified in all the composites after oxidation at 1223K (950°C).

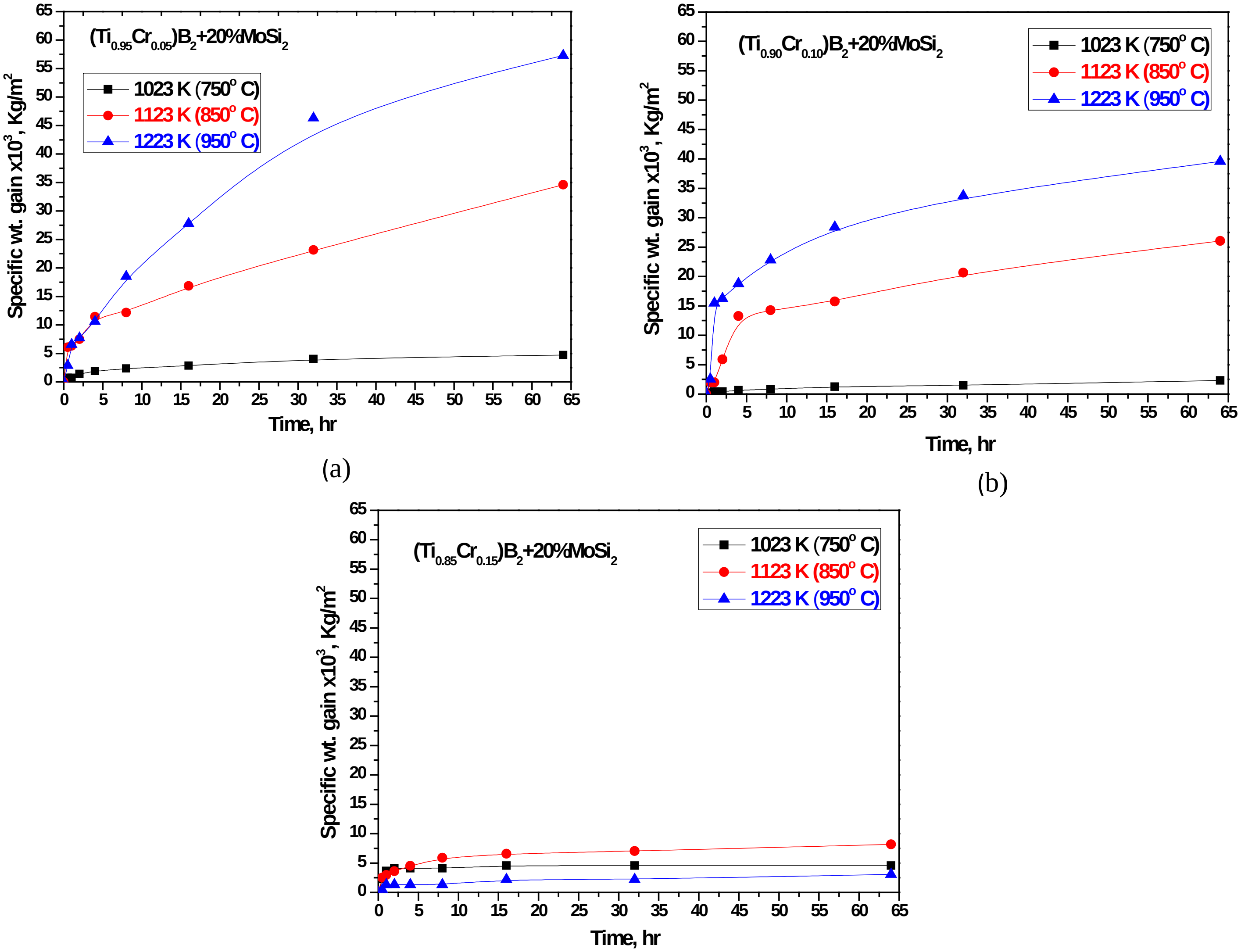

(a)

(b)

(c)

Fig. 6.44 Specific weight gain vs. time plots of a) $(Ti_{0.95}Cr_{0.05})B_2$+20% $MoSi_2$, b) $(Ti_{0.90}Cr_{0.10})B_2$+20% $MoSi_2$ and c) $(Ti_{0.85}Cr_{0.15})B_2$+20% $MoSi_2$ composites oxidized at different temperatures.

SEM images of oxidized surfaces of all composites (5, 10 and 15% CrB_2) at 1023, 1123 and 1223K (750, 850 and 950°C) for 64h are presented in Fig.6.46 to 6.48. At 1023 K (750°C), start of formation of a liquid phase can be seen on (Fig.6.46a) $(Ti_{0.95}Cr_{0.05})B_2$+20% $MoSi_2$ sample. More amount of liquid phase is spreading on the surface of $(Ti_{0.90}Cr_{0.10})B_2$ and $(Ti_{0.85}Cr_{0.15})B_2$+20% $MoSi_2$ composites (Fig. 6.46 b & c). At 1123K (850°C), surface cracks were seen on the $(Ti_{0.95}Cr_{0.05})B_2$ oxidized sample (Fig.6.47a). $(Ti_{0.90}Cr_{0.10})B_2$ and $(Ti_{0.85}Cr_{0.15})B_2$+20% $MoSi_2$ samples were fully covered with dense oxide layer (Fig.6.47 b & c). At 1223K (950°C), more continuous and protective oxide layer was seen with increasing the CrB_2 content in the sample (Fig.6.48a-c).

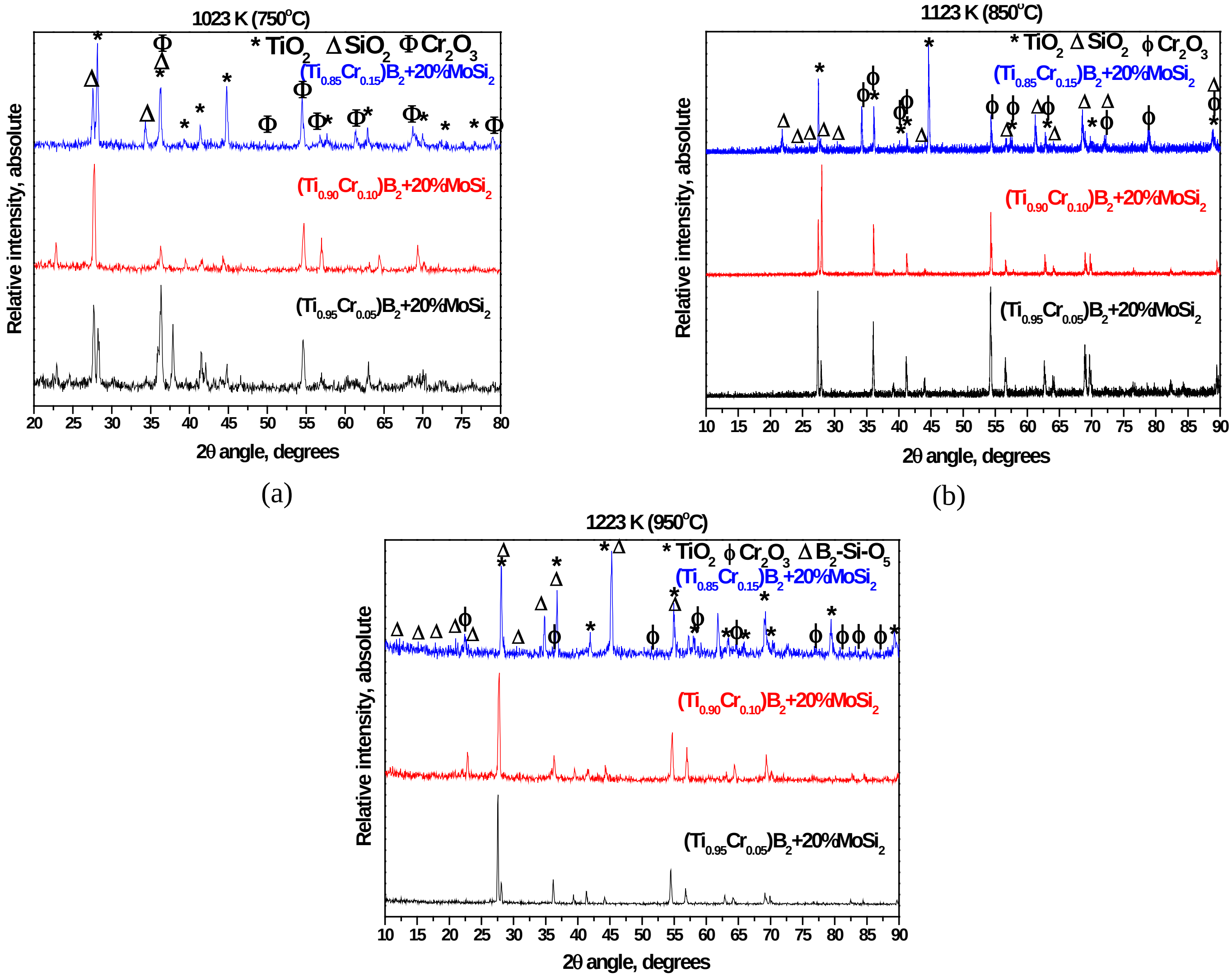

(a) (b)

(c)

Fig. 6.45 XRD patterns of $(TiCr)B_2$+20%$MoSi_2$composites at a)1023, b)1123 and c)1223K

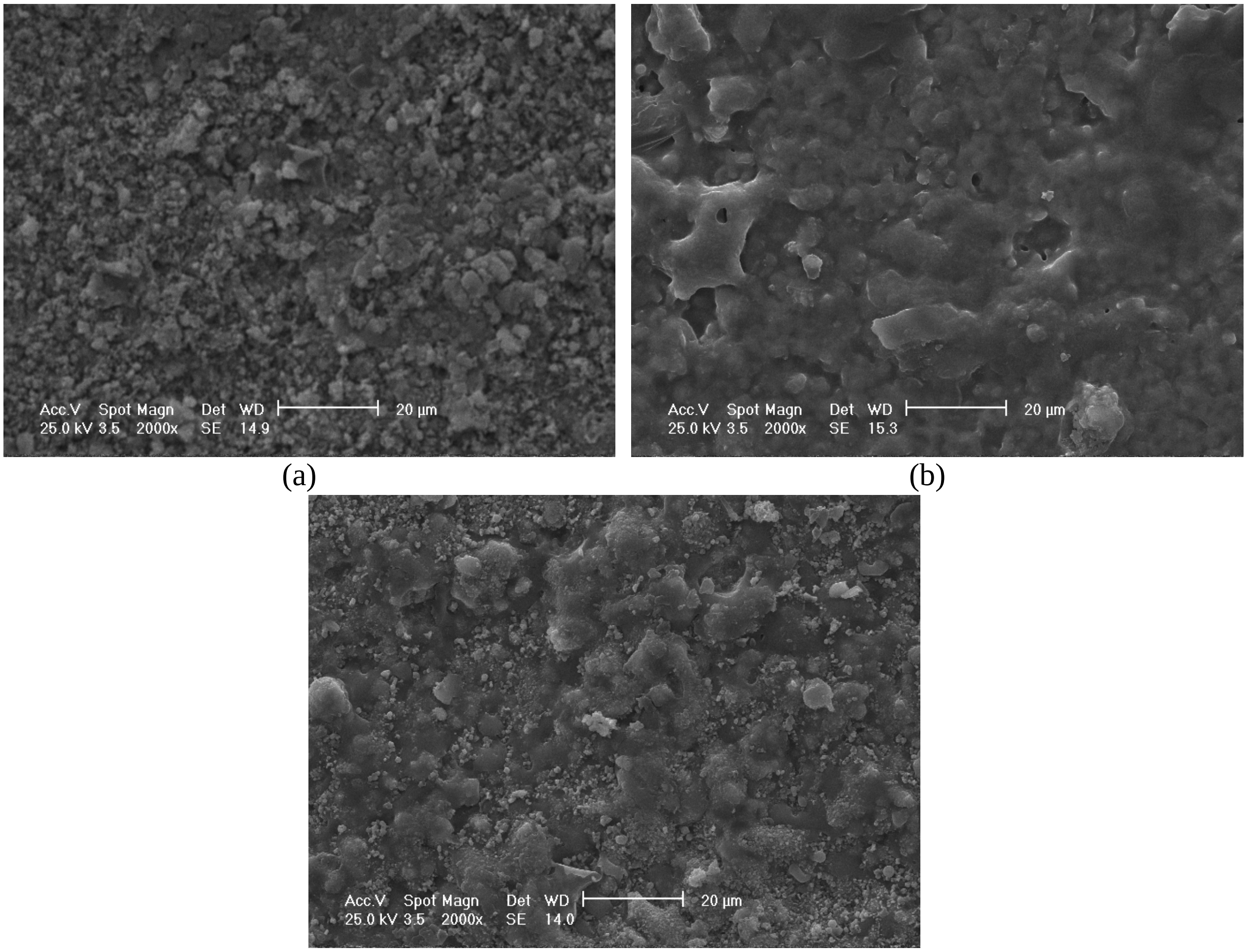

(a) (b)

(c)

Fig. 6.46 SEM images of a) $(Ti_{0.95}Cr_{0.05})B_2$+20% $MoSi_2$, b) $(Ti_{0.90}Cr_{0.10})B_2$+20% $MoSi_2$ and c) $(Ti_{0.85}Cr_{0.15})B_2$+20% $MoSi_2$ composites oxidized at 1023K (750°C) for 64h

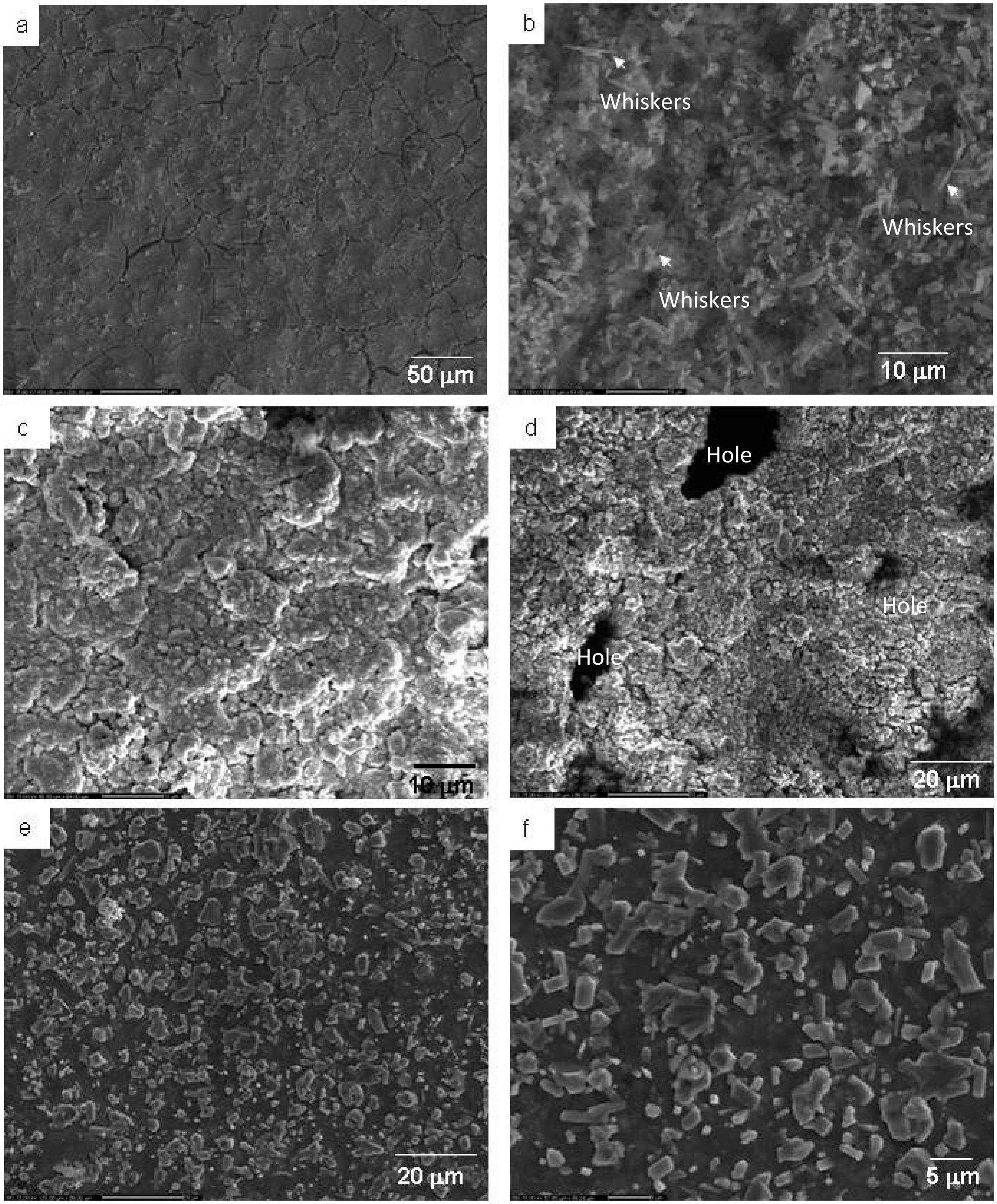

Fig. 6.47 Morphology of the oxidized surfaces of a & b) $(Ti_{0.95}Cr_{0.05})B_2$+20% $MoSi_2$, c & d) $(Ti_{0.90}Cr_{0.10})B_2$+20% $MoSi_2$ and e & f) $(Ti_{0.85}Cr_{0.15})B_2$+20% $MoSi_2$ composites after isothermal oxidation at 1123K (850°C) for 64h in air

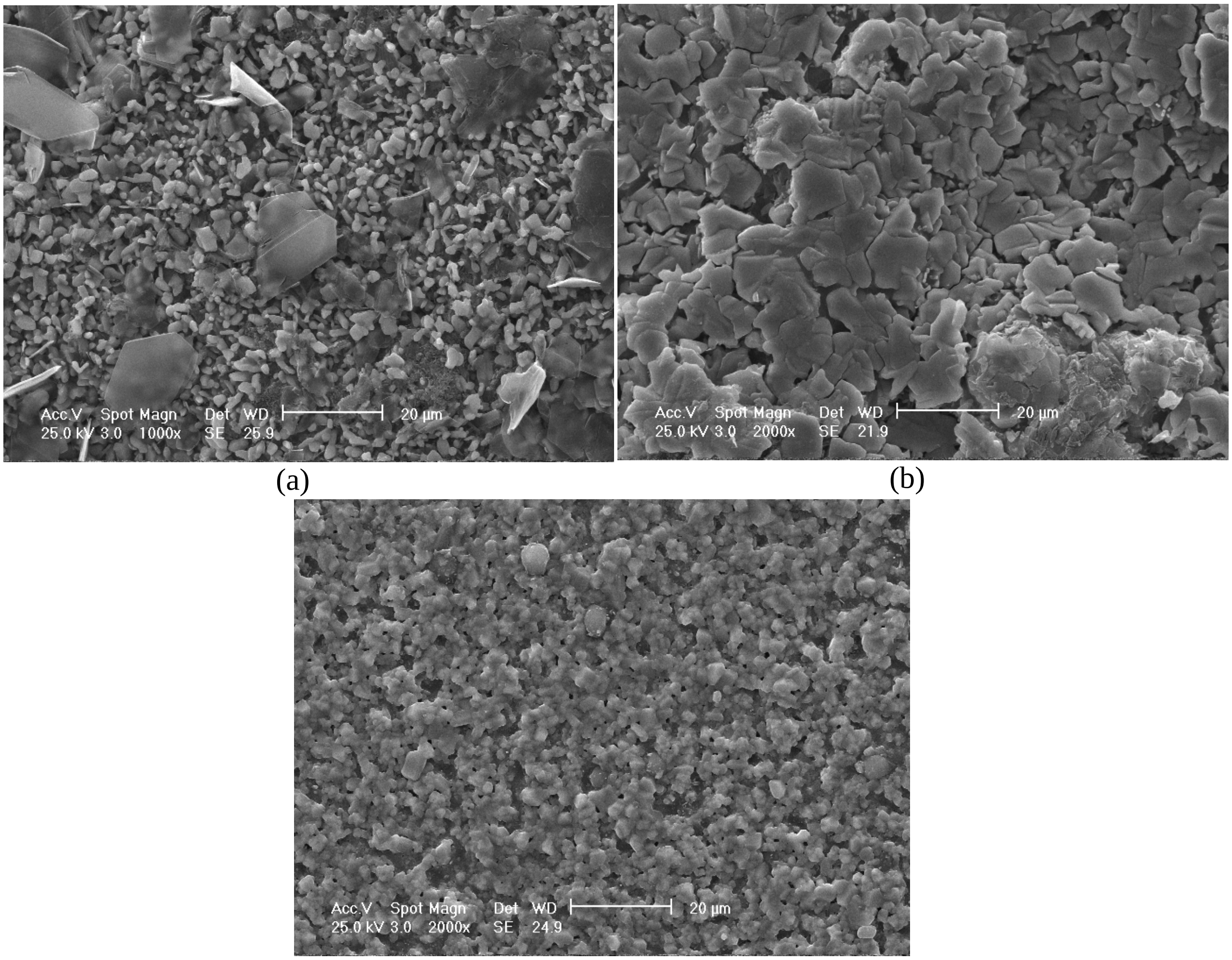

(a) (b)

(c)

Fig. 6.48 SEM images of a) $(Ti_{0.95}Cr_{0.05})B_2$+20% $MoSi_2$, b) $(Ti_{0.90}Cr_{0.10})B_2$+20% $MoSi_2$ and c) $(Ti_{0.85}Cr_{0.15})B_2$+20% $MoSi_2$ composites oxidized at 1223K (950^{o}C) for 64h

To understand the role of various elements during oxidation of $(Ti_{0.85}Cr_{0.15})B_2$ + 20% $MoSi_2$ composite, extended oxidation was carried out at 1123K (850^{o}C) for 256h. Cross section of the 15%CrB_2 contained $(TiCr)B_2$+20%$MoSi_2$ oxidized surface after 256h was characterized by SEM-EDS and is presented in Fig.6.49. The thickness of the oxide layer is <10 μm and the elemental distribution of this layer for Si, Ti, B, Mo, Cr and O is also given. Outer most layer of oxidized surface is seen to be that of silicon oxide. Only in the top layer of upto 10 μm, there is a deficiency of the metallic elements. This layer is dominated by silicon and oxygen, clearly indicating the migration of silicon towards the outer surface. Cross section results of pre-alloyed

$(TiCr)B_2$ composite is compared with the separate addition of TiB_2 and CrB_2 are brought out below. The thickness of the oxide layer is ~100 µm for TiB_2+15%CrB_2+$MoSi_2$ composite, which is much higher than that of $(Ti_{0.85}Cr_{0.15})B_2$+20%$MoSi_2$ composite of <10 µm. Migration of boron towards the outer surface was observed in TiB_2+15%CrB_2+$MoSi_2$ composite, where as migration of silicon in case of $(Ti_{0.85}Cr_{0.15})B_2$+20%$MoSi_2$ composite.

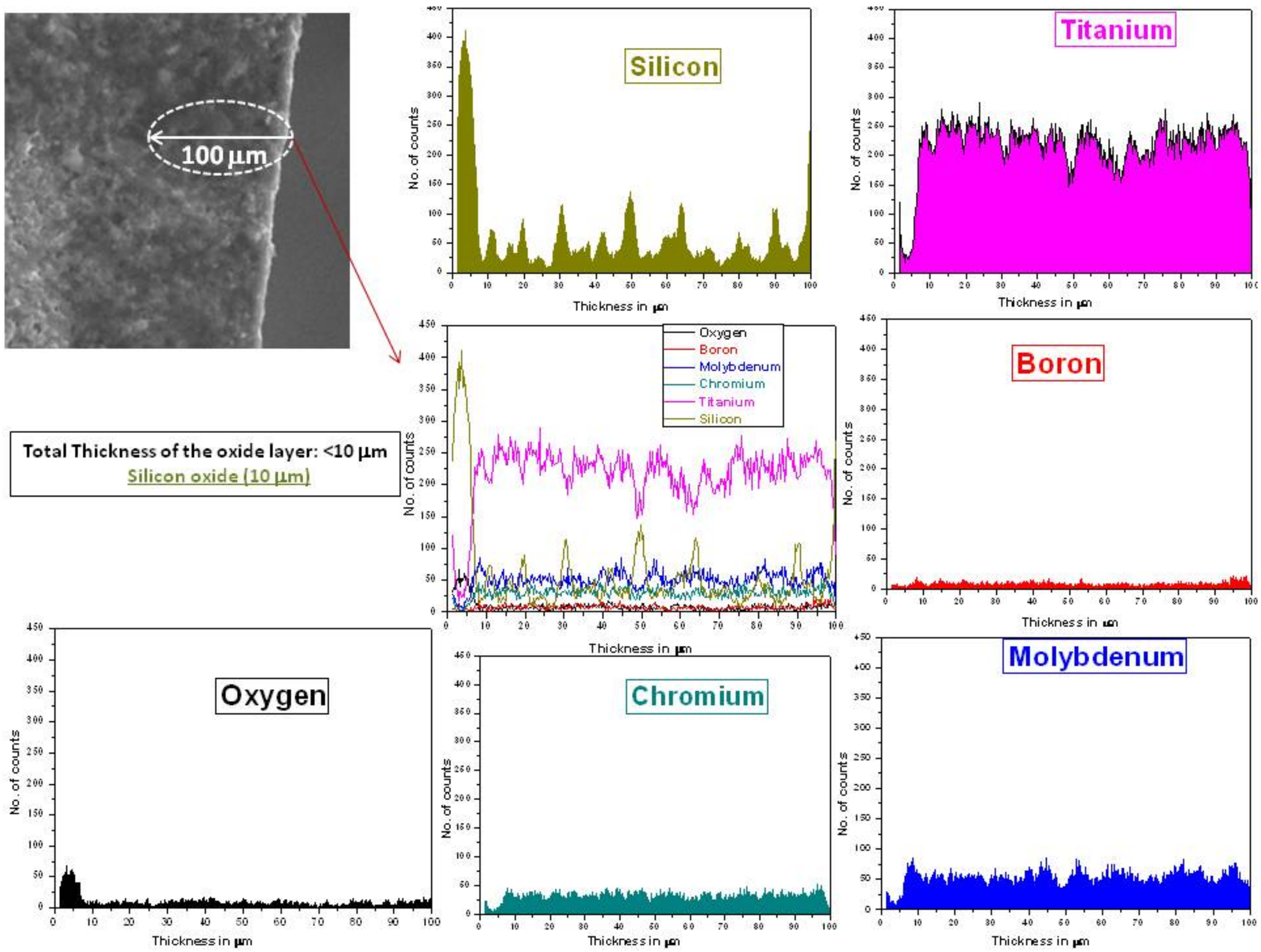

Fig. 6.49 Cross section of $(Ti_{0.85}Cr_{0.15})B_2$+20% $MoSi_2$ oxidized surface after 256h at 1123K

Thermal cycling study was carried out for $(Ti_{0.85}Cr_{0.15})B_2$+20%$MoSi_2$ composite, using a twin zone vertical furnace (Fig.3.8b) with pneumatic movement of the sample holder from hot zone to the cold zone and vice versa. Movement of the sample between zones was rapid (<5 sec). Hot zone and cold zone were maintained at 850^oC and 150^oC respectively. In a single cycle sample remained in each zone for 10 minutes. The samples were tested up to 1000 cycles and the degradation of the material was estimated by measurement of elastic modulus using ultrasonic method (UT 340 pulser receiver system, Canada) as per the ASTM C 1419-99a test procedure. During thermal cycling, defects can be generated either on the surface of the specimen or within the bulk. Surface defects can easily be viewed by various optical techniques. However, to ascertain the presence of defects in the bulk, indirect techniques that provides evidence of the presence of defects. That affect physical properties such as elastic modulus are preferred. There was no change in physical appearance of the sample even after 1000 cycles. Elastic modulus values measured 515 GPa even after 1000 cycles. A small, insignificant variation of 5 GPa in modulus value was observed. This indicates the stability of composite with respect to thermal cycling.

Effect of isothermal oxidation (1123K for 64h) behavior of TiB_2 composites are compared with that of different individual additives such as $MoSi_2$[1], WSi_2, $CrSi_2$, $TiSi_2$ and CrB_2 and all the data is summarized in Table.6.7. Weight gain of WSi_2 composite is relatively lower compared with other additives as indicated above. Addition of $MoSi_2$ have been reported to be ineffective due to degradation of oxide layer by the evaporation of MoO_3[1]. Formation of a protective SiO_2/ borosilicate glass layer has been observed on the oxide scale, when $TiSi_2$ is added. However, the protective layer was in patches and incomplete. In case of CrB_2, formation of a continuous and protective layer of $CrBO_3$ has been noticed. Continuous and protective layer of SiO_2 is also observed with 15% $CrSi_2$ sample. In the case of WSi_2 addition also, formation of a crack free protective and continuous oxide layer was observed in all the dense composites. Formation of SiO_2 and the solubility of SiO_2 in liquid B_2O_3 to form a stable glass could be the reasons for the improved oxidation resistance of $CrSi_2$ & WSi_2 composites. Effect of isothermal oxidation (1123K for 64h) behavior of TiB_2 composite is with combined addition of $MoSi_2$ and CrB_2 compared with that of different additives such as $MoSi_2$[1], WSi_2, $CrSi_2$, $TiSi_2$ and CrB_2 (Table.6.7). Weight gain of TiB_2 composite is with combined addition of $MoSi_2$ and CrB_2 is relatively lower compared with other additives as indicated above.

Effect of isothermal oxidation (1123 K for 64h) behavior of $(TiCr)B_2$+20%$MoSi_2$ composites are compared with that of composites without pre-alloyed TiB_2+ CrB_2+20% $MoSi_2$ additive (Table. 6.7, 6.8 and 6.9). Weight gains of pre-alloyed composites are relatively lower compared to the admixed composites without pre-alloying. Pre-alloyed $(TiCr)B_2$+20%$MoSi_2$ composite has better oxidation resistance compared to TiB_2+ CrB_2+20% $MoSi_2$ composites prepared from mixture of individual components. Reason for improved oxidation resistance in this $(TiCr)B_2$+20%$MoSi_2$ composite is due to the migration of silicon towards the outer surface, which forms a protective glassy phase, impeding further oxidation.

Overall observations on the effect of sinter additives on the oxidation resistance are summarized in Table 6.8 for all the composites. The order therefore is (from least resistant to most resistant): $TiB_2 + TiSi_2 < TiB_2 + CrB_2 < TiB_2 + CrSi_2 < TiB_2 + WSi_2 < TiB_2 + CrB_2 + MoSi_2 < (TiCr)B_2 + MoSi_2$.

Table 6.7 Specific weight gain and rate constants after 64h of oxidation

Sample	% additive	Sp.wt. gain, kg/m^2 x 10^3	Kp*(kg^{2}m^{-4} s^{-1})	Km$^\$$	m$^\#$
At 1023K (750 °C)					
TiB_2 + x%$CrSi_2$	5	8.82	4.45 x 10^{-10}	3.11 x 10^{-12}	3.003
Ti(x%Cr)B_2 (+20% $MoSi_2$)	5	4.73	1.25 x 10^{-10}	2.69 x 10^{-12}	2.687
	10	2.32	2.32 x 10^{-11}	8.50 x 10^{-12}	2.156
	15	3.06	5.26 x 10^{-11}	3.49 x 10^{-15}	3.590
TiB_2 + x%CrB_2 (+20% $MoSi_2$)	5	14.97	7.73 x 10^{-10}	1.84 x 10^{-9}	1.812
	10	4.26	9.13 x 10^{-11}	1.47 x 10^{-15}	3.906
	15	2.06	1.86 x 10^{-11}	1.67 x 10^{-10}	1.661
At 1123K (850 °C)					
TiB_2 + x%$TiSi_2$	2.5	59.83	1.37 x 10^{-7}	2.28 x 10^{-7}	1.789
	5	12.95	6.11 x 10^{-8}	-	1.990
	10	4.84	1.25 x 10^{-8}	-	2.012
TiB_2 + x%$CrSi_2$	2.5	150.19	8.94 x 10^{-8}	6.67 x 10^{-8}	2.129
	5	122.63	6.91 x 10^{-8}	7.05 x 10^{-8}	1.992
	10	112.69	6.73 x 10^{-8}	1.17 x 10^{-8}	2.716
	15	58.48	1.91 x 10^{-8}	0.37 x 10^{-8}	2.540
TiB_2 + x%CrB_2	2.5	105.25	4.05 x 10^{-8}	5.26 x 10^{-8}	1.901
	5	158.86	9.43 x 10^{-8}	11.60 x 10^{-8}	1.908
	10	155.84	13.08 x 10^{-8}	5.01 x10^{-8}	2.456
Ti(x%Cr)B_2 (+20% $MoSi_2$)	5	34.62	5.24 x 10^{-9}	1.55 x 10^{-9}	2.327
	10	26.07	3.72 x 10^{-9}	3.57 x 10^{-10}	2.602
	15	8.17	1.75 x 10^{-9}	6.80 x 10^{-14}	4.359
TiB_2 + x%CrB_2 (+20% $MoSi_2$)	5	46.94	1.06 x 10^{-8}	2.80 x 10^{-9}	2.396
	10	56.03	1.84 x 10^{-8}	5.23 x 10^{-11}	3.876
	15	27.02	4.91 x 10^{-9}	1.73 x 10^{-11}	3.495
TiB_2 + x%WSi_2	2.5	129.72	14.22 x 10^{-8}	255.2 x 10^{-8}	<1.0
	5	46.76	0.55 x 10^{-8}	19.93 x 10^{-8}	1.500
	5(80%TD)	393.05	74.21 x 10^{-8}	29.40 x 10^{-8}	<1.0
	10	62.76	1.62 x 10^{-8}	2.51 x 10^{-8}	1.860
	15	38.10	0.63 x 10^{-8}	0.22 x 10^{-8}	2.297
TiB_2	0%	305238.6	6.0 x 10^{-8}	-	-
At 1223K (950 °C)					
TiB_2 + x%$CrSi_2$	5	103.50	6.18 x10^{-8}	1.47 x10^{-9}	3.489
Ti(x%Cr)B_2 (+20% $MoSi_2$)	5	57.32	1.46x10^{-8}	2.69 x 10^{-8}	1.807
	10	39.58	9.96x10^{-9}	8.01 x 10^{-11}	3.410
	15	4.58	2.14x10^{-10}	2.43 x 10^{-31}	10.953
TiB_2 + x%CrB_2 (+20% $MoSi_2$)	5	14.14	1.26 x10^{-9}	2.43 x 10^{-14}	4.422
	10	24.10	3.50 x10^{-9}	4.71 x 10^{-14}	4.821
	15	88.76	6.63 x10^{-8}	8.49 x 10^{-14}	7.403

($^*K_p$ – Parabolic rate constant, $^\$K_m$ – Rate constant of general rate equation, $^\#$m- Slope of general rate equation)

Table 6.8 Summary of oxidation results of the presently studied composites

Composite	Surface oxides	Surface morphology	General remarks /observations	Technological nature
TiB_2 + $TiSi_2$	SiO_2, TiO_2	Continuous and crack free glassy layer	Nature of oxidation is near parabolic	Better than monolithic TiB_2
TiB_2 + $CrSi_2$	Cr_2O_3, SiO_2, TiO_2	Continuous and glassy layer	Complete parabolic nature of oxidation	Protective
TiB_2 + WSi_2	SiO_2, TiO_2	Crack free, continuous and glassy layer	Complete parabolic nature of oxidation	Protective
TiB_2 + CrB_2	$CrBO_3$, TiO_2	Continuous and thick glassy film	Parabolic nature of oxidation	Protective
TiB_2 + CrB_2 + $MoSi_2$	Cr_2O_3, SiO_2, TiO_2	Continuous and thick glassy phase	Cubic nature of oxidation	Protective
$(TiCr)B_2$ + $MoSi_2$	Cr_2O_3, SiO_2, TiO_2, B_2-SiO_5	Continuous, crack free and thick glassy phase	Best oxidation resistant composite among all these composites.	Excellent Protective

6.4 Discussion on results of oxidation studies

In this section, the experimental results are analyzed for elucidating a) thermodynamic feasibility of various oxidation reactions b) influence of sinter additives and their quantity on oxidation kinetics, and c) analysis of oxide scale and identification of probable mechanism.

The oxidation mechanism of TiB_2 depends on the temperature, partial pressure of oxygen, duration of exposure, porosity and composition, i.e. quantity of sinter additives. Six different TiB_2 based composites were prepared and subjected to oxidation studies. The objective was to study the effect of sinter additives and their quantities on the oxidation mechanism. All the composites contained either Si and/or Cr as a component. Cr and Si form stable oxides under oxidation conditions at elevated temperatures.

The kinetics of oxidation has been analyzed starting from weight gain per unit surface area ($\Delta W/S$) as a function of time (t) and fitting the data into equations (6.1) and (6.2). Table 6.7 records the oxidation exponent of all the TiB_2 composites. A value of $m = 1$ or 2 or 3 indicates operation of a linear or parabolic or cubic law, respectively. Values of $m = 1.5$ or 2.5 indicates the mixed kinetics.

When TiB_2 is exposed to air at elevated temperatures, the following reactions occur:

$TiB_2 (s) + 5/2\, O_2 (air) \rightarrow TiO_2 (s) + B_2O_3 (l)$

(6.39)

Above 1273K: $B_2O_3 (l) \rightarrow B_2O_3 (g)$ (6.40)

When the oxidation temperature is increased to 1073K (800^oC) the oxide scale on TiB_2 consists of both TiO_2 and B_2O_3 phases [8]. The diffusion coefficients of oxygen in B_2O_3 and SiO_2 are about 10^{-11} and 10^{-13} m^2/s respectively at 1173K (900^oC) [9,10,30]. Whereas, the oxygen diffusivities are much lower for TiO_2 and Cr_2O_3, 10^{-18} and 10^{-19} m^2/s respectively at 1273K (1000^oC) [9,10,31,32]. In the present study composites, consisting of Ti, Cr, B, Mo, Si and B constituents. From the Ellingham diagram, the stabilities of these oxides are seen in the following order: $MoO_3 < Cr_2O_3 < B_2O_3 < SiO_2 < TiO_2$ [33]. TiO_2 is most stable and forms readily. Hence, at or above 1273K (1000^oC) the protective role of TiO_2 increases with increasing temperature, by the formation of rutile scale layer on the samples. At high temperatures (1273-1473K), B_2O_3 evaporates due to its high volatility and is not detected in the oxide scale [30].

The oxidation of TiB_2 composites can be minimized either by providing resistance to the diffusion of oxygen ion into the material or to the diffusion of the base ceramic forming element ions through the oxide to the oxide-air interface. Mitra [34] reported that both SiO_2 and Al_2O_3 can form protective scales on surface and also exhibit low parabolic rate constants for the growth of respective oxides, because of their high thermodynamic stability and low diffusivity for both cations and anions. In case of the oxidation resistant silicides, the amorphous SiO_2 scale is more protective than the crystalline SiO_2, because of the possible grain boundary diffusion in the latter (crystalline phase). In the present case, weight gain of the samples, oxide layer thickness and parabolic rate constant values, all decrease with an increase in the amount of sinter-additive (Table 6.7). Also, there is a decrease in oxidation rate of $(TiCr)B_2$+20%$MoSi_2$. This is attributed to the formation of protective, thin, SiO_2 layer of thickness <10 μm, which acts as a barrier for the diffusion of oxygen ions (Fig. 6.49). It is interesting to note that with increasing sinter additive content from 2.5 to 5 or 10%, nature of oxidation changes from linear to parabolic or cubic in the present study. Similar observations were also noted for specific weight gain change and parabolic rate constants. SEM images of oxidized surfaces provide confirmation of the above cited observations. From the present study, it can therefore be inferred that at least 5 wt% sinter additive is needed to a form protective SiO_2 and/or a borosilicate glass and/or a $CrBO_3$ layer for improving the oxidation resistance of TiB_2.

Present studies on oxidation were carried out below 1273K (1000^{o}C), where liquid B_2O_3 forms that fills all pores/cracks in the oxide scale and provides resistance to further diffusion of oxygen ions. Surface cracks of the oxidized samples are expected in TiB_2 due to volumetric expansion during formation of TiO_2. In general, sinter additives for borides are essential in order to modify chemical composition of the oxide layer and to decrease the inward diffusion of oxygen ions through this oxide layer at high temperatures. In the composites presently chosen, as boron and silicon atoms being small in size, diffuse out and get oxidized readily. B_2O_3 is liquid at the oxidation temperature of ≤1273K (≤1000^{o}C). Both SiO_2 and TiO_2 are soluble in molten B_2O_3[20,21]. In fact, (melting temp of B_2O_3= 800K) eutectic reaction of SiO_2 with B_2O_3 is seen at 724K (451^{o}C) at 5% SiO_2. Hence, formation of B_2O_3 and SiO_2 glass forms and spreads all over the surface and acts as a barrier for diffusion of oxygen ions. Composites that contain Cr based additive in addition to Si, will also form a Cr_2O_3 layer below the top layer of B_2O_3 and SiO_2 (seen in Fig. 6.43 & 6.49). As the outer layers of B_2O_3 and SiO_2 allow only limited oxygen diffusion, it will lead to formation of a more stable Cr_2O_3 layer. (Cr_2O_3 stability will be enhanced in the absence or limited supply of oxygen). The diffusion coefficients of oxygen in B_2O_3 and SiO_2 are about 10^{-11} and 10^{-13} m^2/s respectively at 1173K (900^{o}C) [30,31]. Based on the above observations, improved oxidation resistance is expected in the composites with additives containing both Cr and Si. The oxidation mechanisms involved in the formation of a composite with each specific additive are described in the following sections:

6.4.1 Effect of $TiSi_2$ addition on oxidation behavior of TiB_2

The values of the exponent ‘m’ in the general rate equation (equation- 6.1) obtained were in the range of 1.7 and 2.0. Although strict parabolic behavior was not observed here (except TiB_2+15%$TiSi_2$ composite), the rate constants are in the range of 10^{-7} to 10^{-8} $Kg^2m^{-4}s^{-1}$. The observed parabolic kinetics indicate a diffusion controlled reaction in the composite. The value of K_p showed a decrease with the increase in amount of sinter additive ($TiSi_2$) to TiB_2. This could be due to the availability of more amount of Si. Figure 6.6 shows the variation of rate of change of weight gain per unit surface area with time for oxidation at 1123 K (850^o C).

XRD patterns of the all the oxidized surfaces show the presence of TiO_2 and SiO_2. Scanning electron micrographs show that the oxidized surfaces appear to be continuous and crack free with stable SiO_2 layer and spherical crystalline TiO_2.

The oxidation behavior of the presently investigated composite will now be discussed in reference to literature results. Pugach et al. [2] have reported the presence of TiO_2, SiO_2 and

B_2O_3 on the surface of oxidized TiB_2 + 20 %$TiSi_2$ in the range of 1273-1473 K (1000- 1200^o C). Raju et al.[42] have reported the low oxidation kinetics of TiB_2+10%$TiSi_2$ composites has been attributed to the presence of protective SiO_2 and borosilicate glass layer formation, which acts as a barrier for the diffusion of oxygen ions.

In the present study, isothermal oxidation was carried out at 1123K (850^{o}C). According to literature, B_2O_3 should exist on the oxidized surface of the present composites. However, that B_2O_3 was not detected by XRD indicates that B_2O_3 could either be present in amorphous form or in low quantity. Thermodynamic calculations (equation- 6.4) indicate that $TiSi_2$ is more readily oxidized due to more negative free energy change for oxidation as compared to that for TiB_2 and Ti_5Si_3 (Ti_5Si_3 is a reaction product formed during densification of TiB_2 + $TiSi_2$ composite). Formation of SiO_2 layer on the oxidized surface of TiB_2+$TiSi_2$ appears to be responsible for the parabolic nature and improved oxidation resistance, as diffusivity coefficient of oxygen ion in SiO_2 (10^{-13} m^2/s) is two orders less than that in B_2O_3 (10^{-11} m^2/s) at 1173K (900^{o}C) [30,31]. This inference is further confirmed as the rate of oxidation decreased with the increase of sinter additive ($TiSi_2$). Composites having $\geq$5% $TiSi_2$, showed higher resistance to oxidation due to the formation of a uniform layer providing an effective barrier for oxygen ion diffusion.

6.4.2 Role of $CrSi_2$ addition on oxidation behavior of TiB_2

The weight gain data obtained during isothermal oxidation at 1123K (850^{o}C) as a function of time for 2.5%, 5%, 10% and 15% $CrSi_2$ composites are presented in Fig.6.10. Continuous weight gain with time is observed in all the samples. With increasing $CrSi_2$ content, rate of weight gain decreased. The nature of oxidation appears to be parabolic (m=1.99 to 2.71) for all the composites. Parabolic rate constants of all three composites (2.5, 5 and 10%) are in the same order (6 to 9 x 10^{-8} $kg^2m^{-4}s^{-1}$) indicating the mechanism of oxidation to be diffusion controlled reaction. TiO_2 and Cr_2O_3 phases were identified in all the composites. In addition, SiO_2 peaks were observed in 15% $CrSi_2$ composite. Various possible oxidation reactions of TiB_2 and $CrSi_2$ are presented in equations 6.7 to 6.10. From the data all reactions are thermodynamically feasible and oxidation of TiB_2 is more favorable as compared to $CrSi_2$. XRD results indicate the formation of Cr_2O_3. SEM images of oxidized surfaces of all the samples appear to be crack free. With increasing $CrSi_2$ content, protective and continuous oxide layer was seen. The value of parabolic rate constant is found to decrease with increase of $CrSi_2$ content and Cr_2O_3 and SiO_2 formation on the oxidized surfaces; indicating the effectiveness of $CrSi_2$ addition in improving the oxidation resistance.

During oxidation of the composite, B_2O_3 is formed first and increases in thickness due to the high mobility of small sized boron atom and this liquid layer of B_2O_3 controls further oxidation [10,11]. As oxygen ions need to diffuse through this liquid layer, rate of oxidation decreases further. With limited oxygen supply, the lower oxide of chromium namely Cr_2O_3 is favored as compared to CrO_2 or CrO_3. Among the three probable oxides of Cr namely Cr_2O_3, CrO_2 and CrO_3, the lower oxide Cr_2O_3 is more stable and favorable.

Few bunches of TiO_2 crystals were seen as elongated and acicular shape on the oxidized surfaces. Appearances of crystals with similar morphology have been reported by Koh et al. [7] and Tampieri & Bellosi [8]. The latter have also reported the formation of a continuous needle like TiO_2 oxide scale at temperatures above 1173K (900^oC). In 10% $CrSi_2$ composite, more area of the surface is covered by the glassy phase and the needle like structure (TiO_2) has disappeared (Fig.6.18 c). The surface is fully covered by glassy layer in 15% $CrSi_2$ composite (Fig.6.18 d).

Formation of a protective glassy phase is composed of SiO_2 owing to higher $CrSi_2$ and thereby Si content.

Dasgupta et al [14] have reported good oxidation resistance of $CrSi_2$ powder up to 873K (600^oC) in air. Ma et al. [15] have found that oxidation of $CrSi_2$ starts at 1089K (816^oC) and a weight gain of about 8.6wt% of the sample only on oxidation up to 1273K (1000^oC), due to a protective oxide layer consisting of crystalline Cr_2O_3 and amorphous SiO_2 formation on the surface. Gang et al. [16] observed the formation of Cr_2O_3 and SiO_2 phases on oxidation of $CrSi_2$ at 1773K (1500^oC) for 34h in air. Cr_2O_3 is nonvolatile, insoluble in SiO_2 and helps to form a protective layer on the surface [9]. Naoyuki et al. [18] have reported excellent oxidation resistance of $CrSi_2$ upto 1373K (1100^oC) due to the formation of a thin and dense SiO_2 layer. Both SiO_2 and TiO_2 are soluble in molten B_2O_3 [20,21]. In fact eutectic reaction of SiO_2 with B_2O_3 is seen at 724K (451^oC) at 5% SiO_2 composition.

Parabolic nature of oxidation was observed and with increasing $CrSi_2$ content a decrease in rate of weight gain was observed. This composite was found to possess superior oxidation resistance as compared to other TiB_2 composites with $MoSi_2$ [1] and $TiSi_2$. Increased duration of exposure (up to 64h), higher temperature of oxidation (up to 1273K) and higher content of $CrSi_2$ (up to 15wt%) influence the formation of a continuous and protective glassy layer on the surface. The top layer of the oxidized surface contains B_2O_3 and SiO_2 in liquid or glassy form due to the small radius of B and Si atoms resulting in higher diffusivity. Below this layer Cr_2O_3 is stable due to the presence of only limited oxygen and acts as a further barrier. Although some amount of oxygen ions may diffuses through B_2O_3 (10^{-11} m^2/s at 1173K) and SiO_2 (10^{-13} m^2/s at 1173K) layers, further diffusion across the Cr_2O_3 layer is very difficult due to the low diffusivity coefficient (10^{-19} m^2/s at 1273K) of oxygen in Cr_2O_3 [30-32].

6.4.3 Influence of WSi_2 addition on oxidation behavior of TiB_2

Continuous weight gain with time is observed in all the samples containing WSi_2. With increasing WSi_2 content, decrease in weight gain rate is seen. The nature of oxidation appears to be linear and para-linear (in between parabolic and linear) for 2.5% ($m<1.0$) and 5% ($m=1.5$) composites respectively, close to parabolic ($m=1.86$) and complete parabolic for 10% and 15% ($m=2.297$) composites respectively. Parabolic rate constants (Table 6.3) of all three composites (5, 10 and 15%) are in the same order (0.55 to 1.62 x 10^{-8} $kg^2\ m^{-4}\ s^{-1}$) indicating the mechanism of oxidation to be diffusion controlled. TiO_2 and SiO_2 phases have been identified in all the composites. Number of SiO_2 peaks and their intensities increase with the increase in WSi_2 addition.

Various possible oxidation reactions of TiB_2, WSi_2 and W_5Si_3 were calculated (equations 6.11 to 6.25). W_5Si_3 appears to be a reaction product of TiB_2+WSi_2 composite during densification. It is evident that all the reactions are thermodynamically feasible. From the data, oxidation of TiB_2 (reactions -6.11 &6.12) and WSi_2 (reaction-6.16) appear to be more favorable compared to the oxidation of W_5Si_3. The formation of solid/glassy phases (TiO_2(s), B_2O_3(glass), B_2O_3(s), WO_3(s), WO_2(s)) has been confirmed by the weight gain data of the samples during oxidation.

The surface of sample with 2.5% WSi_2 (Fig. 6.25) appears to be crack free with continuous oxide layer. SEM images of 5% WSi_2 oxidized sample also show it to be crack free with a number of cuboid shaped particles, which were confirmed to be TiO_2 by EDS. Appearance of highly textured crystals with similar morphology have been reported by Koh et al. [7] and Tampieri & Bellosi [8]. The surfaces of composites containing 10 & 15% WSi_2 appear similar to that of 2.5% sample but with higher amount of glassy phase. With the increased addition of WSi_2, quantity of SiO_2 glass formed would be higher during oxidation, which explains the absence of TiO_2 cuboids. As both boron and silicon atoms are smaller in size, outward diffusion of either atom is easier [10,11].

SiO_2 and WO_3 have been reported on the surfaces of WSi_2 oxidized at 1373 K (1100^{o} C) and only SiO_2 at 1573 K (1300^{o} C) [22]. A similar observation has been made for oxidation of WSi_2 films, where the formation of SiO_2 and WO_3 were reported [23].

Microscopic observation of the 10% WSi_2 oxidized surface presented a crack free continuous and protective glassy layer on the surface. In the present composite diffusion of oxygen ions takes place through B_2O_3 liquid layer and subsequently through SiO_2 glassy phase, which is the rate controlling step.

As WSi_2 and $CrSi_2$ are the two additives which form a stable protective oxide layer on TiB_2, the comparisons between these two additives are brought out below. Origin of the TiB_2 powder, processing and oxidation conditions of both the composites were same. Parabolic rate constants obtained were lower in case of composite with WSi_2 (except 2.5%) compared to that of $CrSi_2$ on isothermal oxidation at 1123K (850^{o}C) for 64h in air (see in Table 6.7 & 6.8).

6.4.4 CrB_2 role in the oxidation behavior of TiB_2 composites

Continuous weight gain with time is observed in all the samples. With increasing CrB_2 content, increase in the weight gain also is recorded. The nature of oxidation is near parabolic (m=1.901) for 2.5% and (m=1.908) 5% CrB_2 samples, with complete parabolic nature (m= 2.5) for TiB_2+10%CrB_2 composite. Parabolic rate constants of all three composites are in the same order (4-13 x 10^{-8} Kg^2m^{-4} s^{-1}) indicating the mechanism of oxidation to be diffusion controlled process. TiO_2 and $CrBO_3$ peaks are identified on the oxidized surface. Though B_2O_3 starts evaporating above 1273 K (1000^o C), $CrBO_3$ is stable up to 1473 K (1200^o C) and at higher temperatures decomposes in the presence of oxygen to Cr_2O_3 and B_2O_3 [27].

Standard free energy of formation for the possible oxidation reactions are calculated (equations from 6.26 to 6.30). From the thermodynamic data, all reactions appear to be thermodynamically possible. Oxidation of CrB_2 is more favorable as compared to TiB_2 as seen from the Fig.6.36. This could be the reason for the higher weight gain of the samples on oxidation with increased CrB_2 content. Reaction 6.26, 6.27 and 6.30 results in weight gain whereas reactions 6.28 and 6.29 result in weight loss due to the gaseous nature of CrO_2 and CrO_3 at 1123K (850^oC). The overall weight gain observed during oxidation studies point to the fact that reactions leading to formation of non-volatile oxide species are predominant.

SEM images of the surface after oxidation at 1123K (850^oC) indicate that the oxide layer is crack free in all the composites. With increasing CrB_2 content, one can see higher flow of liquid phase and disappearance of individual particles (Fig.6.35b). With 10% $CrB_{2,}$ a continuous protective layer is seen to have formed on the surface (Fig.6.35c). As the formation of Cr_2O_3 increases with increased CrB_2 content in the composite, a thick protective layer of $CrBO_3$ is formed. Increase in CrB_2 content in the sample also increases B_2O_3, a glassy phase, indicated by the absence of clear/definite peaks (Fig.6.34).

Okada *et al.*[24] have studied the oxidation behavior of CrB_2 single crystal and reported that, oxidation begins at 997K (740^oC) resulting in the formation of Cr_2O_3 and $CrBO_3$ phases. Emiliani [25] have reported that oxidation of hot pressed CrB_2 at 1373K (1100^oC), a massive chromium borate ($CrBO_3$) scale gets formed which results in weight gain. Tombs *et al.* [26] have identified the formation of a stable compound $CrBO_3$, by reaction of Cr_2O_3 and B_2O_3 in a melt containing excess B_2O_3. Samsanov *et al.* [27] have reported the formation of a tenacious oxide film consisting of B_2O_3 and $CrBO_3$ on oxidation of CrB_2 at 1173-1273K (900-1000^oC). TiO_2 is an n-type oxide, which exhibits both titanium interstitial ions and oxygen vacancies. Due to such defect structure, TiO_2 is prone to oxidation by diffusion of both cations as well as anions [35].

The nature of oxidation of the present composite appears to be parabolic at 1123K (850^oC). Protective oxide layer $CrBO_3$ was identified on the surface of the oxidized samples. Formation of a protective, continuous and thick glassy film was observed with increased CrB_2 content (up to 15 wt%) in the composite. $CrBO_3$ is more stable compound compared with B_2O_3 [27]. Rate controlling step in this composite is diffusion of oxygen thorough $CrBO_3$ layer.

It is worthwhile here to compare the oxidation behavior of TiB_2+CrB_2 composites with that of TiB_2+CrSi_2 composites (Table 6.7 & 6.8). Parabolic rate constants obtained were lower in case of composite with $CrSi_2$ compared to that of CrB_2 on isothermal oxidation at 1123K (850^oC) for 64h in air (Table 6.7). Specific weight gain vs. time of TiB_2 + 5%CrB_2 and TiB_2 + 5%$CrSi_2$ are compared in Fig.6.1. Oxidation of $CrSi_2$ starts at 873K (600^oC) where as that of CrB_2 composite at a lower temperature of 733K (460^oC). Specific weight gain of TiB_2 + 5% $CrSi_2$ composite at all temperatures is lower than that of TiB_2+CrB_2 composite. Total weight gain of the composite with $CrSi_2$ is much lower at 19.28 x 10^{-3} compared to that of with CrB_2 which was high at 54.83 x 10^{-3} kg/m^2. Hence, it can be concluded that TiB_2 composite with

$CrSi_2$ is a more oxidation resistant material than that with CrB_2. Silicon based additives to transition metal borides, improve oxidation protection due to the formation/stability of the outer layer of borosilicate glass that acts as a barrier to diffusion of oxygen to the substrate [17].

6.4.5 Effect of combined addition of CrB_2 and $MoSi_2$

Continuous weight gain with time is observed in all the samples. With increasing CrB_2 content, decrease in weight gain rate is seen. Comparing the weight gain between 1023 and 1123K (750 and 850°C), it is noticed that weight gain increases with temperatures for all the composites. The nature of oxidation appears to be near parabolic (m=1.6 to 2.0) at 1023K (750°C) for all the composites, which alters to cubic (m>3) at 1123K (850°C). Parabolic rate constant of 5, 10 and 15% CrB_2 composites are measured as 7.73, 0.91, 0.19 x 10^{-10} $kgm^{-4}s^{-1}$ respectively at 1023K (750°C). Two orders higher parabolic rate constants are measured for the same composites at 1123K (850°C) in the range of 0.5 to 1.8 x 10^{-8} $kgm^{-4}s^{-1}$. The above parabolic rate constant values at 1023 and 1123K (750 and 850°C) indicate that mechanism of oxidation to be diffusion controlled. The value of parabolic rate constant is found to decrease with increase of CrB_2 content from 5 to 15%, indicating the effectiveness of CrB_2 addition in improving the oxidation resistance.

Specific weight gain of TiB_2 composites with only CrB_2 addition was higher at all time intervals compared with TiB_2+20%$MoSi_2$+x%CrB_2 **(**x=5,10,15) samples. TiB_2 composites with only 20%$MoSi_2$ addition have also been reported to record very high weight gain which is about 3 orders of magnitude higher (34790 x10^{-3} kg/m^2) [1] as compared to the composite containing both the CrB_2 and $MoSi_2$. From the above, it is seen that a composite with combined additions of

CrB_2 and $MoSi_2$ has low specific weight gain during oxidation compared to TiB_2 composites that were formed with additions of either CrB_2 or with $MoSi_2$ alone. Lower order parabolic rate constant value was also observed in TiB_2 composite containing both $MoSi_2$ and 15% CrB_2 (Table 6.5) as compared to the composite containing either CrB_2 or $MoSi_2$ alone during oxidation at 1123K (850^{o}C).

TiO_2, Cr_2O_3 and SiO_2 phases were identified in all the composites. XPS analysis of oxidized surfaces shows the presence of MoO_3 and B_2O_3 phases in addition to TiO_2, Cr_2O_3 and SiO_2. Oxidation of TiB_2+$MoSi_2$+CrB_2 composite is represented by the possible overall reactions (equations 6.31 to 6.38). It is evident that reactions (6.31)-(6.37) are thermodynamically feasible. Oxidation of CrB_2 (reaction 6.34) is more favorable compared to TiB_2 and $MoSi_2$. However, the reactions for the formation of B_2O_3 (glass), Cr_2O_3(s), MoO_3(s) have more negative free energy change compared to reactions leading to gaseous product phases. Formation of the solid/glass phases as indicated above were confirmed by the weight gain data, XRD and SEM-EDS analysis of the samples during oxidation.

At 1123K (850^{o}C), the oxidized surface of 5% CrB_2 composite shows the formation of glassy phase partially covering the surface (Fig. 6.42a). At 1223K (950^{o}C) the glassy layer completely covered the surface (Fig. 6.42b). Though the weight gain data shows that evaporation is more at higher temperature for this composite, the higher temperature has also helped in the formation of liquid glassy phase. With 10% CrB_2 composite globules of oxidized particles are seen covered with the glassy layer (Fig. 6.42c) at 1123K (850^{o}C). At the higher temperature, the glassy layer appears to be discontinuous by the evaporating species (Fig. 6.42d) and the oxide crystals appear to be bigger in size. This is in conformity with the results of weight gain data on oxidation. With further increase in CrB_2 (15%) the oxidized surface appears to be crack free, continuous and with cuboids shaped crystalline particles after oxidation at 1123K (850^oC) (Fig 6.42e). After oxidation at 1223K (950^oC) the surface of the same composite appears fully covered with a wavy pattern (uneven surface) (Fig. 6.42f). This feature goes well with the weight gain pattern shown by this composite at 1223K (950^oC) with lower evaporation and higher weight gain.

To understand the role of various elements during oxidation of TiB_2 composites extended oxidation was carried out at 1123K (850^oC) for 256h. Cross section of the TiB_2+15%CrB_2+20%$MoSi_2$ oxidized surface after 256h was characterized by SEM-EDS (Fig.6.43). The thickness of the oxide layer is ~100 μm. Outer most layer of oxidized surface is seen to be composed of boron oxide. Boron content decreases drastically up to 20 μm and then gradually increases up to 100 μm from the top layer of the oxidized surface. Beyond 100 μm, the boron content is uniform. This clearly indicates that the outward diffusion of boron across the oxide layer is taking place. The next inner layer is seen to be composed of silicon oxide. Silicon content is seen to increase from 5 to 60 μm from the outer layer, indicating thereby the outward diffusion to be dominant. Qualitative analysis of this oxide layer shows that boron migrates towards the surface layer and is seen evaporating. Silicon combined with oxygen forms the barrier layer for further oxidation. Both SiO_2 and TiO_2 are soluble in molten B_2O_3[20,21]. Crystalline B_2O_3 and TiO_2 were found on the oxidized surfaces of TiB_2 at 973 and 1073K (700 and 800^oC) [8]. The large volume expansion that occurs during the oxidation of TiB_2 to TiO_2 causes cracking of the oxide layer, resulting in an increase in the active area for further oxidation [12,13]. $CrBO_3$ phase has been identified on oxidation of CrB_2 [24,25,27]. This particular compound was not identified on the oxidized surface of the TiB_2 + 20%$MoSi_2$ + x%CrB_2

(x=5,10,15) composites. It is well-established that the excellent oxidation resistance of $MoSi_2$ at high temperatures is attributed to the formation of a self-healing, glassy silica (SiO_2) layer. But during low temperature (673-873 K) oxidation, it exhibits pesting behavior. Pesting indicates disintegration of the material (the disintegrated $MoSi_2$ results in powdery products) [1].

The nature of oxidation of the TiB_2+15%CrB_2+20%$MoSi_2$ composite was observed to be parabolic at 750 and cubic at 850^oC. Protective oxide layers of B_2O_3 and SiO_2 were identified on the surface of the oxidized samples. Formation of a continuous and protective thick glassy phase was observed with increased CrB_2 (up to 15%) content in the composite. This composite is found to be a more oxidation resistant material compared to the composite containing either CrB_2 or $MoSi_2$ only. Boron and silicon diffuse towards the surface during the oxidation was mainly observed. Due to limited oxygen supply from top layers of B_2O_3 and SiO_2, forms a sable Cr_2O_3 as third layer, which acts as a diffusion barrier for further diffusion of oxygen ions (Fig. 6.43).

6.4.6 Oxidation studies of (TiCr)B_2 +20%$MoSi_2$ composites

This section deals with oxidation behavior of composites consisting of (TiCr)B_2 and 20%$MoSi_2$. The study deals with effect of varying the CrB_2 content from 5, 10 and 15 wt% in the TiB_2 composite while the $MoSi_2$ content is constant at 20%. The pre-alloyed (TiCr)B_2 with varying CrB_2 Content is consolidated in the presence of $MoSi_2$. The nature of oxidation appears to be complete parabolic (m=2.1 to 2.6) for $(Ti_{0.95}Cr_{0.05})B_2$ and $(Ti_{0.90}Cr_{0.10})B_2$+20% $MoSi_2$ composites and cubic ($m\geq3$) for $(Ti_{0.85}Cr_{0.15})B_2$+20% $MoSi_2$ composite at 1023K (750^oC). Parabolic rate constant of $(Ti_{0.95}Cr_{0.05})B_2$, $(Ti_{0.90}Cr_{0.10})B_2$ and $(Ti_{0.85}Cr_{0.15})B_2$+20% $MoSi_2$ composites are measured as 1.25, 0.23, 0.53 x 10^{-10} kg m^{-4} s^{-1} respectively at 1023K (750^oC). One order higher parabolic rate constants are measured for the same composites at 1123K (850°C) in the range of 3 to 5 x 10^{-9} kg m^{-4} s^{-1}. The above parabolic rate constant values at 1023 and 1123K (750 and 850°C) indicate that mechanism of oxidation to be diffusion controlled. The value of parabolic rate constant is found to decrease with increase of CrB_2 content from 5 to 15%, indicating the effectiveness of CrB_2 addition in improving the oxidation resistance. Specific weight gain in the case of TiB_2+CrB_2+20%$MoSi_2$ composites was higher at all time intervals compared with the pre-alloyed $(TiCr)B_2$ +20%$MoSi_2$ samples. From the above, it can be inferred that the composite with pre-alloyed $(TiCr)B_2$ with addition of 20%$MoSi_2$ has low specific weight gain during oxidation compared to TiB_2 composites that were formed without pre-alloyed (TiB_2 + CrB_2). This could probably be due to the more uniform distribution at the atomic level of Cr in the $(TiCr)B_2$ composite.

TiO_2, Cr_2O_3 and SiO_2 phases were identified in all the composites after oxidation at 1023 and 1123K (750 and 850°C). In addition, B_2SiO_5 (solid solution of B_2O_3 and SiO_2) phase was also observed when oxidized at 950°C. This clearly inferred the formation of a borosilicate consisting of both B_2O_3 and SiO_2 during oxidation of these composites. In case of $MoSi_2$-30 vol% TiB_2 composite, the oxide scale reportedly consisted of TiO_2 and glassy SiO_2 after the oxidation at 1473K (1200°C) for 24h [36].

SEM image at 1023K (750°C) indicating the start of formation of a liquid phase can be seen in sample $(Ti_{0.95}Cr_{0.05})B_2$+20%$MoSi_2$ (Fig.6.46a). High amount of liquid phase is seen on the surfaces of $(Ti_{0.90}Cr_{0.10})B_2$ and $(Ti_{0.85}Cr_{0.15})B_2$+20% $MoSi_2$ composites (Fig. 6.46b & c). To understand the role of various elements during oxidation of $(Ti_{0.85}Cr_{0.15})B_2$+20% $MoSi_2$ composite, oxidation for extended duration was carried out at 1123K (850°C) for 256 h. Cross section of the $(Ti_{0.85}Cr_{0.15})B_2$+20%$MoSi_2$ was characterized by SEM-EDS (Fig.6.49). The thickness of the oxide layer is <10 μm. Entire oxide layer of oxidized surface is seen to be composed of silicon oxide. This layer is dominated by silicon and oxygen, clearly indicating the outward diffusion of silicon ions and form SiO_2.

Oxidation and Cross section results of pre-alloyed $(Ti_{0.85}Cr_{0.15})B_2$+20%$MoSi_2$ composite is compared with the individual addition of TiB_2 and CrB_2 are presented in Table 6.9.

Table 6.9 comparison of oxidation and cross section results of pre-alloyed $(Ti_{0.85}Cr_{0.15})B_2$+20%$MoSi_2$ and TiB_2+15%CrB_2+20%$MoSi_2$

Feature/observation/result	TiB_2+15%CrB_2+20%$MoSi_2$	$(Ti_{0.85}Cr_{0.15})B_2$+20%$MoSi_2$
Thickness of the oxide layer	~100 μm	<10 μm
Diffusion of ions towards the outer surface	Boron	Silicon
Surface oxides	Cr_2O_3, SiO_2, TiO_2	Cr_2O_3, SiO_2, TiO_2, B_2-SiO_5
Surface morphology	Continuous and thick glassy phase	Continuous, crack free and thick glassy phase
Nature of oxidation	Parabolic	Cubic

The thickness of the oxide layer is ~100 μm for TiB_2+15%CrB_2+$MoSi_2$ composite, as compared to less than 10 μm in the case of $(Ti_{0.85}Cr_{0.15})B_2$+20%$MoSi_2$. The thickness of the oxide layer is low in the case of pre-alloyed composite of $(TiCr)B_2$ mainly due to the extremely low outward diffusion of Si ions as also the inward diffusion of oxygen ions appear to be rate controlling. Koh et al.[37] reported the observation of a very thick oxide layer (~170 μm) on the surface of TiB_2 after the oxidation in air at 1473K (1200°C) for 10h. When TiB_2+2.5 wt% Si_3N_4 specimen is exposed at 1200°C for 2h, a single TiO_2 oxide layer of 100 μm was noticed [7]. In the present composite thickness of the oxide layer was only <10 μm, but oxidized at only 1123K (850°C) for a long stretch of 256h.

The nature of oxidation of the composite changed from parabolic to cubic with increase of CrB_2 content from 5 to 15%. Protective oxide layers of TiO_2, Cr_2O_3 and SiO_2 were identified on the surface of the oxidized samples at 750 and 850°C. B_2-SiO_5 phase was identified instead of SiO_2 when oxidized at 950°C. Formation of a continuous, crack free and protective thick glassy phase was observed with increased CrB_2 content in the composite. This composite is found to be a more oxidation resistant material compared to the all other composites studied in the present work. Diffusion of boron towards the outer surface was observed in TiB_2+15%CrB_2+$MoSi_2$ composite, where as diffusion of silicon in case of $(Ti_{0.85}Cr_{0.15})B_2$+20%$MoSi_2$ composite. This could be due to that boron is attached with solid solution of $(TiCr)B_2$, which is in low energy state compared with TiB_2 and CrB_2. Hence, boron is not readily available to diffuse out and oxidizes. Next smallest available element of silicon diffuses out and readily gets oxidized. SiO_2 glassy layer is more protective compared with B_2O_3 as diffusivity coefficient of oxygen in SiO_2 (10^{-13} m^2/s) is two orders less than that of B_2O_3 (10^{-11} m^2/s) at 1173K (900°C) [30,31]. Further diffusion of oxygen through thin glassy SiO_2 layer (<10 μm) is not allowed to increase the thickness of the oxide layer. It is evident from the SEM-EDX line scanning of the cross section of the oxidized surface (Fig. 6.49). As Silicon diffuse towards the surface is responsible for better oxidation resistance of $(TiCr)B_2$ +20%$MoSi_2$ composite

Usually 15 to 25% of the sinter additive forms good protective silica and/or borosilicate oxide glass layers and provides oxidation resistance [38-40]. For example, the presence of SiC particles improved the oxidation resistance in the HfB_2 +19vol%SiC +5.8vol%Si_3N_4 composite and this is attributed to the formation of a protective borosilicate glassy coating on the exposed surfaces at temperatures of higher than 1400°C [38]. For the pressureless sintered ZrB_2 +20vol% $MoSi_2$ composite, Sciti et al.[39] mentioned that the silica, resulting from $MoSi_2$ facilitated the oxidation resistance at 1200°C. These ZrB_2 composites are reported to exhibit good room temperature mechanical properties and also could retain four-point flexural strength of 500 MPa up to 1773K (1500^{o}C) [40]. Whereas such higher amounts of sintering additives (~ 20% SiC or $MoSi_2$), would impart deleterious effect on the densification and mechanical properties of TiB_2 [41]. It is plausible that the addition of more amounts (> 10 %) of sintering additive may improve the oxidation resistance of TiB_2; however, one has to optimize the sinter additive amount to retain the unique properties of TiB_2.

6.5 Conclusions

Oxidation resistance of TiB_2 + $TiSi_2$ composite is found to be superior to that of TiB_2+$MoSi_2$. Addition of $MoSi_2$ have been reported to be ineffective due to degradation of oxide layer by the evaporation of MoO_3[1]. The formation of SiO_2 layer in addition to TiO_2 on the surface improves the oxidation resistance of TiB_2 + $TiSi_2$ composite.

Oxidation of TiB_2+$CrSi_2$ composite starts at 873K (600^{o}C) and a steep increase in the oxidation rate was noted above 1073K (800^{o}C). Parabolic nature of oxidation was observed. With increasing $CrSi_2$ content rate of weight gain decreased. This composite was found to be a superior oxidation resistant material as compared to other TiB_2 composites with $MoSi_2$, $TiSi_2$ and CrB_2. TiO_2 and Cr_2O_3 were observed on the oxidized surface. When the oxidation temperature was high at 1273K (1000^{o}C) or $CrSi_2$ content high at 15%, formation of SiO_2 was also observed in addition to the above two oxides. Microscopic observation of the oxidized surface presented a crack free oxide layer and the formation of glassy phase. Increased duration of exposure, higher temperature of oxidation and higher content of $CrSi_2$ influence the formation of a continuous glassy layer on the surface, which is protective.

Parabolic oxidation was observed and with increasing WSi_2 content rate of weight gain decreased. This composite exhibits superior oxidation resistance as compared to other TiB_2 composites with $MoSi_2$, $TiSi_{2,}$ CrB_2 and $CrSi_2$. Microscopic observation of the 10% WSi_2 oxidized surface presented a crack free continuous glassy layer on the surface. The nature of oxidation of the composite was observed to be parabolic at 1023K (850^{o}C).

Protective oxide layers of TiO_2 and $CrBO_3$ were identified on the surface of the oxidized TiB_2+CrB_2 samples. Formation of liquid phase ($CrBO_3$) was noticed at 1073K (800^{o}C) and glassy liquid patches at 1273K (1000^{o}C). Formation of a protective, continuous and thick glassy film was observed with increased CrB_2 content in the composite.

The nature of oxidation of TiB_2 + $MoSi_2$ + CrB_2 composite was observed to be parabolic at 1023K (750^{o}C) and cubic at 1123K (850^{o}C). Protective oxide layers of TiO_2, Cr_2O_3 and SiO_2 were identified on the surface of the oxidized samples of TiB_2 + $MoSi_2$ + CrB_2 composite. Formation of a continuous and protective thick glassy phase was observed with increased CrB_2 content in the composite. This composite is found to be a more oxidation resistant material compared to the composite containing either CrB_2 or $MoSi_2$ only. Boron and silicon diffuse towards the surface during the high temperature oxidation of TiB_2 + $MoSi_2$ + CrB_2 composite.

Weight gain due to oxidation of pre alloyed $(TiCr)B_2$+20%$MoSi_2$ composites is relatively lower compared with all composites. Protective oxide layers of TiO_2, Cr_2O_3 and SiO_2 were identified on the surface of the oxidized samples at 1023 and 1123K (750 and 850^{o}C). B_2-SiO_5 phase was identified instead of SiO_2 when oxidized at 1223K (950^{o}C). Formation of a continuous, crack free and protective thick glassy phase was observed with increased CrB_2 content in the $Ti(Cr)B_2$+20%$MoSi_2$ composite. This composite is found to be a more oxidation resistant compared to the composite without pre-alloyed TiB_2+ CrB_2+20% $MoSi_2$. Silicon is seen to diffuse towards the outer surface during the high temperature oxidation.

6.6 References

[1] T.S.R.Ch.Murthy, R.Balasubramanian, B.Basu, A.K.Suri and M.N.Mungole, Oxidation of monolithic TiB_2 and TiB_2-20wt% $MoSi_2$ composite at 850^oC, J.Eur.Cer.Soc. 2006;26:187-192

[2] E.A. Pugach, E.I. Golovko, and Y.H.Koh, S.Y. Lee and H.E. Kim, Oxidation behavior of titanium boride at elevated temperatures, J. Am. Ceram. Soc., 2001;84[1]:139–141

[3] L.I. Dvorina; High temperature oxidation of TiB_2 – $TiSi_2$ alloys, Powder Metallurgy, 2007;2:34-37 (in Russian)

[4] T. Graziani, E. Landi and A. Bellosi, Oxidation of TiB_2–20 vol. %B_4C composite, J. Mater. Sci. Lett., 1993;12:691–694

[5] Kulpa and T. Troczynski, “Oxidation of TiB_2 powders below 900 ˚C,” *J. Am. Ceram. Soc.*, 1996; **9**[2]:518–520

[6] Barin, Thermochemical data of pure substances, vol. 1&2, third ed., VCH, Weinheim, 1995 and FactSage software version 6.3

[7] Y.H Koh, S.Y Lee, H.E Kim. Oxidation behavior of titanium boride at elevated temperatures. J Am Ceram Soc 2001;84[1]:239-241

[8] A Tampieri, A Bellosi. Oxidation of monolithic TiB_2 and of Al_2O_3-TiB_2 composite. J Mater Sci 1993;28:649-653

[9] G.V Samsonov, V.A Lavrenko, L.A Glebov. Oxidation of chromium disilicide in oxygen. Translated from Poroshkovaya Metallurgiya 1974;1[133]:46-49

[10] V.A Lavrenko, S.S Chuprov, A.P Umanskii, T.G Protsenko, E.S Lugovskaya. High-temperature oxidation of composite materials based on titanium diboride. Soviet Powder Met Metal Ceram 1987;761–762

[11] M Singh, H Wiedemeier. Chemical interactions in diboride reinforced oxide-matrix composites. J Am Ceram Soc 1991;74[4]:724–727

[12] A Tampieri, E Landi, A Bellosi. J Therm Anal 1992;38:2657-2668

[13] L Zhou, Y Zheng, S Du, H Li. Oxidation behavior of AlN-SiC-TiB_2 ceramics synthesized by SHS-HIP. J Alloys Compd 2009;478:173-176

[14] T Dasgupta, A.M Umarji. Role of milling parameters and impurity on the thermoelectric properties of mechanically alloyed chromium silicide. J Alloys Compd 2008;461:292-297

[15] J Ma, Y Gu, L Shi, L Chen, Z Yang, Y Qian. Synthesis and thermal stability of nanocrystalline chromium disilicide. J Alloys Compd 2004;376:176-179

[16] F.Q Gang, L.H Jun, S.X Hong, L.X Ling, L.K Zhi, H Min. Microstructure and anti-oxidation property of $CrSi_2$-SiC coating for carbon/carbon composites. Appl Surf Sci 2006;252:3475-3480

[17] W.G Fahrenhltz, G.E Hilmas; Oxidation of ultra-high temperatura transition metal diboride ceramics; 2012;57[1]:61-72

[18] T Naoyuki, Y Akira, K Kazuya. High-temperature oxidation behavior of $CrSi_2$ fabricated by spark plasma sintering. Appl Plasma Sci 2004;12:153-157

[19] T Shishido, S Okada, Y Ishizawa, K Kudou, K Iizumi, Y Sawada, et al. Molten metal flux growth and properties of $CrSi_2$. J Alloys Compd 2004;383:319-321

[20] T.J Rockett, W.R Foster. Phase relations in the system boron oxide-silica. J Am Ceram Soc 1965;48[2]:75-80

[21] Acers-NIST phase equilibria Diagrams. CD-ROM data base version 3.1.0 Volume 06. Fig: 06456

[22] Z.A Md, S Sabyasachi, S Bijoy, K.D Dipak. Formation of WSi_2 coating on tungsten and its short-term cyclic oxidation performance in air. Int. Journal of Refractory Metals and Hard Mateirals 2011;29:54-63

[23] F Mohammadi, K.C Saraswat, J.D Meindl. Kinetics of thermal oxidation of WSi_2. Appl. Phys. Lett. 1979;35[7]:529-531

[24] S Okada, K Kudou, K Iizumi, K Kudaka, I Higashi, T Lundstrom. Single –crystal growth and properties of CrB, Cr_3B_4, Cr_2B_3 and CrB_2 from high-temperature aluminum solutions. J Crystal growth 1996;166:429-435

[25] M.L Emiliani. Characterization and oxidation resistance of hot pressed chromium diboride. Mater Sci Eng A 1993;172:111-124

[26] N.C Tombs, W.J Croft, H.C Mattraw. Preparation and properties of chromium borate. Inorganic chemistry 1963;2[4]:872-873

[27] G.V Samsonov, O.P Sharkin, A.D Panasyuk, L.V D'yakonov. Electron microprobe investigations of interfacial reactions in systems composed of a refractory compound and a liquid metal, 2. Effects of oxide films on the character of the interfacial reaction in the system CrB_2-Ni", Translated from Poroshkovaya Metallurgiya 1974;8[140]:68-73

[28] http://www.us.schott.com/english/download/technical_glass_guide_us.pdf

[29] http://www.camglassblowing.co.uk/gproperties.htm

[30] V. B. Voitovich, V. A. Lavrenko and V. M. Adejev, "High-temperature oxidation of titanium diboride of different purity," Oxidation of Metals, 1994;42 [1/2]:145-161.

[31] http://dx.doi.org/10.1063/1.1943506

[32] http://link.springer.com/article/10.1007%2FBF00739299#page-1

[33] http://showard.sdsmt.edu/MET320/Handouts/EllinghamDiagrams/Ellingham_v22_Macro.pdf

[34] R. Mitra, "Mechanical behavior and oxidation resistance of structural silicides", International Materials Reviews, 2006:51[1]:13-64.

[35] A. Agarwal, L. R. Katipelli and N. B. Dahotre, "Elevated temperature oxidation of laser surface engineered composite boride coating on steel," Metal. Mater. Trans. A, 2000;31: 461-473.

[36] J. Cook, A. Khan, E. Lee and R. Mahapatra, "Oxidation of $MoSi_2$-based composites," Mater. Sci. Eng. A, 1992;155:183-198.

[37] Y. H. Koh, H. W. Kim and H. E. Kim, "Improvement in oxidation resistance of TiB_2 by formation of protective SiO_2 layer on surface," J. Mater. Res., 2001;16 [1]:132-137.

[38] F. Monteverde and A. Bellosi, "The resistance to oxidation of an HfB_2-SiC composite," J. Eur. Ceram. Soc., 2005;25:1025-1031.

[39] D. Sciti, M. Brach and A. Bellosi, "Oxidation behavior of a pressureless sintered ZrB_2-$MoSi_2$ ceramic composite," J. Mater. Res., 2005;20[4]:922-930.

[40] D. Sciti, S. Guicciardi, A. Bellosi and G. Pezzotti, “Properties of a pressureless-sintered ZrB_2-$MoSi_2$ ceramic composite,” J. Am. Ceram. Soc., 2006;89[7]:2320-2322.

[41] B. Basu, G. B. Raju and A. K. Suri, “Processing and properties of monolithic TiB_2-based materials,” International Materials Reviews, 2006;51[6]:352-374.

[42] G.B. Raju, K. Biswas and B. Basu, “Microstructural characterization and isothermal oxidation behavior of hot-pressed TiB_2–10 wt.% $TiSi_2$ composite”, Scripta Materialia 2009;61:104–107.

CHAPTER 7

CHAPTER-7

SUMMARY AND SCOPE FOR FUTURE WORK

7.1 Summary of the present work

Syntheses of single-phase refractory metal borides from elemental constituents are expensive. CVD techniques are complex, generally used for coatings and not for commercial production of powders. Borothermic reduction involves loss of expensive boron in the form of boron oxides. Thus, boron carbide reduction method is a better method for the synthesis of refractory metal borides considering both start materials availability and ease of process comfort. B_4C serves both as a reducing agent (due to the presence of carbon) as well as the source of boron to form borides. Hence, the present study of synthesis of borides by carbothermic reduction in the presence of boron carbide leads to obtain a single phase refractory metal borides. By using this method, single phase TiB_2, CrB_2, $(Ti_{0.95}C_{0.05})B_2$, $(Ti_{0.90}C_{0.10})B_2$ and $(Ti_{0.85}C_{0.15})B_2$ materials were synthesized successfully in the present thesis.

Consolidation of TiB_2 is a challenge due to its high melting point; covalent nature requires high temperatures for sintering. However, borides undergo an abnormal grain growth at high temperatures. The occurrence of microcracking at the grain boundaries is also promoted with the increase in grain size. Thus, it is very difficult to achieve crack free dense borides by the conventional cold compaction and sintering, as no shape accommodation occurs without an external pressure and large pores tend to coarsen during high temperature sintering. A thin oxygen rich layer (mainly TiO_2 and B_2O_3) is usually present on the surface of TiB_2 powder, irrespective of synthesis route. The presence of oxygen finally results in increase in grain size and coarsening of pores because the presence of oxides increases the surface diffusivity. In order to overcome the above issues it is very essential to add a suitable sinter additive. Choice of sinter additive is a challenge to obtain a density without losing its (TiB_2) inherent properties. In literature, various metallic/non metallic additives were used to lower the densification temperature. Although metallic additives helps to lower the densification temperature, from the perspective of high temperature applications, the presence of metallic binder is not desirable, the low melting point of either sintering reaction product or metallic additives leads to incipient fusion and consequent degradation of high temperature properties. The principal objective of non-metallic additives is therefore to improve sinterability of TiB_2 without promoting grain growth thus circumventing limitations of metallic additives. Silicides have not been used extensively in the past for densification of TiB_2. Silicides have attracted considerable interest due to their compatibility with borides to densify at lower temperatures. In the present investigations, various silicides were used to densify the TiB_2 by hot pressing. Silicides not only lowered the densification temperature, but also helped to improve the toughness and oxidation resistance. Reactive sintering and liquid phase sintering were the main densification mechanism in all the cases. Silicon in the silicides helped to reduce the surface oxides of TiB_2, which is advantageous as mentioned above. Presence of reaction product/secondary phase helped to improve the fracture toughness by crack deflection or bridging mechanisms. However, presence of silicon also helped to improve the oxidation resistance by formation of a thin glassy layer on the surface. Effect of various silicides and its quantity on the densification, properties and oxidation behavior was mainly studied in this thesis.

Densification results of all composites prepared in this work using TiB_2 of same origin are summarized. Density of TiB_2 composites with varying $MoSi_2$, $TiSi_2$, WSi_2, $CrSi_2$, CrB_2 and composites of $(TiCr)B_2$+20%$MoSi_2$ are presented in Fig.5.44. In all cases, one can see a significant improvement in density with a small addition of 2.5% sinter additive. With higher additions in the case of $TiSi_2$, WSi_2 and CrB_2 content in $(TiCr)B_2$+20%$MoSi_2$ an increase in the density is observed, whereas in other cases a decrease in density is seen. The mechanism of sintering is different in each case and the sintering temperatures also vary as explained above. In the case of sintering with $TiSi_2$ or WSi_2 it is liquid phase sintering. In case of $MoSi_2$, the major contribution in densification is due to compressive deformation of $MoSi_2$ in addition to the formation of liquid reaction product of $TiSi_2$. Whereas during additions of $CrSi_2$, formation of a reaction product of Si was mainly observed, which leads to deteriorate the densification due to its existence in the gaseous phase at the hot pressing temperature under vacuum of 0.001Pa (10^{-5} m.bar). Near theoretical density TiB_2+CrB_2 composites were not obtained due to the absence of liquid phase sintering. At the same time, high dense composites (>96% TD) of TiB_2 were obtained by combined additions of CrB_2 and $MoSi_2$. Dual mechanism of sintering was observed in TiB_2+CrB_2+$MoSi_2$ composites namely: reactive liquid phase sintering and solid solution formation of $(Ti,Cr)B_2$. High dense composite (>99%) of pre-alloyed $(Ti_{0.85}Cr_{0.15})B_2$+20%$MoSi_2$ were also obtained.

From the above, it is clear that addition of silicides to TiB_2 helps to enhance the density by liquid phase sintering and/or activated sintering. When CrB_2 is added to TiB_2 liquid phase sintering was not seen. However, improvement in densification was seen due to the higher mobility of CrB_2 and formation of solid solution with TiB_2. Mechanical and physical properties were evaluated for all these composites.

Effect of isothermal oxidation (850^o C for 64h) behavior of TiB_2 composites are brought here. Weight gain of WSi_2 composite is relatively lower compared with other additives such as $MoSi_2$, $CrSi_2$, $TiSi_2$ and CrB_2. Addition of $MoSi_2$ was found to be to be ineffective due to degradation of oxide layer by the evaporation of MoO_3 at 850^{o}C. Formation of a protective SiO_2/ borosilicate glass layer has been observed on the surface oxide scale, when $TiSi_2$ is added. However, the protective layer was in patches and incomplete. In case of CrB_2, formation of a continuous and protective layer of $CrBO_3$ has been noticed. Continuous and protective layer of SiO_2 is also observed with 15% $CrSi_2$ sample. In the case of WSi_2 addition also, formation of a crack free protective and continuous oxide layer was observed in all the dense composites. Formation of SiO_2 and the solubility of SiO_2 in liquid B_2O_3 to form a stable glass could be the reasons for the improved oxidation resistance of $CrSi_2$ & WSi_2 composites.

It is worthwhile here to compare the oxidation behavior of TiB_2+CrB_2 composites with that of TiB_2+$CrSi_2$ composites. Parabolic rate constants obtained were lower in case of composite with $CrSi_2$ compared to that of CrB_2 on isothermal oxidation at 850^o C for 64h in air. Oxidation of $CrSi_2$ starts at 600^o C where as that of CrB_2 composite at a lower temperature of 460^o C. Specific weight gain of TiB_2 + 5% $CrSi_2$ composite at all temperatures is lower than that of TiB_2+CrB_2 composite. Total weight gain of the composite with $CrSi_2$ is much lower at 19.28 x 10^{-3} Kg/m^2 compared to that of with CrB_2 which was high at 54.83 x 10^{-3} Kg/m^2.

As WSi_2 and $CrSi_2$ are the two additives which form a stable protective oxide layer on TiB_2, the comparisons between these two additives are brought out below. Parabolic rate constants obtained were lower in case of composite with WSi_2 (except 2.5%) compared to that of $CrSi_2$ on isothermal oxidation at 850^o C for 64h in air. Total weight gain of the composite with 15% WSi_2 is much lower at 38.10 x 10^{-3} Kg/m^2 compared to that of with $CrSi_2$ which was high at 58.48 x 10^{-3} Kg/m^2. Hence, it can be concluded that TiB_2 composite with WSi_2 exhibits better oxidation resistance than that with $CrSi_2$.

Effect of isothermal oxidation (850^o C for 64h) behavior of TiB_2 composite is with combined addition of $MoSi_2$ and CrB_2 compared with that of different TiB_2 composites with additives such as $MoSi_2$, WSi_2, $CrSi_2$, $TiSi_2$ and CrB_2. Weight gain of TiB_2 composite is with combined addition of $MoSi_2$ and CrB_2 is relatively lower compared with other composites as indicated above. Hence, it can be concluded that TiB_2 composite with combined addition of $MoSi_2$ and CrB_2 exhibits better oxidation resistance than that of other composites.

Effect of isothermal oxidation (850^o C for 64h) behavior of $(TiCr)B_2$+20%$MoSi_2$ composites are compared with that of composites without pre-alloyed TiB_2+ CrB_2+20% $MoSi_2$ additive. Weight gains of pre-alloyed additive composites are relatively lower compared to composites without pre-alloyed TiB_2+ CrB_2+20% $MoSi_2$ additive. After 256h of oxidation, thickness of the oxide layer was found only <10 µm for $(Ti_{0.85}Cr_{0.15})B_2$+20%$MoSi_2$ composite, where as it was ~100 µm for TiB_2+15%CrB_2+$MoSi_2$ composite. It is clear that pre-alloyed $(TiCr)B_2$+20%$MoSi_2$ composite has the better oxidation resistance compared to TiB_2+ CrB_2+20% $MoSi_2$ composites. Reason for improved oxidation resistance in this $(TiCr)B_2$+20%$MoSi_2$ composite is due to the migration of silicon towards the outer surface, which forms a protective glassy phase, impeding further oxidation (Fig. 6.43 and Fig. 6.49).

7.2 Scope for future work

In this work, only hot pressing and pressureless sintering was used for densification. Advanced processing technique i.e. Spark Plasma Sintering (SPS) can be attempted in future for the densification of these composites. Conventional pressure assisted consolidation techniques like hot pressing, hot isostatic pressing etc., require long processing time and high temperature in order to produce high density composites. The driving force for densification by SPS is provided by passing current directly through the particle material, with simultaneously applying pressure in separate steps. High shear force in combination with pulsed electric power is initially applied to the particle material to generate electrical discharge that activates the particle surface by evaporation of oxide film, impurities and moisture. Subsequently bonding is accomplished by resistance heating at the contact points between the activated particles in the presence of high pressure. The time and temperature required for consolidation is lowered as high current density is applied in addition to high pressure which leads to localized heating and plastic deformation at interparticle contact areas. The rapid sintering which preferably lasts for less than a few minutes prevents grain growth and allows the particles to retain their microstructure. Spark plasma sintering (SPS), Plasma activated sintering (PAS), Plasma pressure consolidation (PPC) and instrumented pulse electro-discharge consolidation are the different names given for the same process.

In the present investigation, the oxidation studies are conducted using isothermal or continuous heating. Considering the fact that TiB_2 materials would experience thermal cycling during high temperature applications, future studies should focus on oxidation resistance behavior in terms of the stability/protectiveness of oxide scale during thermal cyclic oxidation behavior.

Present developed materials have potential for wear resistant applications due to their high hardness and elastic modulus. Hence, tribological studies of these materials can be carried out under different temperatures and atmospheric conditions. In the present study, only refractory metal silicides and borides are used as sintering aids, but in future rare earth metal silicides and borides can be used to enhance the high temperature oxidation properties. In the present study only particulate composites were prepared; in future fiber/whisker reinforced composites can be developed in order to enhance the fracture toughness of the composites.